

GMe



Gesellschaft für
Mikro- und Nanoelektronik

Gesellschaft für
Mikro- und
Nanoelektronik

The Society for Micro- and Nanoelectronics

Annual Report

2003

Vienna, September 2004

GMe



Gesellschaft für
Mikro- und Nanoelektronik

Gesellschaft für
Mikro- und
Nanoelektronik

The Society for Micro- and Nanoelectronics

Annual Report

2003

Society for Micro- and Nanoelectronics

c/o Vienna University of Technology

Institute of Sensor and Actuator Systems

Gusshausstrasse 27-29/366, A-1040 Vienna, Austria

Vienna, September 2004

Editor: Karl Riedling

Layout: Claudia Benedela
Karl Riedling

ISBN: 3-901578-12-9

© 2004 Gesellschaft für Mikro- und Nanoelektronik (GMe)
c/o Technische Universität Wien
Institut für Sensor- und Aktuatorssysteme
Gusshausstraße 27-29/366, A-1040 Wien

The Society for Micro- and Nanoelectronics (GMe — Gesellschaft für Mikro- und Nanoelektronik)

E. Gornik, K. Riedling
Gesellschaft für Mikro- und Nanoelektronik,
c/o Institut für Sensor- und Aktuatorssysteme, TU Wien
Gußhausstraße 27 – 29, A-1040 Wien

Goals of the Society for Micro- and Nanoelectronics

The Society for Micro- and Nanoelectronics (GMe) has been founded in 1985 as “*Society for Microelectronics - Gesellschaft für Mikroelektronik*” with the aim to “*support microelectronics technology and its applications*” in Austria. With the shift of the focus in research from micro to nano technologies the goals of the GMe changed accordingly. Therefore, the GMe has changed its name into “*Society for Micro- and Nanoelectronics — Gesellschaft für Mikro- und Nanoelektronik*” in 2003.

The GMe defines its tasks as follows:

- Support of university-based “high-tech” research in the areas of micro- and nanoelectronics, semiconductor technology, sensors, and opto-electronics;
- Operation of research facilities;
- Support and consulting for industry, in particular, for small and medium enterprises, within the area of micro- and nanoelectronics.

The central task of the GMe is to provide an internationally competitive *infra-structure* in the area of micro- and nanoelectronics technology. The GMe allocates funds to maintain research projects in the fields of semiconductor technology, sensors, opto-electronics, and ASIC design. Thus the infra-structure support generates a base for research projects that are funded by other funding agencies.

Activities of the Society

Due to funding constraints, the present focal point activity of the GMe is the operation of university-based laboratories for microelectronics technology. Nevertheless, the GMe tries to support the other activities mentioned above in their submission and administration of certain projects.

The main task of the GMe in the area of microelectronics technology is the operation of the cleanroom laboratories in Vienna and Linz. The GMe has coordinated the construction of the Microstructure Center (MISZ — Mikrostrukturzentrum) in Vienna; the funds were supplied by the Austrian Federal Ministry of Science and Research. The GMe now finances a significant part of the operation costs for the cleanroom laboratories in Vienna and Linz.

Microelectronics Technology — Cleanroom Vienna

The following university institutes receive support within this focal point activity:

- Vienna University of Technology (*TU Wien*):
 - Institute of Solid State Electronics (*Institut für Festkörperelektronik*)
 - Institute of Industrial Electronics and Material Science (*Institut für Industrielle Elektronik und Materialwissenschaften*)
(since 2004: Institute of Sensor and Actuator Systems – *Institut für Sensor- und Aktuatorssysteme*)

Microelectronics Technology — Cleanroom Linz

The following university institutes receive support within this focal point activity:

- Johannes Kepler University Linz:
 - Institute of Semiconductor and Solid State Physics (*Institut für Halbleiter- und Festkörperphysik*)

Other Activities of the Society

One of the declared tasks of the GMe is to provide information on current Austrian academic activities in the field of microelectronics to industry, in particular to Austrian small- and medium enterprises (SMEs). To enhance the distribution of the results of the research work done with GMe support, the GMe has put the contents of its annual reports — 1995 through 2003 — and the proceedings of the latest seminars organized by the GMe on its Web server. This server provides a variety of search facilities into the reports, thus acting as a Microelectronics Knowledge Base. The GMe Web server is available under the address:

<http://gme.tuwien.ac.at/>

The “GMe Forum 2003”

The biennial seminar of the GMe, the “*GMe Forum*”, took place at the Vienna University of Technology on April 10 and 11, 2003. The intention of the “*GMe Forum*” is to present application-oriented results of international industrial and academic research and to indicate trends for future applications of research results. The “GMe Forum 2003” focused on the technologies and issues involved in the transition from a micro to an nano technology. Ten distinguished speakers from research and industry in Europe and the USA gave plenary lectures. In five invited oral and 22 poster presentations, members of the university institutes that receive support from the GMe presented their results, which would have been impossible to achieve without the contributions of the GMe to the laboratory infrastructure.

The program of the “GMe Forum 2003” was as follows:

Thursday, April 10, 2003**Opening:**

- 09:00 – 09:30 E. GORNIK (President of the GMe)
P. SKALICKY (President of the Vienna University of Technology)

SOI and Waferbonding:

- 09:30 – 10:15 U. GOESELE, S. CHRISTIANSEN (MPI Halle): “*Strained Si and Wafer-Bonding*”
10:15 – 11:00 G. CELLER (Soitec, Summit, NJ, USA): “*SOI: Developments, Challenges, and Applications*”
11:00 – 11:15 Coffee Break
11:15 – 12:00 P. LINDNER, T. GLINSNER, V. DRAGOI, J. WEIXLBERGER, C. SCHAEFER (EV Group, Schärding): “*Key Enabling Process Technologies for Advanced Semiconductors, MEMS and Nanomanufacturing*”

Semiconductor Intellectual Property:

- 12:00 – 12:45 M. KÄSTNER (NewLogic, Lustenau): “*Semiconductor Intellectual Property Industry*”

- 12:45 – 14:00 Lunch – Catering

System on a Chip:

- 14:00 – 14:45 D. DRAXELMAYR, R. PETSCHACHER (Infineon, Villach): “*Mixed-Signal Design for SoCs*”

Nano-Technology:

- 14:45 – 15:30 E.J. FANTNER (IMS, Wien): “*Micro@Nano-Fabrication-Austria*”
15:30 – 16:00 Coffee Break
16:00 – 16:45 E. HAMMEL (Electrovac, Klosterneuburg): “*Applications of Micro- and Nano-Technologies*”
16:45 – 17:30 H.G. CRAIGHEAD (Cornell, Ithaca): “*Nanomechanical Systems*”
17:30 Panel Discussion: “*Can Austria Keep Up Internationally in the Area of Nano-Technology?*”

Friday, April 11, 2003**Organic Electronics:**

- 09:00 – 09:45 G. LEISING (AT&S, Leoben): “*Integrated Organic Electronics*”

Sensors:

- 09:45 – 10:30 M. BRANDL, CH. FÜRBOCK, F. SCHRANK, V. KEMPE (AMS, Unterpremstätten): “*A Modular MEMS Accelerometer Concept*”
10:30 – 11:00 B. JAKOBY (TU Wien): “*Sensors and Interface Electronics for Oil-Condition Monitoring*”

- 11:00 – 11:15 Coffee Break

Thermal Imaging:

- 11:15 – 11:45 D. POGANY (TU Wien): “*Local Thermal and Current Imaging of Power Devices*”

Opto-Electronics:

- 11:45 - 12:15 W. SCHRENK (TU Wien): “*Quantum Cascade Lasers*”
12:15 - 12:45 T. FROMHERZ (JKU Linz): “*Light from Silicon: SiGe Quantum Cascade Structures*”
12:45 - 13:15 K. SCHMIDEGG (JKU Linz): “*In-situ Growth Monitoring and On-Line Composition Determination of MOCVD GaN by Spectroscopic Ellipsometry*”
13:15 Snacks and Poster Exhibition

The Annual Report for 2003 of the Society for Micro- and Nanoelectronics

The GMe is currently supporting the microelectronics technology activities of the cleanroom laboratories in Vienna and Linz. All projects described in this report were, at least partly, carried out in the cleanrooms in Vienna and Linz, respectively. They are *not* specific projects of the GMe but were funded by a variety of other sources. They all have in common that they use the infra-structure provided by the GMe. It would therefore not have been possible to carry out these projects without the support by the GMe.

In addition to the two sections on the central activities in the cleanroom laboratories in Vienna and Linz, there is a "Sensor Systems" section. The sensor system activities are closely linked with the cleanroom at the Vienna University of Technology, and partly carried out using the infrastructure of this cleanroom. The piece of equipment that was co-financed with GMe funds is, in fact, located in the Microstructure Center of the TU Vienna, and available to all groups using the cleanroom facilities. Still, some sensor technology processes require separate equipment due to material or process incompatibilities, and therefore separate laboratories. For reasons of clarity, we chose to put the sensor activities into a separate section of this report.

Contents

Preface	3
E. Gornik, K. Riedling: The Society for Micro- and Nanoelectronics (GMe – Gesellschaft für Mikro- und Nanoelektronik)	3
Microelectronics Technology — Cleanroom Vienna	9
G. Strasser: Cleanroom Vienna	11
M. Austerer <i>et al.</i> : Surface Emitting Quantum Cascade Laser	31
C. Pflügl <i>et al.</i> : Interferometric Temperature Mapping of GaAs-based Quantum Cascade Laser	33
W. Schrenk <i>et al.</i> : Tuning Quantum-Cascade Lasers by Postgrowth Rapid Thermal Processing	37
P. Schwaha <i>et al.</i> : Light Field in Quantum Cascade Ring Lasers.....	39
V. Tamošiūnas <i>et al.</i> : Terahertz Quantum-Cascade Lasers in a Magnetic Field	41
S. Golka <i>et al.</i> : Fabrication of Dry Etched Planar Photonic Crystals for THz Regime	45
M. Coquelin <i>et al.</i> : Plasmon Enhanced THz Emission.....	49
J. Darmo <i>et al.</i> : Heterostructure-Based Photoconductive Terahertz Emitters	53
J. Kröll <i>et al.</i> :Metallic Anti-Reflection Coating for Terahertz Technology	55
T. Müller <i>et al.</i> :Ultrafast Intraband Dynamics in InAs/GaAs Quantum Dots.....	59
F.F. Schrey <i>et al.</i> : Confocal Micro-Photoluminescence and Micro- Photoluminescence Excitation Spectroscopy on Single Self Assembled InAs Quantum Dots	61
G. Fasching <i>et al.</i> :Photocurrent and Photoluminescence Measurements of InAs Quantum Dots	65
G. Pillwein <i>et al.</i> : Fabrication and Characterization of Lateral Quantum Dots in GaAs Heterostructures.....	67
M. Kast <i>et al.</i> : High-Resolution Hot-Electron Spectroscopy in Parallel Magnetic Fields.....	71
D. Rakoczy <i>et al.</i> : BEEM/BEES Investigations on AlAs/GaAs Single Barriers and RTDs	75
M. Heer <i>et al.</i> : Magnetic Tunnel Transistors Studied by Ballistic Electron Emission Microscopy.....	79
S. Bychikin <i>et al.</i> : Thermal Mapping of the SMARTIS SOI Devices under the vf-TLP and TLP Stress Conditions	81
V. Dubec <i>et al.</i> : A Dual-Beam Interferometer for Investigation of ESD Protection Devices under vf-TLP Stress.....	83
M. Blaho <i>et al.</i> : Hot Spot Dynamics in Vertical DMOS under ESD Stress	87
E. Auer <i>et al.</i> : Investigation of the Parasitic FET in Sub-100 nm Trench-DRAM	91
H. Langfischer: Focused Ion Beam Prepared Contacts of Tungsten to Silicon Characterized by a Cross-Bridge Kelvin Resistor Approach.....	95
H. Wanzenboeck <i>et al.</i> :Active Field Effect Transistor Fabricated by FIB- Implantation.....	97
G. Otto <i>et al.</i> : Simulations of Ion Beam Induced Damage in Silicon: Coupled Kinetic Monte Carlo and Molecular Dynamics Simulations	101

A. Lugstein <i>et al.</i> : Advanced Nanoscale Material Processing with Focused Ion Beams — Metallic Nano Dots Realized by a Subtractive Self Organisation Process	103
W. Brezna <i>et al.</i> : Quantitative Scanning Capacitance Spectroscopy.....	107
T. Roch <i>et al.</i> : X-Ray Investigation of Interface Broadening by Rapid Thermal Processing.....	109
H.D. Wanzenboeck <i>et al.</i> : Cell Growth on Prestructured Microelectronic Materials	113
M. Coquelin <i>et al.</i> : Recent Structures for Plasma Instability Search.....	117
J. Kuzmik <i>et al.</i> : Electrostatic Discharge Effects in AlGaN/GaN High-Electron-Mobility Transistors	121
M. Trinker: Development of a Silicon Deep Reactive Ion Etching Process for the Fabrication of Large Area Silicon Phase Gratings.....	125
Microelectronics Technology — Cleanroom Linz	127
G. Bauer <i>et al.</i> : Micro- and Nanostructure Research: Cleanroom Linz.....	129
T. Fromherz <i>et al.</i> : Si/SiGe Cascade Injector QWIPs for Resonator Enhanced, Voltage Tuneable Two-Band Detection.....	149
M. Böberl <i>et al.</i> : Midinfrared continuous-Wave Photoluminescence of Lead Salt Structures up to Temperatures of 190 °C	153
G. Kocher-Oberlehner <i>et al.</i> : Erbium Doped Waveguides in SOI Layers	157
J. Zorbakhsh <i>et al.</i> : Simulation and Fabrication of Photonic Crystals	161
T. Berer <i>et al.</i> : Electron Beam Lithography of Silicon-Based SET Structures.....	165
H. Lichtenberger <i>et al.</i> : Step-Bunching in Si with Faceted Si _{0.55} Ge _{0.45} Top-Layers on High-Miscut Substrates	169
G. Pillwein <i>et al.</i> : Fabrication and Characterization of Lateral Quantum Dots in GaAs Heterostructures.....	173
R.T. Lechner <i>et al.</i> : Ordering in PbSe Quantum Dot Superlattices Investigated by Anomalous X-Ray Diffraction	177
W. Schwinger <i>et al.</i> : Transmission Electron Microscopy of Nanostructures	183
Z. Zhong <i>et al.</i> : Site-Controlled and Size-Homogeneous Ge Islands on Prepatterned Si	187
K. Wiesauer <i>et al.</i> : Strain Relaxation and Misfit Dislocation Interactions in PbTe on PbSe (001) Heteroepitaxy	191
K. Schmidegg <i>et al.</i> : In situ Characterization of MOCVD Growth by High Resolution X-Ray Diffraction	197
W. Jantsch <i>et al.</i> : Spin Relaxation in Si Quantum Wells Suppressed by an Applied Magnetic Field	201
D. Gruber <i>et al.</i> : Device Processing for Spintronics Applications	205
G. Brunthaler <i>et al.</i> : Two-Dimensional Metallic State in Silicon-on-Insulator Structures	209
Sensor Systems.....	213
M.J. Vellekoop: Sensor Systems	215
J.H. Nieuwenhuis <i>et al.</i> : Integrated Flow-Cells for Adjustable Sheath Flows.....	225
J.H. Nieuwenhuis <i>et al.</i> : Particle Behavior in a Non-Coaxial Sheath Flow.....	233
J.H. Nieuwenhuis <i>et al.</i> : An Integrated Projection Cytometer	239
P. Svasek <i>et al.</i> : Micromachined Mixing Device for FTIR-Spectroscopy	243

Microelectronics Technology — Cleanroom Vienna

Cleanroom Vienna

G. Strasser

**Micro Structure Center of the Vienna University of Technology,
Floragasse 7, A-1040 Vienna, Austria**

In this report a summary of the main activities in the MISZ TU Wien (Mikrostrukturzentrum der Technischen Universität Wien) during the year 2003 will be given. Till the end of 2003, the MISZ was a central institution of the TU Wien. Since 2004, the institution is part of the Electrical Engineering department and was renamed to demonstrate the strong position it takes in the development of novel concepts and down-scaling strategies. The new name – *Zentrum für Mikro- und Nanostrukturen* – underlines the twofold mission we see in the development of mature technologies and the introduction of new concepts. Within this report we describe projects taking intensive use of the cleanroom and the available technologies within. This includes state of the art growth of III-V nanostructures and silicon processing, structuring techniques utilizing standard contact lithography, the production of patterned masks, ion milling as well as dry etching and plasma enhanced chemical vapor deposition, electron beam writing, focused ion beam etching and depositing, and different metallization techniques. A major part of the mission of the ZMNS is the development and production of optoelectronic and microelectronic prototype devices.

Introduction

An overview of the main research efforts with a high need of technological input is presented within this scientific report. This summary includes the majority of experimental projects of the solid state electronics institute (Festkörperelektronik TU Wien) during the year 2003. All the projects described below like transport studies in low dimensional semiconductor nanostructures, scanning probe spectroscopy, realization of new and improved optoelectronic devices, quantum cascade lasers, THz sources, and the characterization of microelectronic devices take full advantage of the technologies installed in the cleanroom of the MISZ (Reinraum Mikrostrukturzentrum der TU Wien), which is now part of the ZMNS.

To structure this yearly increasing number of various activities, six research areas are introduced, namely:

- Optoelectronics & THz technology
- Quantum Dots
- Transport in III-V Semiconductors
- Silicon Device Testing
- Focused Ion Beam Developments
- Novel Characterization Techniques and Devices

To satisfy this variety of topics and demonstrate e.g. optoelectronic devices as well as basic research and the development of new tools for semiconductor industry, different technologies have to be kept at state of the art performance.

This includes growth of semiconductor nanostructures (molecular beam epitaxy), as well as a complete process line including structure definition (lithography), structure transfer (reactive ion etching, focussed ion beam etching, ion milling, wet chemical etching techniques) and coating with metals and/or dielectrics (plasma-enhanced

chemical vapor deposition, sputtering, electron gun evaporation, focussed ion beam deposition). Surface morphology as well as local carrier concentration probing is done with a conventional Atomic Force Microscope (AFM) in combination with a Scanning Capacitance Microscopy (SCM) extension.

All the equipment necessary for the above mentioned technologies needs the cleanroom environment (cooling, filtered air, constant temperature and humidity, high quality water, various inert gases) as well as periodic maintenance of the equipment and the cleanroom itself, e.g. pumping systems (rotary pumps, turbo pumps), exhaust filtering, liquid nitrogen, and cleaning and repair. Testing of the cleanroom quality and adjustment (laminar airflow, filters, cooling, humidity, and temperature) is done periodically.

For a more general overview the listed projects and the attached publication list may give more insides on the broad range of activities in our facility.

Optoelectronics/THz technology

M. Austerer, C. Pflügl, W. Schrenk, T. Roch, and G. Strasser:

Surface Emitting Quantum Cascade Laser

C. Pflügl, M. Litzenberger, W. Schrenk, D. Pogany, E. Gornik, G. Strasser:

Interferometric Temperature Mapping of GaAs-based Quantum Cascade Laser

W. Schrenk, S. Anders, T. Roch, C. Pflügl, G. Strasser:

Tuning Quantum-Cascade Lasers by Postgrowth Rapid Thermal Processing

P. Schwaha, S. Anders, V. Tamosiunas, W. Schrenk, and G. Strasser:

Light field in Quantum Cascade Ring Lasers

V. Tamosiunas, R. Zobl, G. Fasching, J. Ulrich, G. Strasser, K. Unterrainer, R. Colombelli, C. Gmachl, L.N. Pfeiffer, K.W. West, F. Capasso:

Terahertz Quantum-Cascade Lasers in a Magnetic Field

S. Golka, W. Schrenk, and G. Strasser:

Fabrication of dry etched planar Photonic Crystals for THz regime

M.Coquelin, R.Zobl, G.Strasser, E.Gornik:

Plasmon Enhanced THz Emission

J. Darmo, G. Strasser, J. Kröll, and K. Unterrainer:

Heterostructure-Based Photoconductive Terahertz Emitters

Josef Kröll, Juraj Darmo, and Karl Unterrainer:

Metallic Anti-Reflection Coating for Terahertz Technology

Quantum dots

T. Müller, F. F. Schrey, G. Fasching, G. Strasser, and K. Unterrainer:

Ultrafast Intraband Dynamics in InAs/GaAs Quantum Dots

F.F. Schrey, G. Fasching, T. Müller; G. Strasser, and K. Unterrainer:

Confocal Micro-Photoluminescence and Micro-Photoluminescence Excitation Spectroscopy on Single Self Assembled InAs Quantum Dots

G. Fasching, F. F. Schrey, G. Strasser, and K. Unterrainer:

Photocurrent and Photoluminescence Measurements of InAs Quantum Dots

G. Pillwein, G. Brunthaler, G. Strasser:

Fabrication and Characterization of Lateral Quantum Dots in GaAs Heterostructures

Transport in III-V Semiconductors

M. Kast, C. Pacher, M. Coquelin, W. Boxleitner, G. Strasser, E. Gornik:
High-Resolution Hot-Electron Spectroscopy in Parallel Magnetic Fields

D. Rakoczy, G. Strasser, and J. Smoliner:
BEEM/BEES Investigations on AIAs/GaAs Single Barriers and RTDs

R. Heer, J. Smoliner, J. Bornemeier, H. Brückl:
Magnetic Tunnel Transistors Studied by Ballistic Electron Emission Microscopy

Silicon Device Testing

S. Bychikhin, D. Pogany, E. Gornik, M. Graf, F. Dietz, V. Dudek, W. Soppa, H. Wolf:
Thermal Mapping of the SMARTIS SOI Devices Under the vf-TLP and TLP Stress Conditions

V. Dubec, S. Bychikhin, M. Blaho, D. Pogany, E. Gornik, J. Willemen, N. Qu, W. Wilkening, L. Zullino, A. Andreini:
A Dual-Beam Interferometer for Investigation of ESD Protection Devices under vf-TLP Stress

M. Blaho, V. Dubec, D. Pogany, M. Denison, M. Stecher, E. Gornik:
Hot Spot Dynamics in Vertical DMOS under ESD Stress

E. Auer and E. Bertagnolli:
Investigation of the Parasitic FET in Sub-100 nm Trench-DRAM

Focused Ion Beam Developments

H. Langfischer:
Focused Ion Beam Prepared Contacts of Tungsten to Silicon Characterized by a Cross-Bridge Kelvin Resistor Approach

H. Wanzenboeck, E. Bertagnolli:
Active Field Effect Transistor Fabricated by FIB-implantation

G. Otto, G. Hobler:
Simulations of Ion Beam Induced Damage in Silicon: Coupled Kinetic Monte Carlo and Molecular Dynamics Simulations

A. Lugstein, B. Basnar, M. Weil, J. Smoliner, and E. Bertagnolli:
**Advanced Nanoscale Material Processing with Focused Ion Beams
Metallic Nano Dots Realized by a Subtractive Self Organization Process**

Novel Characterization Techniques and Devices

W. Brezna, M. Schramboeck, A. Lugstein, S. Harasek, H. Enichlmair, E. Bertagnolli, E. Gornik, J. Smoliner:
Quantitative Scanning Capacitance Spectroscopy

T. Roch, W. Schrenk, S. Anders, C. Pflügl, G. Strasser:
X-ray Investigation of Interface Broadening by Rapid Thermal Processing

H. D. Wanzenboeck, C. Almeder, C. Pacher, E. Bertagnolli, E. Bogner, M. Wirth, F. Gabor:
Cell Growth on Prestructured Microelectronic Materials

M. Coquelin, R. Zobl, G. Strasser, E. Gornik:
Recent Structures for Plasma Instability Search

J. Kuzmík, D. Pogany, E. Gornik, P. Javorka and P. Kordoš:

Electrostatic Discharge Effects in AlGaIn/GaN High-Electron-Mobility Transistors

M. Trinker:

Development of a Silicon Deep Reactive Ion Etching Process for the Fabrication of Large Area Silicon Phase Gratings

Project Information

Project Manager

Cleanroom MISZ TU Wien (since 2004 ZMNS TU Wien)

G. Strasser, Floragasse 7, A-1040 Wien

Project Group

Last Name	First Name	Status	Remarks
Anders	Solveig	postdoc	
Auer	Erwin	student	
Austerer	Maximilian	student	
Basnar	Bernhard	postdoc	
Beiter	Klaus	student	
Bertagnolli	Emmerich	o. prof.	
Blaho	Matej	dissertation	
Boxleitner	Winfried	postdoc	
Bychikhin	Sergey	postdoc	
Brezna	Wolfgang	dissertation	
Coquelin	Michael	dissertation	
Darmo	Juraj	postdoc	
Dubec	Viktor	dissertant	
Dzidal	Elvira	technician	
Fasching	Gernot	dissertation	
Fürnhammer	Felix	dissertation	
Golka	Sebastian	dissertation	
Gornik	Erich	o. prof.	
Gruber	Karl	student	
Harasek	Stefan	dissertation	
Hobler	Gerhard	ao. prof.	
Kamvar	Parvis	student	
Kast	Michael	dissertation	
Kröll	Josef	student	
Kröll	Peter	technician	
Kuzmik	Ian	postdoc	
Langfischer	Helmut	dissertation	
Litzenberger	Martin	dissertation	
Lugstein	Alois	univ. ass.	
Müller	Thomas	dissertation	

Last Name	First Name	Status	Remarks
Otto	Gustav	dissertation	
Pacher	Christoph	dissertation	
Pogany	Dionyz	univ. ass.	
Prinzinger	Johannes	technician	
Pflügl	Christian	dissertation	
Rebohle	Lars	postdoc	
Rakoczy	Doris	dissertation	
Riegler	Erich	technician	
Roch	Tomas	postdoc	
Schinnerl	Markus	technician	
Schenold	Helmut	technician	
Schrenk	Werner	cleanroom director	
Schrey	Frederik	dissertation	
Schwaha	Philipp	student	
Smoliner	Jürgen	ao. prof.	
Steinesberger	Gernot	dissertant	
Strasser	Gottfried	ao. prof.	
Tamosiunas	Vincas	postdoc	
Ulrich	Jochen	dissertation	
Unterrainer	Karl	ao. prof.	
Wanzenböck	Heinz	univ. ass.	
Zobl	Reinhard	dissertation	

Books and Contributions to Books

1. S. Anders, G. Strasser, E. Gornik; "Long wavelength laser diodes"; in Handbook of Laser Technology and Applications; Ed.: C. Webb, IoP Publishing, Bristol, UK

Publications in Reviewed Journals

1. M. Lackner, C. Forsich, F. Winter, S. Anders, and G. Strasser: "Investigation of biomass steam gasification gas using a GaAs based quantum cascade laser emitting at 11 μm ", Optics Communications 216, 357 (2003)
2. C. Pflügl, M. Litzenberger, W. Schrenk, D. Pogany, E. Gornik, G. Strasser; "Interferometric study of thermal dynamics in GaAs-based quantum cascade lasers"; Appl. Phys. Lett. 82, 1664 (2003)
3. Selected for the Virtual J. of Nanoscale Science & Technology 7 (12) 2003
4. D. Rakoczy, R. Heer, G. Strasser, J. Smoliner; "High Energy Ballistic Transport in Hetero- and Nanostructures"; Physica E 16, 129 (2003)
5. W. Brezna, H. Wanzenböck, A. Lugstein, E. Bertagnolli, E. Gornik, J. Smoliner, "Focussed Ion Beam Induced Damage in Silicon Studied by Scanning Capacitance Microscopy", Semicond. Sci. Technol. 18, 195 (2003)

6. J. Darmo, T. Müller, G. Strasser, K. Unterrainer, G. Tempea; "Terahertz emitter with an integrated semiconductor Bragg mirror"; *Electron. Lett.* 39, 460-462 (2003)
7. S. Harasek, H.D. Wanzenboeck, E. Bertagnolli, "Compositional and electrical properties of zirconium dioxide thin films chemically deposited on silicon", *J. Vac. Sci. Technol. A* 21, 653-658 (2003)
8. S. Anders, W. Schrenk, A. Lugstein, G. Strasser; "Room temperature lasing of electrically pumped quantum cascade micro-cylinders"; *Physica E* 17, 626-628 (2003)
9. L. Rebohle, F.F. Schrey, S. Hofer, G. Strasser, K. Unterrainer; "Energy level engineering in InAs quantum dot stacks embedded in AlAs/GaAs superlattices"; *Physica E* 17, 42-45 (2003)
10. W. Brezna, H. Wanzenböck, A. Lugstein, E. Bertagnolli, E. Gornik, J. Smoliner, Focussed ion beam induced damage in silicon investigated with scanning capacitance microscopy, *Physica E* 19, 178, (2003)
11. A. Lugstein, B. Basnar, J. Smoliner, and E. Bertagnolli, "FIB processing of silicon in the nanoscale regime", *Appl. Physics A*. 76, 545-548 (2003)
12. A. Kueng, C. Kranz, B. Mizaikoff, A. Lugstein, E. Bertagnolli, "Combined Scanning Electrochemical Atomic Force Microscopy for Tapping Mode Imaging", *Appl. Phys. Lett.* 82, 1592(2003)
13. W. Schrenk, S. Anders, C. Pflügl, E. Gornik, G. Strasser, C. Becker, C. Sirtori; "Improved temperature performance of GaAs/AlGaAs quantum cascade lasers"; *Inst. Phys. Conf. Ser.* 174 (5); IOP Publishing Ltd., 385 (2003)
14. C. Pflügl, M. Litzenberger, W. Schrenk, S. Anders, D. Pogany, E. Gornik, G. Strasser; "Interferometric temperature mapping of GaAs-based quantum cascade laser"; *Inst. Phys. Conf. Ser.* 174 (5); IOP Publishing Ltd., 375 (2003)
15. M. Blaho, D. Pogany, E. Gornik, M. Denison, G. Groos, M. Stecher, "Study of internal behavior in a vertical DMOS transistor under short high current stress by an interferometric mapping method", *Microel. Reliab.*, 43 545 (2003)
16. F. F. Schrey, E. E. Chaban, M. J. Matthews, and J. W. P. Hsu, "A Microscope for Imaging, Spectroscopy, and Lithography at the Nanometer Scale: Combination of a Two-photon Laser Scanning Microscope and an Atomic Force Microscope", *Rev. Scient. Instr.* 74, 1211 (2003)
17. H. Langfischer, E. Bertagnolli, "Focused ion beam prepared contacts of tungsten to silicon characterized by a cross-bridge Kelvin resistor approach", *Journal of Applied Physics*, 93, 5827 (2003)
18. A. Lugstein, W. Brezna, M. Stockinger, B. Goebel, L. Palmetshofer, E. Bertagnolli, "Nonuniform-channel MOS device" *Appl. Phys. A* 76, 1035-1039 (2003)
19. S. Anders, L. Rebohle, F. F. Schrey, W. Schrenk, K. Unterrainer, and G. Strasser, "Electroluminescence of a quantum dot cascade structure", *Appl. Phys. Lett.* 82, 3862 (2003)
20. Selected for the *Virtual J. of Nanoscale Science & Technology* 7 (23) 2003
21. M. Kast, W. Boxleitner, C. Pacher, G. Strasser, E. Gornik, "Hot Electron Spectroscopy in parallel magnetic fields", *Appl. Phys. Lett.* 82, 3922 (2003)
22. D. Pogany, V. Dubec, , S. Bychikhin, C. Fürböck, M. Litzenberger, S. Naumov, G. Groos, M. Stecher, E. Gornik, "Single-shot nanosecond thermal imaging of semiconductor devices using absorption measurements", *IEEE Trans. Dev. Mat. Reliab.*, 3, 85 (2003)

23. V. Dubec, S. Bychikhin, M. Blaho, D. Pogany, E. Gornik, J. Willemen, N. Qu, W. Wilkening, L. Zullino, A. Andreini, "A dual-beam Michelson interferometer for investigation of trigger dynamics in ESD protection devices under vf-TLP stress", *Microel. Reliab.* 43, 1557 (2003)
24. S. Harasek, A. Lugstein, H.D. Wanzenboeck, E. Bertagnolli, "Slow Trap Response of Zirconium Dioxide Thin Film on Silicon", *Appl. Phys. Lett.* 83, 1400 (2003)
25. A. Kueng, C. Kranz, A. Lugstein, E. Bertagnolli, B. Mizaikoff, "Integrated atomic force scanning electrochemical microscopy in tapping mode: Simultaneous topographical and electrochemical imaging of enzyme activity", *Angew. Chem. Int. Ed.* 42, 3238 (2003)
26. A. Kueng, C. Kranz, A. Lugstein, E. Bertagnolli, B. Mizaikoff, "Simultane topographische und elektrochemische Abbildung von Enzymaktivität in integrierten AFM-SECM-Rasternahfeldsonden im AFM-Tapping-Modus", *Angew. Chem.* 115, 3358 (2003)
27. D. Rakoczy, G. Strasser, J. Smoliner; "Imaging Impurities in AlAs/GaAs Single Barrier Structures in the Regime of the Mott Transition"; *Phys. Rev. B* 68, 073304 (2003)
28. Selected for the *Virtual J. of Nanoscale Science & Technology* 8 (10) 2003
29. J. W. P. Hsu, F. F. Schrey, and H. M. Ng, "Spatial distribution of yellow luminescence related deep levels in GaN", *Appl. Phys. Lett.* 83, 4172 (2003)
30. W. Brezna, M. Schramboeck, A. Lugstein, S. Harasek, H. Enichlmair, E. Bertagnolli, E. Gornik, J. Smoliner, "Quantitative Scanning Capacitance Spectroscopy", *Appl. Phys. Lett.* 83, 4253 (2003)
31. J. W. P. Hsu, N. G. Weimann, M. J. Manfra, K. W. West, D. V. Lang, F. F. Schrey, and O. Mitrofanov, R. J. Molnar, "Effect of dislocations on local transconductance in AlGaIn/GaN heterostructures as imaged by scanning gate microscopy", *Appl. Phys. Lett.* 83, 4559 (2003)
32. E. Bertagnolli: "Nanoelektronik", e&i (Elektrotechnik und Informationstechnik) *Verbandszeitschrift* 9, 267 (2003)
33. D. Pogany ; S. Bychikhin ; J. Kuzmik ; V. Dubec ; N. Jensen ; M. Denison ; G. Groos ; M. Stecher ; E. Gornik: "Thermal Distribution During Destructive Pulses in ESD Protection Devices Using a Single-Shot, Two-Dimensional Interferometric Method", *IEEE Trans. on Dev. and Mat. Reliab.*, 3 (2003)
34. J. Kuzmik, D. Pogany, E. Gornik, P. Javorka, P. Kordoš: "Electrostatic discharge effects in AlGaIn/GaN HEMTs", *Appl. Phys. Lett.* 83, 4655 (2003)
35. C. Pflügl, W. Schrenk, S. Anders, G. Strasser, C. Becker, C. Sirtori, Y. Bonetti, A. Müller, "High temperature performance of GaAs-based bound-to-continuum quantum cascade lasers", *Appl. Phys. Lett.* 83, 4698 (2003)
36. Selected for the *Virtual J. of Nanoscale Science & Technology* 8 (24) 2003
37. J.W.P. Hsu, F.F. Schrey, M.J. Matthews, S.L. Gu, T.F. Kuech, "Impurity Effects on Photoluminescence in Lateral Epitaxially Overgrown GaN" *J. of electric materials*, 32, 322 (2003)
38. C. Pacher, E. Gornik, "Adjusting the coherent transport in finite periodic superlattices" *Phys. Rev. B* 68, 155319 (2003)
39. S. Bychikhin, V. Dubec, M. Litzenberger, D. Pogany, E. Gornik, G. Groos, K. Esmark, M. Stecher, W. Stadler, H. Gieser, H. Wolf "Investigation of ESD

- protection elements under high current stress in CDM-like time domain using backside laser interferometry" J. of Electrostatics 59, 241 (2003)
40. V. Tamosiunas, R. Zobl, J. Ulrich, K. Unterrainer, R. Colombelli, C. Gmachl, F. Capasso, K. West, L. Pfeiffer, "Terahertz Quantum Cascade Lasers in a Magnetic Field", Appl. Phys. Lett. 83, 3873 (2003)
 41. T. Müller, F. F. Schrey, G. Strasser, and K. Unterrainer, "Ultrafast intraband spectroscopy of electron capture and relaxation in InAs/GaAs quantum dots", Appl. Phys. Lett. 83, 3572 (2003)
 42. Selected for the Virtual J. of Nanoscale Science & Technology 8 (18) 2003
 43. Selected for the Virtual Journal of Ultrafast Science 2 (11) 2003
 44. J. N. Heyman, N. Coates, A. Reinhardt, G. Strasser; "Role of Diffusion and Drift in Terahertz Emission at GaAs Surfaces"; Appl. Phys. Lett. 83, 5476 (2003)
 45. U. Merc, C. Pacher, M. Topic, F. Smole, E. Gornik, "Electron velocity in superlattices", Eur. Phys. J. B 35, 443 (2003).
 46. A. Lugstein, W. Brezna, G. Hobler, and E. Bertagnolli, "A novel method to characterize the 3D-distribution of focused ion beam induced damage in silicon after 50 keV Ga⁺ irradiation", J. Vac. Sci. Technol. A 21, 1644 (2003)
 47. G. Hobler and G. Otto, "Status and open problems in modeling as-implanted damage in silicon", Mat. Sci. Semicond. Proc. 6, 1(2003)
 48. G. Hobler and G. Otto, "Amorphous pocket model for silicon based on molecular dynamics simulations", Nucl. Instr. Meth. B 206, 81 (2003)
 49. G. Otto, G. Hobler, and K. Gärtner, "Defect characterization of low-energy recoil events in silicon using classical molecular dynamics simulation", Nucl. Instr. Meth. B 202, 114 (2003)

Conference Proceedings

1. W. Brezna, S. Harasek, H. Enichlmair, E. Bertagnolli, E. Gornik, and J. Smoliner, "ZrO₂ as Dielectric Material for Device Characterization with Scanning Capacitance Microscopy", Electrochemical Society Proceedings vol. 2003-03 378 (2003)
2. M. Blaho, D. Pogany, E. Gornik, H. Wolf, H. Gieser, L. Zullino, E. Morena, R. Stella, A. Andreini: "Internal behavior of BCD ESD protection devices under very-fast TLP stress"; Proc. of IRPS'03, 235 (2003)
3. D. Pogany, S. Bychikhin, E. Gornik, M. Denison, N. Jensen, G. Groos and M. Stecher: "Moving current filaments in ESD protection devices and their relation to electrical characteristics", Proc. of IRPS'03, 241 (2003)
4. S. Anders, W. Schrenk, C. Pflügl, E. Gornik, G. Strasser, C. Becker, and C. Sirtori; "Room temperature operation of GaAs-based quantum cascade lasers processed as ridge and microcavity waveguides"; IEE Proc.-Optoelectron. 150, 282 (2003)
5. T. Le, G. Tempea, A. Stingl, J. Darmo, G. Strasser, K. Unterrainer; "Compact THz-source based on femtosecond Ti:S laser and intracavity photoconductive antenna"; Photonics West Proc., San Jose, USA, 25.-31.1.2003
6. C. Pflügl, M. Litzenberger, W. Schrenk, D. Pogany, E. Gornik, G. Strasser; "Thermal characteristics of GaAs-based quantum cascade lasers"; CLEO 2003, ISBN 1-55752-733-4, Technical Digest 55 (2003)

7. K. Unterrainer, J. Darmo, T. Müller, G. Strasser, G. Tempea, T. Le, A. Stingl; "Cavity enhanced few-cycle THz generation and coherent spectroscopy"; CLEO 2003, ISBN 1-55752-733-4, Technical Digest 35 (2003)
8. D. Pogany, "Local Thermal and current imaging of power devices", ISBN: 3-901578-10-2, Proceedings GMe Forum 2003, 51 (2003)
9. S. Harasek, H. D. Wanzenboeck, B. Basnar, J. Smoliner, E. Bertagnolli: "Zirconium Dioxide Thin Films for Microelectronics Deposited by Metal Organic Chemical Vapor Deposition", ISBN: 3-901578-10-2, Proceedings GMe Forum 2003, 157 (2003)
10. H. D. Wanzenboeck, S. Harasek, H. Langfischer, E. Bertagnolli: "Deposition Mechanism of Direct-Write Processes – An Application-Oriented Approach to Custom-Tailored Material Properties", ISBN: 3-901578-10-2, Proceedings GMe Forum 2003, 149 (2003)
11. M. Kast, C. Pacher, G. Strasser, E. Gornik; "Transport through Wannier-Stark states in biased finite superlattices"; ISBN: 3-901578-10-2, Proceedings GMe Forum 2003, 165 (2003)
12. F.F. Schrey, L. Rebohle, T. Müller, S. Anders, W. Schrenk, K. Unterrainer, G. Strasser; "Modification of the photoresponse by energy level engineering in InAs quantum dot nanostructures"; ISBN: 3-901578-10-2, Proceedings GMe Forum 2003, 97 (2003)
13. T. Müller, W. Parz, G. Strasser, K. Unterrainer; "Time-resolved measurement of intersubband population dynamics "; ISBN: 3-901578-10-2, Proceedings GMe Forum 2003, 93 (2003)
14. J. Darmo, G. Strasser, T. Müller, T. Roch, K. Unterrainer; "New generation of photoconductive Terahertz emitters"; ISBN: 3-901578-10-2, Proceedings GMe Forum 2003, 85 (2003)
15. P. Schwaha, S. Anders, T. Roch, W. Schrenk, and G. Strasser; "Electrically pumped quantum cascade ring lasers"; ISBN: 3-901578-10-2, Proceedings GMe Forum 2003, 77 (2003)
16. W. Schrenk, S. Anders, C. Pflügl, E. Gornik, G. Strasser; "Quantum Cascade Lasers"; ISBN: 3-901578-10-2, Proceedings GMe Forum 2003, 61 (2003)
17. S. Harasek, H.D. Wanzenboeck, W. Brezna, J. Smoliner, E. Gornik, and E. Bertagnolli: "Utilizing MOCVD for high-quality Zirconium Dioxide Gate Dielectrics in Microelectronics", Electrochemical Society Proceedings vol. 2003-08 894 (2003)
18. G. Strasser; "GaAs-based Quantum Cascade Lasers"; Proc. of 11th Int. Symp. Nanostructures: Physics and Technology; ISBN 5-93634-009-0, 6 (2003)
19. M. Denison, M. Blaho, D. Silber, J. Joos, N. Jensen, M. Stecher, V. Dubec, D. Pogany, E. Gornik: "Hot spot dynamics in quasi vertical DMOS under ESD stress", Proc. of ISPSD'03, 80 (2003)
20. J. Kuzmík, M Blaho, D. Pogany, E. Gornik, A. Alam, Y. Dikme, M. Heuken, P. Javorka, M. Marso, and P. Kordoš, " Backgating, high-current and breakdown characterisation of AlGaIn/GaN HEMTs on silicon substrates" Proc. ESSDERC'03, 319 (2003)
21. M. Graf, V. Dudek, W. Soppa, H. Wolf, S. Bychikhin, D. Pogany E. Gornik, "Impact of layer thickness variations of SOI-wafer on ESD robustness", Poc. EOS/ESD 2003 Symposium, 116 (2003)
22. V.Dubec, S. Bychikhin, M. Blaho, D. Pogany, E. Gornik, J. Willemen, N. Qu, W. Wilkening, L. Zullino, A. Andreini, A dual-beam Michelson interferometer for

- investigation of trigger dynamics in ESD protection devices under very fast TLP stress, *Microel. Reliab.*, 1557 (2003)
23. D. Pogany, S. Bychikhin, M. Blaho, V. Dubec, J. Kuzmik, M. Litzenberger, C. Pflügl, G. Strasser, E. Gornik, "Transient interferometric mapping of temperature and free carriers in semiconductor devices", *Conf. Proc. LEOS '03, IEEE 03CH37460*, 666 (2003)
 24. G. Strasser; "Growth and Technology of QC lasers"; *Crystal Growth and Epitaxy, Proc. Rev. Conf. on scientific coop. between Austria & Poland*; ISBN 83-88443-21-6, 191 (2003)
 25. S. Anders, E. Gornik, W. Schrenk, G. Strasser; "GaAs-based Quantum-Cascade Laser Diodes"; *LEOS Proc. of 15th Int. Conf. on InP and Related Materials*, 235, *IEEE 03CH37413* (2003)
 26. M. Coquelin, C. Pacher, M. Kast, G. Strasser, E. Gornik; "Transport studies on double period superlattices utilizing Hot Electron Spectroscopy"; *Proc. 26th Int. Conf. on the Physics of Semiconductors (ICPS26)*, P154; ed. A.R. Long and J.H. Davies, IOP, Bristol (2003)
 27. C. Pacher, G. Fasching, M. Kast, G. Strasser, E. Gornik; "Study of Electron-Phonon Scattering in wide GaAs Quantum Wells utilizing Hot Electron Spectroscopy"; *Proc. 26th Int. Conf. on the Physics of Semiconductors (ICPS26)*, P168; ed. A.R. Long and J.H. Davies, IOP, Bristol (2003)
 28. F. Eickemeyer, K. Reimann, M. Woerner, T. Elsaesser, S. Barbieri, C. Sirtori, G. Strasser, T. Müller, R. Bratschitsch, K. Unterrainer: "Ultrafast gain dynamics in quantum cascade laser structures"; *Proc. 26th Int. Conf. on the Physics of Semiconductors (ICPS26)*, M1.3; ed. A.R. Long and J.H. Davies, IOP, Bristol (2003)
 29. M. Kast, C. Pacher, G. Strasser, E. Gornik; "Transport through Wannier-Stark states in biased finite superlattices"; *Proc. 26th Int. Conf. on the Physics of Semiconductors (ICPS26)*, D137; ed. A.R. Long and J.H. Davies, IOP, Bristol (2003)
 30. N. Jensen, G. Groos, M. Denison, J. Kuzmik, D. Pogany, E. Gornik, M. Stecher, "Coupled bipolar transistors as very robust ESD protection devices for automotive applications", *Proc. 25th Annual International EOS/ESD Symposium*, 313-318 (2003)
 31. W. Stadler, K. Esmark, K. Reynders, M. Zubeidat, M. Graf, W. Wilkening, J. Willemen, N. Qu, S. Mettler, M. Etherton, H. Wolf, H. Gieser, W. Soppa, V. De Heyn, M. Natarajan, G. Groeseneken, E. Morena, R. Stella, A. Andreini, M. Litzenberger, D. Pogany, E. Gornik, C. Foss, D. Nuernbergk, A. Konrad, M. Frank "Test Circuits for Fast and Reliable Assessment of CDM Robustness of I/O stages", *Proc. of EOS/ESD Symposium*, 319 (2003)
 32. M. Blaho, M. Denison, V. Dubec, D. Pogany, M. Stecher and E. Gornik: "Hot spot mapping in the DMOS devices for automotive applications", *Beitraege der Informationstagung Mikroelektronik* 329 (2003)

Presentations

1. V. Tamosiunas, R. Zobl, G. Fasching, J. Ulrich, G. Strasser, K. Unterrainer, R. Colombelli, C. Gmachl, F. Capasso, K. West, L. Pfeiffer; "Terahertz quantum cascade lasers in strong magnetic fields"; *IOP-meeting on Quantum Cascade Lasers*, Univ. of Leeds, UK, 15.1.2003

2. J. Darmo, T. Müller, G. Strasser, K. Unterrainer, T. Le, and A. Stingl (invited), "Bragg mirror enhanced THz antennas for intracavity THz generation and mode-locking", Workshop on Quantum Heterostructures and THz electronics, Regensburg, Germany 23.1.2003
3. C. Pflügl, M. Litzenberger, W. Schrenk, S. Anders, D. Pogany, E. Gornik, G. Strasser; "Thermal Dynamics of GaAs-based quantum cascade lasers"; Photonics West, San Jose, USA, 25.-31.1.2003
4. S. Anders, P. Schwaha, W. Schrenk, and G. Strasser; "Electrically pumped quantum cascade ring lasers"; 12th Euro-MBE Workshop, Bad Hofgastein, Austria, Feb. 16.-19.2.2003
5. J. Darmo, T. Roch, G. Strasser, T. Müller, K. Unterrainer; "Resonant-cavity based THz photoconductive emitters"; 12th Euro-MBE Workshop, Bad Hofgastein, Austria, Feb. 16.-19.2.2003
6. F. F. Schrey, T. Müller, S. Anders, L. Rebohle, W. Schrenk, K. Unterrainer, G. Strasser; "Dynamics between electronic levels in InAs Quantum dots"; 7th Int. Workshop on Nonlinear Optics and Excitation Kinetics in Semicond. (NOEKS 7); Karlsruhe, Germany, 24.-28.2.2003
7. W. Brezna, H. Wanzenböck, A. Lugstein, E. Bertagnolli, E. Gornik, J. Smoliner; "Focused ion beam induced damage in silicon investigated with scanning capacitance microscopy", 4th Int. Symposium on Nanostructures and Mesoscopic Systems 2003 (NANOMES 2003); Tempe, Arizona, USA, 17.-21.2.2003
8. D. Rakoczy, G. Strasser, J. Smoliner; "BEEM/BEES investigations on AlAs/GaAs single barriers and RTDs", 4th Int. Symposium on Nanostructures and Mesoscopic Systems 2003 (NANOMES 2003); Tempe, Arizona, USA, 17.-21.2.2003
9. K. Unterrainer, "Dynamik in Halbleiternanostrukturen", Laserseminar Mauterndorf 2003, Mauterndorf, 17.-21.3. 2003.
10. C. Pflügl, J. Darmo, R. Bratschitsch, T. Müller, W. Schrenk, S. Anders, T. Roch, K. Unterrainer, and G. Strasser, "High power mid- and far-infrared semiconductor emitters", Laserseminar Mauterndorf 2003, Mauterndorf, 17.-21.03.2003
11. T. Müller, J. Darmo, R. Bratschitsch, W. Parz, G. Strasser, and K. Unterrainer, "Probing electron dynamics in nanostructures by ultrabroadband THz pulses", Laserseminar Mauterndorf 2003, Mauterndorf, 17.-21.03.2003
12. C. Pflügl, M. Litzenberger, W. Schrenk, D. Pogany, E. Gornik, G. Strasser; "Thermal characteristics of GaAs-based quantum cascade lasers"; CLEO, Baltimore, USA, 1.-6. June 2003
13. W. Brezna, S. Harasek (TU Wien), H. Enichlmair (Austria Mikro Systeme International AG), E. Bertagnolli, E. Gornik, and J. Smoliner (TU Wien), ZrO₂ as Dielectric Material for Device Characterization with Scanning Capacitance Microscopy, 203rd Meeting of the Electrochemical Society, ALTECH2003, (Paris)
14. T. Le, J. Darmo, K. Unterrainer, A. Stingl, G. Tempea, 'Compact THz-source based on femtosecond Ti:S laser and intracavity photoconductive antenna,' Photonics West 2003, San Jose, California, USA, 25 –31- January 2003.
15. M. Blaho, D. Pogany, E. Gornik, H. Wolf, H. Gieser, L. Zullino, E. Morena, R. Stella, A. Andreini: "Internal behavior of BCD ESD protection devices under very-fast TLP stress"; International reliability physics symposium (IRPS 2003), Dallas, USA, 30.9-3.4.2003

16. D. Pogany, S. Bychikhin, E. Gornik, M. Denison, N. Jensen, G. Groos and M. Stecher: "Moving current filaments in ESD protection devices and their relation to electrical characteristics", International reliability physics symposium (IRPS 2003), Dallas, USA, 30.9-3.4.2003
17. C. Kranz, A. Kueng, A. Lugstein, E. Bertagnolli, B. Mizaikoff: "Simultaneous Tapping Mode Topographical and Electrochemical Imaging of Enzyme Activity with AFM-Tip Integrated Nanoelectrodes PITTCON 2003, Orlando, FL/U.S.A., March 9-14, 2003
18. D. Pogany (invited), "Local Thermal and current imaging of power devices", Gesellschaft für Mikroelektronik (Microelectronics Society) GME Forum, April 10-11, 2003 Vienna, Austria
19. S. Harasek, H. D. Wanzenboeck, B. Basnar, J. Smoliner, E. Bertagnolli: "Zirconium Dioxide Thin Films for Microelectronics Deposited by Metal Organic Chemical Vapor Deposition", Gesellschaft für Mikroelektronik (Microelectronics Society) GME Forum, April 10-11, 2003 Vienna, Austria
20. H. D. Wanzenboeck, S. Harasek, H. Langfischer, E. Bertagnolli: "Deposition Mechanism of Direct-Write Processes – An Application-Oriented Approach to Custom-Tailored Material Properties", Gesellschaft für Mikroelektronik (Microelectronics Society) GME Forum, April 10-11, 2003 Vienna, Austria
21. M. Kast, C. Pacher, G. Strasser, and E. Gornik: "Transport through Wannier-Stark states in biased finite superlattices", Gesellschaft für Mikroelektronik (Microelectronics Society) GME Forum, April 10-11, 2003 Vienna, Austria
22. S. Harasek, H.D. Wanzenboeck, W. Brezna, J. Smoliner, E. Gornik, and E. Bertagnolli: "Utilizing MOCVD for high-quality Zirconium Dioxide Gate Dielectrics in Microelectronics", 203rd Meeting of the Electrochemical Society, 27. April-02. May 2003, Paris, France
23. H.D. Wanzenboeck, S. Harasek, H. Langfischer, E. Auer, E. Bertagnolli, H. Hutter, and H. Stoeri: "Focused Ion Beam induced Chemical Vapor Deposition (FIB-CVD) for Local Nanodeposition of Dielectric Material", 203rd Meeting of the Electrochemical Society, 27. April-02. May 2003, Paris, France
24. H. Langfischer, S. Harasek, H. Wanzenboeck, A. Lugstein, B. Basnar, and E. Bertagnolli: "Morphological Studies of Focused Ion Beam Induced Tungsten Deposition", 203rd Meeting of the Electrochemical Society, 27. April-02. May 2003, Paris, France
25. H.D. Wanzenboeck (invited), S. Harasek, E. Bertagnolli, H. Hutter, J. Brenner, H. Stoeri, P. Pongratz: "Direct-Write Deposition of Silicon Oxide - The Express Lane towards patterned thin Films", 203rd Meeting of the Electrochemical Society, 27. April-02. May 2003, Paris, France
26. E. Gornik, W. Schrenk, G. Strasser (invited); "GaAs-based Quantum Cascade Laser Diodes"; 15th Int. Conf. on InP and Related Materials; Santa Barbara, USA, 12.-16.5.2003
27. M. Kast (invited), "Current spectroscopy of quantum states in semiconductor superlattices", 38th IUVSTA Workshop on Electronic Processes and Sensing on the Nano-Scale, May 25-29 2003, Eilat, Israel
28. J. Kuzmik, D. Pogany, M. Blaho, E. Gornik, P. Javorka, M. Marso, P. Kordos: "Breakdown and degradation processes in AlGaIn/GaN HEMTs during electrostatic discharge", 27th workshop on compound semiconductor devices and integrated circuits (WOCSDICE'03), May 25-28 2003, Fürigen, Switzerland

29. K. Unterrainer, J. Darmo, T. Müller, G. Strasser, G. Tempea, T. Le, A. Stingl (invited), "Cavity enhanced few-cycle THz generation and coherent spectroscopy", Conference on Lasers and Electro-Optics CLEO/QELS 2003, June 1-6, Baltimore, Maryland.
30. K. Unterrainer (invited), "Few-cycle terahertz generation and spectroscopy of nanostructures", Royal Society Meeting "The terahertz gap: the generation of far-infrared radiation and its applications", London, UK, 4-5 June, 2003.
31. J. Darmo, J. Kröll, G. Strasser, K. Unterrainer, and C. Kremser: "Spectroscopy and imaging with few-cycle Terahertz radiation" International Workshop on Applied Physics of Condensed Matter (APCOM) 2003, June 11-13 2003, Mala Lucivna, Slovakia
32. G. Strasser (invited); "GaAs-based quantum cascade lasers"; 11th Int. Symp. Nanostructures: Physics and Technology; St. Petersburg, Russia, 23.-28.6.2003
33. J. Darmo, G. Strasser, T. Roch, T. Müller, K. Unterrainer, and G. Tempea, "New generation of photoconductive few-cycle Terahertz emitters" International conference on Ultrafast Optics (UFO IV.), June 29 – July 4, 2003, Vienna, Austria.
34. H.D. Wanzenboeck, S. Harasek, E. Bertagnolli, L. Jolivet, J.P. Piel, and E. Hartmann; "Layer analysis of focused ion beam deposited silicon oxide - Characterisation challenges with thin microstructures", 3rd International Conference on Spectroscopic Ellipsometry (ICSE-3), 7.-11.07.2004, Vienna, Austria
35. T. Müller, F. F. Schrey, G. Strasser, and K. Unterrainer; "Interband pump - intraband probe spectroscopy of quantum dots"; Ultrafast Optics IV, Vienna, Austria, 29.06.-3.07.2003
36. W. Schrenk, S. Anders, C. Pflügl, E. Gornik, G. Strasser; "Quantum cascade structures and unipolar dot emitters"; 11th Int. Conf. on Modulated Semiconductor Structures (MSS11), Nara, Japan, 14.-18.7.2003
37. F.F. Schrey, T. Müller, S. Anders, L. Rebohle, W. Schrenk, K. Unterrainer, G. Strasser; "Dynamics between electronic levels in InAs quantum dots"; 11th Int. Conf. on Modulated Semiconductor Structures (MSS11), Nara, Japan, 14.-18.7.2003
38. M. Kast, W. Boxleitner, C. Pacher, G. Strasser, E. Gornik; "Magnetic field controlled scattering processes in GaAs"; 11th Int. Conf. on Modulated Semiconductor Structures (MSS11), Nara, Japan, 14.-18.7.2003
39. C. Pacher, M. Kast, E. Gornik; "Adjusting the coherent transport and tunneling time in finite periodic superlattices"; 11th Int. Conf. on Modulated Semiconductor Structures (MSS11), Nara, Japan, 14.-18.7.2003
40. M. Kast, C. Pacher, G. Strasser, E. Gornik; "Ballistic Electron Spectroscopy of Wannier-Stark states in short period superlattices"; 15th Int. Conf. on Electronic Properties of 2-Dimensional Systems (EP2DS-15), Nara, Japan, 14.-18.7.2003
41. T. Müller, W. Parz, G. Strasser, K. Unterrainer; "Intraband relaxation of photoexcited electrons in GaAs/AlGaAs quantum wells and InAs/GaAs self-assembled quantum dots"; 13th Int. Conf. on Nonequilibrium Carrier Dynamics in Semiconductors (HCIS13), Modena, Italy, 28.7.-1.8.2003
42. F. Rizzi, G. Scamarcio, G. Strasser; "Three-terminal mid-IR tunable emitters based on Wannier-Stark ladder transitions in semiconductor superlattices"; 13th Int. Conf. on Nonequilibrium Carrier Dynamics in Semiconductors (HCIS13), Modena, Italy, 28.7.-1.8.2003

43. V. Tamosiunas, R. Zobl, G. Fasching, J. Ulrich, G. Strasser, K. Unterrainer, R. Colombelli, C. Gmachl, F. Capasso, K. West, L. Pfeiffer; "Magnetic Field Effects in Terahertz Quantum Cascade Lasers"; 13th Int. Conf. on Nonequilibrium Carrier Dynamics in Semiconductors (HCIS13), Modena, Italy, 28.7.-1.8.2003
44. C. Pflügl, S. Anders, W. Schrenk, P. Schwaha, G. Strasser; "Electrically pumped GaAs-based quantum cascade microcavities"; 13th Int. Conf. on Nonequilibrium Carrier Dynamics in Semiconductors (HCIS13), Modena, Italy, 28.7.-1.8.2003
45. D. Rakoczy, G. Strasser, C. Pacher, J. Smoliner; "Ballistic Electron Microscopy on Doped AlAs Barriers in the Regime of the Mott Transition"; 13th Int. Conf. on Nonequilibrium Carrier Dynamics in Semiconductors (HCIS13), Modena, Italy, 28.7.-1.8.2003
46. V. Spagnolo, G. Scamarcio, W. Schrenk, G. Strasser; "Influence of the band-offset on the electronic temperature of GaAs/Al(Ga)As superlattice quantum cascade lasers"; 13th Int. Conf. on Nonequilibrium Carrier Dynamics in Semiconductors (HCIS13), Modena, Italy, 28.7.-1.8.2003
47. C. Pacher, M. Kast, G. Strasser, E. Gornik; "Determination of the GaAs/AlAs/GaAs band structure and the intervalley scattering rates by ballistic electron spectroscopy"; 13th Int. Conf. on Nonequilibrium Carrier Dynamics in Semiconductors (HCIS13), Modena, Italy, 28.7.-1.8.2003
48. C. Pflügl, W. Schrenk, S. Anders, G. Strasser; "Quantum dot intersubband emitter"; 7th Int. Conf. on Intersubband Transitions in Quantum Wells (ITQW), Evolène, Switzerland, 1.-5.9.2003
49. T. Müller, W. Parz, G. Strasser, K. Unterrainer; "Quantum Interference of Intersubband Transitions in GaAs/AlGaAs Quantum Wells"; 7th Int. Conf. on Intersubband Transitions in Quantum Wells (ITQW), Evolène, Switzerland, 1.-5.9.2003
50. V. Tamosiunas, R. Zobl, G. Fasching, J. Ulrich, G. Strasser, K. Unterrainer, R. Colombelli, C. Gmachl, K. West, L. Pfeiffer, F. Capasso; "Magnetic Quantization in Terahertz Quantum Cascade Lasers"; 7th Int. Conf. on Intersubband Transitions in Quantum Wells (ITQW), Evolène, Switzerland, 1.-5.9.2003
51. W. Schrenk, C. Pflügl, S. Anders, C. Becker, C. Sirtori, G. Strasser; "High temperature performance of GaAs/AlGaAs quantum cascade lasers"; 7th Int. Conf. on Intersubband Transitions in Quantum Wells (ITQW), Evolène, Switzerland, 1.-5.9.2003
52. T. Müller, F. F. Schrey, G. Strasser, K. Unterrainer; "Electron Capture and Relaxation in InAs/GaAs Self-Assembled Quantum Dots"; 7th Int. Conf. on Intersubband Transitions in Quantum Wells (ITQW), Evolène, Switzerland, 1.-5.9.2003
53. W. Schrenk, S. Anders, T. Roch, C. Pflügl, and G. Strasser; "Wavelength adjustment of quantum cascade lasers by rapid thermal annealing"; 7th Int. Conf. on Intersubband Transitions in Quantum Wells (ITQW), Evolène, Switzerland, 1.-5.9.2003
54. F. F. Schrey, G. Fasching, T. Müller, K. Unterrainer, G. Strasser; "THz/MIR Manipulation of Excitonic levels in InAs Quantum Dots"; oral contribution on the 7th Int. Conference on Optics of Excitons in Confined Systems (OECS 8); Lecce, Italy, 15.-17.9.2003
55. M. Denison, M. Blaho, D. Silber, J. Joos, N. Jensen, M. Stecher, V. Dubec, D. Pogany, E. Gornik; "Hot spot dynamics in quasi vertical DMOS under ESD stress", ISPSD 2003, Cambridge, UK

56. J. Kuzmík, M Blaho, D. Pogany, E. Gornik, A. Alam, Y. Dikme, M. Heuken, P. Javorka, M. Marso, and P. Kordoš, " Backgating, high-current and breakdown characterisation of AlGaIn/GaN HEMTs on silicon substrates" ESSDERC'03, September 16-18, 2003, Estoril, Portugal
57. M. Graf, V. Dudek, W. Soppa, H. Wolf, S. Bychikhin, D. Pogany E. Gornik, "Impact of layer thickness variations of SOI-wafer on ESD robustness", EOS/ESD 2003 Symposium, September 21-25, 2003 , Las Vegas, USA
58. H.D. Wanzenboeck, S. Harasek, H. Langfischer, E. Bertagnolli, H. Hutter, H. Störi; "Local Deposition on Semiconductor Surfaces with a Focused Beam", 12. Tagung Festkörperanalytik, Wien 22.-24.09. 2003
59. H. D. Wanzenboeck, S. Harasek, H. Langfischer, E. Bertagnolli, U. Grabner, G. Hammer, P. Pongratz; "Cross-sectional Analysis of Semiconductor Samples utilising a Focused Ion Beam", 12. Tagung Festkörperanalytik, Wien 22.-24.09. 2003
60. J. Darmo, J. Kröll, G. Strasser, C. Kremser, and K. Unterrainer, "Few-cycle THz properties of bio-molecules", 11th International Conference on Terahertz Electronics, Sendai, Japan, 24.-26.9.2003
61. J. Darmo, G. Strasser, T. Roch, T. Müller, K. Unterrainer, and G. Tempea, "New generation photoconductive few-cycle terahertz emitters", 11th International Conference on Terahertz Electronics, Sendai, Japan, 24.-26.9.2003
62. V. Dubec, S. Bychikhin, M. Blaho, D. Pogany, E. Gornik, J. Willemen, N. Qu, W. Wilkening, L. Zullino, A. Andreini, A dual-beam Michelson interferometer for investigation of trigger dynamics in ESD protection devices under very fast TLP stress, ESREF03, Arcachon, France, 6-10. Oct. 2003
63. H. Langfischer, S. Harasek, B. Basnar, W. Brezna, J. Smoliner, E. Bertagnolli, J. Brenner, C. Tomastik, H. Stoeri, P. Pongratz, H. Hutter, H.D.Wanzenboeck, "Characterisation of Nanopatterned Surfaces Fabricated by FIB-CVD"; ME03 Vienna (Informationstagung Mikroelektronik), October 1 - 2, 2003, Vienna, Austria
64. H.D. Wanzenboeck, S. Harasek, B. Eichinger, A. Gruen, M. Karner, M. Hetzl, E. Bertagnolli, "Direct Write Deposition - A Maskless Prototyping Technique"; ME03 Vienna (Informationstagung Mikroelektronik), October 1 - 2, 2003, Vienna, Austria
65. S. Harasek, H.D. Wanzenboeck,, B. Basnar, J. Smoliner, E. Bertagnolli, "Zirconium Dioxide as high-k Gate Dielectric for Future CMOS", ME03 Vienna (Informationstagung Mikroelektronik), October 1 - 2, 2003, Vienna, Austria
66. D. Pogany, S. Bychikhin, C. Pflügl, V. Dubec, J. Kuzmik, M. Blaho, M. Litzenberger, G. Strasser, E. Gornik (invited), "Thermal mapping of semiconductor devices with nanosecond resolution", European Microwave week 2003, GaAs conference, Munich Germany, 6-10 October 2003
67. D. Pogany, S. Bychikhin, M. Blaho, V. Dubec, J. Kuzmik, M. Litzenberger, C. Pflügl, G. Strasser, E. Gornik (invited), "Transient interferometric mapping of temperature and free carriers in semiconductor devices", Lasers and Electro-Optics for Semiconductor Testing (IEEE-LEOS), Tucson, Arizona October 26-30. USA
68. F. F. Schrey, T. Müller, K. Unterrainer, G. Strasser; "THz Manipulation of Excitonic levels in InAs Quantum Dots"; talk at 2003 MRS Fall Meeting; Boston/MA, USA, 01.-05.12.2003
69. T. Müller (invited), "Electron dynamics in semiconductor quantum dots", Workshop on Charged-Particle Transport through Nanostructures and Solids, Debrecen, Hungary, 14.11. – 16.11.2003.

70. G. Otto and G. Hobler, "Coupled kinetic Monte Carlo and molecular dynamics simulations of implant damage accumulation in silicon", 2003 MRS Fall Meeting; Boston/MA, USA, 01.-05.12.2003
71. G. Hobler, A. Lugstein, W. Brezna, and E. Bertagnolli, "Simulation of focused ion beam induced damage formation in crystalline silicon", 2003 MRS Fall Meeting; Boston/MA, USA, 01.-05.12.2003
72. A. Lugstein, B. Basnar, G. Strasser, and E. Bertagnolli, "A new approach for the formation of size and site controlled metallic nano dots seeded by focused ion beams", Material Research Society Fall Meeting (MRS), Boston/MA, USA, 01.-05.12.2003
73. H. D. Wanzenboeck, C. Almeder, C. Pacher, E. Bertagnolli, E. Bogner, M. Wirth, F. Gabor; "Cell Growth on Prestructured Microelectronic Semiconductor Materials", Material Research Society Fall Meeting 2003 (MRS), Boston/MA, USA, 01.-05.12.2003
74. H. D. Wanzenboeck, B. Eichinger, A. Gruen, M. Karner, K. Dominizi, P. Hagl, J. Wissenwasser, E. Bertagnolli, "Express Pattern Fabrication - Single Step processing by Direct-write Deposition", Material Research Society Fall Meeting 2003 (MRS), Boston/MA, USA, 01.-05.12.2003
75. H. Wanzenboeck, S. Harasek, H. Langfischer, B. Basnar, W. Brezna, J. Smoliner, and E. Bertagnolli, "Local Modification of Microstructure and of Properties by FIB-CVD", Material Research Society Fall Meeting 2003 (MRS), Boston/MA, USA, 01.-05.12.2003
76. N. Jensen, G. Groos, M. Denison, J. Kuzmik, D. Pogany, E. Gornik, M. Stecher, "Coupled bipolar transistors as very robust ESD protection devices for automotive applications", submitted to 25th Annual International EOS/ESD Symposium, September 21-25, 2003, Las Vegas, USA
77. W. Stadler, K. Esmark, K. Reynders, M. Zubeidat, M. Graf, W. Wilkening, J. Willemen, N. Qu, S. Mettler, M. Etherton, H. Wolf, H. Gieser, W. Soppa, V. De Heyn, M. Natarajan, G. Groeseneken, E. Morena, R. Stella, A. Andreini, M. Litzenberger, D. Pogany, E. Gornik, C. Foss, D. Nuernbergk, A. Konrad, M. Frank "Test Circuits for Fast and Reliable Assessment of CDM Robustness of I/O stages", 25th Annual International EOS/ESD Symposium, September 21-25, 2003, Las Vegas, USA
78. M. Blaho, M. Denison, V. Dubec, D. Pogany, M. Stecher and E. Gornik: "Hot spot mapping in the DMOS devices for automotive applications", Informationstagung Mikroelektronik 2003, 1.-2. Oct. 2003, Wien
79. A. Kueng, C. Kranz, A. Lugstein, E. Bertagnolli, B. Mizaikoff, "Simultaneous Electrochemical and Tapping Mode Imaging of Soft Biological Samples with AFM Tip Integrated Nanoelectrodes and Nanobiosensors" 250th International Symposium of the American Vacuum Society, Baltimore/MD, November 3-7, 2003
80. C. Kranz, A. Kueng, A. Lugstein, E. Bertagnolli, B. Mizaikoff, "Simultaneous Electrochemical and Tapping Mode Imaging of Soft Biological Samples with Nanoelectrodes Integrated into AFM Tips Scanning Probe Microscopy", Sensors and Nanostructures 2003, Oxford, England, May 23-26, 2003.
81. C. Kranz, A. Kueng, A. Lugstein, E. Bertagnolli, B. Mizaikoff, "Simultaneous electrochemical and AFM Imaging in Tapping Mode of Soft Samples with Bifunctional Scanning Probe Tips", ACS Fall National Meeting 2003, New York/NY, September 7-11, 2003.

Habilitations

1. Dionyz Pogany, "Reliability and Testing of Semiconductor Devices", TU Wien, March 2003

Doctor's Theses

1. Gernot Steinlesberger, "Scaling limits of copper damascene lines for future interconnect technology", TU Wien, April 2003
2. Martin Litzenberger, "Investigation of Internal Behavior in CMOS ESD Protection Devices under High Current Stress", TU Wien, Juni 2003
3. Helmut Langfischer, "Focused Ion Beam basierte Metallisierung für sub-100nm-Bauelemente", TU Wien, Juni 2003
4. Stefan Harasek, "Zirkoniumdioxiddünnschichten als hoch-e Gate-isolatoren für die Siliziumtechnologie", TU Wien, September 2003
5. Michael Kast, "High-Resolution Hot-Electron Spectroscopy", TU Wien, November 2003
6. Thomas Müller, "Ultrafast THz Response of Optically Exited Quantum Semiconductor Structures", TU Wien, November 2003

Diploma Works

1. Johann Kreuter, "Long wavelength GaAs/AlGaAs quantum cascade lasers with low-loss waveguide", TU Wien, März 2003
2. Josef Kröll, "Few-cycle Terahertz spectroscopy and imaging", TU Wien, Mai 2003

Cooperations

1. Universität Linz, G. Bauer, W. Heiss, F. Schäffler, L. Palmetshofer, W. Jantsch
2. Universität Wien, H. Kauffmann, G. Kresse
3. TU Wien, H. Hutter, P. Pongratz, G. Lendl
4. Universität für Bodenkultur Wien, U.Sleytr, D. Pum
5. Montanuniversität Leoben, F. Kuchar
6. AMS-Unterbremstätter, H. Enichlmair, K. Tschernay F. Unterleitner
7. Philips Consumer Electronics, E. Kaun
8. Femtolasers, Wien, A. Stingl
9. High Q Laser, Hohenems, Dr. D. Kopf
10. NMP, Weiz, M. Schatzmeier
11. Siemens AG, E. Wolfgang, G. Sölkner, W. Maurer, A. Felder, Deutschland
12. Infineon München, M. Stecher, W. Stadler, Deutschland
13. ATMEL, Heilbronn, M. Graaf, Deutschland
14. TU-München, G. Abstreiter, P. Vogl, Deutschland

15. Universität Regensburg, W. Wegscheider, Deutschland
16. Friedrich-Schiller-Universität Jena, K. Gärtner, Deutschland
17. TU Braunschweig, D. Schneider, Deutschland
18. Forschungszentrum Jülich, P. Kordos, Deutschland
19. Technische Universität Berlin, A. Wacker, Deutschland
20. Heinrich Hertz Institut, Berlin, H. Künzel, Deutschland
21. Paul Drude Institut, Berlin, H. Grahn, Deutschland
22. Universität Bremen, D. Hommel, Deutschland
23. Forschungszentrum Rossendorf, Dresden, M. Helm, Deutschland
24. Bosch, Reutlingen, W. Wilkening, Deutschland
25. XFAB, Erfurt, C. Foss, Deutschland
26. IZM Fraunhofer Institut, München, H. Grieser, Deutschland
27. Centre National de la Recherche Scientifique, Laboratoire de Microstructures et de Microelectronique, B. Etienne, Cedex, Frankreich
28. Thales, Orsay, H. Page, D. Corbin, Frankreich
29. Universite Paris Sud, F. Julien, Frankreich
30. Universite Paris 7, C. Sirtori, Frankreich
31. AMIS, Mietec, K. Reynders, Belgien
32. Interuniversity Microelectronics Center (IMEC), Leuven, Belgien
33. Ioffe Physico-Technical Institute, St. Petersburg, Y. Ivanov, Rußland
34. Sub-Micron Center, Weizmann Institute, Rehovot, M. Heiblum, Israel
35. Avant! Corp., V. Moroz, USA
36. Univ. of California, Lawrence Berkeley Laboratories, E. E. Haller, USA
37. Univ. of California, Los Angeles, S. Prussin, USA
38. Univ. of California, Santa Barbara, J. Allen, A. Gossard, USA
39. Columbia University, New York, H. Störmer, USA
40. Princeton University, S. Lyon, USA
41. IBM Fishkill, C.S. Murthy, USA
42. Lucent Technologies, C. Gmachl, USA
43. Boston College, Boston, MA, K. Kempa, P. Bakshi, USA
44. EPI MBE Components, St. Paul, Minnesota, USA
45. Univ. Osaka, C. Hamaguchi, Japan
46. Univ. Nagoya, N. Sawaki, Japan
47. RIKEN, K. Ishibashi, Japan
48. Herriot Watt University, Edinburgh, C. Pidgeon, Schottland
49. Univ. Glasgow, C. Ironside, Schottland
50. Imperial College, London, C. Phillips, England
51. Univ. Leeds, M. Chamberlain, England

-
52. University of Sheffield, M. Skolnick, J. Coburn, England
 53. University of Surrey, B.N. Murdin, England
 54. INFN-SNS Pisa, F. Beltram, Italien
 55. TASC Trient, L. Sorba, Italien
 56. Universita Bari, G. Scamarcio, Italien
 57. STMicroelectronics, A. Andreini, Italien
 58. Technische Universität Delft, Wenckebach, Holland
 59. University Neuchatel, J. Faist, Schweiz
 60. EPFL Lausanne, M. Illegems, Schweiz
 61. ETH Zürich, W. Fichtner, Schweiz
 62. Orbisphere Semiconductor Lasers, Schweiz
 63. Alpes Lasers, Neuchatel, A. Müller, Schweiz
 64. Slovak Academy of Sciences, Bratislava, Slowakei

Surface Emitting Quantum Cascade Laser

M. Austerer, C. Pflügl, W. Schrenk, T. Roch and G. Strasser
Institute of Solid State Electronics, TU Vienna, Austria

We present high power surface-emitting single mode GaAs-based quantum cascade lasers (QCLs) in the mid infrared. By using an air-AlGaAs waveguide combined with second-order distributed feedback processing, we obtained optical output via the surface above 3W. Surface-normal dual-lobe light emission exceeds the emission from one as-cleaved facet by a factor of six.

Quantum cascade lasers are based on intersubband transitions [1]. Selection rules for transitions in quantum wells allow gain only for TM polarized electromagnetic waves. Therefore conventional vertical cavity surface emitting laser design is not suitable for QCLs. If one wants to exploit the advantages of surface normal emission another approach must be taken. We have chosen a distributed feedback design where the feedback is given through a second-order Bragg grating etched into the surface of the laser ridge. Such surface emitting QCLs have been realized both in the InGaAs/InAlAs/InP [2] and also in the GaAs/AlGaAs material system [3]. Appropriate etch depths, a low loss top air cladding, and metallization of the grating peaks only, lead to high power surface emission. The far field of such lasers exhibits an asymmetric dual lobe pattern, because the near field close to the emitting surface also includes interference terms. An in-detail investigation shows that the relative position of the grating and the end mirrors determines the ratio of the two lobe intensities [4]. The single mode emission wavelength is continuously tuneable by the heat sink temperature.

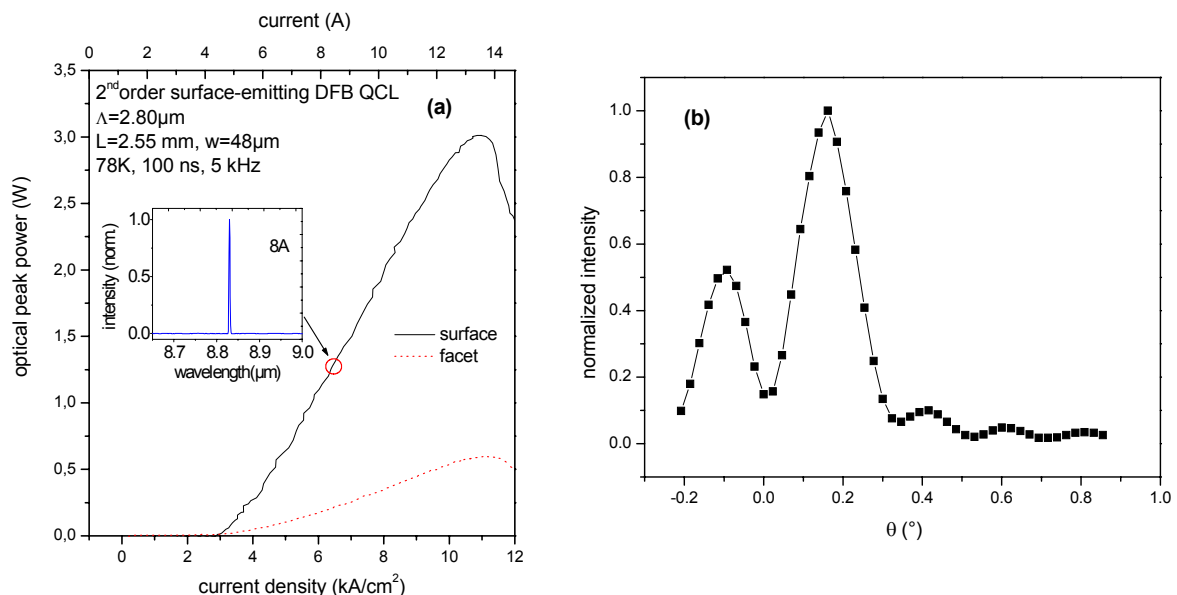


Fig. 1: (a) Emission spectrum and light-intensity curves for surface and facet emission. The emission wavelength is the same in both cases. (b) Angular dependence of the far-field 124 cm away from the laser chip. An asymmetric dual lobe pattern is observed.

A three-well GaAs/Al_{0.45}Ga_{0.55}As quantum cascade active region [5] was grown by means of molecular beam epitaxy on a <100> GaAs substrate. For waveguiding an air/AIGaAs cladding was used in order to reduce absorption losses. Our calculations yield a waveguide loss coefficient of $\alpha = 3.8 \text{ cm}^{-1}$, whereas another structure with the same active region at the same wavelength, but a double-plasmon waveguide has α -values of 12 cm^{-1} . Taking the waveguide structure and the desired wavelength of $8.9 \mu\text{m}$ into account, a suitable grating period, duty cycle and grating depth were calculated. The MBE grown material was processed into DFB laser ridges by means of optical lithography and reactive ion etching (RIE). The laser ridges were cleaved to different lengths in order to investigate the critical DFB coupling length. Lasers that are shorter than 1.4 mm , thus having a product of DFB coupling coefficient $\kappa = 7 \text{ cm}^{-1}$ and length (cm) smaller than one, do not experience sufficient feedback from the surface grating and are showing typical Fabry-Perot modes. The samples were mounted substrate-down on a turnable cold finger and operated under pulsed bias (100 ns, 5 kHz) at 78 K. By turning the cold finger we could observe both edge and surface emission.

In Fig. 1 (a) absolute light output power versus bias current density for a 2.55 mm long laser is plotted. Single mode emission is observed for all bias currents above threshold. Light power was measured using a calibrated thermopile detector. In the case of edge emission an $f/1$ AR-coated ZnSe lens was used to collect the light from the highly divergent beam. In both cases the light power was focused onto the thermopile detector by means of a gold coated off-axis parabola. The ratio between surface emission and single-facet emission is determined to be 6 for this device.

The far field distribution (Fig. 1 (b)) of the laser emission was measured using a $1 \text{ mm} \times 1 \text{ mm}$ sensitive area liquid-nitrogen cooled HgCdTe detector at a distance of 124 cm away from the laser chip. Lateral resolution of 1 mm results in an angular resolution of 0.046° . The two beam lobes are separated by 0.25° and have an FWHM beam divergence of 0.2° in laser ridge parallel direction. Beam divergence in ridge normal direction is determined by the ridge width, here FWHM beam divergences are in the range of 10° to 20° .

We have shown the high-power capabilities of surface emitting DFB quantum cascade lasers. Single lobe emission surface emission of second order DFB QCLs is proposed by introducing a phase shift into the surface grating. Such low divergence emission pattern would further improve practical usability. In contrary to facet emitters, for many applications no collimating lens would be necessary.

This work was partly supported by EC (NMP-project) ANSWER, Austrian FWF (SFB-ADLIS) and the Austrian GMe.

References

- [1] J. Faist, F. Capasso, D.L. Sivco, C. Sirtori, A.L. Hutchinson, A.Y. Cho, *Science* **264**, 553 (1994)
- [2] D. Hofstetter, J. Faist, M. Beck, U. Oesterle, *Appl. Phys. Lett.* **75**, 3769 (1999)
- [3] W. Schrenk, N. Finger, S. Gianordoli, L. Hvozdar, G. Strasser, E. Gornik, *Appl. Phys. Lett.* **77**, 2086 (2000)
- [4] H. Kogelnik, C. V. Shank, *J. Appl. Phys.* **43**, 2327 (1972)
- [5] H. Page, C. Becker, A. Robertson, G. Glastre, V. Ortiz, C. Sirtori, *Appl. Phys. Lett.* **78**, 3529 (2001)

Interferometric Temperature Mapping of GaAs-based Quantum Cascade Laser

C. Pflügl, M. Litzenberger, W. Schrenk, D. Pogany, E. Gornik and G. Strasser

Institute of Solid State Electronics, TU Vienna, Austria

Quantum cascade lasers (QCLs) based on intersubband / interminiband transitions in GaAs/AlGaAs are unipolar semiconductor lasers [1], [2]. Compared to InP-based QCLs ([3] and references within), GaAs-based QCLs offer the advantage of higher flexibility in the engineering of the electronic states. In spite of the improvements concerning output power [4], threshold current [5], single mode operation and maximum operating temperature [6] their performance is still limited by strong heating of the active region due to poor heat dissipation. Improving the lasers with respect to better thermal characteristics requires knowledge about the thermal dynamics in the laser under operation.

We want to report on a technique, namely the interferometric thermal laser mapping technique, which we used to investigate GaAs-based QCLs under operation. Comparing the experimental results with a thermal model enables to determine the heat distribution of the working devices and reveals the heat conductivity of the multilayered active region.

An infrared laser probe beam (wavelength of 1.3 μm , well below the GaAs bandgap), is directed to the sample from the device backside, passes through the substrate and laser active area and is back reflected on the surface metallization. The current-induced heating causes a temperature increase in the active region, which induces changes in the semiconductor refractive index. The resulting phase shift, which is detected interferometrically, provides quantitative information on the thermal dynamics [7], [8].

The investigated QCL has an active region consisting of 50 periods of a chirped $\text{Al}_{0.45}\text{Ga}_{0.55}\text{As}$ /GaAs superlattice. This active region is embedded into a double plasmon enhanced waveguide. Ridge waveguides with a width of 10 μm are fabricated by etching 10 μm trenches. The extended TiAu contacts are insulated with SiN. The length of the laser is 1.3 mm.

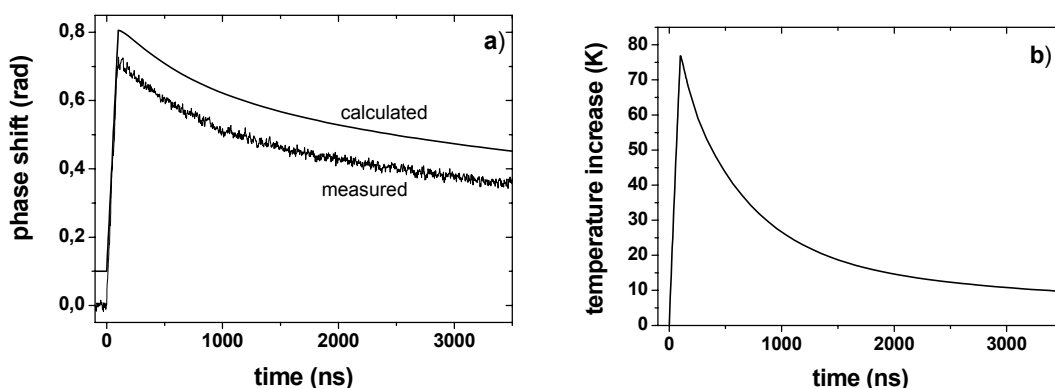


Fig. 1: (a) Calculated and measured phase shift in the middle of the laser ridge. The calculated graph is shifted by 0.1 rad for clarity. (b) From the phase shift extracted temperature increase in the middle of the active region.

We measured the transient phase shift during pulsed mode operation at room temperature, with a typical pulse length for GaAs based QCLs of 100 ns. The time evolution of the phase shift in the middle of the laser ridge (see Fig. 1 (a)) can be used to determine the anisotropic heat conductivity of the multilayered active region, $k_{ar}=(k_{||}, k_{\perp})$, where $k_{||}$ is the in-plane heat conductivity and k_{\perp} the cross-plane component perpendicular to the layers. For all parameter in this model standard literature data are used except the anisotropic heat conductivity of the active region, which was fitted. A best fit was obtained with an anisotropic heat conductivity $k_{||} = 0.25$ W/Kcm and $k_{\perp} \approx 0.015$ W/Kcm [9]. After the heating during the pulse ($t < 100$ ns) the first strong cooling is determined by the in-plane heat conductivity. After the in-plane heat fluxes are mostly saturated the further cooling depends on the low cross-plane heat conductivity. This model also reveals the temperature distribution of the working devices. Figure 1 (b) shows the calculated temperature increase in the middle of the active region. The maximum temperature increase in the active region at the end of the pulse, we found to be 77 K at an applied current of 3.1 A corresponding to a dissipated power in the active region of 63 W (1.24 W/cm³) during the pulse.

The reduced in-plane heat conductivity compared with the weighted average of its constituents ($k = 0.31$ W/Kcm [10]) can be explained by partly diffusive scattering of the phonons at the interfaces in the multilayered active region. The cross-plane conductivity was found to be much smaller than the heat conductivity of an Al_{0.17}Ga_{0.83}As alloy ($k = 0.18$ W/Kcm [10], the average Al-content of the investigated active region is 17 %). In our superlattice structure the width of the single layers is in the range of a few nm and thus is much smaller than the mean free path of thermal phonons in GaAs at 293 K ($\lambda \approx 50$ nm [11]). In this case the heat conductivity is no longer determined by the properties of the involved materials but rather it must be considered that the effect of the superlattice is to modify the phonon-dispersion relation [12]. This crucial difference of the two components shows that the best way to improve the lasers with respect to a better thermal behavior is to support the in-plane fluxes. This can be done e.g. by fabricating the lasers as buried heterostructures or thicker gold layers in the trenches.

In conclusion, we have shown that the presented technique is a valuable tool to investigate the thermal dynamics in GaAs-based QCLs. Comparing the experiment with a thermal model enables us to extract the anisotropic heat conductivity of the multilayered active region as well as the temperature distribution in the working devices. The ratio of the two components of the heat conductivity $k_{||}/k_{\perp}$ was found to be in the range of 15-20. The maximum temperature increase in the investigated active region is up to 80 K depending on the applied current.

Acknowledgement

This work was supported by the European Community-IST project SUPERSMILE and the Austrian FWF (SFB-ADLIS).

References

- [1] C. Sirtori, et al., Appl. Phys. Lett. **73**, 3486 (1998)
- [2] G. Strasser, et al., Appl. Phys. Lett. **75**, 1345 (1999)
- [3] M.Beck, et al., Science **295**, 301 (2002)
- [4] C. Pflügl et al., to be published
- [5] S. Anders, et al., Appl. Phys. Lett. **80**, 1864 (2002)
- [6] C. Pflügl et al., Appl. Phys. Lett. **83**, 4698 (2003)

- [7] C. Fürböck, et al., J.Electrostatics **49** 195 (2000)
- [8] C. Fürböck, et al., Microel. Reliab. **40** (8-10), 1365 (2000)
- [9] C. Pflügl, et al., Appl. Phys. Lett. **82**, 1664 (2003)
- [10] S. Adachi, *GaAs and related materials*, World Scientific (1994)
- [11] J. S. Blakemore, J. Appl. Phys. **53** (10), 123 (1982)
- [12] G. Chen, Phys. Rev. B **57**, 14958 (1998)

Tuning Quantum-Cascade Lasers by Postgrowth Rapid Thermal Processing

W. Schrenk, S. Anders, T. Roch, C. Pflügl and G. Strasser
Institute of Solid State Electronics, TU Vienna, Austria

We report on postgrowth heat treatment of quantum-cascade lasers. Intermixing of the atoms at the barrier-well interfaces in the temperature range between 850 and 875 °C shifts the energy levels and thus the gain of the structure. The achieved emission wavelength shift is from 10.3 to 11.9 μm.

The QCLs described here were grown by solid source molecular beam epitaxy on doped n^+ GaAs (100) substrates with a doping concentration of $n_{Si} = 2 \times 10^{18} \text{ cm}^{-3}$. $\text{Al}_{0.45}\text{Ga}_{0.55}\text{As}$ was used for the barriers and GaAs for the wells. We performed rapid thermal processing (RTP) on the structure shown in Fig. 1. The lasing is based on a bound-to-continuum transition similar to a sample described elsewhere [1]. The lasing transition takes place between levels 2 and 1. Temperature-induced diffusion of atoms grades the bandstructure. An effect similar to diffusion may be achieved by growing a digitally graded structure. Such a structure has been calculated with the aim of maximizing the gain. [2]

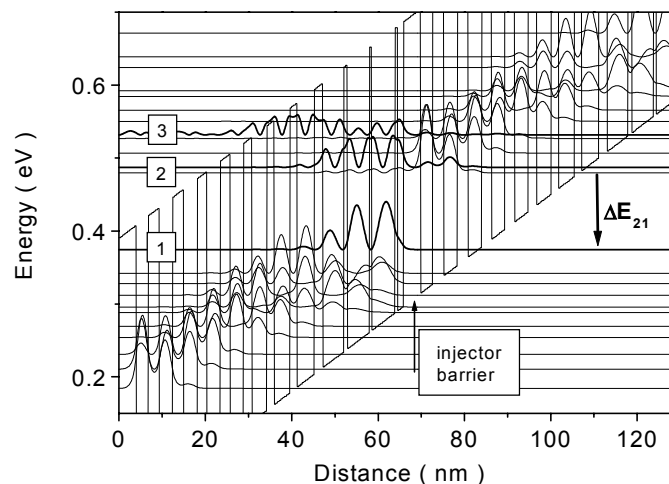


Fig. 1: Calculated conduction band structure of an active cell embedded between two injectors for an external field of 45 kV/cm at room temperature.

The heat treatment parameters were 60 s at 850, 860, 870 and 875 °C for four different pieces covered with SiO. After removing of the SiO with hydrofluoric acid, the samples were processed into ridge waveguides with as-cleaved facets. The length of the ridges was approximately 1.9 mm. Their widths were 20 and 10 μm. The QCLs were mounted into a cryostat cooled with liquid nitrogen. The lasing spectra were measured by driving the device with a pulse length and repetition rate of 100 ns and 5 kHz, respectively, at a current density just above the threshold. Spontaneous emission was measured with a pulse length and repetition rate of 300 ns and 67 kHz, respectively, at less than half of

the threshold. The optical signals were detected by a mercury cadmium telluride detector. The spectra were obtained by a Fourier transform infrared spectrometer.

Figure 2 shows that both spontaneous and lasing emission shift to longer wavelengths as the RTP temperature is increased. Apparently, the intermixing of the interface atoms causes the bandstructure to round such that the energy level spacing is smaller, and hence the gain is shifted to lower energies. We may compare this to a result on MOVPE-grown QCLs. In contrast to MBE-grown samples, which have relatively abrupt interfaces, the interfaces of MOVPE-grown devices are always graded because of finite switching times. J. S. Roberts *et al.* [3] find that the emission wavelength of their MOVPE-grown QCLs is consistent with a grading of two monolayers at each interface.

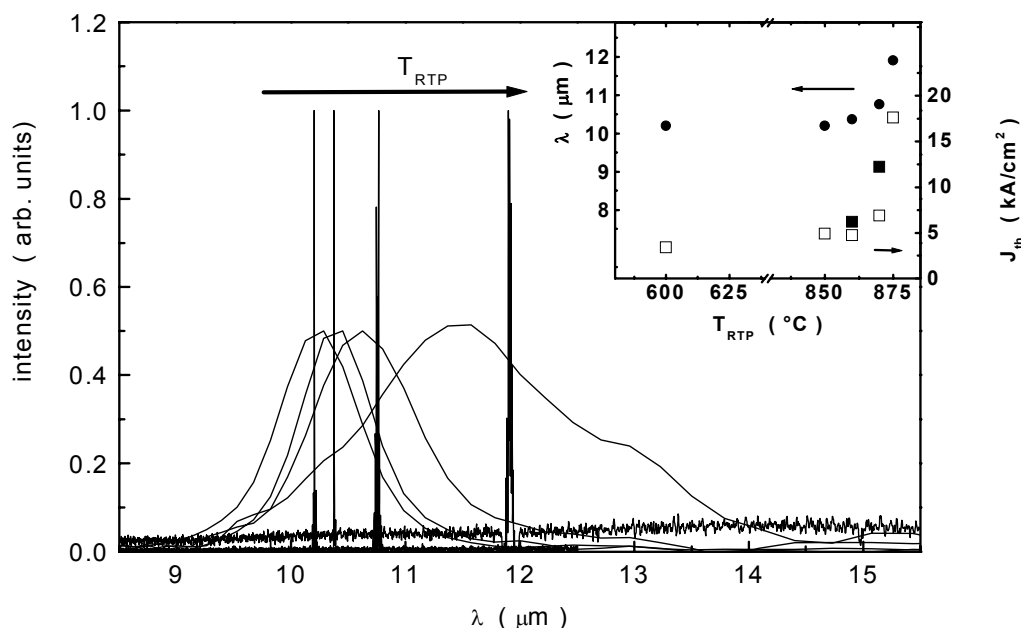


Fig. 2: Spontaneous emission (normalized to 0.5) and lasing (normalized to 1). Samples were heat treated for 1 min at 850, 860, 870 and 875 $^{\circ}\text{C}$ (from left to right). Inset, circles: Shift of the lasing signal with increasing RTP temperature. All data are from 20 μm wide ridges. Inset, squares: Shift of the threshold with increasing RTP temperature. Open symbols: laser width is 20 μm ; closed symbols: 10 μm . In the inset, the data for the sample that was not heat treated are shown at 600 $^{\circ}\text{C}$, which is a typical growth temperature for QCLs.

This work was supported by the European Community-IST project SUPERSMILE, by the Austrian Microelectronics society and the Austrian FWF (SFB-ADLIS).

References

- [1] C. Pflügl, W. Schrenk, S. Anders, G. Strasser, C. Becker, C. Sirtori, Y. Bonetti, A. Muller, *Appl. Phys. Lett.* **83**, 4698 (2003).
- [2] D. Indijn, S. Tomic, Z. Ikonc, P. Harrison, R. W. Kelsall, V. Milanovic, and S. Kocinac, *Appl. Phys. Lett.* **81**, 2163 (2002).
- [3] J. S. Roberts, R. P. Green, L. R. Wilson, E. A. Zibik, D. G. Revin, J. W. Cockburn, and R. J. Airey, *Appl. Phys. Lett.* **82**, 4221 (2003).

Light Field in Quantum Cascade Ring Lasers

P. Schwaha, S. Anders, V. Tamosiunas, W. Schrenk and G. Strasser
Institute of Solid State Electronics, TU Vienna, Austria

Several geometries of circular micro resonators have already been investigated in the past with micro disks, micro cylinders and rings among them. These devices showed appealing performance characteristics such as a low threshold and lasing up to room temperature [1]. Theory on the distribution of light within such devices predicted the concentration of the light at the periphery in lowest order whispering gallery modes [2], [3]. This assumption motivated the exploration of electrically pumped quantum cascade lasers with ring shaped cavities. Several devices with varying inner and outer diameters were manufactured in the course of this investigation. The measurements performed on these devices indicated that the light is not confined to extreme periphery of the device but also extended into the center region of the device. It is the aim of this report to explain the distribution of the light field within these devices.

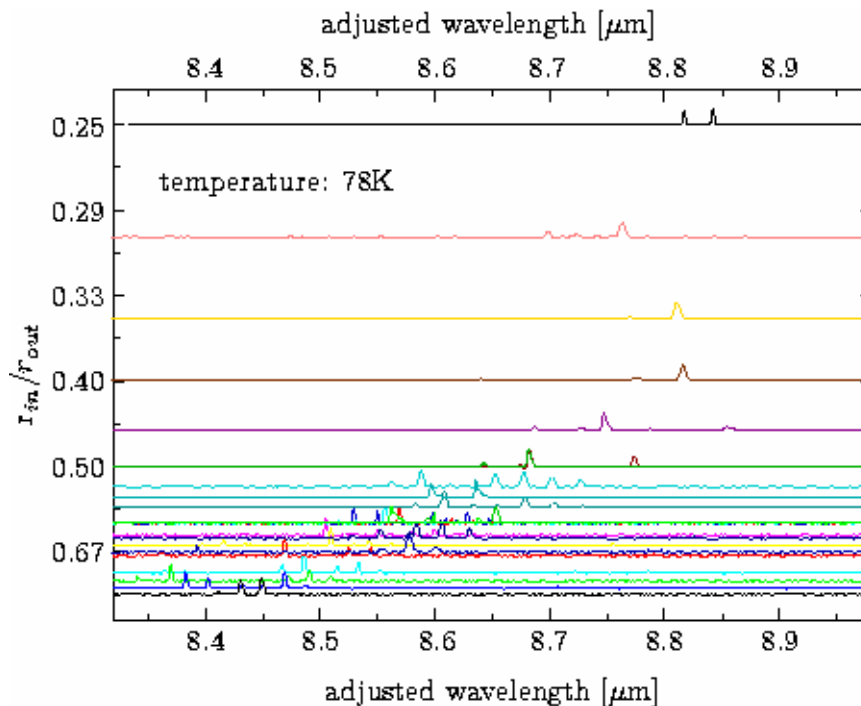


Fig. 1: The spectra begin to blue shift as the inner to outer diameter ratio exceeds the value of 0.4.

An important observation can be made by closely examining the emitted spectra. Since the emission wavelengths already shift with the change of the outer diameter at a constant ratio between inner and outer diameters, an adjustment of the emitted spectra is necessary to easily compare the different devices. Figure 1 shows these adjusted spectra. The spectra of the smallest devices (200 μm) were left unchanged, while the spectra of the larger devices (300 and 400 μm) were horizontally shifted by constant

factors. The vertical position of the normalized spectrum is defined by the ratio of the inner to outer to diameters of the originating device. It can be seen that the emitted wavelength is constant up to a ratio of 0.4. Devices having a diameter ratio beyond this exhibit an increasing blue shift of the emitted wavelengths.

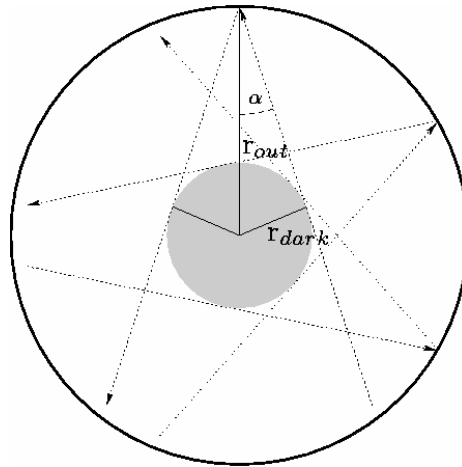


Fig. 2: The light reflected at the interface cannot enter the innermost region of the device.

A simple model based on ray optics can be used to explain this behavior. At the air-semiconductor interface total internal reflection occurs up to a certain critical angle. This critical angle depends on the refractive indices of the two adjoining media and in this case can be calculated at 18.4° . Light with a smaller angle of incidence than this critical angle is not reflected but will be refracted and leave the cavity. It thereby also limits the angle under which light is reflected back into the device. In this way it defines a central region that light, which is reflected at the border, cannot enter. This is shown in Fig. 2. The radius of the “dark zone” can be calculated as the sine of the angle of total internal reflection. As long as the inner diameter of a ring device is smaller than this “dark zone” the device’s operation remains undisturbed. As soon as the hole in the middle is bigger than the dark zone it pushes the light outward, resulting in the observed blue shift. The calculated value of inner to outer radius at which the spectra begin to shift is 0.32 and agrees reasonably well with the measured result. Simulations performed for ring shaped cavities [4] also agree with the assumption that the light field extends further into the central section of the device, than previously anticipated. This can be explained by the occurrence of higher order whispering gallery modes.

References

- [1] S. Anders, W. Schrenk, E. Gornik and G. Strasser; *Physica* **E 17**, 626 (2003).
- [2] S. Gianordoli, L. Hvozdar, G. Strasser, T. Maier, N. Finger, K. Unterrainer and E. Gornik; *Physica* **E 7**, 29 (2000).
- [3] C. Gmachl, F. Capasso, E. E. Narimanov, J. U. Noeckel, A. D. Stone, J. Faist, D. L. Sivco, and A. Y. Cho, *Science* **280**, 1556 (1998).
- [4] S. Anders, V. Tamosiunas, W. Schrenk, G. Strasser; *Phys. Rev.* **B 69**, 073309 (2004).

Terahertz Quantum-Cascade Lasers in a Magnetic Field

V. Tamošiūnas, R. Zobl, G. Fasching, J. Ulrich, G. Strasser and
K. Unterrainer

Institute of Solid State Electronics, TU Vienna, Austria

R. Colombelli, C. Gmachl, L.N. Pfeiffer and K.W. West
Bell Laboratories, Lucent Technologies, Murray Hill, New Jersey 07974

F. Capasso

Harvard University, Division of Engineering and Applied Sciences,
Cambridge, MA 02138

Terahertz quantum-cascade lasers (QCLs) are coherent sources of far-infrared radiation based on semiconductor heterostructures. Operation of QCLs in the Terahertz range of the electromagnetic spectrum was demonstrated just recently and the further improvement of the THz QCLs is a challenge for several reasons related to the intersubband population dynamics and to the waveguide properties. Electron-electron and interface roughness scattering represent the main scattering mechanisms at low temperatures in this range of intersubband energies. They lead to fast carrier relaxation and they counteract population inversion. It was proposed to increase the intersubband lifetime by applying a magnetic field normal to the epitaxial layers. The additional quantization (induced by the magnetic field) of the in-plane electronic motion dramatically modifies the electron-electron scattering in the Landau-quantized energy spectrum.

In this contribution, we report on the behavior of a 4.5 THz QCL in an external magnetic field. The structure consists of 100 periods of a layer system of GaAs wells and $\text{Al}_{0.15}\text{Ga}_{0.85}\text{As}$ barriers sandwiched between two n+-doped contact layers, and it was grown on a semi insulating GaAs substrate using molecular beam epitaxy.

The system used in the emission experiments consists of a FTIR spectrometer and a 4.2 K Si bolometer. For the magnetic field measurements, the THz QCL is mounted in a magnet cryostat with two superconducting magnets. In this cryostat, detection is possible by a magnetic field tunable InSb cyclotron resonance detector, by a broadband Ga doped Ge detector, or by the external FTIR (Fig. 1).

The broadband Ge detector was used to obtain the laser intensity as a function different sample magnetic fields which is presented in Fig. 2. The laser emission intensity increases substantially for certain values of the magnetic field when compared to $B = 0$ T. For increasing magnetic fields we observe oscillations with a larger period. The application of a magnetic field increases the laser intensity by a factor of more than five at $B = 4.2$ T. This effect is understood as a consequence of the discretization of the energy spectrum. A magnetic field breaks the subbands into ladders of Landau levels with energies:

$$E_2 - E_1 = \frac{\hbar e B_N}{m^*} N$$

where $E_2 - E_1$ is the energy difference, \hbar the Planck constant, e the elementary charge, B_N magnetic flux density, m^* effective mass, N an integer. For certain values of the magnetic field it is possible to achieve favorable conditions for fast energy relaxation in the injector and to suppress nonradiative relaxation in the active region. This

leads to an increase of the population inversion and to an increase of the emission intensity.

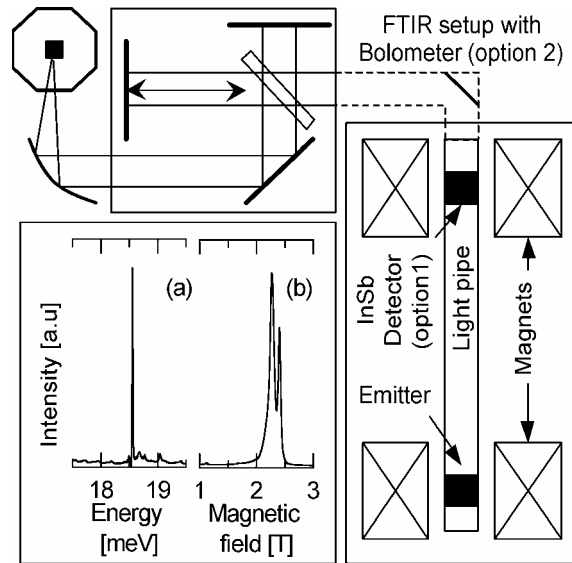


Fig. 1: Set-up for high resolution spectral measurements.
 (a) High-resolution spectrum of the laser without applied magnetic field at the emitter sample.
 (b) Response of the InSb detector versus applied detector magnetic field when illuminated by the THz laser.

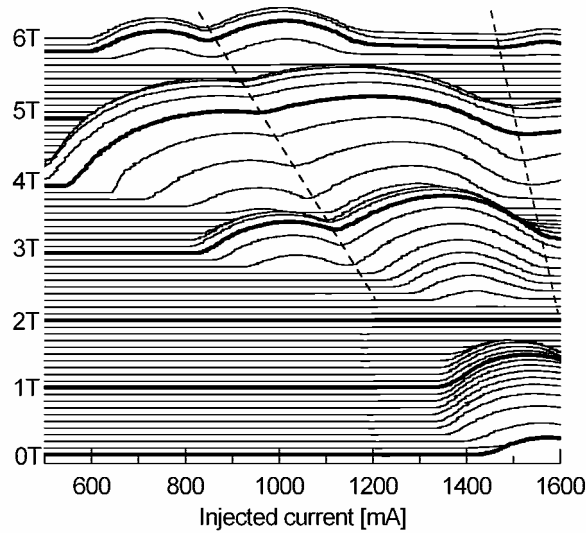


Fig. 2: Laser emission intensity as a function of the injected current at different magnetic fields applied to the sample. The pulse width was 150 ns at 90 kHz repetition rate.

Figure 3 summarizes the spectral features observed in the magnetic field. A substantial spectral shift is consistently observed in addition to a conventional Stark shift. A combination of Bloch gain, conventional intersubband gain, and many body effects like the depolarization effect can cause these emission line shifts. However, a future research is required to evaluate the possible contribution of each effect.

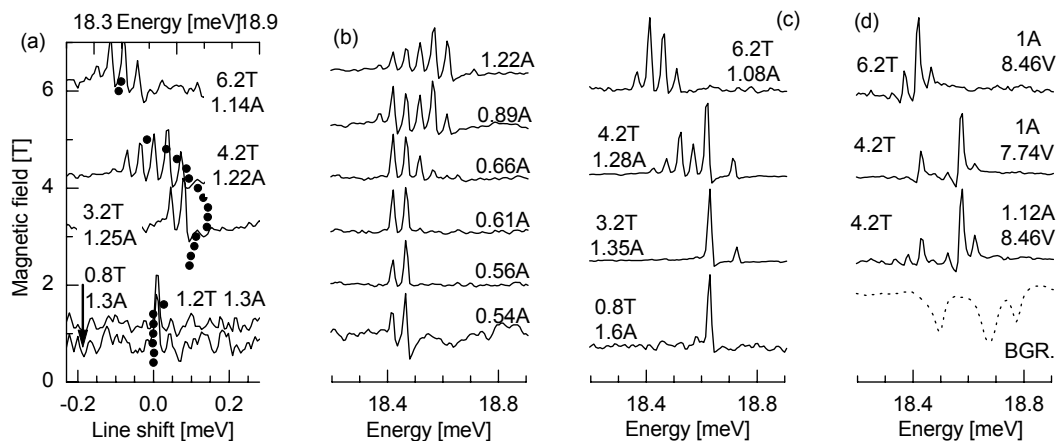


Fig. 3: (a) Frequency of the emission line vs magnetic field applied to the sample, measured by the InSb detector (dots), and high-resolution spectra measured by the external FTIR for several different magnetic fields (lines). (b) High-resolution spectra for different injected currents at a fixed magnetic field of 4.2 T. Multimode emission and a Stark shift are observed. (c) Constant bias voltage measurement: The measured voltage was set to 9.5 V for all measurements at a pulse length of 200 ns and at a repetition rate of 94 kHz. An additional emission line appears consistently above 18.7 meV at 3.2 and 4.2 T. The 18.65 meV emission line is not recorded due to a water absorption line. (d) Long pulse (400 ns) measurements at 6.2 T (1 A and 8.46 V, as measured on the sample), and for 4.2 T at constant voltage and current. A background spectrum with water vapor absorption lines is also presented (BGR).

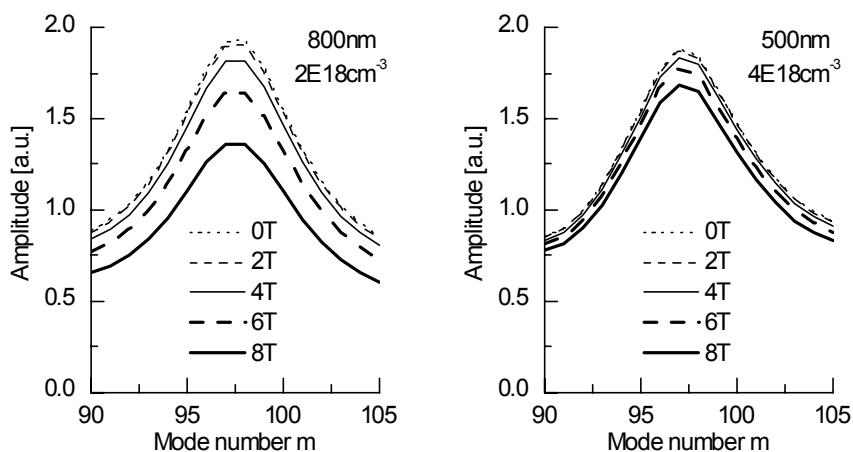


Fig. 4: Maximum amplitude versus resonator mode number simulation results for two different n^+ layers.

We have employed a finite-difference time domain (FDTD) based algorithm to investigate the changes of the waveguide properties in a magnetic field. Two waveguide designs are compared in Fig. 4. A broader operating range is predicted for our waveguide design when compared the design of Ref. [1]. A predicted intensity reduction in strong magnetic fields is also consistent with the experiment.

In conclusion, we have observed a reduction of the threshold current density, a simultaneous enhancement of the laser emission intensity in a magnetic field and clear shifts of the emission spectra when the external magnetic field is applied, while operating the device at constant voltage or current. Our FDTD simulation results for the QCL waveguide are consistent with the experimentally observed reduction of QCL emission intensity.

Acknowledgement

The authors acknowledge support from the FWF (SFB-ADLIS).

References

- [1] V. Tamosiunas, R. Zobl, J. Ulrich, K. Unterrainer, R. Colombelli, C. Gmachl, F. Capasso, K. West, L. Pfeiffer, *Applied Physics Letters*, **83**, 3873 (2003).
- [2] V. Tamosiunas, R. Zobl, G. Fasching, J. Ulrich, G. Strasser, K. Unterrainer, R. Colombelli, C. Gmachl, F. Capasso, K. West, L. Pfeiffer; "Magnetic Field Effects in Terahertz Quantum Cascade Lasers"; *Semiconductor Science and Technology*, to be published.

Fabrication of Dry Etched Planar Photonic Crystals for THz Regime

S. Golka, W.Schrenk and G. Strasser
Institute of Solid State Electronics, TU Vienna, Austria

Photonic Crystals (PhCs) in III-V semiconductors will play an decisive role in future telecom optoelectronic integrated circuits (OICs). Undoubtedly this is valid for related fields such as THz emitters and novel compound semiconductors as well. Besides the light guiding aspect many new phenomena which are very desirable for THz applications, such as enhancement of optical nonlinearities and efficient vertical coupling to continuum, can be observed in deep etched InGaAsP PhCs. In such devices the basic idea is to exploit the large degree of freedom one has with such PhCs in tailoring symmetries and shapes of cavity modes or high reflectivity mirrors but at the same time leaving a contiguous surface that allows for easy subsequent processing. In most cases the optical mode confinement is achieved by the “substrate approach”, e.g. planar light guiding by deep hole patterns and vertical guiding by a epitaxially grown high index layer as opposed to membranes or surface plasmon guiding. Heat and electric conduction to the substrate are provided for and multi-step fabrication is much easier than in membranes for example. Furthermore, the comparatively large minimum pattern size as required for THz allows for subsequent processing that is aligned to and/or in the same area of the PhC [1], such as top contacts. Etch depth [2] becomes the most critical parameter for these emitters, since epitaxial layers typically are several micron thick and holes need to penetrate the substrate much further than the guided light mode.

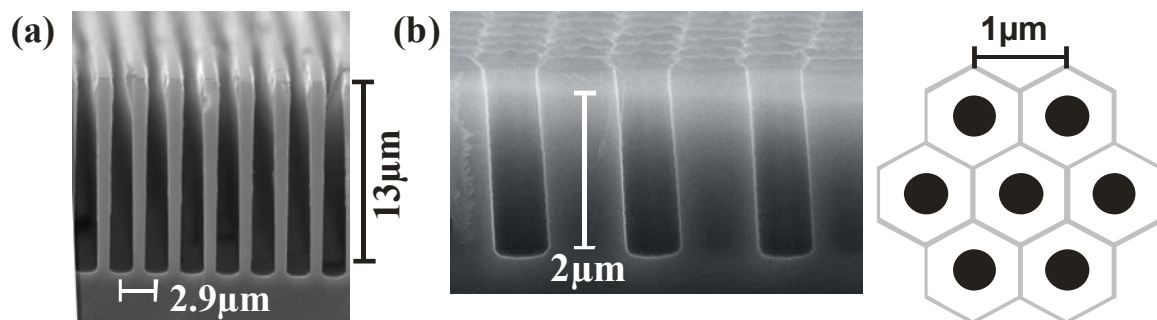


Fig. 1: (a) SEM picture of cleaved sample with $N_2/SiCl_4$ process with 1:1 molecular flow, duration 38 min, best sidewall protection obtained so far; (b) same etch process applied on a two dimensional PhC with 1 μm pitch etched for only 13 min. Pattern was generated with 30 KV EBL in 400nm PMMA 950K resist. Roughness on the top is the remainder of the SiN_x mask after deep etching that could be easily removed by HF or SF_6 plasma. Etch duration was limited by stability of PMMA resist in SF_6 .

Due to the importance of deep etching in a first step we solely focus on the process for GaAs. In order to achieve sufficient etch selectivity a hard mask with good adhesion such as SiN_x is needed. A two step process of first structuring the SiN_x from a resist with SF_6 plasma and then, after resist removal, etching with $SiCl_4$ high density plasma

has proven very convenient. This also has the advantage of easy migration to novel lithography methods as stamp-imprinting or deep UV. In the case of standard UV lithography (Fig. 1 (a)) 500nm of AZ5214 resist will suffice to etch 500 nm of SiN_x . In the case of electron beam lithography (EBL, Fig. 1 (b)) a plasma-stable resist is needed.

In deep etching very high aspect ratio is needed in densely packed hole patterns, $F=30\%$, so some mechanism must be present to inhibit underetch. With free standing walls, back-sputtering of etch products would serve as such mechanism, but in deep trenches/holes the ratio of floor to wall area is too small for efficient side wall coverage. In our inductively coupled plasma reactive ion etcher (ICP-RIE) we tried both an Ar/SiCl_4 and N_2/SiCl_4 gas mixture. Both mixtures showed fundamentally different behavior in the plasma (Fig. 2 (b)). For Ar [3] chemically sticky GaCl_x might be expected for proper parameters that is sputtered off the floor by Ar but not off the walls. But decent results were obtained with N_2 only. We believe that the nitrogen in the plasma enhances saturation or deposition of some Si containing species on the hole sidewalls that is not volatile even at slightly elevated temperatures, which is not surprising thinking of SiCl_4 as a precursor in Silicon technology [4]. It therefore provides for sidewall protection even at very large etch depths (Fig. 1 (a)). This also is consistent with the dependence of etch rate on flow ratio (Fig. 2 (b)) in which the rate is slightly enhanced by Ar surface cleaning but degraded by too much N_2 induced deposition which is valid at least for the process window where we found each process to work at all for small patterns.

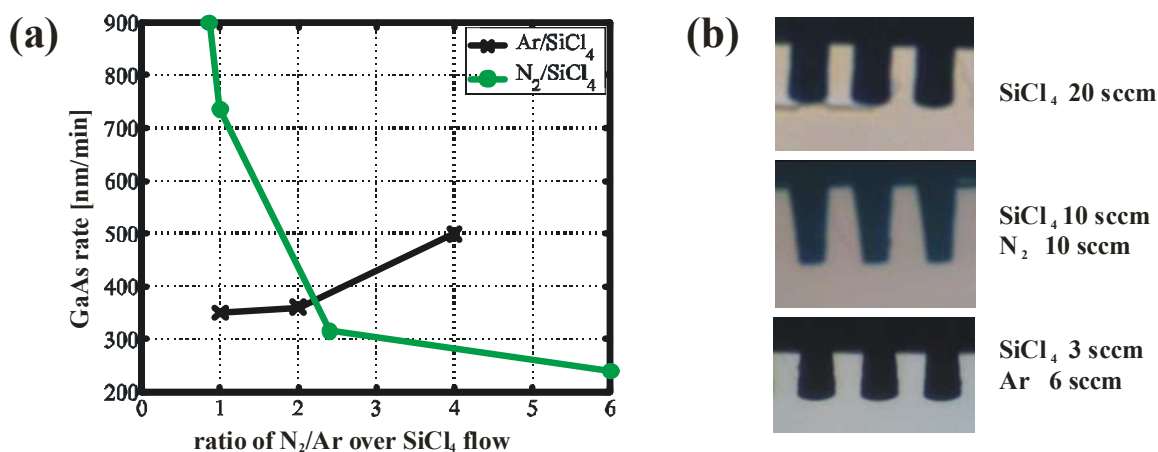


Fig. 2: (a) Typical trench profiles for different kinds of physical etching contribution in ICP processes;
 (b) etch rate dependence on physical/chemical ratio at $P = 3$ mtorr, gas flows were 3 times lower in the case of Ar intentionally due to severe underetch, hence the lower vertical etch rate;

In conclusion, we have shown the main contribution of process parameters to SiCl_4 ICP-RIE where we distinguished between adding Ar or N_2 . Etch depths of $13\ \mu\text{m}$ were achieved for N_2 with a mask that could be easily fabricated in a 2 step procedure with one more SF_6 etch. The achieved trench depth will be sufficient for low scattering losses in high index guided structures. Furthermore we fabricated two dimensional PhCs with E-Beam lithography with the same process.

References

- [1] R. Colombelli, M. Troccoli, K. Srinivasan, O. Painter, C. Gmachl, F. Capasso, D. M. Tennant, A.M. Sergent, D. L. Sivco, and A. Y. Cho, *Proc. ITQW 2003*, Evolene, Switzerland
- [2] R. Ferrini, B. Lombardet, B. Wild, R. Houdr'e, and G.-H. Duan. Hole depth- and shape-induced radiation losses in two-dimensional photonic crystals, *Appl. Phys. Lett.* 82(7), 2003
- [3] R. J. Shul, G. B. McClellan, R. D. Briggs, D. J. Rieger, S. J. Pearton, C. R. Abernathy, J. W. Lee, C. Constantine, and C. Barratt, *J. Vac. Sci. Technol.* 15(3), 1997
- [4] I. Endler, A. Leonhardt, M. Schonherr, and E. Wolf, *J. of Material Science* 26(3), 1991

Plasmon Enhanced THz Emission

M. Coquelin, R. Zobl, G. Strasser and E. Gornik
 Institute of Solid State Electronics, TU Vienna, Austria

In 2001, a three energy level structure, based on the GaAs/AlGaAs material system, was proposed [1] as the active region of a plasma instability driven THz radiation source. The basic idea of this structure is to reach population inversion between the second and third energy level, while the lowest energy level is filled. Therefore electrons are injected in the third level and extracted from the second one which is in resonance to the extraction level of an RTD. We investigated a novel design now, based on the GaAs/InGaAs material system (Fig. 1). The active region of the new sample g564 consists of an $\text{In}_{0.05}\text{Ga}_{0.95}\text{As}$ -well between a GaAs drift region and the extracting RTD followed by another GaAs layer. This well is an efficient electron trap. Thus we can assume the lowest level to be filled with electrons. The whole “unit cell” shown in Fig. 1 is repeated 10 times to increase the radiation output of the sample.

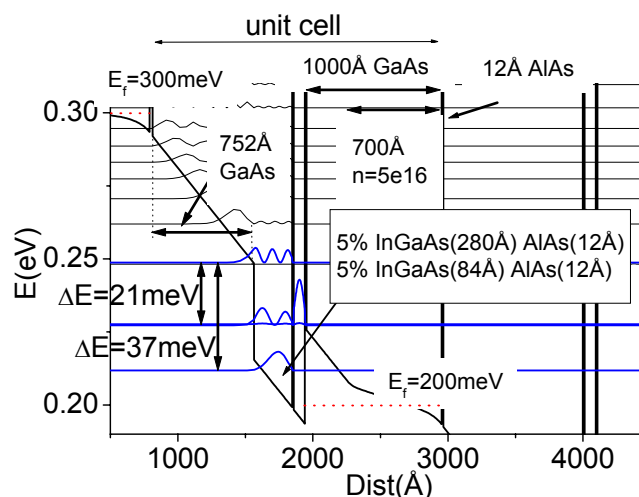


Fig. 1: Conduction band of g564 at working bias

The emission spectra of this structure were measured by using a FTIR step scan spectrometer. Figure 2 shows two typical spectra for each bias direction measured at 4K. Figure 2 (a) shows the emission in forward direction. The electrons are injected from the drift region and extracted through the RTD. One can see three sharp lines between 118 cm^{-1} and 125 cm^{-1} and a broad emission peak at around 145 cm^{-1} . In contrary to the broad peak, the sharp lines occur also in the spectra of the inverse biased sample (Fig. 2 (b)). Due to the asymmetric structure of the sample we cannot reach the needed population inversion in this case. This means that plasmon instability is not the origin of the sharp lines. While these lines seem to be insensitive to the applied bias the broad line shifts to higher energies with increasing bias (Fig. 3) and increasing current densities, until it vanishes at current densities higher than 60 Acm^{-2} . The energy of this peak is in good agreement to $\Delta E_{13}/2$, which is the expected energy region of the instability, but the current densities are too small to reach the required population inversion.

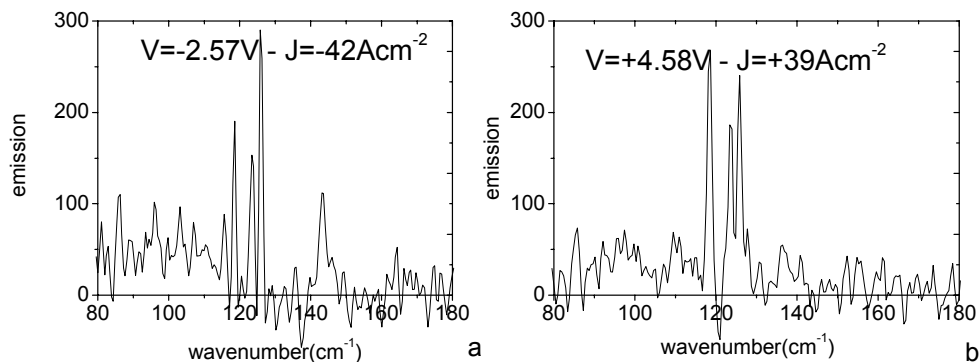


Fig. 2: Step scan measurements at 4K achieved from a negative biased device (a) and positive (inverse) biased device (b)

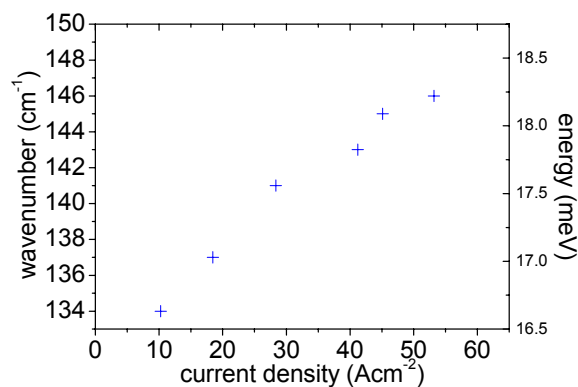


Fig. 3: Peak positions of the intersubband emission peak of g564 versus the current density

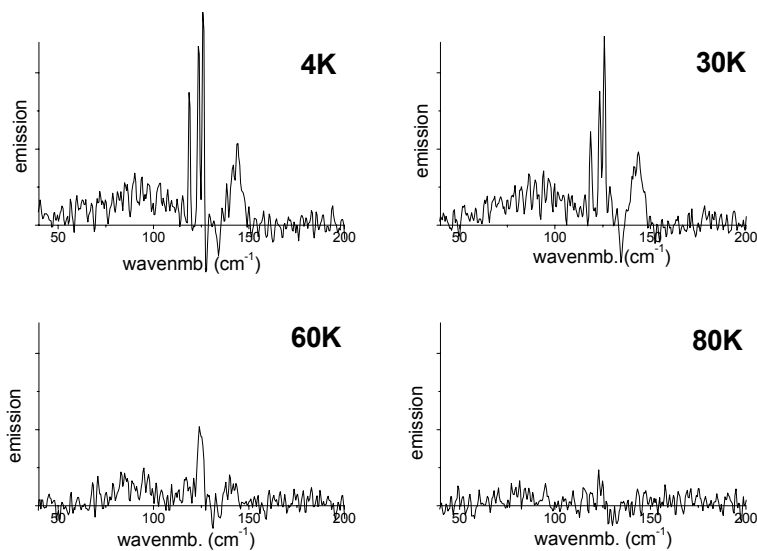


Fig. 4: Emission of g564 at different temperatures

A good proof for plasmon instability is the temperature dependence of the emission, because the instability is a many body effect and therefore is less sensitive to high temperatures than intersubband emission. Figure 4 shows the emission of the sample at different temperatures. One can see that the intensity of all features in the spectra decreases with increasing temperature and vanishes at temperatures around 80 K. This means that the emission of this sample is caused by intersubband scattering.

References

- [1] GME Report 2001: "Search for Plasma Instability Driven THz Radiation Sources", E. Gornik, G. Strasser, R. Zobl, M. Kast, C. Pacher

Heterostructure-Based Photoconductive Terahertz Emitters

J. Darmo, G. Strasser, J. Kröll and K. Unterrainer
Institute of Solid State Electronics, TU Vienna, Austria

Generation of THz radiation within a femtosecond mode-locked laser cavity using a photoconductive emitter was recently demonstrated [1]. The emitter is based on an AlGaAs/AIAs Bragg reflector with low-temperature-grown (LTG) GaAs. The LTG GaAs has two functions: as a saturable absorber and as an active photoconductive layer of the THz emitter. In order to achieve optimal emitter performance, we have focused on tuning the properties of LTG GaAs to maximise THz output power.

The THz emitter comprises a Bragg mirror stack made of the AlGaAs/AIAs layers and LT GaAs layer grown usually at 220 °C and annealed at 600 °C. The parameters of LTG GaAs strongly depend on the growth temperature and post-growth thermal history (i.e., annealing temperature and time). Changing growth temperature thus allows modifying the charge carriers' lifetime and mobility. In the standard LTG GaAs, the carrier lifetime is in the sub-picosecond range, while carrier mobility is about 30 times lower than in normal GaAs. Therefore, we have prepared a set of emitter structures with LTG GaAs grown at different temperatures between 220 and 350 °C.

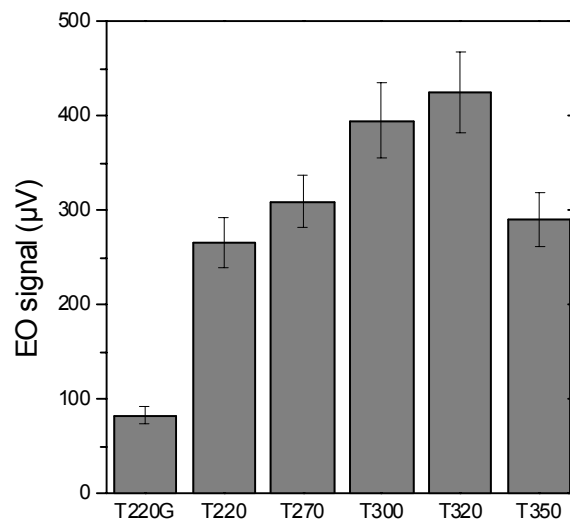


Fig. 1: Output THz radiation from LT/BR emitters with LTG GaAs layer grown at different temperatures. Emitters were biased at 150 V.

Figure 1 shows the output THz power from the emitter at a bias of 150 V. The efficiency of emitters increases with the LTG GaAs growth temperature, but for temperature of 350 °C efficiency already drops. The emitters are also compared to one labelled T220G (standard photoconductive THz emitter without Bragg mirror) exhibiting significantly lower THz emission efficiency. The gradual increase of emission efficiency with the LTG GaAs growth temperature is explained by a synergetic effect of longer lifetime and the higher mobility of charge carriers [2]. Final drop in THz emission efficiency is due to an enormously increased dark conductivity of the emitter.

Another problem that we have addressed is a fatal breakdown of the THz emitter when a certain optical power is exceeded. This breakdown is related to a local increase of the temperature of the emitter due to the deposited optical power. We have studied the thermal resistance of the emitter structures. An attenuated laser beam at 800 nm was focused to an area of about 100 μm in diameter. The local temperature was monitored by means of a deposited platinum strip. Figure 2 shows the thermal resistance we observed for four different emitters structures – LTG GaAs on GaAs substrate, with AIAs and AlGaAs/AIAs Bragg mirror stack, and SI GaAs substrate only. The LTG GaAs exhibits reduced thermal conductivity in comparison to the standard GaAs, therefore, all structures with LTG GaAs have a higher thermal resistance. The insertion of a thermally well conductive layer (AIAs or AlGaAs/AIAs) helps to reduce the overall device thermal resistance. In practice it means that the local temperature of the THz emitter can be reduced by more than 50 K when a convenient structure is used.

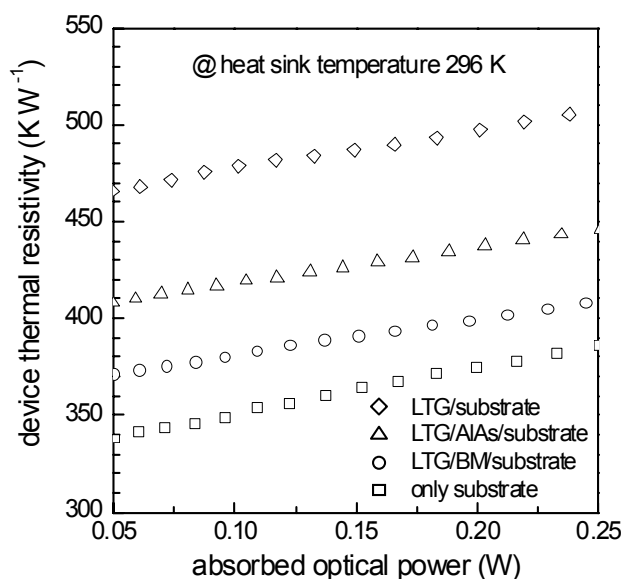


Fig. 2: Thermal resistance of THz emitters with different structure layout. The size of the focus was about 100 μm in diameter

In conclusion, we have improved the performance of the photoconductive THz emitter (i) by means of optimised parameters of the LTG GaAs active layer; and (ii) by improving the heat management of the emitter.

References

- [1] J. Darmo, T. Müller, G. Strasser, K. Unterrainer, G. Tempea; "Terahertz emitter with an integrated semiconductor Bragg mirror"; *Electron. Lett.* **39**, 460-462 (2003).
- [2] J. Darmo, J. Kröll, T. Müller, G. Strasser, and K. Unterrainer, "Cavity enhanced THz generation", *Terahertz and Gigahertz Electronics and Photonics III*, part of the *Photonics West Symposium Optoelectronics 2004: Integrated Optoelectronics Devices*, San Jose, California, USA, 24-29 January 2004.

Metallic Anti-Reflection Coating for Terahertz Technology

J. Kröll, J. Darmo and K. Unterrainer
Institute of Solid State Electronics, TU Vienna, Austria

The recent progress in the Terahertz technology widens the field of application of far infrared radiation [1] – [3]. There is a big interest to characterize various organic and non-organic materials [4] in this frequency region. One of the problems occurring in Terahertz time-domain spectroscopy (THz-TDS) measurement based on electro-optic detection [5] are reflections of the THz wave within the electro-optic crystal. As known from the Fourier transformation of a time shifted signal, these reflections manifest themselves as a modulation of the original spectrum with the period given by the delay time. Depending on the magnitude of the reflection peak it is very difficult to identify narrow absorption lines since they are hidden or blurred within this modulation. Till now no complete solution for this problem has been found. The reflected wave can be shifted out of the measured time window by attaching a long non-active electro-optic crystal (EOC) to the backside of the active EOC. Another method is to avoid that the reflection is detected by applying a tilt between the Terahertz and probe beam. Both these methods, however, decrease the data quality. The standard optics approach to a solution is to use an anti-reflection coating that means a layer of optical thickness of $\lambda/4$. For 300 μm wavelength (~ 1 THz) the required layer thickness is about 50 μm which is difficult to deposit. The other possibility is to use an anti-reflection principle coming from the electrical engineering where two regions of different wave impedance are connected by using a well adjusted resistor between them to avoid any reflection.

In this contribution, we report on a high resolution THz-TDS system using an electro-optic crystal (EOC) with an anti-reflection coating consisting of thin chromium layer. We apply this system to study molecular and lattice related optically active vibrational modes of benzoic acid in the frequency range 0.1 – 5 THz with a resolution of 20 GHz.

The benzoic acid is measured in a pure crystalline form and mixed with polyethylene (PE). Latter samples are in the form of the pressed pellets. PE is chosen as a matrix material because of the low index of refraction and negligible absorption at the frequencies of interest. These two types of samples are used to distinguish between molecular and lattice vibrational modes.

Figure 1 shows our THz-TDS system. It uses a Ti:Sapphire laser with 80 femtosecond long NIR pulses to generate coherent THz radiation from a biased GaAs emitter and to gate an electro-optic GaP detector. With this system, a bandwidth of 5 THz and a signal-to-noise of more than 1000 is reached.

To avoid reflections at the air/GaP interface we use an EOC coated with a 81 Å thick chromium layer. Due to the optimized sheet resistance of the metal layer, the wave impedance of the GaP is matched to that of air and no back propagating THz electromagnetic wave exits in GaP. The improved signal quality is demonstrated in Fig. 2. It can be seen that the chromium coating reduced the magnitude of the reflection at time delay of 7 ps after main pulse. As a result, the strong periodic modulation of the spectrum is fully suppressed and the high frequency resolution of THz-TDS is enabled.

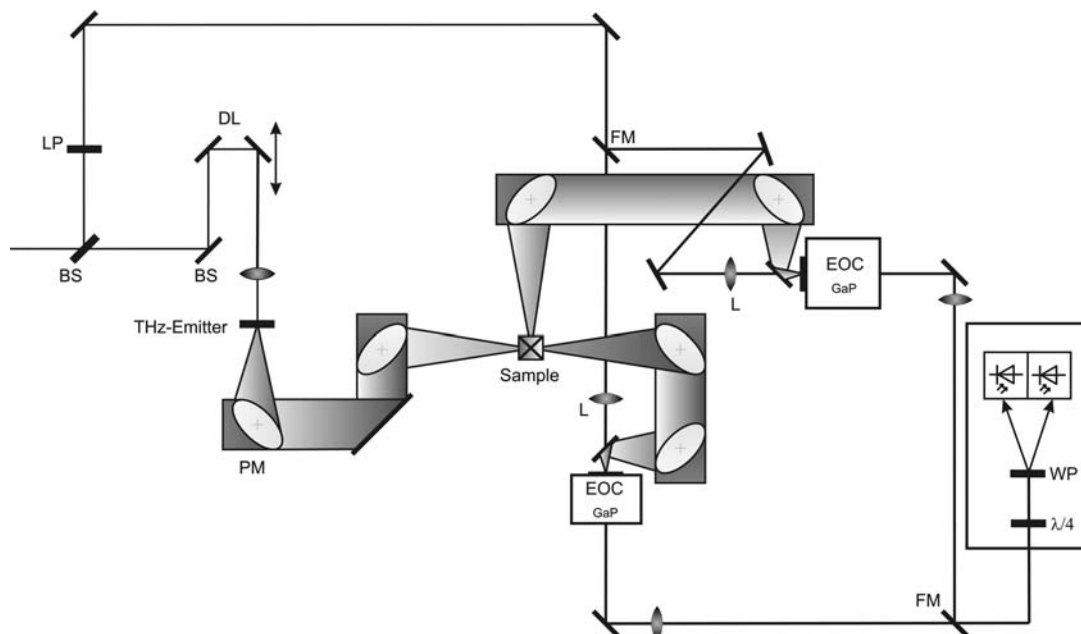


Fig. 1: Schematic of the Terahertz time-domain spectrometer with time resolved measurement of absorption and reflectivity option (BS-NIR beam splitter; DL delay line; EOC electro-optic crystal; L lens; PM off-axis parabolic mirror; WP Wollaston prism; FM folding mirror).

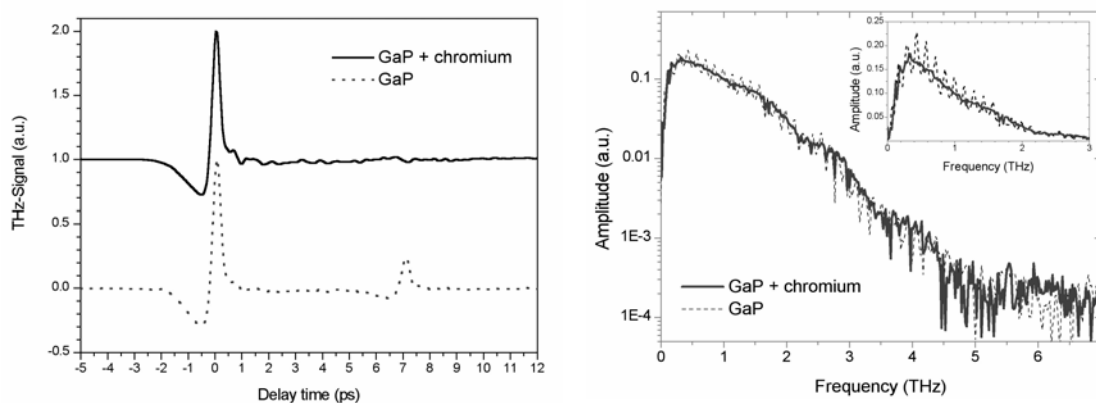


Fig. 2: Comparison of the THz signal in time-domain (left panel) and frequency-domain (right panel) of a gallium-phosphid electro-optic crystal with and without chromium coating. The inset: linear scale.

We apply the improved THz-TDS system to study the optically active vibrational mode of the benzoic acid. Fig. 3 shows typical absorption spectra of a benzoic acid crystal measured at room temperature for two different angles between the crystal orientation and polarization of the coherent THz radiation. Their absorption spectra contain a narrow absorption line at 0.9 THz and a broad band beginning at 1.2 THz. The difference in the weight of the individual frequency components is due to projection of corresponding dipoles to the plane of polarization of the probe radiation.

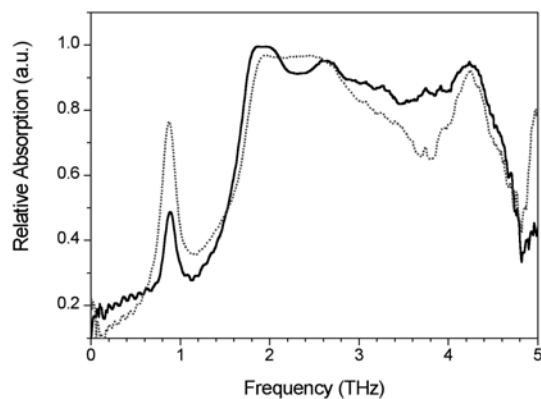


Fig. 3: Relative absorption spectrum of a benzoic acid crystal at two different crystal orientations.

Acknowledgement

The authors acknowledge support from the Austrian “Gesellschaft für Mikro- und Nanoelektronik” and FWF (SFB-ADLIS).

References:

- [1] J. Darmo *et al.*, “Terahertz emitter with integrated semiconductor Bragg mirror”, *Electronics Letters*, vol. 39, p. 460, 2003.
- [2] J. Darmo *et al.*, “Few-cycle THz generation for imaging and tomography applications”, *Physics in Medicine and Biology*, vol. 47, p.3691, 2002.
- [3] K. Unterrainer *et al.*, “Few-cycle THz spectroscopy of nanostructures”, *Physica-E.*, vol. 7, p. 693, 2000.
- [4] M. Walther *et al.*, “Collective Vibrational Modes in Biological Molecules Investigated by Terahertz Time-Domain Spectroscopy”, *Biopolymers (Biospectroscopy)*, vol. 67, p. 310, 2002.
- [5] Q. Wu, and X.-C. Zhang, “Free-space electro-optic sampling of Terahertz beams”, *Appl. Phys. Letters*, vol. 67, p. 3523, 1995.

Ultrafast Intraband Dynamics in InAs/GaAs Quantum Dots

T. Müller, F. F. Schrey, G. Fasching, G. Strasser and K. Unterrainer
Institute of Solid State Electronics, TU Vienna, Austria

The dynamics of carriers in semiconductor quantum dots (QDs) has attracted much attention during the last decade because of their physical interest and their important implications on the performance of novel optoelectronic devices. Most of the experiments have been performed by interband spectroscopy, where the signal reflects the combined electron-hole dynamics. Here we report an interband pump – intraband probe experiment which is sensitive to the capture and relaxation of electrons only [1].

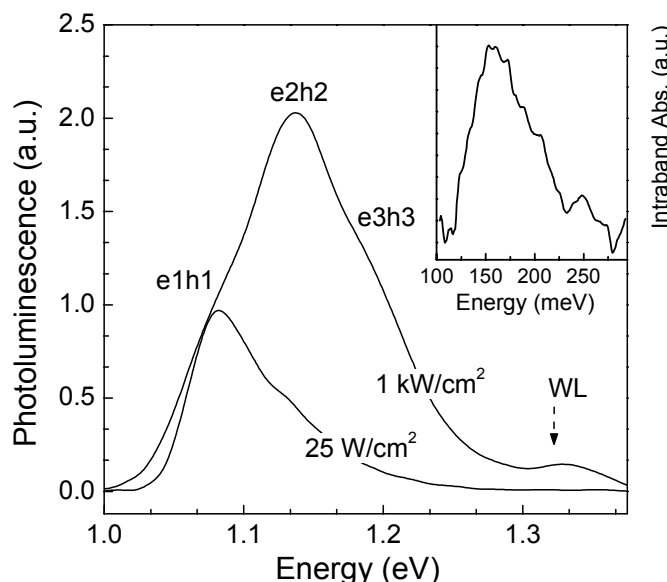


Fig. 1: PL ($T = 300$ K) spectra at two different excitation densities. Inset: Photo-induced $e1$ – WL intraband absorption spectrum at $T = 5$ K.

The $T = 300$ K photoluminescence (PL) spectra of the QD sample (30 layers of InAs QDs separated by 50 nm thick GaAs barriers) at excitation densities of 25 W/cm^2 and 1 kW/cm^2 are shown in Fig. 1. We observe three QD transitions, corresponding to $e1h1$ emission at 1.081 eV, $e2h2$ emission at 1.137 eV and $e3h3$ emission at 1.194 eV, as well as luminescence at 1.333 eV from the underlying InAs WL. From the PL we estimate the intraband transition energy between the QD ground state $e1$ and the WL to be ~ 160 meV. This value is in good agreement with the energy obtained from the photo-induced intraband absorption spectrum shown in the inset. Accordingly, we expect intraband transitions from the excited states $e2$ and $e3$ to the WL at energies of ~ 105 meV and ~ 50 meV, respectively. For time-resolved measurements of the intraband transitions we used a mode-locked Ti:sapphire laser that delivers 12 fs pulses (780 nm wavelength). Half of the laser intensity serves as an interband pump to inject electrons and holes in the GaAs barriers. The other part is used to generate the tunable (70 – 155 meV) mid-infrared (MIR) probe pulses by phase-matched difference frequency mixing in a 0.5 mm GaSe crystal.

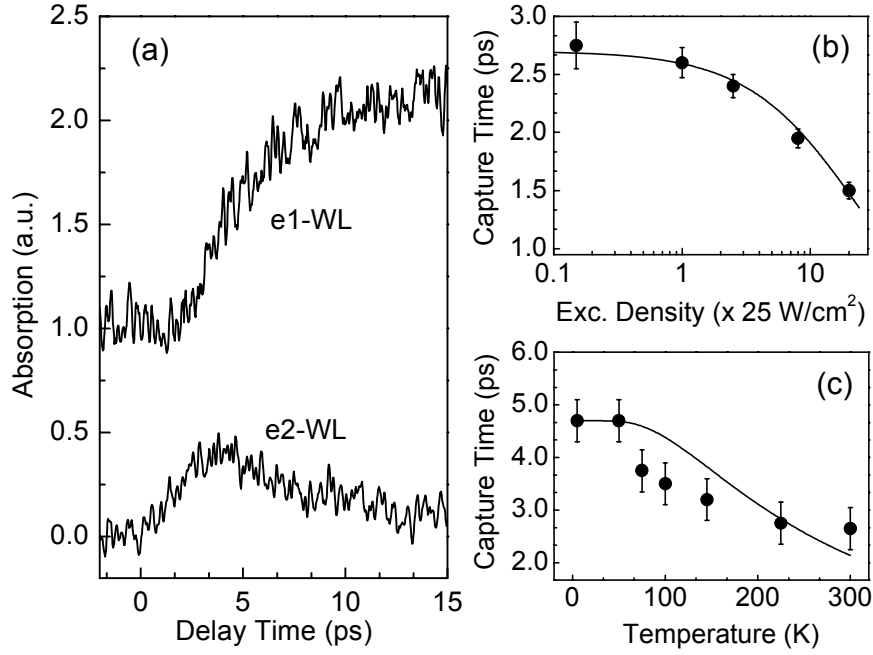


Fig. 2: (a) Photo-induced MIR absorption signals as a function of pump-probe delay at probe energies of 155 meV (upper curve) and 105 meV (lower curve), corresponding to the e1 – WL and e2 – WL intraband transitions, respectively. (b) Excitation density dependence and (c) temperature dependence of the capture time.

Figure 2 (a) shows typical pump-probe signals ($I_p = 25 \text{ W/cm}^2$) at $T = 5 \text{ K}$ when the probe is tuned into resonance with the e1 – WL and the e2 – WL transition, respectively. After excitation the photo-excited electrons relax very fast into the InAs WL, and from the MIR absorption at different probe energies the QD level populations can be determined. From our measurements we find that the QD ground state e1 gets populated via the excited state e2, because the electrons leave e2 with the same time constant as they arrive in e1. As shown in Fig. 2 (b), the excitation density dependence of the capture time exhibits two regimes: At room-temperature it decreases from about 2.7 ps down to 1.5 ps with increasing excitation density above a certain threshold, and it changes only slightly at low excitation densities. The high-power dependence can be explained by electron-electron scattering: An electron is scattered into the QD ground state by transferring its energy to a hot electron in the barrier or the WL. When measuring the temperature-dependence of the capture time we find an increase of τ_c from 2.7 to 4.7 ps upon decreasing the temperature from 300 to 5 K (Fig. 2 (c)). The LO-phonon energy of InAs amounts to $E_{LO} = 29 \text{ meV}$ and the average electron level separation in our QDs is 55-56 meV. Thus, one possible explanation for the observed short capture times could be that electrons scatter between subsequent QD states via repeated emission of two LO-phonons. The corresponding two-phonon scattering rate for this process can be written $\tau_c^{-1} = \Gamma_0 [N_{LO}(T) + 1]^2$, where Γ_0 is the scattering rate at $T = 0 \text{ K}$ and $N_{LO}(T)$ is the Bose-Einstein distribution function for LO phonons. The calculated curve (solid line) can roughly account for the experimental temperature dependence.

References

- [1] T. Müller, F. F. Schrey, G. Strasser, and K. Unterrainer, *Appl. Phys. Lett.* **83**, 3572 (2003).

Confocal Micro-Photoluminescence and Micro-Photoluminescence Excitation Spectroscopy on Single Self Assembled InAs Quantum Dots

F.F. Schrey, G. Fasching, T. Müller, G. Strasser and K. Unterrainer
Institute of Solid State Electronics, TU Vienna, Austria

Carrier dynamics in semiconductor quantum dots (QDs) have attracted much attention during the last decade, since a profound understanding of the underlying processes is essential for the development of novel optoelectronic devices. Furthermore, a direct addressing of the quantum dot states by means of optical coupling between electronic states will open the door for coherent manipulation of these states. However, most of the optical studies in QDs are carried out on dot ensembles because single dot spectroscopy needs high spatial resolution and appropriate dot densities in the range of approximately 10^8 dots/cm² or even less. While dot ensembles imply the advantage of a higher signal to noise ratio due to the higher amount of emitters, their spectroscopic signature suffers at the same time from ambiguities imposed by ensemble broadening and possible dot-dot interactions. Thus, for basic studies of optical QD properties it is desirable to have a tool to access and manipulate single QDs. In this contribution we present first results on our micro-photoluminescence (μ PL) and μ PL-excitation (μ PLe) setup and demonstrate its abilities as a tool for nanophotonic studies on semiconductor QDs.

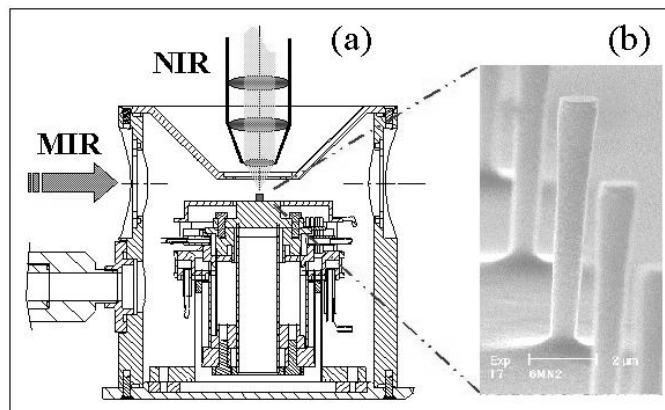


Fig.1: (a) Coupling scheme for the μ PL and μ PLe measurements. The MIR radiation is focussed by parabolic mirrors via the KBr side windows of the cryostat. (b) Typical 1 μ m diameter micropillars on which the single dot experiments are carried out.

The functional part of the experimental setup is sketched in Fig. 1 (a). The near infrared (NIR) excitation path as well as the PL detection path lead through a self-built confocal laser scanning microscope (LSM) with a lateral and axial resolution below 500 nm. The sample is placed in a low drift Oxford LHe flow cryostat and excited through the top window by a picosecond Ti:sapphire-laser at 745 nm with different excitation densities

for the μ PL measurements. For μ PLE the light source is a cw Ti:sapphire-laser, which is continuously tunable between 700 nm and 1080 nm with a linewidth of less than 30 GHz. The μ PL signal is filtered by appropriate long pass filters and dispersed in a 0.5 m spectrometer, which allows a spectral resolution better than 50 μ eV with a nitrogen cooled CCD detector or for small dot ensembles the signal can be recorded by a nitrogen cooled InGaAs photodiode. The CCD limits the spectral region to 1100 nm, while the diode allows detecting signals up to 1500 nm. Depending on the wavelength and the polarization of the emission the spectral efficiency of the setup reaches 3 % to 10 % for low light applications with a high signal to noise ratio. Besides top coupling of light, the cryostat allows superimposing other light sources such as mid-infrared radiation (MIR) via the side windows in a cross correlation scheme.

For the samples a QD density of approximately 10^8 dots/cm² or below is required due to the lateral resolution of the confocal setup. We could obtain this density by a gradient molecular beam epitaxial (MBE) growth, where the rotation of the wafer is stopped while the InAs is deposited on the GaAs. In low density region the ground state emission of the dots varies between 1040 nm and 870 nm. In order to exclude signal contributions from neighboring dots the sample is processed into an array of micropillars as shown in Fig. 1 (b). These pillars, which are approximately 8 μ m high and vary between 1 μ m and 10 μ m in diameter, allow the addressing of single QDs. Furthermore, they act as microantennas for the superimposed MIR radiation.

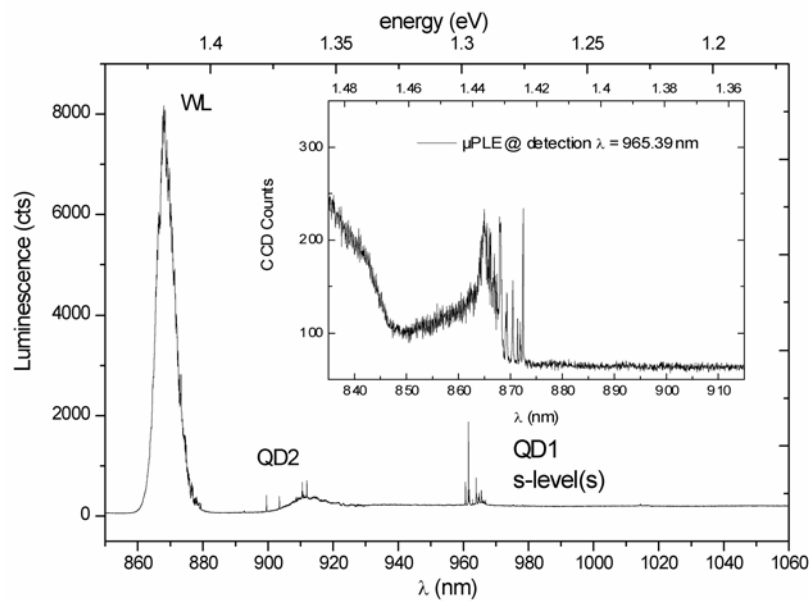


Fig. 2: μ PL spectrum of 2 QDs within a 10 μ m micropillar: The spectrum exhibits two groups of discrete lines, which correspond to the interband transitions of the excitons within the different QDs. The inset shows the μ PLE spectrum of the 965.39 nm transition in QD1. Resonant states are found close to the broadened WL transition.

Figure 2 shows the high excitation μ PL spectrum of a 10 μ m micropillar which contains two quantum dots. The corresponding μ PLE spectrum exhibits some sharp resonances around 873 nm very of the 965.39 nm 1-S exciton transition close to the wetting layer (WL), which is centered around 865 nm with and FWHM of 7 nm. This indicates that for the investigated dot the excited states can be found very close to the wetting layer states. The broadening of these excited states might be due to an interaction of discrete QD states with the broader two dimensional quantum well states of the WL.

In a second experiment we superimpose MIR radiation with the NIR excitation on a similar sample. An Ion-Optics glow bar generates the black body spectrum, which is used as THz/MIR source for the 10 meV to 900 meV radiation. This spectrum is coupled via two parabolic mirrors and through the KBr side window into the cryostat with a focal spot diameter of approximately 1 mm. The measurement in the lower energy level around 960 nm is performed in three steps: First the PL spectrum under NIR laser excitation is recorded with the CCD and labeled as NIR01. In the second step the MIR source is superimposed with the laser excitation and the second spectrum is recorded as MIR01. In a third step we use again only the laser excitation and label the spectrum NIR02. The whole procedure is then repeated for the spectra of the excited levels around 910 nm. Subtraction of the NIR01 spectra from the MIR01 spectra reflects the changes in the count rate for the different levels.

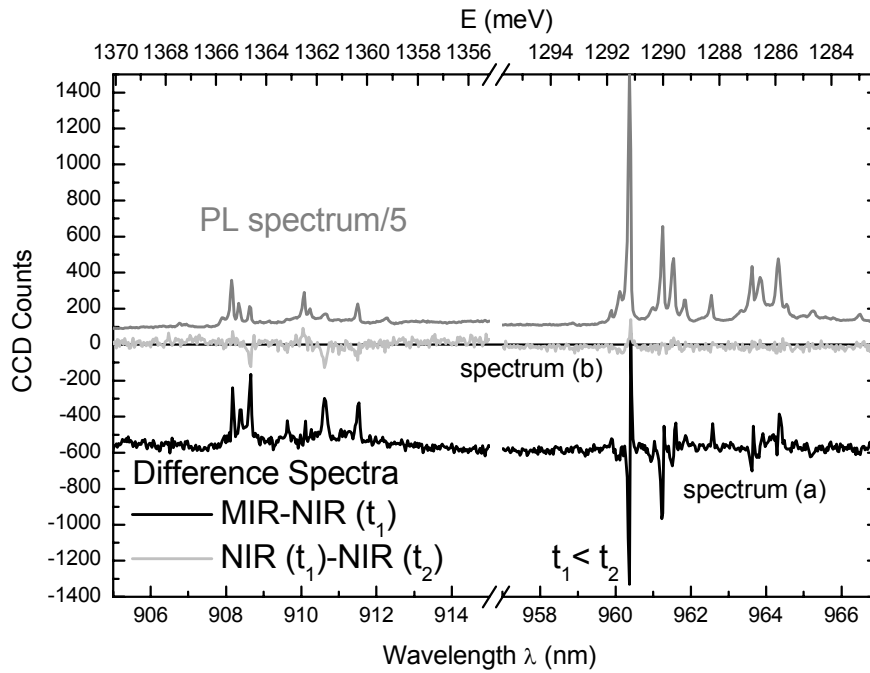


Fig. 3: Near infrared PL spectrum of the SQD at an excitation density of 576 W/cm^2 and corresponding difference spectra: In the case of the superimposed NIR, MIR excitation the level population changes are monitored via the NIR μ PL signal. The count rate in the lower energy states is reduced, while an increase in the upper states can be measured.

Subtracting NIR02 from NIR01 (spectrum (b) in Fig. 3) gives a measure for drift in the whole system. The results in Fig. 3 show the impact of the MIR radiation on the count rate, while the NIR excitation density was kept constant at 1440 W/cm^2 . In the lower energy levels of difference spectrum (a) in Fig. 3 the count rate is clearly reduced while in the higher levels, which are separated by approximately 75 meV from the lower levels, the luminescence is increased. This result strongly suggests that we observe a direct electron transfer from the lower electronic levels of the QD into higher levels. The drift during the experiment is negligible as indicated by spectrum (b). Because of the high cw excitation density, which nearly saturates the lower level PL, we assume that the underlying process for the PL changes results rather from a direct, optically induced transition into higher dot states than a mediated transition via WL or GaAs CB states [1]. The latter process would change the count rate in both levels into the same direction due to the very fast scattering mechanisms within the dot.

In conclusion, we could demonstrate that we built up a powerful microscopy setup, which provides us with the necessary tools for basic quantum dot studies. In first experiments we could already show a direct, optical induced electron transfer between intersublevels within a QD. In a new experiment we will extend the possibilities of the system by combining it with a cross correlation NIR pump, MIR probe setup. In this approach we want to further investigate the electron dynamics of QDs. The ensemble studies [2] will first be intensified on samples with reduced dot densities and finally in a second step single dot dynamics should be monitored by its NIR emission. Thus we can directly study the dynamical behavior of single quantum dots.

References

- [1] F.F. Schrey, T. Müller, G. Strasser, and K. Unterrainer, *phys. Stat. Sol. (c)* 1, 343 (2004)
- [2] T. Müller, F.F. Schrey, G. Strasser, and K. Unterrainer, *Appl. Phys. Lett.* 83, 3572 (2003)

Photocurrent and Photoluminescence Measurements of InAs Quantum Dots

G. Fasching, F.F. Schrey, G. Strasser and K. Unterrainer
Institute of Solid State Electronics, TU Vienna, Austria

Quantum dots are often called artificial atoms due to their nanoscale pyramid or lens shaped structure, which cause a strong three dimensional electron confinement like in atoms. Each quantum dot consists of 10^3 to 10^5 lower band gap material atoms, which are embedded into a matrix of higher band gap material. The δ -function-like density of states and the typical intraband level spacings of 30 to 90 meV turn QDs to promising objects for both applied and fundamental research on zero-dimensional systems.

In this contribution, we report on PL and PC measurements of InAs quantum dots embedded in a quantum dot photodiode. QDs provided with both electric contacts and optical access allows us to vary independently the electric field while measuring the optical or electrical response of the dots. The dot layer is embedded in an intrinsic GaAs region with an ohmic contact on bottom and a Schottky contact on top of the structure (Fig. 1 (a)). In the center of the top contact a $2\ \mu\text{m}$ aperture covered with a 6 nm thick Ti layer serves as an semitransparent shadow mask (optical transmission approximately 60 %) to achieve a homogeneous electric field in the region of the investigated QDs. The band structure under negative bias condition is shown schematically in Fig. 1 (b). Changing the bias from positive to negative voltage reduces the tunneling barrier thickness in z-direction and therefore the tunneling time τ_t of the photoexcited carriers out of dot. When τ_t becomes equal or even smaller than the radiative lifetime of the exciton τ_r ($\approx 1\ \text{ns}$) one changes from the PL regime to the PC measurement regime.

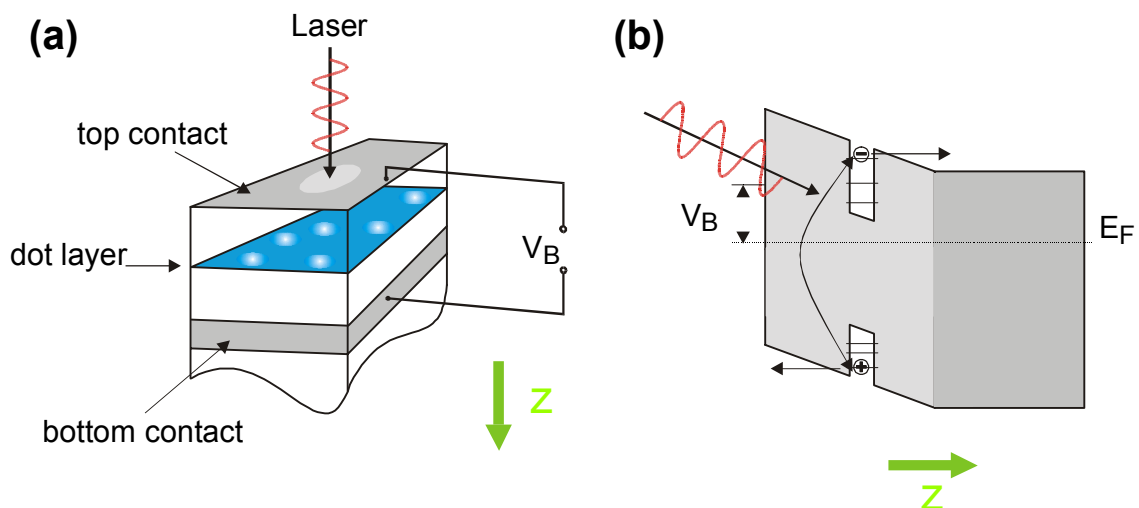


Fig. 1: (a) Sketch of the QD-photodiode. The dots are embedded in an n-i-Schottky diode with a shadow mask on top.
(b) Schematic band diagram under a negative bias V_B .

The experimental setup used in the PL experiments consists of a cw Ti:Sapphire laser (emission at 760 nm), a confocal laser microscope, a low drift LHe flow cryostat, a 850 nm long pass filter, a 0.5 m spectrometer with a nitrogen cooled InGaAs detector, and a remote lock-in amplifier for data acquisition. For the PC measurements we use a tunable cw Ti:Sapphire laser to resonantly excite the QD energy levels, and a self-built current preamplifier with a sensitivity of 10^{-8} V/A for the detection of the PC signal.

Figure 2 shows a typical PL and PC spectrum of the QD's at 4 K. The PL lines in Fig. 2 (a) observed at 1.42 eV and 1.52 eV come from the GaAs matrix and from the InAs wetting layer, respectively. The spectrum shows clearly four, approximately 50 meV separated, luminescence peaks between 1.22 and 1.37 eV, which indicate the ground-state and the excited-state transitions of the InAs QD's. Since the density of the QD's in the sample used is very high ($\geq 10^{11}$ cm $^{-2}$), the PL of the QD's under weak excitation is much stronger than that from the wetting layer. Increasing the excitation intensity fills up the states in the QD's and therefore leads to radiative relaxation from higher energy levels like the InAs wetting layer or the GaAs matrix (see Fig. 2 (a)). The PC spectrum in Fig. 2 (b) show less spectral features than the PL spectrum in Fig. 2 (a). The increasing PC signal beyond 1.4 eV indicates the absorption of the InAs wetting layer and the absorption tail of the GaAs bulk material as well, and is therefore in good agreement with the PL measurements. The measured PC signal of the dots between 1.4 and 1.1 eV is not only a convolution of the tunneling currents of different states of different dots, but also convoluted with the tunneling probabilities of the carriers in the QD's. This means that the position and the amplitudes of the maxima of the PC signal are not only a function of the excitation power (like in the PL experiments), but also a function of the tunneling probability of the photoexcited carriers and therefore of the applied electric field.

In conclusion, we built a device which enables us the optical and electrical access to InAs QD's embedded in a GaAs matrix and measured successfully the PL and the PC spectra of these dots.

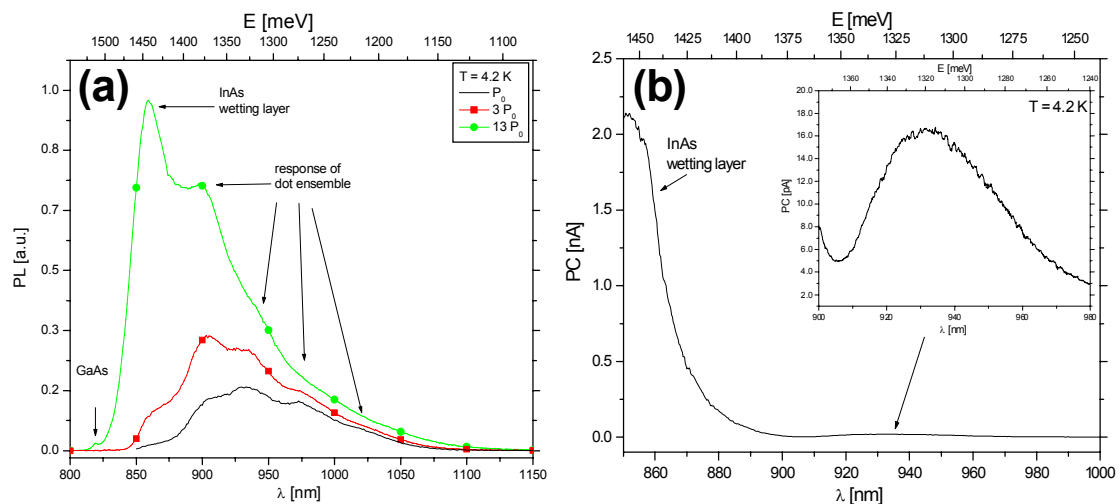


Fig. 2: (a) Broad PL response of the dot ensemble around 930 nm for lower excitation. The maximum shifts with increasing power to higher exciton levels (InAs wetting layer and GaAs). (b) Position of the maximum of the PC signal is equal to the PL signal under low excitation values.

Fabrication and Characterization of Lateral Quantum Dots in GaAs Heterostructures

G. Pillwein¹, G. Brunthaler¹ and G. Strasser²

¹ Institute for Semiconductor Physics, Univ. Linz, Austria

² Institute of Solid State Electronics, TU Vienna, Austria

We have improved the design of our lateral quantum dots, which are fabricated from a two-dimensional GaAs/AlGaAs heterostructure by electron beam lithography. Our split gate geometry, which defines the dot electrostatically by metal gates, has been modified. The devices were characterized electrically in a ³He cryostat at 300 mK. Due to improvements in device design and measurement conditions we can now control the number of electrons in the dot over a wider range. Additionally we have observed reproducible conductance fluctuations overlaid on the Coulomb oscillations.

Introduction

In several recent proposals [1], [2] lateral quantum dots were discussed as a promising option to realize the quantum entanglement necessary for doing quantum computation. We have fabricated quantum point contacts and single lateral quantum dots in the two dimensional electron gas (2DEG) of a GaAs/AlGaAs heterostructure, which are basic elements for more sophisticated devices. Already one year ago we have presented first working devices of this type, but the fabrication process was not very reliable then and measurement results were not reproducible from one device to the next. In the meantime we have improved both the fabrication process and the electrical measurements. In our present devices we have thus greater control over the number of electrons in the quantum dot. Now we can think of combining two or more lateral dots, which will allow us to investigate effects, in coupled dot systems.

Experimental

Our samples are based on a MBE grown GaAs/Al_{0.3}Ga_{0.7}As heterostructure with a 2DEG situated approximately 100 nm below the sample surface. They have a carrier concentration of about $2 \times 10^{11} \text{ cm}^{-2}$ and a mobility of up to $1.4 \times 10^6 \text{ cm}^2/\text{Vs}$. Ohmic contacts were made from an Au/Ni/Ge alloy and Hall bar mesas were wet-etched with H₂SO₄:H₂O₂:H₂O (1:6:150). The quantum dot structure was defined by e-beam lithography and subsequent deposition of Cr/Au metal electrodes (i.e. the split gates) on top of the hall bar mesa. Figure 1 shows all important parts of the sample in different magnifications. By applying a negative voltage to the split gates the underlying 2DEG can be completely depleted. Our new dot design consists of four gate fingers, which define a quantum dot. The two outer gates in connection with the bottom gate define the tunnel barriers, which separate the quantum dot area from the surrounding 2DEG. The top center gate (the plunger gate) can be used to change the electrostatic potential of the dot. In comparison to our previous design the tunnel junctions are further away from the plunger gate, and are thus not so easily influenced by the plunger gate voltage, which has been one of the major problems with the former design. A SEM image of the new split gate geometry is shown in Fig. 1 (b), the old geometry is shown for comparison in the inset. The quantum dot area defined by the metal gates is approximately circle shaped with a diameter of roughly 400 nm in the investigated sample.

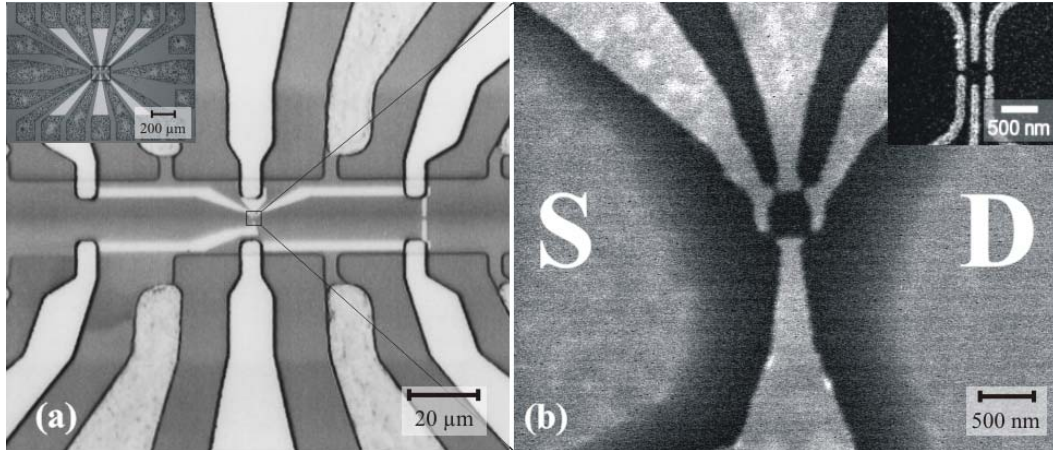


Fig. 1: (a) shows an SEM image of a part of the hall bar containing the split-gate structure. The inset shows the entire structure including the ohmic contacts. (b) SEM image showing enlarged view of the center region marked in Fig. 1 (a). The inset shows the old gate geometry for comparison.

Electrical measurements were carried out in a ^3He cryostat at a temperature of 300 mK using a low frequency lock-in technique ($f = 10$ Hz). To avoid heating of the electrons it is important to keep the excitation voltage lower than the thermal energy, which corresponds to $25 \mu\text{V}$ at 300 mK, thus excitation voltages of $10 \mu\text{V}$ or below have been used. In order to define the quantum dot in the 2DEG, negative voltages have to be applied to the split-gates. By sweeping the plunger gate voltage the number of electrons in the dot is changed. Such a measurement is shown in Fig. 2 (a), where the conductance through the dot is plotted versus the plunger gate voltage. From the period of the conductance peaks a gate capacitance of $C_G = 8.9 \times 10^{-18}$ F can be calculated. Because the plunger gate voltage also has an influence on the tunnel barriers, the peak conductance decreases towards more negative voltages, until it is finally totally pinched off at about $V_G = -0.2$ V.

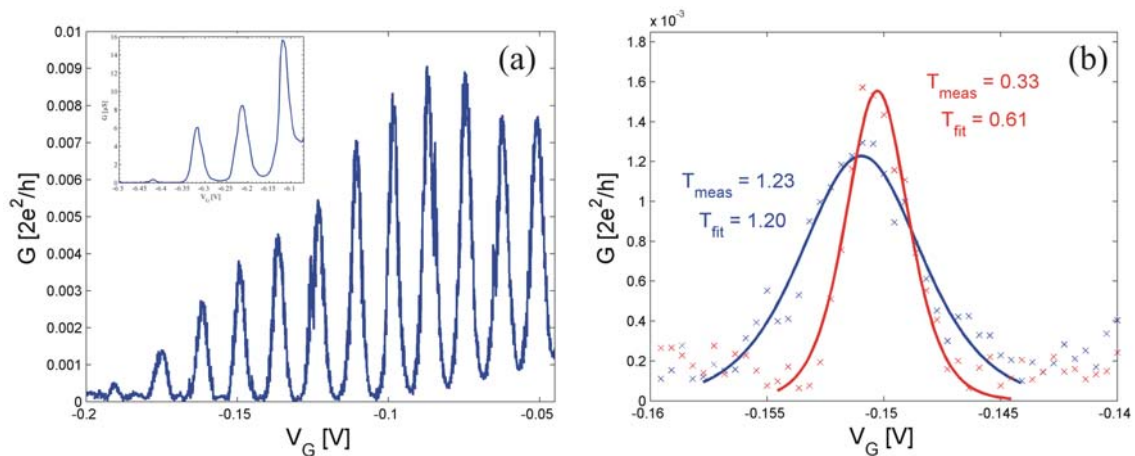


Fig. 2: (a) Coulomb oscillations observed in the conductance G versus plunger gate voltage V_g . The spacing of the peaks gives an estimate of the gate capacitance $C_g = 8.9$ aF. (b) Fit of Coulomb peak lineshape at two different temperatures.

When compared to measurements in our first samples, where only very few for two temperatures are shown in Fig. 2 (b), while at the higher temperature (1.2 K) the fitted temperature is in good agreement with the measured temperature value, at a measured temperature of 0.3 K the fit indicates that the electron gas is heated up to 0.6 K. Therefore we have to further improve our measurement equipment by installation of additional filters, which eliminate any disturbing signals.

Closely looking at the data shown in Fig. 2 (a), one can see that there is a fluctuation superimposed upon the Coulomb oscillations (Fig. 3 (a)). So far we observed these fluctuations in two samples, where the fluctuations have been bigger for the larger dot with a diameter of 900 nm. Figure 3 (b) shows a measurement in the larger dot where the gate voltage was swept up and down (curves are offset for clarity), from which it is obvious that the fluctuation is not some random noise but a reproducible effect. The origin of these fluctuations is not yet clear to us. Oscillations could be seen, the improvement is clearly visible. One of our goals is now to design the gate geometry in a way that transport is possible until only one electron remains in the dot.

The Coulomb peaks have a thermally broadened lineshape and can thus be used to determine the temperature of the electron gas, which may be heated up with respect to the crystal lattice by stray pick-up of RF signals. A fit of the lineshape

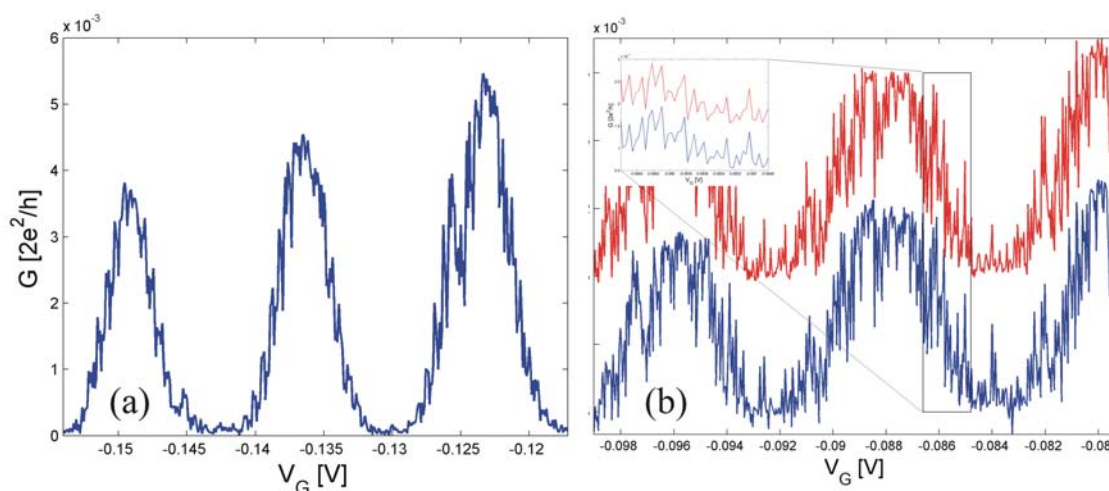


Fig. 3: Conductance fluctuations superimposed on Coulomb oscillations for two dots: (a) 400 nm dot; (b) 900 nm dot: the fluctuations are reproducible on a very small voltage scale.

In addition to changing the plunger gate voltage, we may apply a large DC source drain bias, superimposed by a small AC signal, which is detected by lock-in amplifiers. By doing so we measure the differential conductance dependent on both V_G and V_{SD} . With such a measurement the basic properties of the quantum dot are obtained, including total and source capacitance as well as an estimate of the actual size of the quantum dot. Figure 4 shows a grayscale plot of such a measurement. The horizontal axis corresponds to the plunger gate voltage V_G , the vertical axis to the source-drain voltage V_{SD} . The dark (bright) areas correspond to low (high) G . In the dark parallelogram-shaped regions marked by lines the number of electrons is fixed and no transport is possible due to Coulomb blockade.

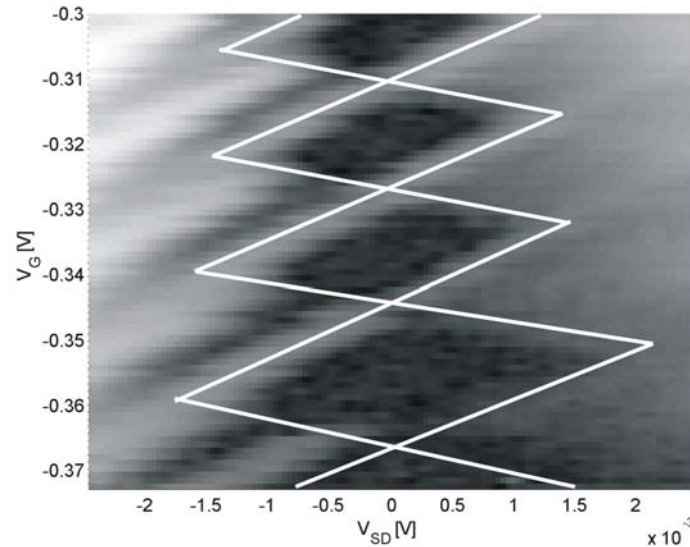


Fig. 4: Differential conductance G versus source-drain voltage V_{SD} and plunger gate voltage V_G . The dark (bright) areas correspond to low (high) G . Coulomb blocked regions are enclosed by the lines.

From the conductance peak spacing ΔV_G at zero source drain voltage the capacitance C_G of the plunger gate can be calculated to be 8.9 aF. From the slopes of the peak lines we obtained the total and the source capacitance to be $C = 103.8$ aF and $C_S = 27.2$ aF. Via the known relation for the charging energy $E_C = e^2/C$ we related the gate voltage scale to an energy scale. From the capacitance of a 2D disk $C = 4\epsilon_0\epsilon_r d$ (for GaAs $\epsilon_r = 12.9$) we estimated the diameter of the electron island to be about 225 nm. Considering that the depletion region will extend around the contours of the split-gates (by a length comparable to the depth of the 2DEG, which is ~ 100 nm), this is in good agreement with the structural diameter of 400 nm.

Conclusion

We have refined the processing our split-gate quantum dot devices and our results confirm that their electrical properties have improved. Further measurements will be performed on these structures to investigate the origin of the observed conductance fluctuations. Because the optimized fabrication process now gives very reproducible results and a good yield, as a next step we will integrate two or more dots into a quantum dot circuit, which may be combined with quantum point contacts for charge readout [3]. A dilution refrigerator, which is currently being installed in our lab, will allow us to reach lower temperature and increase the resolution in upcoming measurements.

References

- [1] D. Loss and D. P. Vincenzo: "Quantum computation with quantum dots", Phys. Rev. A Vol. 57, 1998, pp. 120 – 126.
- [2] L.M.K. Vandersypen et al.: "Quantum computation with electron spins in quantum dots", quant-ph/0207059, 2002.
- [3] J.M: Elzerman et al.: "Few-electron quantum dot circuit with integrated charge read out", Phys. Rev. B Vol. 67, 2003, p. 161308(R).

High-Resolution Hot-Electron Spectroscopy in Parallel Magnetic Fields

M. Kast, C. Pacher, M. Coquelin, W. Boxleitner, G. Strasser and E. Gornik
Institute of Solid State Electronics, TU Vienna, Austria

Hot-carrier spectroscopy is a well established technique to analyze band structure and transport properties of semiconductor bulk and heterostructure material systems. In previous works, this technique was applied to observe ballistic electron and hole transport in bulk GaAs [1], [2], to map miniband positions of finite superlattices [3] and to determine the transition from coherent to incoherent electron transport in GaAs/AlGaAs superlattices [4]. The technique was also used to demonstrate electron transport enhancement through superlattices with antireflection coatings [5]. Recently, the resolution of the spectrometer could be improved considerably to 10 meV [6]. Utilizing this improved design of the hot-electron transistor, the Wannier–Stark splitting and the progressive localization of individual Wannier–Stark states could be observed separately in short superlattices [7].

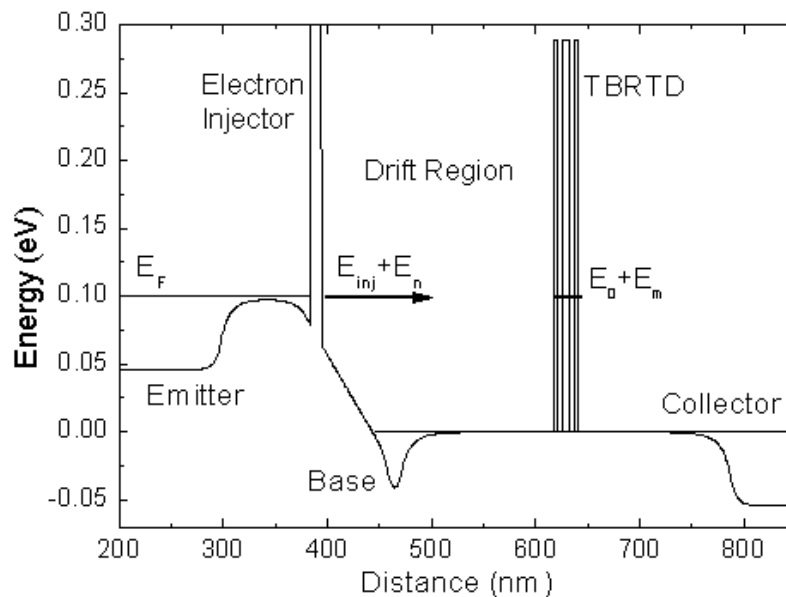


Fig.1: Conduction-band diagram of a three-terminal device along the growth direction incorporating a triple-barrier RTD between the base and collector.

In this work, we focus on the situation where the magnetic field is applied parallel to the current direction which is identical with the growth direction [8]. Figure 1 shows the calculated conduction band structure of the hot-electron transistor presented in Ref. [6]. An energy tunable electron beam is generated by the emitter tunneling barrier (emitter current I_E) and reaches a triple-barrier RTD (TBRTD) with a normal-energy distribution of 17 meV in width after traversing a highly doped n -GaAs base layer and a slightly n -doped GaAs drift region. Electrons which are transmitted through the RTD are measured as collector current I_C . Reflected electrons are collected in the base contact and do not contribute to I_C . Due to the sharp filter characteristic of the TBRTD ($E_0 =$

100 meV, FWHM = 1 meV), the measured transfer ratio $\alpha = I_C/I_E$ is directly proportional to the superposed energy distributions of the ballistic electrons and of the phonon replicas [6].

In the presence of a magnetic field applied parallel to the current direction, all electronic states are quantized in the plane perpendicular to the magnetic field direction into Landau levels of energies $E_n = \hbar\omega_c (n+1/2)$ where n denotes the Landau-level index and $\hbar\omega_c = \hbar eB/m^*$ the Landau splitting. At injection energies where the corresponding Landau levels of the injector and the RTD are aligned ($E_{inj} = E_0$), we get resonant magnetotunneling of ballistic electrons through the GaAs drift region and the RTD. In the absence of elastic or inelastic scattering, inter-Landau-level transitions are forbidden. In the hot-electron transistor, the Landau-level conservation is lifted by inelastic longitudinal optical (LO)-phonon scattering and by elastic scattering processes (charged impurity scattering and electron–electron scattering) in the GaAs drift region. As a consequence the individual peaks in the transfer ratio (ballistic peak and phonon replica peaks) build up satellites shifted by $\Delta n \hbar\omega_c$ according to electrons which changed the Landau-level index by Δn during the scattering process.

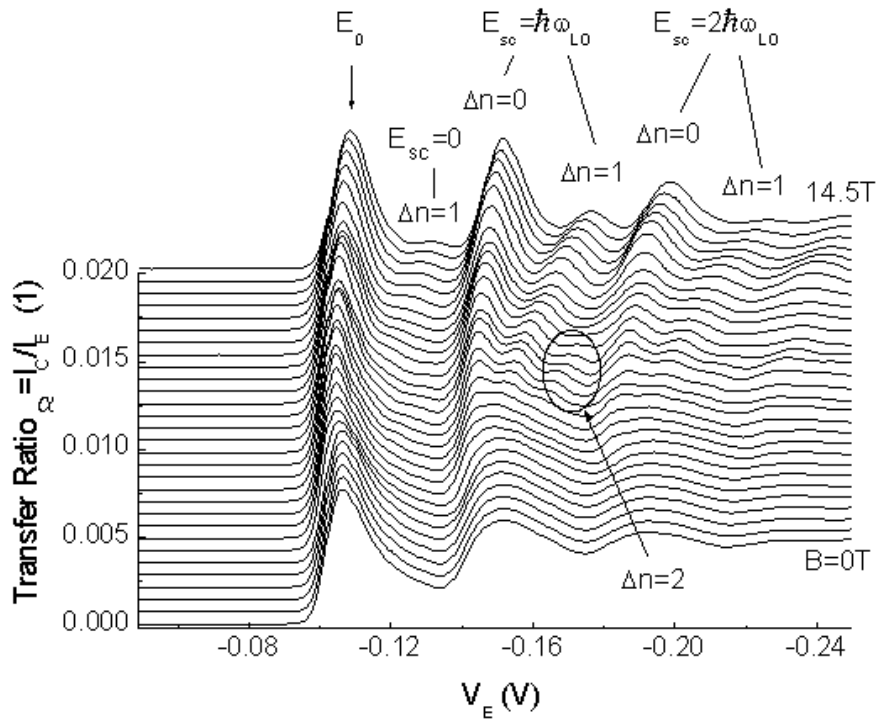


Fig. 2: Transfer ratio vs. emitter bias of the TBRTD at magnetic fields up to 14.5 T in steps of 0.5 T.

Figure 2 shows the measured transfer ratio of the TBRTD as a function of the emitter bias at different magnetic fields up to 14.5 T in steps of 0.5 T. The first peak indicated by ‘ E_0 ’ is attributed to resonant magnetotunneling ($\Delta n = 0$) of hot electrons through the RTD. On the low-energy tail, weak satellites are observed which are equally spaced by $\hbar\omega_c$. Since these peaks are observed well below the energy of the first phonon replica, this is direct evidence of the elastic scattering induced breakdown of the Landau-level conservation. The same splitting is observed in all phonon replicas which is direct evidence of the inelastic scattering induced breakdown of the Landau level conservation by LO phonons.

The peaks which correspond to resonant magnetotunneling $\Delta n = 0$ exhibit nearly no shift with magnetic field due to the collective Landau quantization of all electronic states in the device. The weak dependence of the peak position on magnetic fields is due to (i) magnetic depopulation effects at the emitter side of the injection barrier and (ii) a magnetic field dependent series resistance in the base contact. The peaks which correspond to scattering-assisted inter-Landau level transitions of $\Delta n = 1, 2$ are showing a clear magnetic field dependence. Due to the overlap of the peaks in the transfer ratio, the Landau-level spacing $\hbar\omega_c$ can only be resolved at magnetic fields where the individual peaks are sufficiently separated in energy. From Fig. 2, it follows that the peaks are resolved at magnetic fields higher than 6 T which equals a cyclotron energy of $\hbar\omega_c = 9.4$ meV. This value for the resolution corresponds to the half width at half maximum (HWHM) of $\Delta V_E = 7.8$ mV of the ballistic peak at 6 T.

In conclusion, the performance of a hot-electron transistor in parallel magnetic fields up to 14.5 T has been studied. A triple-barrier RTD with a narrow energy window of 1 meV at $E_0 = 100$ meV was used to scan the energy distributions of the injected electron beam and of the phonon replicas. Scattering-induced inter-Landau level transitions are observed in the ballistic electron peak due to elastic scattering in the highly doped base contact layer as well as in the phonon replicas due to LO-phonon scattering in the drift region of the hot-electron transistor. This way it is possible to study the strength of elastic and inelastic scattering mechanisms simultaneously in a single device.

References

- [1] M. Heiblum, M. I. Nathan, D. C. Thomas, and C. M. Knoedler, *Phys. Rev. Lett.* **55**, 2200 (1985).
- [2] D. Sprinzak, M. Heiblum, Y. Levinson, and H. Shtrikman, *Phys. Rev.* **B55**, 10185 (1997).
- [3] C. Rauch, G. Strasser, K. Unterrainer, B. Brill, and E. Gornik, *Appl. Phys. Lett.* **70**, 649 (1997).
- [4] C. Rauch, G. Strasser, K. Unterrainer, W. Boxleitner, and E. Gornik, *Phys. Rev. Lett.* **81**, 3495 (1998).
- [5] C. Pacher, C. Rauch, G. Strasser, E. Gornik, F. Elsholz, A. Wacker, G. Kießlich, and E. Schöll, *Appl. Phys. Lett.* **79**, 1486 (2001).
- [6] M. Kast, C. Pacher, G. Strasser, and E. Gornik, *Appl. Phys. Lett.* **78**, 3639 (2001).
- [7] M. Kast, C. Pacher, G. Strasser, W. S. M. Werner, and E. Gornik, *Phys. Rev. Lett.* **89**, 136803 (2002).
- [8] M. Kast, W. Boxleitner, C. Pacher, G. Strasser, E. Gornik, *Appl. Phys. Lett.* **82**, 3922 (2003).

BEEM/BEES Investigations on AIAs/GaAs Single Barriers and RTDs

D. Rakoczy, G. Strasser and J. Smoliner
Institute of Solid State Electronics, TU Vienna, Austria

Ballistic Electron Emission Microscopy/Spectroscopy (BEEM/S) [1], a three terminal extension of Scanning Tunneling Microscopy (STM), was used for the local investigation of electrical properties of semiconductor heterostructures. In BEEM/S an STM tip is used to inject hot (ballistic) electrons into a semiconductor via a thin metallic base layer. The resulting ballistic current can be measured on the backside of the sample via a collector contact. Therefore, BEEM/S is, in contrast to STM, able to probe also sub-surface structures with a local resolution of several nanometers.

In this work we present results of BEEM/S on MBE grown AIAs-GaAs double barrier resonant tunneling diodes (DBRTDs) and AIAs single barriers on a GaAs substrate. As a base layer we used in all cases a 7 nm thick, polycrystalline Au layer. The measurements presented here were all carried out at cryogenic temperatures (either 4.2 K or 10 K).

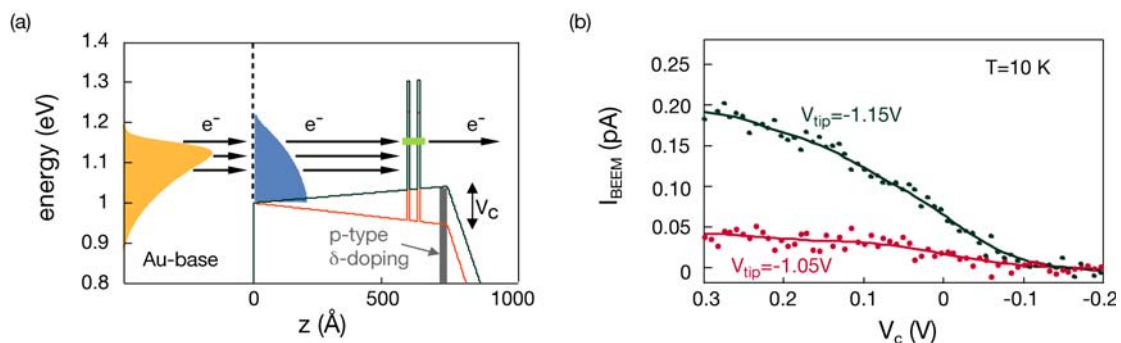


Fig. 1: (a) Band profile of the sample used for the electron refraction measurement, sketched for the unbiased sample and for a positive collector voltage, which lowers the band profile. Also indicated are the electron energy distribution in the Au base layer and the one in the GaAs, showing the massive broadening caused by the refraction. (b) Measured electron energy distribution in the GaAs for two different tunnel voltages.

An important effect influencing the ballistic current on e.g. Au-GaAs samples is the “refraction”, which the ballistic electrons experience at the Au-GaAs interface. For electrons crossing this interface ballistically, the momentum parallel to the interface is conserved. Thus, a change in effective mass and/or potential leads to “electron refraction effects”, which have a significant influence on the BEE spectra. For example, the expected step-like spectrum of a single resonant level in a heterostructure is turned into a linear rise, which is well-known from the BEE spectra of various DBRTDs. Although the effect on the BEE spectra has been demonstrated repeatedly, up to now a direct measurement of the ballistic electron distribution beyond the Au-GaAs interface was, due to various technical problems, missing. To achieve this measurement, we de-

signed a heterostructure with a buried AIAs-GaAs-AIAs-DBRTD and a p- δ -doping (see Fig. 1 (a)). This sample design enabled us to apply a bias voltage between the Au-base and the collector. With a slightly modified BEEM setup we were then able to map directly the energetic distribution of the ballistic electrons in the GaAs by measuring the ballistic current as a function of the sample bias V_c (see Fig.1 (b)), i.e. using the RTD as a tunable energy filter for the ballistic electrons. This measurement confirmed that, in agreement with theory, the refraction leads to a considerable broadening in the energetic distribution of the injected electrons [2].

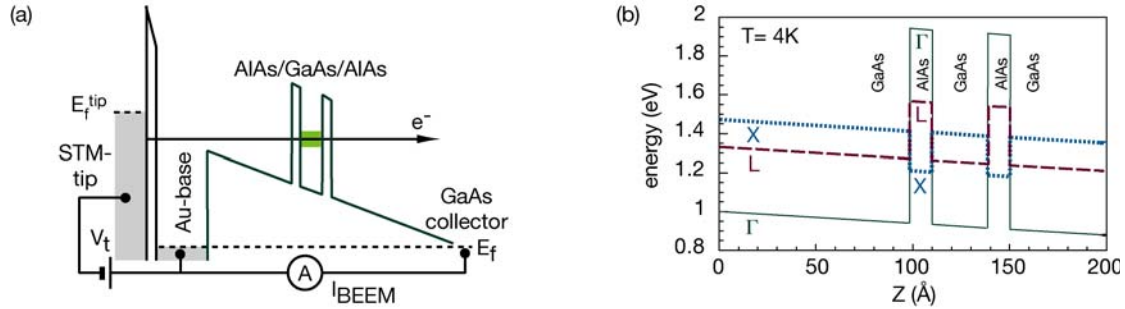


Fig. 2: (a) Sketch of the setup together with the Γ -band profile of a 30Å wide RTD sample, also indicating the position of the resonant level. (b) Close-up view on the RTD, showing besides the Γ - also the X- and the L-valley band profile.

In order to investigate higher conduction bands, we demonstrated ballistic transport through confined states in the L-valley of an AIAs-GaAs-AIAs DBRTD [3]. In contrast to so-called “3-terminal-devices”, a solid state device designed for ballistic transport, BEEM/S is capable of injecting electrons into the L-valley coherently because of the broad momentum distribution in the metallic base layer. The ballistic spectra of the DBRTDs studied (see Fig. 2) show a first onset followed by a pronounced linear regime caused by the first resonant level in the Γ -valley of the DBRTD. Tunneling processes through the L-valley confined states of the DBRTD are observed as additional current onsets (well above the onset caused by the resonant level in the Γ -valley) followed by a very short linear regime (see Fig. 3). These features can be seen more clearly in the first derivative of the ballistic current. Using DBRTDs of different well width (20 Å, 30 Å, 40 Å), we confirmed that the additional onset is dependent on the well width and therefore due to a resonant level in the RTD rather than to a simple barrier overshoot in a higher valley. Measurements on a reference sample with a single AIAs barrier (100 Å thick) show that at cryogenic temperatures the Γ -X-transfer can also be neglected. Finally, the design of our DBRTD rules out any influence of a higher resonant level in the Γ -valley, because the second resonant level in Γ is well above the onset position observed. Therefore, we conclude that we truly observed tunneling through a resonant level in the L-valley. This is further confirmed by the results of a semiempirical tight binding calculation which reproduces the experimental data very well. This calculation can furthermore be used to derive the corresponding ballistic transport mass. As a result, we found that this ballistic transport mass differs significantly from the GaAs and AIAs longitudinal and transversal masses, which is due to the mass anisotropy in the L-valley. Using the ballistic transport mass derived by the tight-binding model as an input parameter, the experimental data can also be reproduced very well with a simple effective mass model.

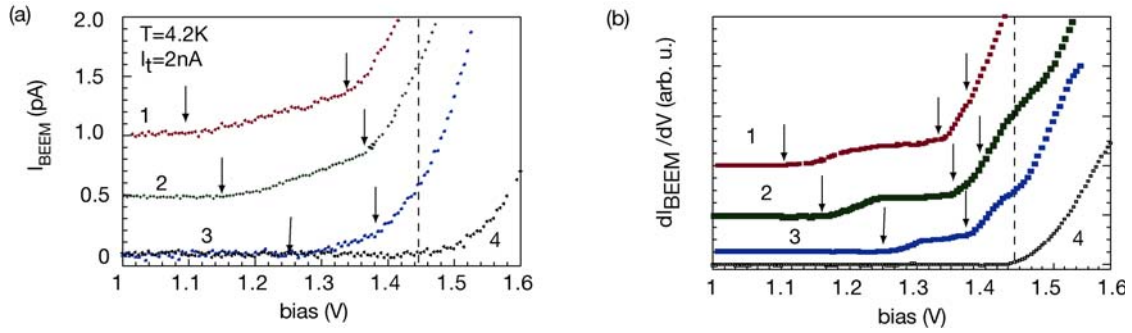


Fig. 3: (a) Measured BEEM spectra. Curves 1–3: RTDs with 40 Å, 30 Å, and 20 Å well width respectively. Curve 4: 100 Å thick AIAs single barrier. The arrows indicate the positions of the resonant levels; the dashed line marks the X-valley at the Au-GaAs interface. (b) First derivative of the spectra shown in (a).

On single AIAs barriers we investigate the local influence of doping on the band structure [4]. For this purpose several, otherwise identical, samples were grown, each having a 100Å thick, single AIAs barrier with a specific donor concentration in the barrier. Up to now we have investigated barriers with doping concentrations of $1e17 \text{ cm}^{-3}$, $3e16 \text{ cm}^{-3}$, and an undoped reference sample. We observe that the onset voltage in the ballistic spectra shifts for higher doping concentrations to lower values. By taking BEEM images of the different samples, an even more direct approach to show the influence of the doping atoms on the band structure was also pursued. Images depict a quite uniform “potential landscape” for the undoped as well as for the highly doped sample. On the other hand, the samples with a doping of $3e16 \text{ cm}^{-3}$ reveal a higher inhomogeneity in the BEEM images, which may be a signature of single impurities (Fig. 4).

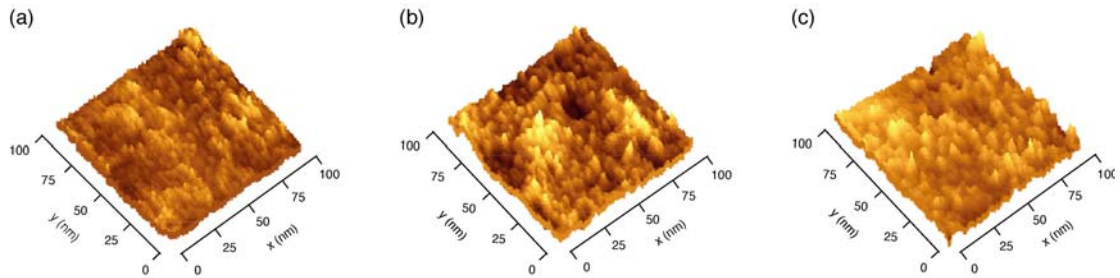


Fig. 4: BEEM images for AIAs single barriers with different doping concentrations. (a) undoped barrier, (b) $N_D = 3e16 \text{ cm}^{-3}$, (c) $N_D = 1e17 \text{ cm}^{-3}$.

References:

- [1] W.J. Kaiser and L.D. Bell, Phys. Rev. Lett. **60**, 1406 (1988)
- [2] D. Rakoczy, G. Strasser, and J. Smoliner, Appl. Phys. Lett. **81**, 4964 (2002)
- [3] D. Rakoczy, G. Strasser, and J. Smoliner, Phys. Rev. B **66**, 33309 (2002)
- [4] D. Rakoczy, G. Strasser, and J. Smoliner, Phys. Rev. B **68**, 73304 (2003)

Magnetic Tunnel Transistors Studied by Ballistic Electron Emission Microscopy

R. Heer and J. Smoliner
Institute of Solid State Electronics, TU Vienna, Austria

J. Bornemeier and H. Brückl
Universität Bielefeld, Dept. of Thin Films and Nanostructures

In this work, spin valve structures as they are employed in the base layers of magnetic tunnel transistor devices are locally characterized by BEEM. For the experiments, n-type ($N_D=10 \times 10^{17} \text{cm}^{-3}$) GaAs [100] bulk wafers were used. As base layer, the following sequence of polycrystalline metal layers was sputtered onto the substrate: Co 4.5 nm, Cu 4.2 nm, Py 3.5 nm. The layers were deposited in the presence of a magnetic bias field along the [100] direction of the GaAs which causes a uniaxial anisotropy in both layers. For STM operation, an additional layer of Au (4.0 nm) was sputtered on top.

Figure 1 (a) shows two typical BEEM spectra, which are the measured collector current as a function of STM bias. At zero magnetic field after saturation of the magnetization, the current onset is observed at $V_t = 1.0 \text{V}$ which is determined by the Schottky barrier height at the Co-GaAs interface. Above that bias, the collector current increases in a roughly quadratic dependence on the bias, as it is typical for BEEM signals on bulk GaAs samples. If the magnetization of the spin-valve is oriented in antiparallel directions at an applied magnetic field of $H = 26 \text{ Oe}$, however, the ballistic collector current is considerably quenched. Here, the collector current is below the detection limit for voltages smaller than $V_t = 1.2 \text{ V}$ and then increases just slowly. In addition, the spectral behavior does not appear typically quadratic and even shows some hints of saturation. This behavior is currently not fully understood and will be subject of further investigations. As a consequence of the significantly quenched BEEM current in the antiparallel state, the “magnetocurrent” MC, usually defined as the ratio of the ballistic current in the parallel ($I_{C,P}$) and antiparallel ($I_{C,AP}$) magnetization configuration minus one ($MC = I_{C,P} / I_{C,AP} - 1$), is surprisingly high. At $V_t = 1.5 \text{ V}$, $I_{C,P} = 0.7 \text{ pA}$ and the value of $I_{C,AP}$ is just 0.1 pA yielding a MC value of 600% at room temperature.

Figure 1 (b) shows the ballistic current as a function of magnetic field along the easy magnetization axis at a fixed value of V_t . The curves were measured at $V_t = 1.5 \text{ V}$ and $I_t = 20 \text{ nA}$. At $H = -67 \text{ Oe}$, the magnetic layers are in parallel configuration and in saturation magnetization. Running from $H = -67 \text{ Oe}$ to $H = +67 \text{ Oe}$, the magnetic layers flip into the antiparallel configuration at $H = +19 \text{ Oe}$ and the BEEM current is quenched. At $H = +43 \text{ Oe}$ the hard magnetic layer changes its orientation too, and the spin filtering effect is switched off again. This behavior is symmetric on the H-field axis. The states are well separated indicating a negligible magnetic interaction between the layers. The sharp switching between the two states can be understood by the local character of the BEEM method. It is caused by a sudden transition of a single domain wall underneath the tip. Within the scanning range of our STM, however, the switching position was always exactly at the same field value within the experimental error and in the absence of pinning centers.

On large area scans ($4 \mu\text{m} \times 4 \mu\text{m}$), magnetic domains are observed in the BEEM images. Figure 2 shows such magnetic domains, which only occur in the vicinity of the switching field of the spin valve. Note, the sample was not exposed to the maximum magnetic field level of $H = 73 \text{ Oe}$ during the imaging. The values were varied between

$H = 0$ Oe (parallel spin configuration) and $H = 30$ Oe (antiparallel spin configuration). The magnetic field level to reach the parallel spin configuration coming from the antiparallel state was $H = 12$ Oe. In image (a), at zero magnetic field, the transmission is high and almost constant in the scanning area. An imperfection in the film is weakly visible on the upper right hand side of this image. Note that this imperfection is just visible in the BEEM image, not in the topographic image, which is not shown here. Image (b) was taken at the switching field of the spin valve from the antiparallel state to the parallel state at $H = 12$ Oe. On the left hand side, the transmission is high, whereas on the right hand side, a domain with low transmission is formed. The imperfection is now clearly visible as a wormshaped and bright feature. The domain is obviously pinned at this defect. Image (c) shows the transmitted current in antiparallel configuration of the spin valve at $H = 30$ Oe. Here the transmission is low everywhere except in the region of the film imperfection. Switching back to the magnetic field of image (b) $H = 12$ Oe, the domain appears again as shown in image (d). However, it has changed its shape. In addition, the overall transmission appears to be somewhat reduced.

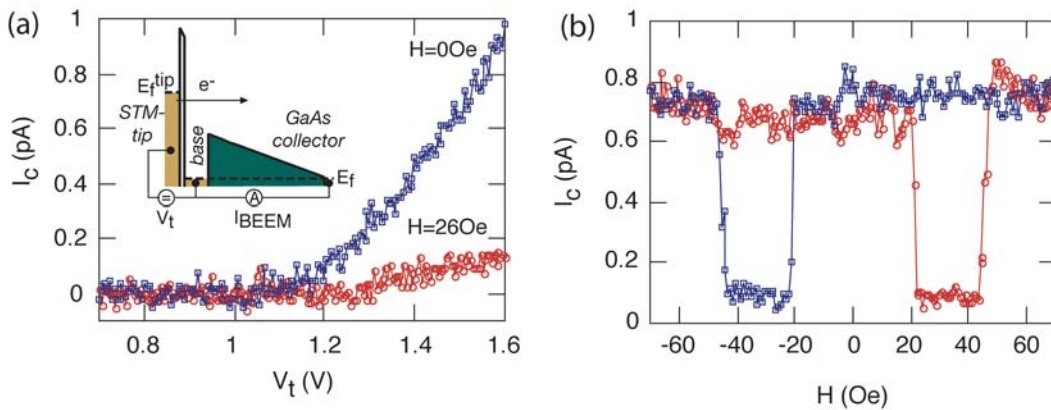


Fig 1: (a) Typical BEEM spectra recorded at $H = 0$ Oe and $H = 26$ Oe. The tunneling current I_t was 20 nA and the temperature 300 K. A schematic setup of the experiment is shown in the inset. (b) Collector current measured as a function of the magnetic field. ($V_t = 1.5$ V, $I_t = 20$ nA, $T = 300$ K)

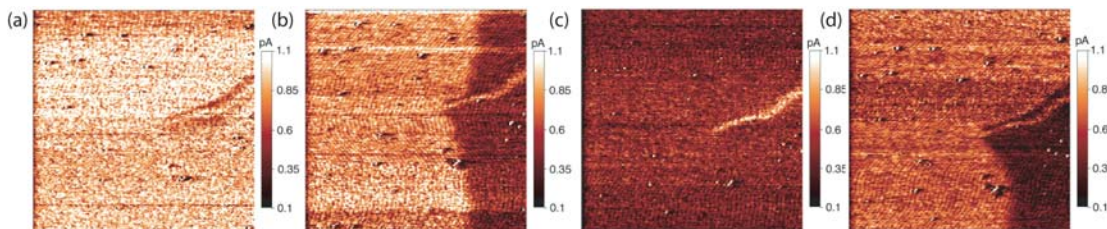


Fig. 2: Large area BEEM images showing magnetic domains in the vicinity of the switching field of the spin valve. Images (a) – (d) were recorded sequentially on the same position at different magnetic field levels of a minor loop. A film imperfection is visible on the upper right hand side of all images. The scan size is $4 \mu\text{m} \times 4 \mu\text{m}$ and the images were recorded $V_t = 1.8$ V, $I_t = 20$ nA and $T = 300$ K)

Thermal Mapping of the SMARTIS SOI Devices under the vf-TLP and TLP Stress Conditions

S. Bychikhin, D. Pogany and E. Gornik
Institute of Solid State Electronics, TU Vienna, Austria

M. Graf, F. Dietz and V. Dudek
Atmel, Theresienstraße 2, D-74025 Heilbronn

W. Soppa
FH Osnabrück, FB Elektrotechnik, Albrechtstraße 30, D-49076 Osnabrück

H. Wolf
Fraunhofer-Institut für Zuverlässigkeit und Mikrointegration (IZM-M/ATIS Analysis and Test of Integrated Systems), Hansastr. 27d, D-80686 Munich

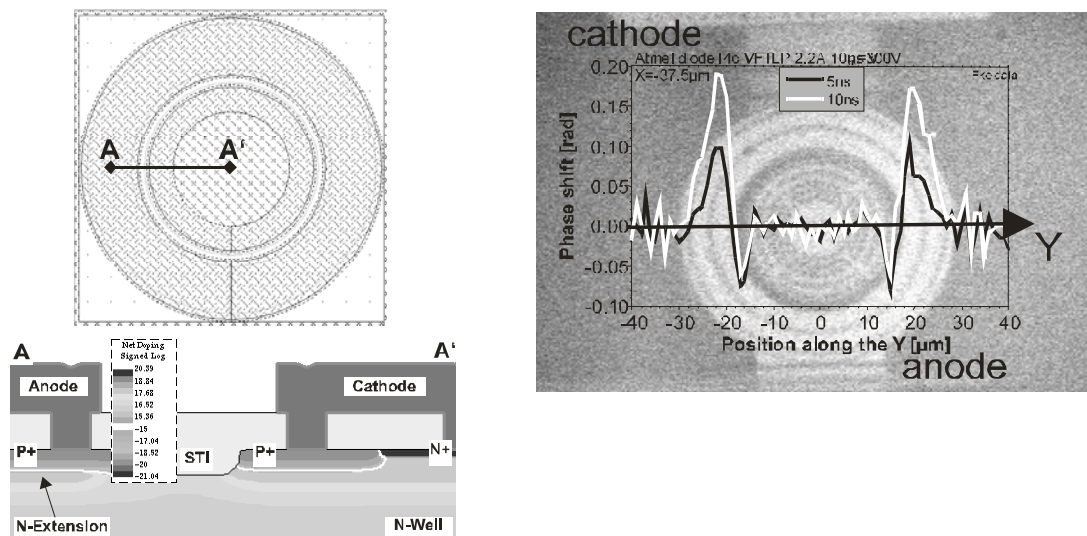
The importance of the microelectronics products in daily needs is steadily growing. The questions of the reliability and ESD robustness of microelectronic chips and circuits gain higher level of significance from year to year. Modern ASICs monitor and control security relevant operations in automotive applications. Electronics become responsible for the health of the passengers in case of an unforeseen event like an accident. Safety critical applications set a new demand for improvement of the ESD hardness of the protection devices. An obvious increase in the integration density and at the same time an improvement of ESD robustness is possible to obtain by using a new kind of technology based on SMARTIS SOI. The approved concepts of the BCD bulk technology cannot be transferred to the SMARTIS SOI due to technological peculiarities (absence of the buried conductive layer). Therefore the development of the effective ESD protection concept for the SOI devices has to start from the beginning.

The prototypes of bipolar protection elements (see Fig. 1 (a)) of SMARTIS SOI technology were investigated under the TLP (100ns) and CDM-like vf-TLP (10ns) stresses. The devices were processed on different kinds of SOI wafers with high variations of the active layer thickness. Pulsed IV characteristics of the devices exhibited variations in the maximum ESD current. These variations could be caused by the inhomogeneous triggering of the devices or by the influence of the active layer thickness on the failure currents.

Using backside thermal interferometric mapping the power dissipation inside of the devices was monitored during the TLP and vf-TLP stresses. Scans along two perpendicular axes (data along Y axis is shown in Fig. 1 (b), the results along the X-axis are similar to the Y-scan) show homogeneous power dissipation in the device. This result helps to understand that the variations in the maximum ESD current of devices are influenced by the active layer thickness only.

With help of the electro-thermal model of the device the influence of the active layer thickness variations on the failure current was simulated. The optical mapping and the simulated temperature profile are in a good qualitative agreement (see Fig. 2). This indicates the correctness of the electro-thermal model of the device that was chosen for simulations.

The results of the investigations could be used in the development of suitable ESD protection for smart power SOI technologies.



a)

b)

Fig. 1: Results of the transient interferometric mapping on SMARTIS SOI bipolar device under the vf-TLP stress 2.2 A 10 ns. The device layout is shown in (a). The thermally induced phase distribution along Y-axis (b) is shown for 5 ns and 10 ns time instants. The background image in (b) is the backside infrared picture of the device; after [1].

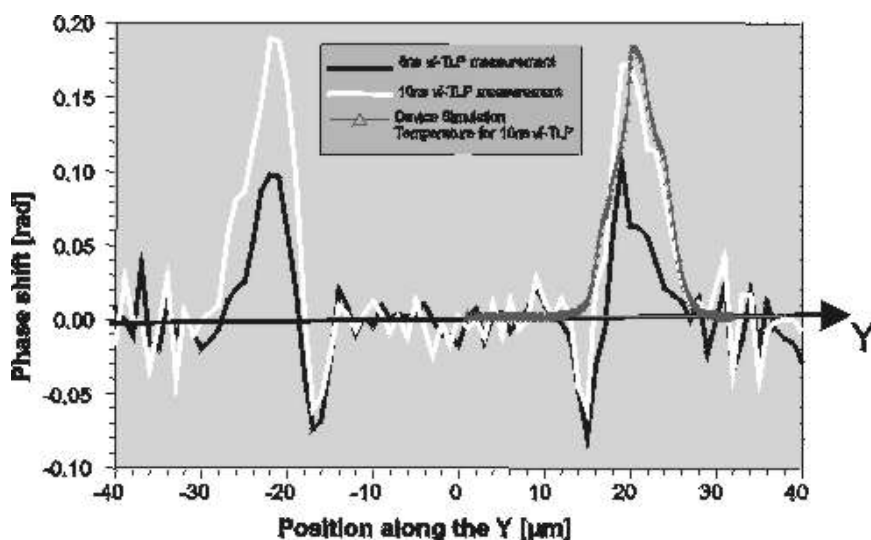


Fig. 2: Comparison between optical mapping (white/black) and simulation (gray line with triangle marks at right half of the Y-axis); after [1].

Reference

- [1] M. Graf, S. Bychikhin, F. Dietz, V. Dudek, D. Pogany, E. Gornik, W. Soppa, H. Wolf 'Impact of Layer Thickness Variations of SOI-Wafer on ESD-Robustness' Proc. EOS/ESD'2003 Symposium, p.116, 2003.

A Dual-Beam Interferometer for Investigation of ESD Protection Devices under vf-TLP Stress

V. Dubec, S. Bychikhin, M. Blaho, D. Pogany and E. Gornik
Institute of Solid State Electronics, TU Vienna, Austria

J. Willemen, N. Qu and W. Wilkening
Robert Bosch GmbH, Germany

L. Zullino and A. Andreini
ST Microelectronics, Italy

Protection against charged device model (CDM) becomes more and more demanded by automotive industry. Understanding device internal behavior and the device interaction within a circuit or a package at short time scale is important for optimization of protection devices against CDM. Recently, backside transient interferometric mapping (TIM) technique in combination with very fast transmission line pulses (vf-TLP) has been used for investigation of trigger delays in ESD protection devices. However, as some devices exhibit pulse to pulse instabilities in triggering behavior, a dual-beam MI has been introduced for the simultaneous measurements of absolute phase shift at two different positions with 0.4 ns time resolution [1].

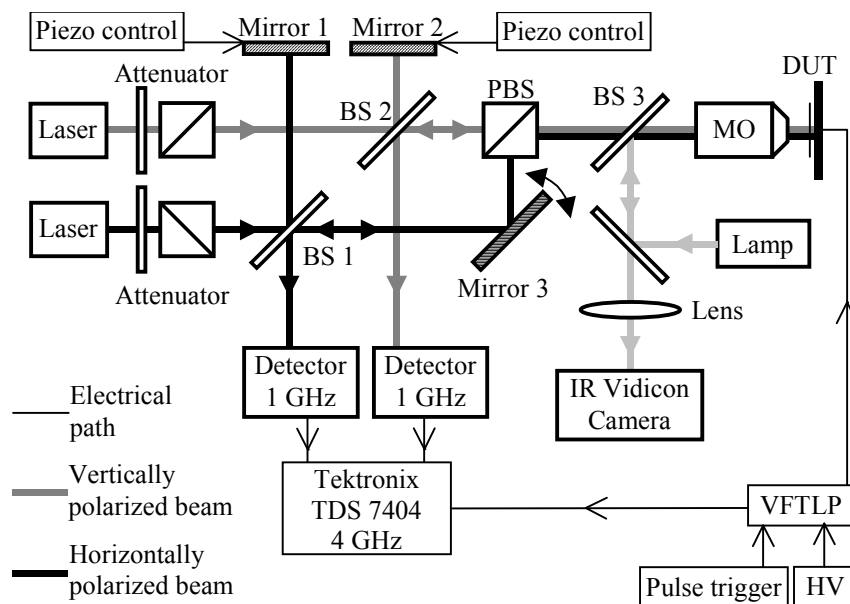


Fig. 1: Simplified schematic of the dual-beam Michelson interferometer setup: BS – beamsplitter, PBS – polarization beamsplitter, MO – microscope objective, DUT – device under the stress; after [1].

The dual beam MI consists of two interferometers combined in one setup, see Fig. 1. Two diode laser sources ($\lambda = 1.3 \mu\text{m}$) are used. In order to reduce optical losses the two beams have orthogonal polarization and are combined using polarization beam

splitters. Each reference branch is piezo controlled for maximal sensitivity adjustment. Both beams are focused by the microscope objective on the device under stress (DUT) mounted on xyz and rotational stages. One of the beams has a fixed position, while the position of a second beam can be adjusted by a mirror (the maximal beam separation is 0 – 500 μm , the beam spot size is 2 μm). The position of the beam spots can be visualized using an infrared (IR) vidicon camera. The interference signals related to two interferometers are detected by two InGaAs detectors with 400 ps rise time and sampled with an oscilloscope together with the voltage waveform of the vf-TLP signal. The current waveform was properly aligned relative to the phase waveforms taking into account all the signal delay lines. The signal is usually averaged 20 – 40 times to improve the signal to noise ratio. For transient phase signals with amplitude higher than 0.1 rad, the transient behavior can also be studied using a single stress pulse. All setup opto-electronic components are shielded to avoid the induction of electromagnetic pick-ups in the interference signal.

As an example, two BCD technology device types were investigated. First structure is an npn transistor with a lateral and buried collector and short-circuited base/emitter, the second structure is an inverted vertical npn transistor with short circuited base and collector. The devices are stressed by a home-built vf-TLP pulser.

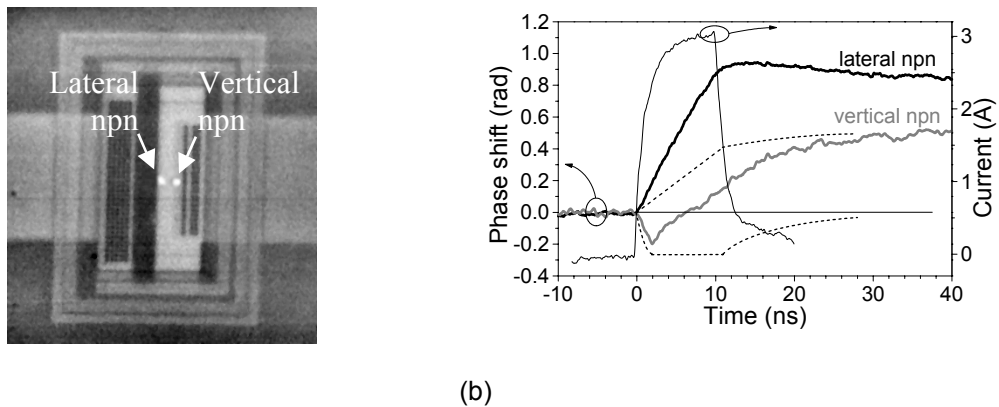
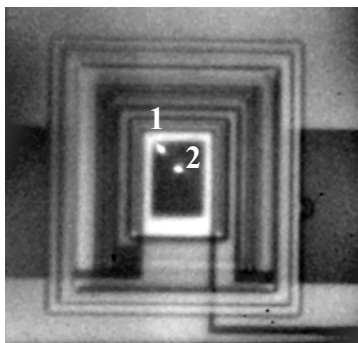


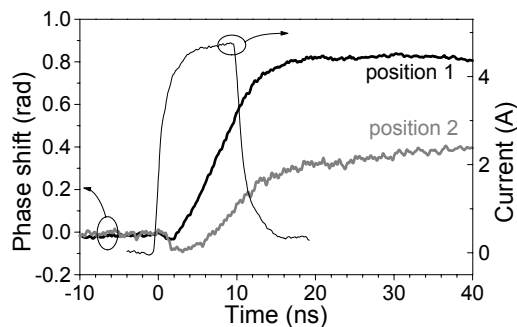
Fig. 2: (a) Backside IR image of the first npn structure with marked laser beam positions;
(b) phase shift development in marked positions; after [1]

Two hot spots have been observed using the scanning TIM method in the first npn ESD structure: a dominant thermal peak at the position of collector edge due to the heating in the lateral npn transistor and a negative peak due to carrier injection under the n-emitter region. The trigger delay between the lateral and vertical transistor was investigated by the dual beam MI. In the lateral npn transistor (see Fig. 2 (a)), immediately with the begin of the pulse the phase shift nearly linearly increases due to the self-heating effect in the impact ionization region of the base-collector junction, see Fig. 2 (b). After the end of the pulse the heat spreads to the surrounding. At the position of vertical transistor (see Fig. 2 (a)) a rapid decrease occurs after the beginning of the pulse followed by a phase increase. The start of both signals from the lateral and vertical npn is well aligned, indicating a trigger delay within 0.4 ns. The signal at vertical npn is caused by a superposition of a free carrier negative signal, acting in a short time scale, and a thermal signal, which is much slower. These two components are separated and also plotted in Fig. 2 (b) (see the dotted lines). The steady state of free carrier signal is obtained after some 2 ns. After the pulse end, a slower tail is observed, as the high concentration of excess carriers has to decay. The thermal component of the signal exhibits a rise after the pulse end, which is due to heat transfer from the surrounding region.

In second npn structure, the scanning TIM revealed hot spots at the device corners. To investigate if these hot spots indicate an earlier triggering at the corners than in the middle of the emitter, the two beams of the dual beam MI were placed at the corner and in the middle positions; see Fig. 3 (a). At these positions a maximum trigger delay may be expected. At both positions the free carrier negative signal dominates at the pulse beginning; see Fig. 3 (b). At later times the heating dominates as the temperature and thermal energy increase with time. No phase delay has been found between the measuring positions within the measurement precision (0.4 ns).



(a)



(b)

Fig. 3: (a) Backside IR image of the second npn structure with marked laser beam positions;
(b) phase shift development in marked positions; after [1].

References

- [1] V. Dubec, S. Bychikhin, M. Blaho, D. Pogany, E. Gornik, J. Willemen, N. Qu, W. Wilkening, L. Zullino, A. Andreini, "A dual-beam Michelson interferometer for investigation of trigger dynamics in ESD protection devices under vf-TLP stress", (*ESREF 2003*), *Microel. Reliab.* 43, 2003, pp.1557-1561

Hot Spot Dynamics in Vertical DMOS under ESD Stress

M. Blaho¹, V. Dubec¹, D. Pogany¹, M. Denison², M. Stecher² and E. Gornik¹

¹Institute of Solid State Electronics, TU Vienna, Vienna, Austria

²Infineon Technologies, Munich, Germany

Double-diffused MOS (DMOS) transistors are widely used as high power switches in automotive applications. Due to harsh environment predominating in cars, these devices are exposed to stresses like electrostatic discharge (ESD). A high current, short duration ESD pulse drives the transistor into avalanche breakdown. Under such condition, the device may fail due to triggering of a parasitic bipolar NPN between source, body and drain.

This work studies experimentally the complex dynamics of grounded gate quasi-vertical DMOS transistors after non-destructive snap-back and explains it using electro-thermal simulations [1], [2]. In particular, the positive action of current delocalization on ESD capability is addressed. Formation, spreading, and movement of the hot spots are investigated under square current pulses of maximal 180 ns duration by means of the 2D Transient Interferometric Mapping (TIM) method. In this technique, a thermally induced phase shift is detected, the later being proportional to 2D thermal energy density in silicon. The thermal image can be obtained during a single stress pulse. The time and space resolutions are 5 ns and 3 μm , respectively. The current pulses are produced by a high power electronic switch. The stress currents were chosen above the snap-back current. The devices under test belong to a 1.2 μm , 90 V Smart Power Technology.

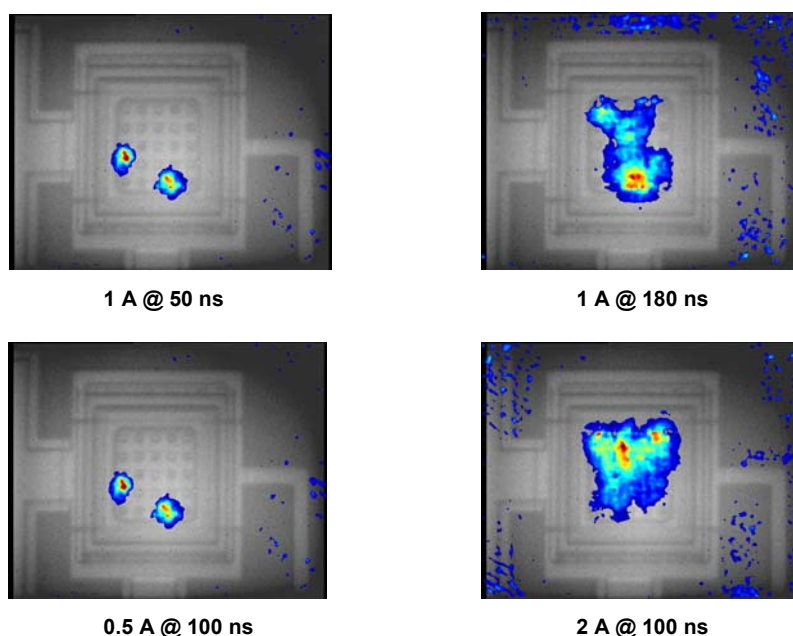
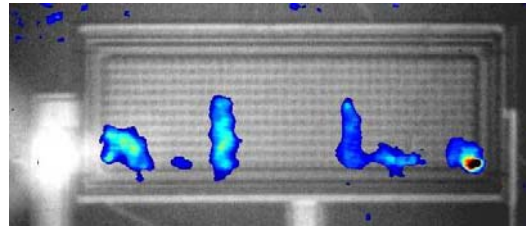


Fig. 1: Examples of extracted TIM pictures of studied small VDMOS device. The stress current level and time instant, when the picture was taken, are indicated below each picture (after [2]).

Figure 1 shows examples of the phase shift distributions in the small device at different time instances and under different stress currents. The phase shift profiles are aligned with the backside infrared images. The heat dissipation starts at the termination and spread with time into the area of the device. This indicates the existence of moving current filaments in the device during this operation condition. With increasing current, the heated area enlarges.

Figure 2 shows the phase shift distribution over a larger device stressed by the current pulse of 3.5 A @ 180 ns. Several hot spots can be observed along the termination of the device. It was found that several filaments could coexist in the device simultaneously.



3.5 A @ 180 ns

Fig. 2: Examples of extracted TIM pictures of studied large VDMOS device. The stress current level and time instant, when the picture was taken, are indicated below the picture (after [2]).

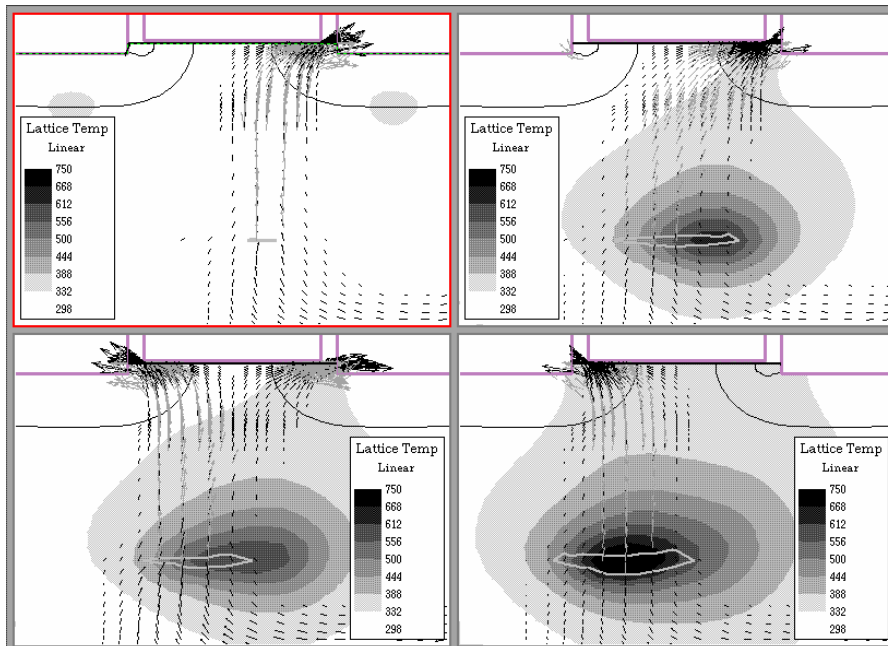


Fig. 3: Electro-thermal simulation of two neighbor VDMOS cells with drain contact on the right side of buried layer, stressed at a similar current density as in the experiments: lattice temperature, hole current density (gray arrows), electron current density (black arrows) and isoline for electric field (thick gray line) after: a) 15 ns: right cell active, b) 35 ns: avalanche region reaches left side, c) 45 ns: both cells triggered and d) 65 ns: left side active (after [1]).

Electro-thermal simulations were performed to help interpreting these results. Figure 3 shows the simulated time evolution of temperature and current densities in two neighbor in-cells for a stress current density of the same order as in the experiments. The right cell triggers first. This is accompanied by a push-out of the maximal field down to the n-epi/n⁺-buried layer junction. A hot spot forms at this place and extends with time. After ca. 35 ns, the avalanching region reaches the left part of the structure. The generated holes first keep flowing to the right cell. At 45 ns however, avalanche multiplication beneath the left cell gets high enough to trigger it. After 65 ns, the left cell has taken over the current. In order to trigger a further cell, the hot spot has first to walk around its last triggered cell. At higher simulated currents, it is observed that the initial cell stays active. In such case one expects the activated area to increase in time as the region of maximal electric field moves through the device. A lower avalanche threshold at this location explains hot spot persistence observed at the termination in the TIM shots.

In conclusion, the mechanism proposed to explain hot spot dynamics in the investigated quasi-vertical DMOS consists in a sequence of hot spots walking around a triggered cell followed by a transfer to a neighbor cell. Under sufficiently high stress current this process leads to a homogenization of the area active in snap-back and allows the studied DMOS to reach an excellent ESD capability.

References

- [1] M. Denison et al: "Hot spot dynamics in quasi vertical DMOS under ESD stress", Proc. of ISPSD 2003, pp. 80-83
- [2] M. Blaho et al: "Hot spot mapping in the DMOS devices for automotive applications", Informationstagung Mikroelektronik 2003, pp. 329-334

Investigation of the Parasitic FET in Sub-100 nm Trench-DRAM

E. Auer and E. Bertagnolli
 Institute of Solid State Electronics, TU Vienna, Austria

Miniaturization of DRAM trench cells quickly progresses towards design rules below 100 nm. This development faces the problem of an increased node resistance due to the continuous shrinkage of the connecting path to the inner trench electrode.

As shown in Fig. 1 (a), a heavily n-doped region, the so-called buried strap, connects the trench-electrode with the drain region of the switching transistor. To separate this region from the n-doped well forming the counter electrode of the trench capacitor, a p-doped well has to be inserted. As shown in Fig. 1 (b), this n-p-n sequence can be considered as the body of an n-channel FET. In this transistor structure the silicon-dioxide collar acts as a gate dielectric and the inner trench performs like a gate electrode. This FET facilitates a possible leakage path, which is capable of discharging the trench capacitor, leading to a malfunction of the DRAM cell. Thus, an accurate knowledge of the electrical behavior of this FET is a necessary precondition for a proper design of the trench, and is therefore a primary concern in any trench-cell based DRAM technology. To optimize the performance of the trench cell, a characterization of this parasitic FET is essential. Due to the fact, that its contacts are not directly accessible, standard electrical methods fail to characterize the parasitic FET. This work proposes a new approach allowing extracting the most important parameters of this embedded parasitic device.

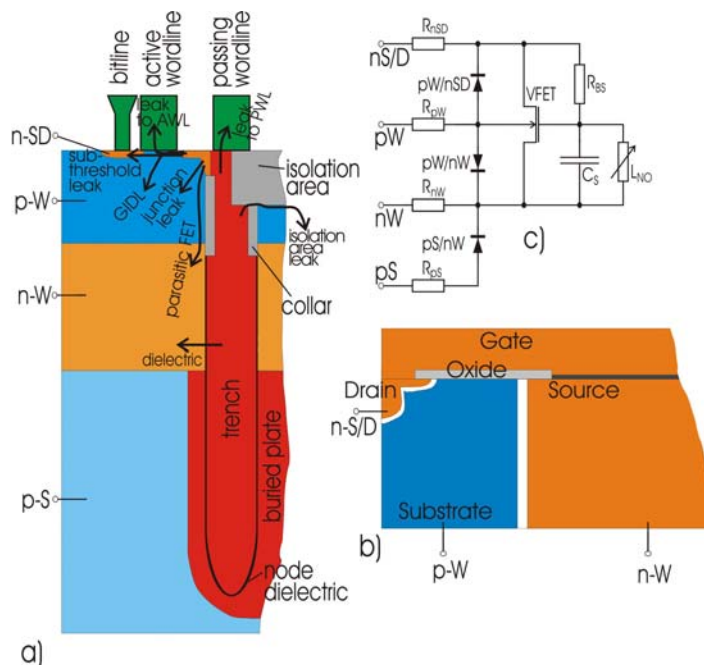


Fig. 1: n-SD...n-doped area of bypassed source and drain of the switching transistor; p-W...p-doped well; n-W...buried n-doped well; p-S...p-doped substrate
 a) Schematic DRAM-trench cell. b) Parasitic FET. c) Circuit diagram of test structure.

As shown in Fig. 1 (a), several leakage paths may modify the charge of the trench capacitor. The key element of our investigation is the parasitic FET as depicted in Fig. 1 (b). Thus, for the electrical characterization a DRAM test-structure is used where the buried strap is directly accessible via a shorted switching transistor. Thereby, any sub-threshold contribution of the switching transistor is excluded.

Setting the voltages for n-SD, p-W, and p-S equally to 0 V while ramping the voltage of n-W to positive values allows to measure the current from n-SD to n-W which is a branch of the leakage path through the oxidized silicon nitride (NO). By usage of the previously described test structure the leakage path through the NO of the capacitor can only be assessed in the polarity where the voltage of the n-W is higher than the voltage of the n-SD. If the inverse polarity is biased, the parasitic FET would turn on and the current through the FET would join the current through the NO. As the gate-dielectric NO consists of oxidized silicon nitride, the branches of current describing the leakage due to electrode polarity will not be symmetric. The measurable leakage current allows approximating the branch with inverse polarity and allows identifying the current through the NO.

Considering all separated leakage paths of the reverse-biased pn junction and taking into account the different magnitudes of the approximated NO leakage the current path through the parasitic FET can be obtained.

To measure the drain current of the parasitic FET in subthreshold or even in inversion mode the potentials applied to the bypassed gate and drain (n-SD) are ramped to positive voltages exceeding the assumed threshold voltage, the source (n-W) is held at 0 V while the bulk of the parasitic FET (p-W) is held at constant voltages equal or less 0 V (see Fig. 1c).

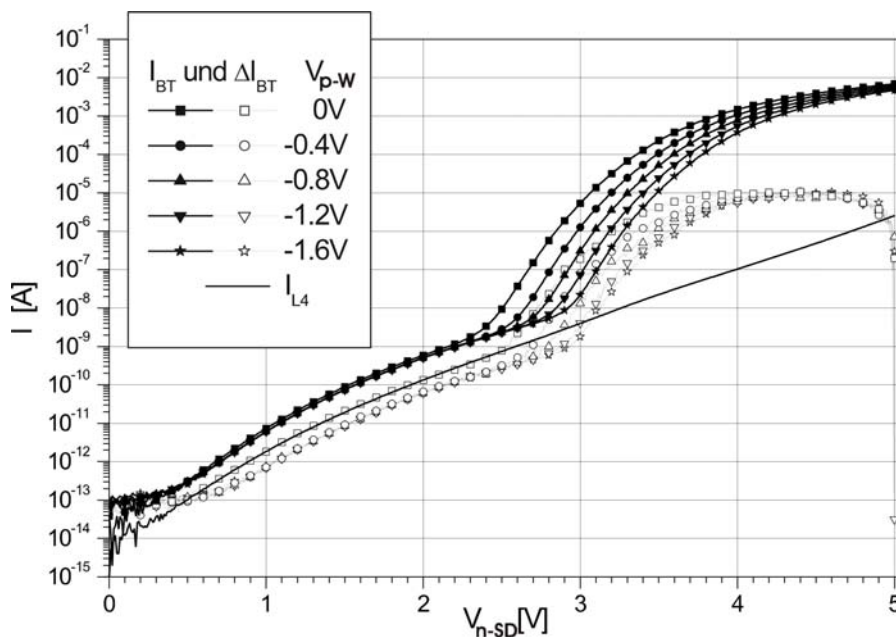


Fig. 2: I_{BT} for five different source-substrate bias-voltages. Empty symbols show the standard deviation of each measured value.

Figure 2 shows I_{BT} for five different source-substrate bias-voltages. The splitting-up shows the existence of a FET drain current due to the variation of the substrate reverse bias. Additionally, the measured current through the NO is shown. The curves below voltages of 2 V display a similar behavior about half an order of magnitude higher than the measured current through the NO and do not split up with different source-

substrate reverse bias. Consequently, the current below 2 V can be identified as the leakage path through the NO under the condition that the voltage of n-SD is higher than the voltage of n-W. Any potential current due to the parasitic FET in this regime is smaller and may be neglected. At a voltage of 2.3 V the transistor current exceeds the current through the NO. As a consequence the current curves coincide again at the end of the scala as the transistor moves towards saturation.

The subthreshold current displays a roughly exponential behavior in dependence on the gate voltage for the long channel approximation. The dimensions of the parasitic FET fulfill the conditions for a long channel FET following an empirical relationship found by Brews et al. [1]. As the subthreshold current of a FET is roughly independent of the source-to-drain voltage it may be extrapolated to the region where the current through the NO exceeds the FET current. This approximation allows estimating the leakage current of the parasitic FET and facilitates optimizing the operational regime in a trench DRAM-product (see Fig. 3).

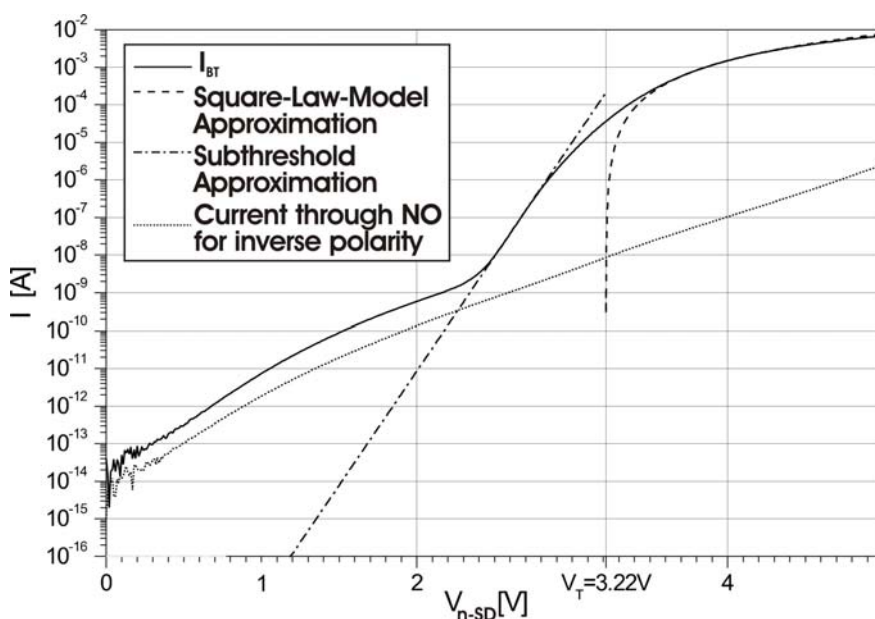


Fig. 3: Current through the parasitic FET.

As drain and gate are linked together the parasitic FET is always operating in saturation. Using the square-law model in saturation the measured data can be also fitted for the FET in inversion mode (see Fig. 3).

While the presented measurement methods were developed using a standard trench-DRAM this approach was already applied on new concepts of trench-DRAM with buried collar [2] at Infineon Technologies Dresden.

References

- [1] J. R. Brews, W. Fichtner, E. H. Nicollian, S. M. Sze: *Generalized Guide for MOSFET Miniaturization*, IEEE Elect. Dev. Letters, vol. **EDL-1**, no. 1, 2 (1980).
- [2] J. Lützen, A. Birner, M. Goldbach, M. Gutsche, T. Hecht, S. Jakschik, A. Orth, A. Sanger, U. Schröder, H. Seidl, B. Sell and D. Schumann: *Integration of capacitor for sub-100-nm DRAM trench technology*, Symposium on VLSI Technology, 178 (2002).

Focused Ion Beam Prepared Contacts of Tungsten to Silicon Characterized by a Cross-Bridge Kelvin Resistor Approach

H. Langfischer
Institute of Solid State Electronics, TU Vienna, Austria

Focused ion beam chemical vapor deposition of tungsten is widely used for circuit repair and prototyping. An extension of this direct write approach from the interconnect metallization level to the device level in CMOS technology requires the demonstration of ohmic low resistance contacts to both types of highly doped source and drain regions. We investigated the metal-silicon contacts of 50 keV Ga⁺ FIB deposited tungsten by a cross-bridge Kelvin resistor approach to extract the contact resistances and we found nonrectifying contacts to both p⁺- and n⁺-silicon. For p⁺-silicon a resistivity of 5.33×10⁻⁶ Ωcm², whereas for n⁺-silicon a higher value of 9.96×10⁻³ Ωcm² is found. Thermal treatment at 450°C for 15 minutes deteriorates the contact properties of p⁺-silicon. In contrast, the annealing process reduced the resistivity of the tungsten to n⁺-silicon contacts by factor of 100 to a value of 1.07×10⁻⁴ Ωcm².

The experimental setup to characterize the contacts relies on Kelvin type four point cross-bridge structures providing terminals that allow a separate measurement of the forced electrical current through the contact region and the resulting voltage drop at the contact. As shown in Fig. 1, the metal tracks are connected to the doped silicon region via the contact zone consisting of a metal filled contact hole embedded in the dielectric layer separating the two conducting layers.

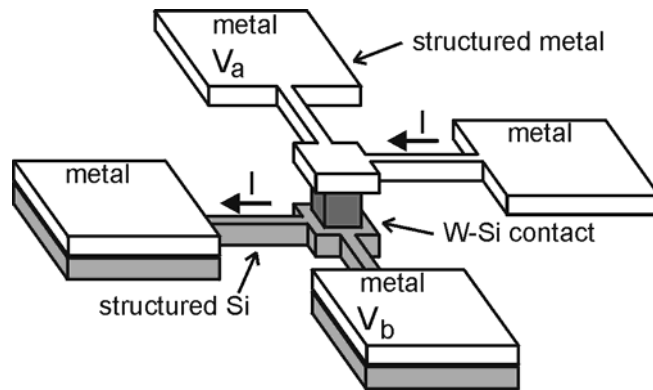


Fig. 1: Cross-bridge Kelvin resistor

The filling of the contact hole is made by FIB-CVD of tungsten. The striking advantage of the four-point measurement is that the detection of the voltage drop $\Delta V = V_a - V_b$ can be measured directly at the contact region. The contact resistance R_C of an ohmic metal-semiconductor contact investigated by means of the described Kelvin structure is then

$$R_C = \frac{V_a - V_b}{I} = \frac{\Delta V}{I}. \quad (1)$$

Figure 2 shows a cross sectional FIB secondary electron microscope (FIB-SEM) image of the contact region of one Kelvin structure.

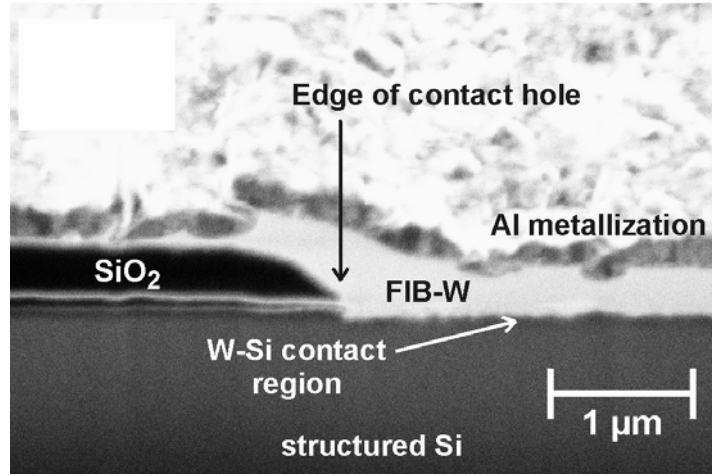


Fig. 2: FIB-SEM image of a FIB cross section through a contact region.

On the left side of the image, the SiO_2 interlayer is visible as a dark region forming a tapered sidewall to the contact hole. The FIB tungsten filling appears bright and compact and is covered with the aluminum metallization. The relationship between the contact resistance R_C measured on the structure and the actual contact resistivity ρ_C is determined by

$$\rho_C = R_C A, \quad (2)$$

where A is the area of the metal-semiconductor contact region.

To determine the contact resistance of the FIB-CVD tungsten-silicon contact the voltage-current characteristics of the Kelvin structures were measured. The resulting ΔV versus I plots showed linearity (i. e. ohmic characteristics) and allowed the extraction of R_C referring to (1). The measured contact resistance data are summarized in Table 1.

Table 1: Resistivity data for FIB-CVD-tungsten-silicon contacts

substrate	annealing process	contact resistivity	standard deviation
p^+ -Si	none	$5.33 \times 10^{-6} \text{ } \Omega\text{cm}^2$	2.5%
p^+ -Si	15 min at 450°C	$1.48 \times 10^{-5} \text{ } \Omega\text{cm}^2$	28.2%
n^+ -Si	none	$9.96 \times 10^{-3} \text{ } \Omega\text{cm}^2$	4.4%
n^+ -Si	15 min at 450°C	$1.07 \times 10^{-4} \text{ } \Omega\text{cm}^2$	7.1%

The lowest contact resistivity of $5.33 \times 10^{-6} \text{ } \Omega\text{cm}^2$ is obtained when tungsten is deposited on the p^+ -silicon substrate and the sample is not subjected to any thermal treating after deposition.

As a conclusion, we found that FIB-CVD tungsten to silicon contacts are not simply metal-semiconductor interfaces, but exhibit an architecture characterized by an inter-medial layer of tungsten-silicide, which is a key issue to the understanding of the electrical and the thermal behavior of these contacts.

Active Field Effect Transistor Fabricated by FIB-Implantation

H. Wanzenboeck and E. Bertagnolli
Institute of Solid State Electronics, TU Vienna, Austria

Focused ion beam technology has successfully proven its potential for fabrication and modification of interconnect layers. The major benefit of this approach is the fact that a photomask is redundant for microstructure generation. In this work, a focused gallium ion beam has been utilized to generate an active device. The incorporation of the ions in the substrate can be utilized for a local implantation. With this approach a field effect transistor was fabricated by implantation of Ga forming the source and drain regions. The p-channel transistor was proven to operate both in the ohmic as well as in saturation mode. This device demonstrates the versatile potential of focused ion beam processing for prototype generation.

Introduction

A FIB operated with gallium ions also allows implantation of Ga into silicon for fabrication of active devices. The high energetic ions of the FIB may also be used for implantation to obtain p-doped regions. By Ga-doping p/n-junctions in n-Si have been processed [1] – [3]. This work demonstrates the wide capabilities of direct-write deposition of materials for microelectronic prototype devices. The deposition of metallic as well as dielectric structures is shown. Using the focused ion beam the feasibility of prototyping doped regions was demonstrated by building a field effect transistor.

Experimental

High energetic 50 keV Ga⁺-ions were extracted from a liquid metal ion source with an ion current tunable between 4 pA and 2 nA and could be focused down to a 10 nm effective beam diameter. A deflection system for scanning operation provided control of the focused beam for a local deposition. Semiconductor materials such as Si (100), GaAs as well as commercial microchips could be used as substrates. For fabrication of the transistor prototypes the ion beam was exclusively scanned over the source and drain regions to obtain an ultrashallow Ga implantation. The implantation dose was $6,5 \times 10^{+14}$ ions/cm² at 50 keV followed by thermal activation of the doped region at 650 °C. A 200 nm thick silicon nitride acted as gate dielectric. Metallization was performed using standard lithographic techniques. The prototype transistor had a gate length of 32 μm with a channel width of 100 μm. All electrical measurements of the transistor were performed with a semiconductor analyzer controlling voltage and current of gate, drain, source and bulk.

Results

The schematic setup of the FIB-fabricated prototype field effect transistor is shown in the left image of Fig. 1 (a). By gallium implantation into n-doped Si ultrashallow p-doped source/drain regions with a thickness below 100 nm were fabricated. For the first time the fabrication of ultrathin active devices by FIB-implantation could be demonstrated.

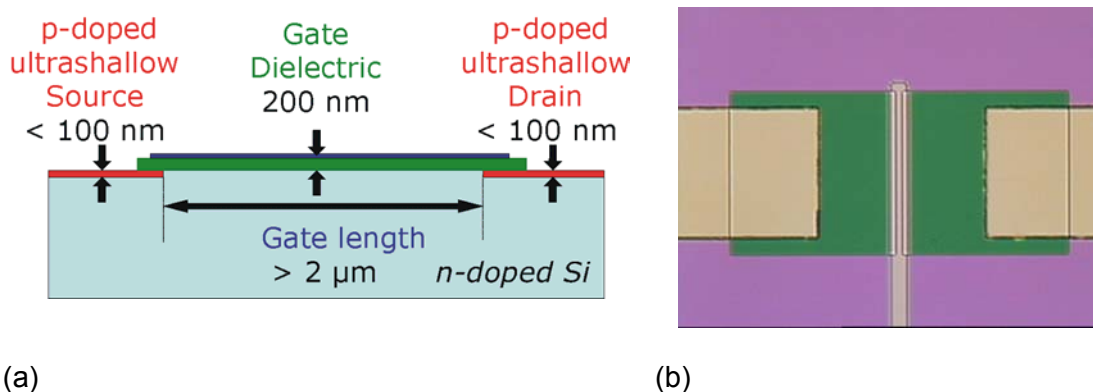


Fig. 1: Schematic illustration (a) and optical image (b) of the FET obtained by direct-write implantation of Ga.

The source and drain metal contacts to the two doped regions as well as the thin gate structure in the image center separating the doped regions are visible in the top view image of the transistor (Fig. 1 (b)). The current-voltage curves of source/bulk respectively drain/bulk measurements displayed the typical diode characteristics. The dielectric layer had negligible leakage currents in the nA range up to a -20 V gate voltage. The measurement of the output characteristics (Fig. 2) was measured for a drain voltage down to -20 V and for a gate voltage down to -15 V. The ohmic region and the current source region can be clearly distinguished in Fig. 2. A very high threshold voltage around -7 V was observed. It is assumed that the 200 nm thick silicon nitride deposited by plasma enhanced CVD contains trapped charges that significantly diminish the effective field in the channel region.

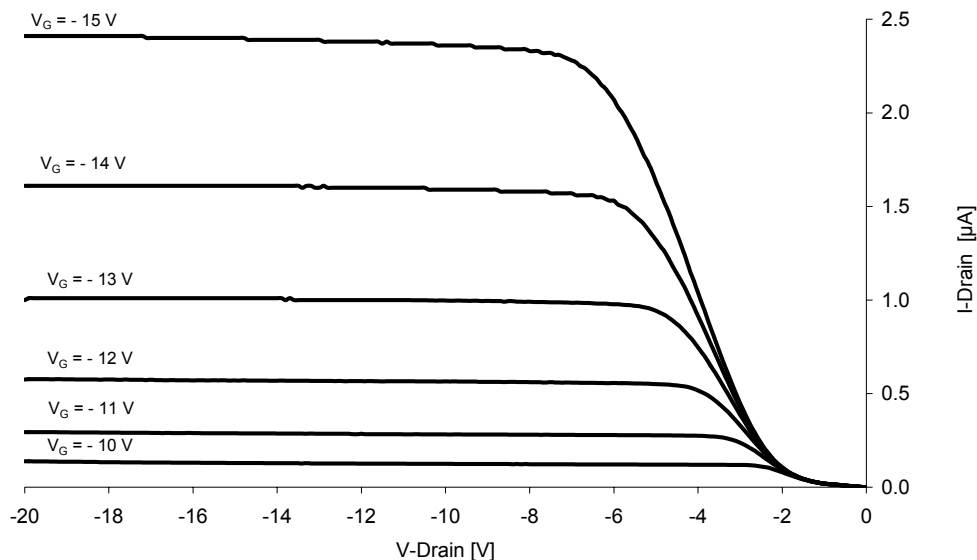


Fig. 2: Output characteristics of the FIB-processed prototype transistor

The mask-less fabrication of the p-MIS transistor providing with the full functionality as amplifier or as a switch by direct-write implantation complements the application range

of direct-write deposition. Direct-write deposition and direct-write implantation allow to assess front-end and backend prototyping of silicon-based microelectronic devices.

Conclusion

Direct-write processing with a focused particle beam has been proven a powerful technique for prototype development. Using a focused beam controlled by a scan generator, arbitrary areas may be doped with gallium. This laterally confined doping supplements the potential of the FIB for direct-write deposition. The fabrication of a field effect prototype with ultrashallow source/drain regions shows the versatility of maskless direct-write technologies. This renders direct-write processing the long sought maskless method for rapid prototype development also of active microelectronic devices.

Acknowledgement

The Austrian Society for Microelectronics (GMe) is acknowledged for financial support facilitating this research. Erich Gornik is thanked for providing the clean room facility of the microstructure center of the Vienna University of Technology. John Melingailis and Lothar Frey are acknowledged for their encouragement and for constructive discussions.

References

- [1] Mogul H.C., Steckl A.J., Ganin E., "Electrical properties of Si p⁺-n junctions for sub-0.25 μm CMOS fabricated by Ga FIB implantation", IEEE Transactions on Electron Devices 40(10), 1823-9 (1993)
- [2] Okubo A., Fukatsu S., Shiraki Y., "Local Ga implantation with focused ion beam and ambipolar lateral carrier transport in strained Si_{1-x}Ge_xSi quantum wells", Applied Physics Letters 65(20), 2582-4 (1994)
- [3] Chih-Chieh-Shen; Murguia J.; Goldsman N.; Peckerar M.; Melngailis J.; Antoniadis D.A.; "Use of focused-ion-beam and modeling to optimize submicron MOSFET characteristics" IEEE-Transactions-on-Electron-Devices 45(2), 453-9 (1998)]

Simulations of Ion Beam Induced Damage in Silicon: Coupled Kinetic Monte Carlo and Molecular Dynamics Simulations

G. Otto and G. Hobler
Institute of Solid State Electronics, TU Vienna, Austria

Introduction

Damage formation during ion implantation is a complex process that cannot accurately be modeled by binary collision simulations alone. Molecular Dynamics (MD) simulations are an accurate method to simulate ion implantations at low temperatures. However, because lattice vibrations have to be resolved by the MD time steps, MD cannot simulate thermally activated processes at time scales that occur in industrial processing steps. On the contrary, kinetic Monte Carlo simulations (kMC) consider only events that change the structure of the crystal. Due to this fact, it is possible to treat thermal processes with kMC. Nevertheless, kMC cannot handle ballistic processes because the binding and formation energies of complex defect clusters are often unknown. However, both ballistic and thermally activated processes need to be taken into account in order to predict the amount and types of defects depending on the implant parameters, such as ion species, energy and temperature. To combine the advantages of both simulation methods we have introduced and tested a coupling scheme of MD and kMC. Doing this, one has to be careful not to lose too much information of the coordinates and of the kind of defects when transforming them from one scheme to the other. Otherwise, complex defects cannot be restored in MD any more once they have been transformed.

Scheme of Coupling

We couple binary collision (BC)/MD and kLMC simulations. The BC calculations are used to generate the initial recoils for the MD simulations. Details of the binary collision program IMSIL can be found in [1] and the description of the MD scheme is given in [2], [3]. As input for the lattice kinetic Monte Carlo (kLMC) simulation, physical quantities like formation and binding energies of point or extended defects are required, which we take from ab-initio simulations [4] – [8]. The crucial point in coupling MD and kMC simulations is to minimize the loss of information about the defects by caused by their transformation them from MD to kMC and vice versa. We achieve this using the following scheme. First, we identify the defects generated in MD. The atom positions are analyzed with respect to spheres centered on ideal lattice sites with radii equal to half the nearest neighbor distance in the ideal lattice. If a sphere contains no atom, the lattice position is labeled as a nearest-neighbor-sphere (NN) vacancy. If an atom is outside all of the spheres, its position is labeled as NN interstitial. When transforming the kLMC defects to the MD scheme one obtains only nearest neighbor (NN) defect immediately, but not atoms that are shifted less than half the nearest neighbor distance from their lattice sites. However, such defects are generated if the MD cell including the NN defects is relaxed. We tested the stability of defects and almost the whole damage ($96\% \pm 2.2\%$) is reproduced.

Results

To demonstrate the coupling we examine the differences in the damage generation for the implantation of heavy and light ions at room temperature. As heavy ion, we have chosen arsenic and as light ion, boron. We have performed a BC simulation of a 1 keV As ion and put the generated recoils into a MD simulation. After 5 ps the MD simulation is stopped and the identified NN defects are transformed to the kLMC model. The kLMC simulation is performed until all single vacancies have disappeared leaving only two main clusters, which are transformed back to MD and relaxed for 5 ps. In the next step, another As cascade which overlaps partly with the first cascade is simulated. The cluster generated by the first cascade has shrunk in the final defect configuration due to a recrystallization initiated by the recoils of the second cascade. As a second example, we have implanted 1 keV boron ions into silicon. We produced a predamaged crystal by a coupled BC/kLMC simulation. We implanted a dose of $5 \times 10^{14}/\text{cm}^2$, which caused about 4% of the lattice atoms to be displaced. The damage was transformed to MD and relaxed. Another boron cascade has then been simulated with MD in the predamaged crystal, and the additional damage has then been compared with the damage produced by a boron cascade generated by the same primary recoils in an undisturbed crystal. In the undisturbed cascade, the boron implantation generated 20 NN defects, in the predamaged cascade 12 additional defects, indicating a sublinear increase in damage concentration.

Conclusion

A scheme of coupling kLMC with MD has been introduced, which allows an almost complete reconstruction of MD clusters once they have been transformed to kLMC. With this coupling, both the quenching of collision cascades and the thermally activated processes can now be considered in one simulation.

Acknowledgements

This work was sponsored in part by the Austrian Science Fund, Project No. 15872-N08.

References

- [1] G. Hobler, Nucl. Instr. Meth. 96, 155 (1995).
- [2] K. Gärtner *et al.*, Nucl. Instr. Meth. B 102, 183(1995).
- [3] G. Otto, G. Hobler, and K. Gärtner, Nucl. Instr. Meth. B 202, 114 (2003).
- [4] A. Bongiorno *et al.* Europhys. Lett. 50, 608 (2000).
- [5] A. Bongiorno and L. Colombo, Phys. Rev. B 57, 8767 (1998).
- [6] M. Tang *et al.* Phys. Rev. B 55, 14279 (1997).
- [7] L. Marques *et al.* Phys. Rev. B 64, 045214 (2001).
- [8] J. Zhu, Comp. Mat. Sci. 12, 309 (1998).
- [9] H. Hensel and H. M. Urbassek, Phys. Rev. B 57, 4756 (1998)

Advanced Nanoscale Material Processing with Focused Ion Beams — Metallic Nano Dots Realized by a Subtractive Self Organisation Process

A. Lugstein, B. Basnar, M. Weil, J. Smoliner and E. Bertagnolli
Institute of Solid State Electronics, TU Vienna, Austria

Nanoscale structuring opportunities are prerequisites for any nanoscale engineering. In particular, resist-less focused ion beam techniques are most suited for the combination of top-down structuring with selective bottom-up self-assembling techniques. To keep up with the trend of structures to shrink in dimensions, the response of ion induced material modifications will have to be controlled on a nanometer scale. A prerequisite thereof is a deep understanding of the ion beam interaction with the processed substrate material.

We demonstrate surface modifications caused by focused ion beam irradiation, addressing the primary mechanisms leading to material swelling, amorphization and preferential etching. In detail, we have studied the impact of shrinking feature sizes on the sputter efficiency of focused ion beams for Si, GaAs and InAs. Milling of nano dots exhibits fundamental features for FIB patterning. Based on our experimental results, a sputter yield promoting self-focusing effect combined with a sputter rate increase at oblique angles, an opposing dose deficiency effect and material re-deposition for milling aspect ratios >1 are identified to be responsible for the complex sputter response of Si and GaAs. In addition, for GaAs the observed preferential etching of arsenic results in precipitates of mobile Ga-rich residues influencing the fundamental characteristics of FIB patterning, like sputter yield, crater bottom flatness, and ripple formation.

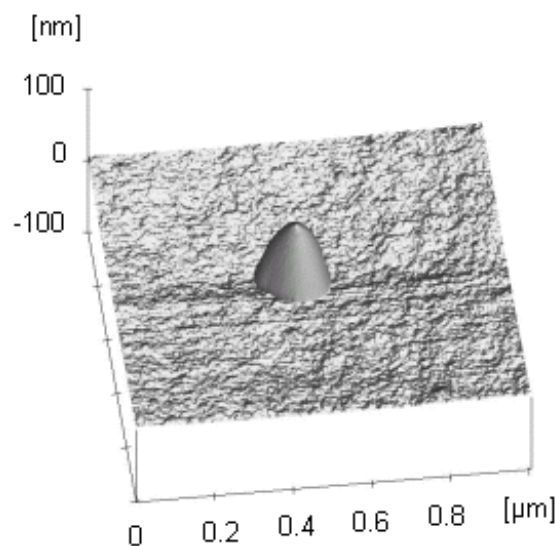


Fig. 1: Topographic AFM image of a Ga dot generated by FIB milling on GaAs.

Due to the high-energy injection during FIB milling and the low melting point of Ga the precipitations behave like a liquid under milling conditions. The lowest energy configuration corresponds to equilibrium determined by the minimization of the total interfacial free energy and results in spherical calotte shaped droplets (Fig. 1). Nanometer sized metallic dots can be formed in a size and position controlled fashion by combining a focused ion beam induced self-organized formation technique and a subsequent rapid thermal annealing (Fig. 2). Since GaAs quantum dot formation from Ga droplets has been reported, our technique is considered a candidate for the fabrication of highly ordered GaAs quantum dot array structures.

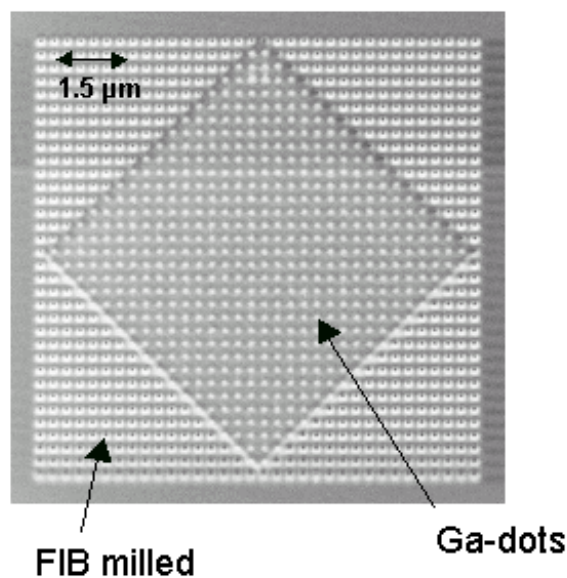


Fig. 2: The FIB-SEM image shows an array of freestanding Ga dots achieved by a two-step process. In the first step, we generated an array consisting of 34x34 nominally 75 nm deep holes with a spacing of 300 nm between them. Subsequently, milling of a box on the prepatterned array of holes leads to the arrangement of a regular pattern of freestanding Ga dots.

The optical microscopy and AFM analysis reveals the decomposition of the FIB modified GaAs surface layer when the temperature increases above 200 °C, whereby the dots formed during FIB exposure act as catalytic sites for thermal driven decomposition (Fig. 3). The chemical and morphological evolution of the GaAs surface due to FIB exposure and subsequent annealing has also a strong impact on the electrical properties of the GaAs surface which has been investigated by conventional 4 point van der Pauw measurement.

Further, we have shown that FIB bombardment of InAs produces indium crystallites, and the size of the crystallites increases with ion dose and ranges from 80 nm to 1.5 μm (Fig. 4). The influence of the ion dose, the beam energy, the sample temperature and the dose rate on the surface evolution has been investigated for further III/V compound semiconductors by atomic force microscopy, scanning electron microscopy, auger electron spectroscopy and X-ray diffraction measurements.

In summary, the surface topography resulting from FIB bombardment is being investigated for possible use in nano-technology applications. This technique, based on a subtractive self-organization process, may lead to a new fabrication process for three-dimensional metallic nanostructures.

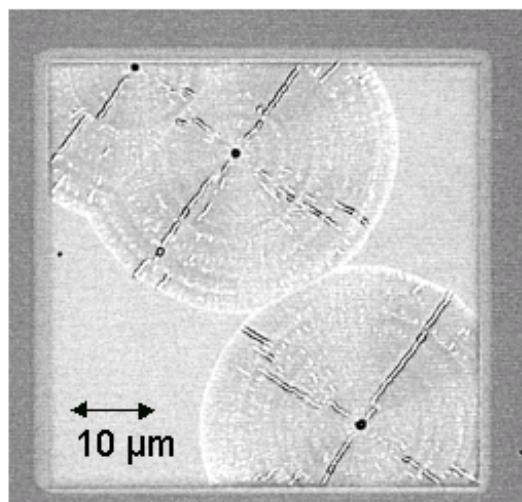


Fig. 3: The Optical microscope image shows the effect of the annealing on the surface evolution of the ion bombarded GaAs. After annealing the dots previously observed are still present, but quite different to the former now surrounded by micellar-like features incorporating straight lines (jets). These jets follow the [011] and [0-11] directions equivalent to the cleaving planes of the (100) GaAs sample. AFM investigations reveal that these micelle-like features are depressions of about 4 nm and the height of the jets piles up to more than 50 nm. We assume that annealing of the samples leads to a further destabilization of the heavily irradiated GaAs surface whereby the existing dots serve as anchor points.

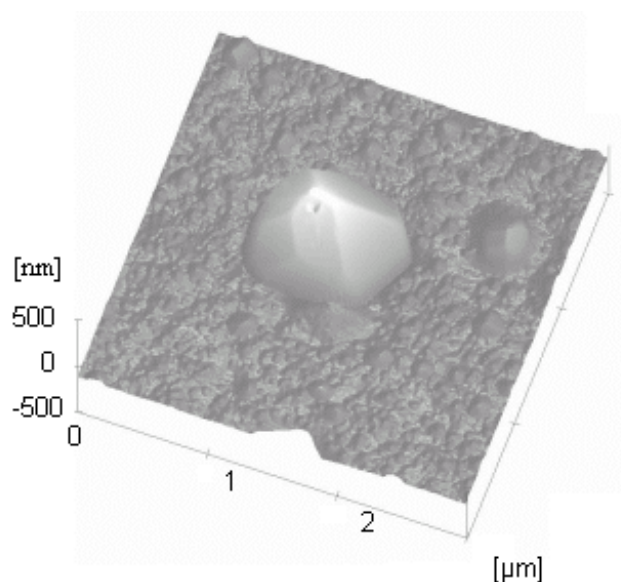


Fig. 4: Topographic AFM image of the InAs surface after FIB exposure at 50 kV acceleration voltage and of an ion dose of 5×10^{16} ions/cm². The image shows a nearby perfect crystallite with obvious facets in close contact with the substrate.

Quantitative Scanning Capacitance Spectroscopy

**W. Brezna, M. Schramboeck, A. Lugstein, S. Harasek, H. Enichlmair,
E. Bertagnolli, E. Gornik and J. Smoliner
Institute of Solid State Electronics, TU Vienna, Austria**

In this work, we introduce a setup for quantitative scanning capacitance spectroscopy on nanoscopic scales. The setup consists of a commercially available atomic force microscope (AFM) for tip positioning. An ultrahigh precision capacitance bridge measures the tip-sample capacitance in the aF regime under well controlled, small signal conditions. This is a big advantage over commercial scanning capacitance microscopes (SCM) which work in the large signal regime and provide a signal that is the first derivative of the capacitance (dC/dV). To guarantee a constant tip-sample contact area we used highly doped, conductive diamond tips because of their high resistance against abrasion. As samples, we used low p-doped Si wafers covered with two types of dielectrics: industry quality SiO₂ and metal-organic chemical vapor deposition grown ZrO₂.

To test the reliability of our results, both macroscopic measurements on large area 100 × 100 μm² MOS capacitors with Al top electrode, and AFM based nanoscopic investigations were carried out on identical pieces of samples. In Fig. 1 (a), a comparison between the C(V) data of a reference MOS capacitor, and a nanoscopically measured C(V) curve is shown. An interface charge density Q_{it} of about 5 × 10¹¹ cm⁻² can be calculated from the slope of the macroscopic reference curve. The smaller slope of the nanoscopic curve is due to the very small area of the AFM tip and a correlated high influence of electrostatic edge effects in the area of the tip. Figure 1 (a) can be used to calculate the work function W_{tip} of diamond tips: W_{tip} = ΔW + W_{Al} = 5.5 eV, where ΔW = e × ΔU is proportional to the voltage difference ΔU in Fig. 1 (a) and W_{Al} = 4.2 eV is the known work function of the Al top electrode. W_{tip} = 5.5 eV is in agreement with the value of 5.165 eV found in literature for highly p-doped, deposited diamond.

The setup is also capable of measuring details of the interface trap energy distribution. This is shown by a comparison of macroscopic and nanoscopic capacitance measurements on a ZrO₂ covered Si sample in Fig. 1 (b). Interface traps lead to a decrease of the slope of the C(V) curve. If most of the interface traps are activated within a small energy interval, the transition between accumulation and depletion in the C(V) curve contains regions of reduced slope or kinks. Both the macroscopic reference curve as well as the nanoscopic C(V) curve in Fig. 1 (b) exhibit a pronounced kink, which demonstrates that both curves have a comparable energy resolution. Such measurements are currently not available with standard commercial SCM equipment because of the large modulation voltages. This is demonstrated in Fig. 1 (c) where the nanoscopic dC/dV curve shows more features than the standard SCM curve. The nanoscopic C(V) curve was numerically differentiated to obtain the dC/dV curve in Fig. 1 (c).

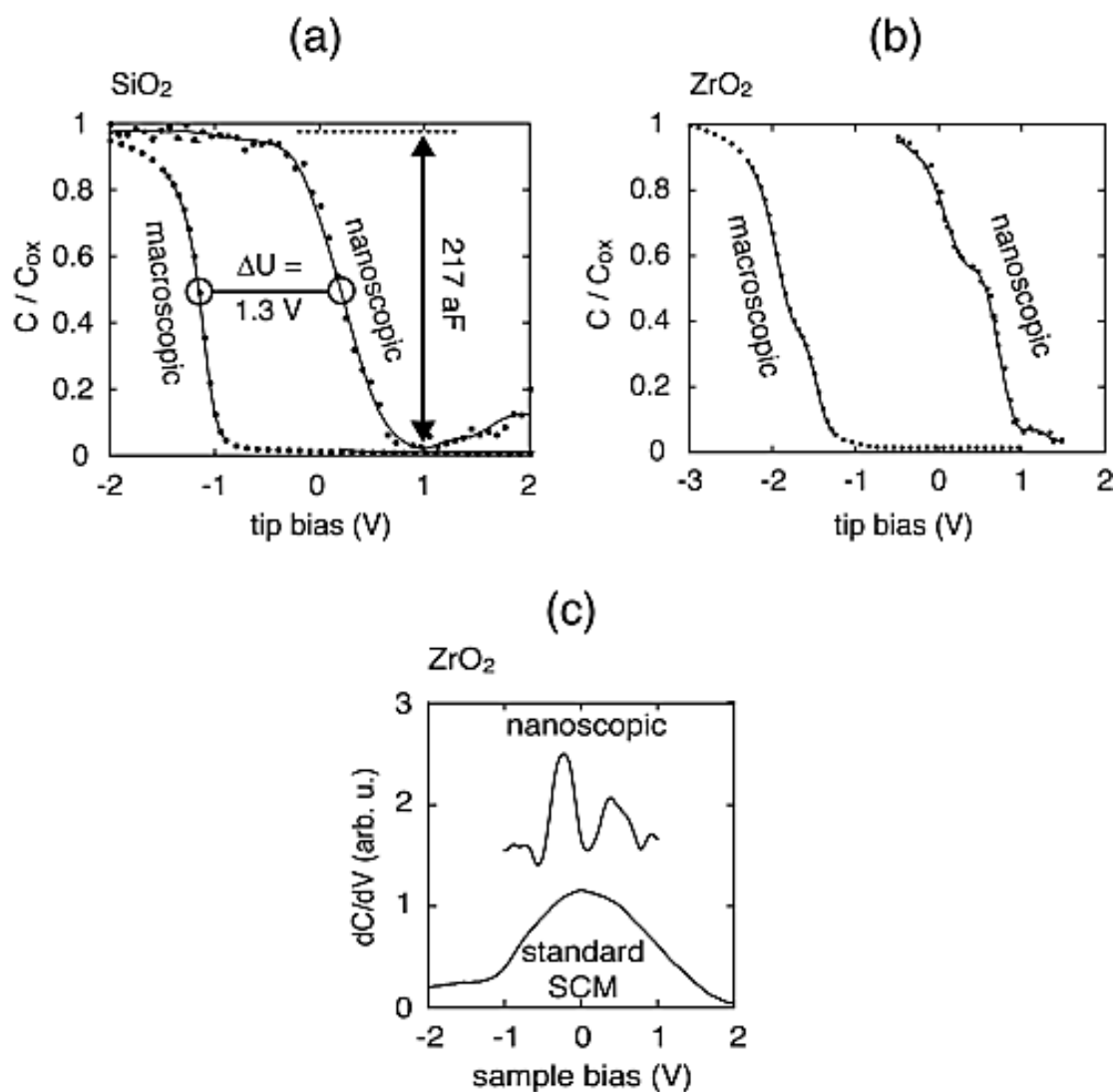


Fig. 1: (a) Comparison of a macroscopic and a nanoscopic $C(V)$ curve on a SiO_2 covered sample.
 (b) Comparison of the energy resolution of macroscopic and nanoscopic $C(V)$ curves on a ZrO_2 covered sample.
 (c) Comparison of a (derivated) nanoscopic capacitance curve and data obtained by standard SCM equipment.

X-Ray Investigation of Interface Broadening by Rapid Thermal Processing

T. Roch, W. Schrenk, S. Anders, C. Pflügl and G. Strasser
Institute of Solid State Electronics, TU Vienna, Austria

Quantum cascade lasers (QCLs) [1] – [3] can be tuned by post-growth rapid thermal processing. Interdiffusion at the barrier-well interfaces in the temperature range between 850 and 875 °C shifts the energy levels and thus the gain and emission wavelength of the structure in the range from 10.3 to 11.9 μm [4]. The diffusion has been investigated quantitatively by high-resolution x-ray diffraction measurements. Rocking curves ($\omega - 2\theta$) measured on a thermally processed set of samples confirm Al-Ga intermixing at the interfaces.

Because of the complexity of QCL structures, the x-ray measurements were done on a periodic superlattice structure. The structure period of 35 nm GaAs ($n_{\text{Si}} = 5 \times 10^{15} \text{ cm}^{-3}$) and 5 nm $\text{Al}_{0.4}\text{Ga}_{0.6}\text{As}$ ($n_{\text{Si}} = 3 \times 10^{15} \text{ cm}^{-3}$) is repeated 60 times and buried under 300 nm GaAs ($n_{\text{Si}} = 1 \times 10^{17} \text{ cm}^{-3}$). Prior to the RTP, all samples were covered with 200 nm SiO to prevent outdiffusion of As. Four different pieces were then heat-treated for 60 s at 850, 875, 900 and 950 °C in forming gas atmosphere. After heating the samples to 200 °C, the temperature was ramped to 650 °C with 37.5 °C/s and then to the target temperature with 20 °C/s.

X-ray diffraction $\omega - 2\theta$ spectra were measured using a high-resolution double crystal diffractometer. $\text{CuK}\alpha 1$ radiation was used and a 0.2° receiving slit in front of detector served to increase the signal-to-background ratio. The data were recorded around the GaAs (002) substrate reflection where we can achieve suitable contrast due to larger difference between the scattering factors of Al and Ga.

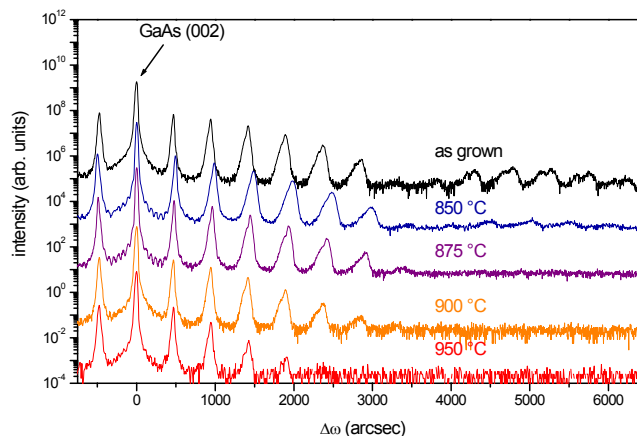


Fig. 1: X-ray diffraction $\omega - 2\theta$ scans around the GaAs(002) reflection. The measured curves are shifted in y-direction for clarity. Due to a slight period inhomogeneity over the wafer, the satellites do not appear at the exactly the same angular positions.

Figure 1 shows series of measured data curves for as-grown and heat treated periodic superlattice structures. The main substrate peak at zero arcsec is accompanied by several of superlattice peaks at constant angular separation, which represent the reciprocal space picture of the superlattice in the growth direction. Higher order satellites, at larger angular distance from the substrate peak, provide information about the finer details of the interfaces. By increasing the order, the satellite heights decrease due to their broadening. Therefore, we have used integrated intensities of satellites for the analysis of the data. The measured data were fitted with a computer calculation using dynamical x-ray diffraction theory with the layer thicknesses and Al content as fit parameters (Fig. 2a). The envelope of the calculated pattern matches very well with the envelope curve of the integrated satellite intensities. The modulation of the envelope curves shows a systematic decrease with the RTP temperature. This effect corresponds to an increase of Al-Ga interdiffusion at the AlAs/GaAs and GaAs/AlAs interfaces. The Al concentration gradients at the interfaces were included into fitting model by simple linear gradients. Results of fitting of the envelope curves of the measured data are shown in Fig. 2 (b). The increase of the interface width (compared to the as-grown sample), Δw , is plotted vs. temperature. Already at 850 °C and 875 °C, the interface width has increased by about 1 nm (3.6 monolayers) and 2.5 nm (8.9 monolayers), respectively.

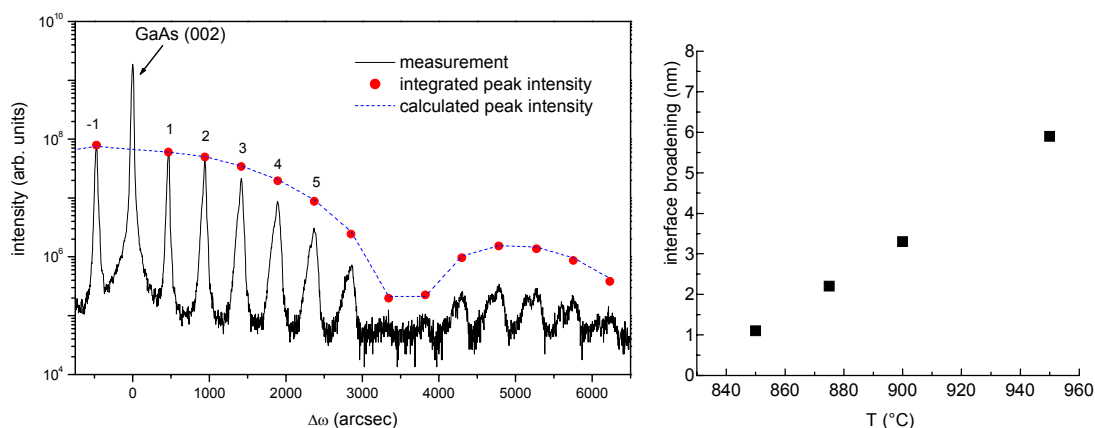


Fig. 2: (a) X-ray $\omega - 2\theta$ spectrum of as-grown sample. The integers indicate the order of the superlattice satellites. Dots are the integrated satellites intensities; dashed curve is the calculation.
(b) Change of the AlAs/GaAs interface width Δw due to RTP.

Si as a dopant as well as a constituent of the SiO layer that was applied for RTP is known to increase the Al-Ga interdiffusion.[5] – [7] Therefore, the interdiffusion width of the investigated superlattice is presumably somewhat higher than it would be for a sample without any Si. In the QCLs, on the other hand, the active region is separated by a 3.2 μm thick layer from the highly doped ($n_{\text{Si}} = 4 \times 10^{18} \text{ cm}^{-3}$) cap layer. Thus, the interdiffusion in QCLs should not be enhanced by Si. Therefore, the values obtained by x-ray diffraction measurements for the reference sample represent an upper limit for the interdiffusion.

Acknowledgement

This work was supported by the European Community-IST project SUPERSMILE, by the Austrian Microelectronics Society and the Austrian FWF (SFB-ADLIS).

References

- [1] C. Sirtori, et al., Appl. Phys. Lett. **73**, 3486 (1998)
- [2] G. Strasser, et al., Appl. Phys. Lett. **75**, 1345 (1999)
- [3] J. Faist, et al, Appl. Phys. Lett. **72**, 680 (1998).
- [4] S. Anders, et al, Appl. Phys. Lett. **84**, 164 (2004).
- [5] P. Mei, et al, Appl. Phys. Lett. **50**, 1823 (1987).
- [6] J. D. Ralston, et al, Appl. Phys. Lett. **52**, 1511 (1988).
- [7] L. J. Guido, et al, J. Appl. Phys. **61**, 1372 (1987).

Cell Growth on Prestructured Microelectronic Materials

H. D. Wanzenboeck¹, C. Almeder¹, C. Pacher¹, E. Bertagnoli¹
E. Bogner², M. Wirth² and F. Gabor²

¹ Institute of Solid State Electronics, TU Vienna, Austria

² University of Vienna, Institute of Pharmaceutical Technology and Biopharmaceutics

Bioelectronic transducers offer powerful new analytical tools with major applications in medicine, pharmaceutical research, environmental diagnostics and the food and processing industries. The interface between inorganic materials and living cells is crucial for the operation of biosensors. The viability and the adhesion of colon carcinoma cells (Caco-2) was tested on an assortment of commonly used metals, dielectrics and semiconductor materials. Growth inhibiting materials such as copper and blank gallium arsenide have been identified as well as highly biocompatible materials such as silicon, silicon nitride, chromium and gold. In addition, the growth on the metal-dielectric boundary was performed and neither the sub-200 nm height step nor the change of the material showed to affect the cell growth. Several materials have been successfully tested to facilitate the growth of cell structures. The results allow a versatile application for microelectrode arrays.

Keywords: direct write deposition, focused ion beam, FIB, 3-dimensional, chemical composition

Introduction

Methods for the investigation of living cells have historically been of significant importance for research in neuroscience and cell biology. For cell-based biosensors, the signal is originating from the presence or the metabolism of the living cell. Classical measurement techniques utilize the patch-clamp method where the single cell is contacted with a micropipet containing the electrode. For the high-throughput testing of drugs, electrical methods are most promising, as the characterization of a large amount of cells may be performed simultaneously [1]. During the last decade, the research on cell-based biosensors has experienced increased scientific activity [2], [3]. While a variety of different measurement techniques exist, microelectrode arrays [4] provide a simple interface for monitoring the electrical activity and impedance characteristics of populations of cultured cells over extended periods. Wide ranging applications of this emerging technology can be expected not only to the detection of chemical and biological warfare agents, but also to the testing of new pharmaceuticals and the monitoring of medical parameters [9]. Various metals, dielectrics and semiconductor materials have been tested as substrates for culturing cells. Also a composite substrate consisting of two materials — a dielectric and a metal simultaneously present on the surface — has been investigated. This work clarifies the suitability of microelectronic materials for sensors monitoring the activity of living cells.

Experimental

For this study, sample chips of 5x5 mm size were fabricated out of different materials. The pure semiconductor materials tested during this study were silicon (Si), Germanium (Ge) and gallium arsenide (GaAs). As insulating materials dielectrics such as sili-

con oxide (SiO_2), silicon nitride (Si_3N_4) and polymers such as polymethylmetacrylate (PMMA) or the photosensitive resist recipes maN410 and maP were used. The metals Al, Ti, Au, Cr, Pt, W and Cu were separately deposited as a thin film on silicon wafers. Standard glass slides of sodium potassium silicates were processed as reference material.

The prepatterned surfaces were fabricated by sequentially depositing a continuous Au layer and a silicon nitride layer on top of a Si-wafer. A silicon nitride grating with a periodicity in the 50- μm range was fabricated by local etching. The resulting patterned surface displayed lines of Au and Si_3N_4 in a regular arrangement.

Human colon carcinoma cells (Caco-2) were selected as an exemplary cell culture. The Caco-2 cells were obtained from the American Type Culture Collection (Rockville, MD, USA). The cells were cultured in RPMI-1640 cell culture medium supplemented with 10% fetal calf serum, 4 mM glutamine and 150 $\mu\text{g}/\text{ml}$ gentamycin. The cell cultures were grown in microtiter plates at 37 °C in a humidified 5% CO_2 / 95% air atmosphere for a period of 10 to 14 days. The progress of the cell growth was repeatedly controlled by visual inspection. For inspection, the substrates with a Caco-2 tissue attached to the surface were placed under a microscope to evaluate the viability on the substrate.

Results

The first efforts were directed at clarifying the biocompatibility of semiconductor materials themselves. Caco-2 cells were cultivated on top of a microelectronic substrate. A dense coverage with cells on the surface was obtained with silicon and germanium, while only few cells were found on the gallium arsenide surface. Dielectric interfaces to cells are relevant for capacitive biosensors. Homogeneous cell coverage was achieved with silicon nitride, deposited by plasma enhanced chemical vapor deposition, and silicon oxide generated by thermal oxidation of silicon. With thermal silicon oxide, the cells appear rather round-shaped suggesting a not so good adhesion. The polymer polymethylmetacrylate is not considered an ideal growth substrate for biological materials. For biosensors interacting with the cells over electrodes, the interface to the cell is a conductive material.

A homogeneous surface coverage of Caco-2 cells was found on chromium and gold surfaces. With tungsten and titanium, a low cell coverage around 50% was obtained. On aluminum, cells also appear to be healthy and the shape suggests a sufficient attachment to the surface. However, experimental results concluded that copper intoxicates the cells and is a totally unsuitable material.

Microelectronic biosensors are constructed as integrated circuits acting as signal transducers for biological systems. Such microelectronic systems usually consist of several material layers and may have metallic surface areas such as microelectrodes next to dielectric areas acting as passivation for the circuitry. A prestructured sample with gold and silicon nitride structures coexisting on the surface was fabricated (Fig. 1 (a)). The Caco-2 cells cultured on this composite surface displayed a dense tissue with the cells grown together so continuously that the entire surface was covered (Fig. 1 (b)). The shape of the cells suggests a good adhesion on the entire surface. It is concluded that both materials together establish a biocompatible surface.

A close examination of the sharp boundary between the gold structure and the silicon nitride area has been performed (Fig. 1 (c)). The cells have grown over this rim totally unaffected. Even the 200 nm height difference at the interface between the gold layer and the silicon nitride layer left the growth totally unaffected. The cell growth showed no orientation to the border between these materials. It can be assumed that the cell activity remains totally unchanged on microelectrode circuits utilizing gold and silicon nitride.

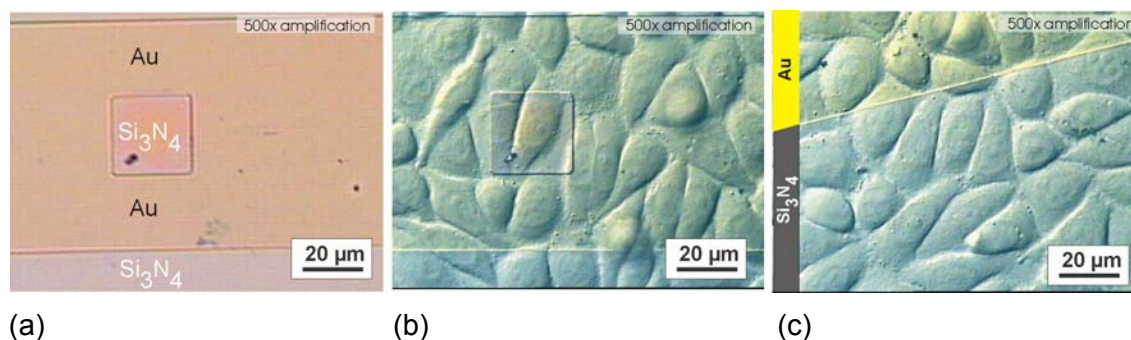


Fig. 1: Optical images (500x magnified) of a prestructured microelectronic sample with (a) the original surface with gold and silicon nitride structures, (b) a Caco-2 cell layer grown over the surface, (c) another sample spot with cells growing over the edge between the different materials.

This result opens the path for the application of this material system for the development of cell-based biosensors to assess the vital parameters of these cells.

Conclusion

In this study, the biocompatibility of materials frequently used in microelectronics was determined by an examination of Caco-2 cells cultivated on various surfaces. The feasibility to grow cells on prestructured surfaces with conductive and insulating materials has been demonstrated. It has been demonstrated that the cell growth remains unaffected by structuring of the surface. On prestructured composite surfaces with a metal and dielectric present in direct vicinity, cell growth was observed over the interface between those materials.

This initial study has provided reliable experimental data on the biocompatibility of microelectronic materials and shines an optimistic light on the future development of microelectronic biosensing devices.

Acknowledgement

The Austrian Society for Microelectronics (Gesellschaft für Mikroelektronik) is acknowledged for financial support. We thank Prof. E. Gornik for providing the clean room of the microstructure center for structuring the semiconductor surfaces.

References

- [1] H. Theilecke, A. Mack, A. Robitzki; Proceedings of the Microtec 2000 VDE World Microtechnologies Congress 2000, 2, 405
- [2] L. Billings, I.B. Schwartz, J.J. Pancrazio, J.M. Schnur; Physics Letters A, 286(2-3), 217 (2001)
- [3] A. Abdelghani, C. Abdelghani-Jacquin, H. Hillebrandt, E. Sackmann; Materials Science & Engineering C, Biomimetic and Supramolecular Systems, C22(1): 67 (2002)
- [4] M. Sandison, A. S. G. Curtis, C. D. W. Wilkinson; Journal of Neuroscience Methods, 114(1), 63-71 (2002).

Recent Structures for Plasma Instability Search

M. Coquelin, R. Zobl, G. Strasser and E. Gornik
Institute of Solid State Electronics, TU Vienna, Austria

Due to the experimental limitations, the high current density domain (where instability can occur at high frequencies) was not accessed in previous experiments. A new set of structures, the sample g595 as a modified version of g494, was designed to bring the instability phenomenon within the range of experimental observation. The dimensions of the parabolic and the pocket regions were increased to bring down the intersubband energies, thus ensuring that instability will occur at lower frequencies, possibly in the detection region of the InSb setup, i.e. below 25 meV. Half of the digital grown parabolic injector region which lies next to the active region was replaced by an 10 nm wide layer with constant Al-content ($x = 0.0462$) and the width of the active region was increased from 15.5 nm to 18.5 nm.

Simultaneously, the thickness of the entry barrier was increased from 1.2 nm to 1.8 nm and the RTD barriers were increased from 2.4 nm to 2.8 nm and thus the extraction rate of the RTF slightly reduced. This was aimed at reducing the current flow while keeping a high density of carriers inside the active region. This would allow instabilities to occur at lower current densities, thus avoiding heating.

Figure 1 shows the conduction band and the energy levels of the eigenstates in the injector region and the active region of G595. At the bias given in Fig. 1 the second level of the pre well locks to the RTD level.

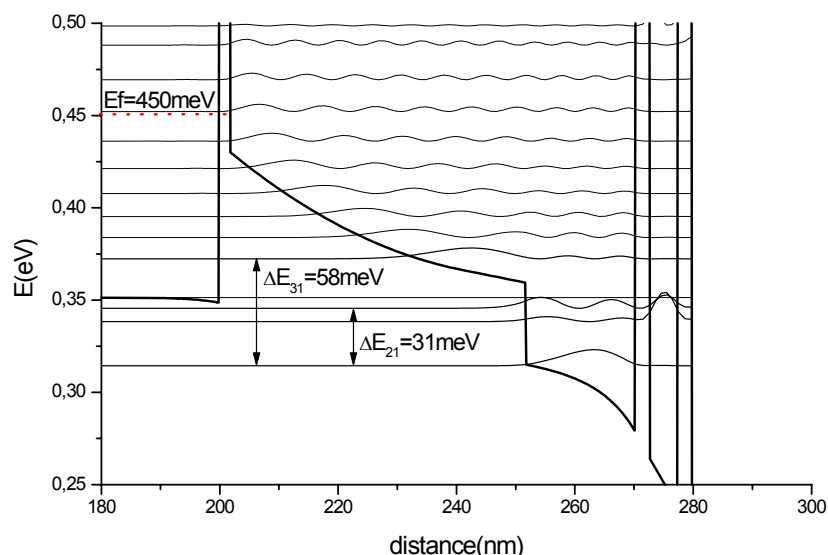


Fig. 1: Conduction band of G595 including squared electronic wave functions for $V = 450\text{mV}$ bias enabling resonant tunneling out of the middle level of the pre well.

Figure 2 shows the differential conductivity versus the bias voltage. At low bias voltages up to $V = 400\text{mV}$ (ΔV_1) one finds low differential conductivity with pronounced oscillations. These oscillations indicate the quantization of the parabolic injection region. At higher voltages (ΔV_2) the differential conductivity raises. This indicates the locking between the second level of the active region and the RTD level.

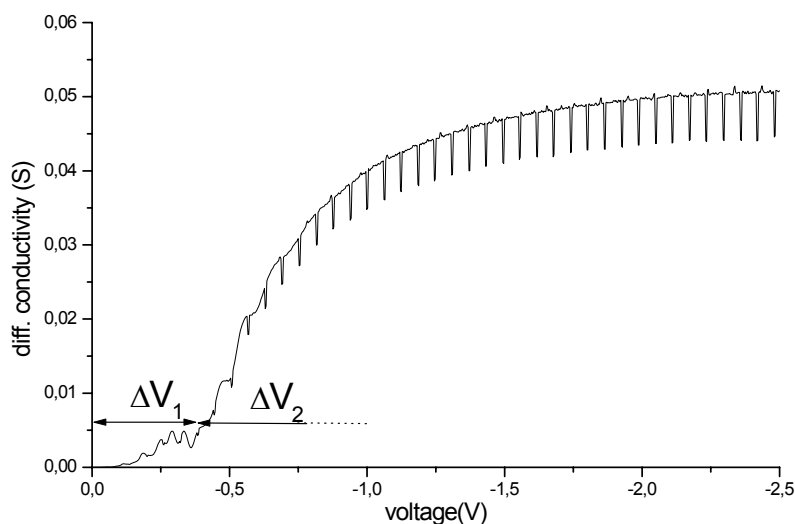


Fig. 2: Differential conductivity vs. bias voltage of G595 (periodic breakdown is from digitized measurement).

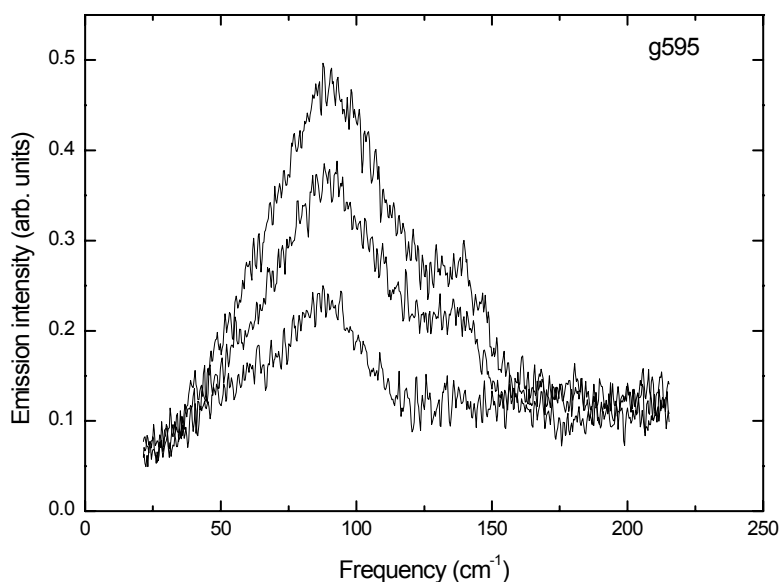


Fig. 3: Emission of g595 under normal operating bias direction.

The emission spectra of g595 were recorded by the InSb setup. Figure 3 shows the emission obtained when the electrons enter the structure through the single barrier on the left. The three curves (from bottom to top) represent biases and currents (-2.28 V , -0.132 A), (-2.48 V , -0.160 A), (-2.94 V , -0.237 A), respectively. The emission in-

creases with the magnitude of the current. The approximate total area of the emission strips is $4 \times 10^{-3} \text{ cm}^2$. There are two noteworthy features. There is a strong peak at 90 cm^{-1} (about 11 meV, or 2.75 THz), whose strength increases with current. There is also a second feature at 140 cm^{-1} , clearly visible in the upper two curves. Based on the transport model and response calculations we interpret the peak around 11 meV to be due to the oscillation frequency of the electrons in the parabolic section of our active region (the Kohn resonance). The second peak can be ascribed to an intersubband transition in the pocket region. The second feature has a half width of about 1.25 meV. This is much smaller than the line width of radiation from the earlier structure g301. That sample had internal doping in the active region, causing scattering and a resulting half width of 2.5 meV. A reduction of line width by eliminating internal doping therefore has clearly been demonstrated by Fig. 3. The instrumental broadening contributes about 0.5 meV to the line width. Thus, the collisional (including interface scattering) effects only amount to 0.75 meV in g595.

Achieving plasma instability growth of 1 meV, or more, should therefore suffice to have a positive net growth rate in such structures.

Electrostatic Discharge Effects in AlGaN/GaN High-Electron-Mobility Transistors

J. Kuzmík, D. Pogany and E. Gornik
Institute of Solid State Electronics, TU Vienna, Austria

P. Javorka and P. Kordoš
Institute of Thin Films and Interfaces, Research Centre Juelich, Germany

Devices may face electrostatic discharge events during manufacturing, handling, or device operation. Typical current pulses are in the ampere range with durations between nanoseconds and microseconds. These transient conditions may facilitate high-current pulses before thermal runaway terminates device functionality. The importance of failure mechanism study in III-nitride transistors is given by their usage as power devices in many defense and commercial applications where harsh environment conditions are expected.

100 ns long rectangular current pulses using a transmission line pulser (TLP) were used for stressing of the HEMT drain contact. The pulsed I - V characteristics were extracted using a digital oscilloscope. We used backside interferometric mapping technique to localize current path (dissipated power) in HEMTs during the TLP stress. The mapping was performed using an infrared laser beam scanning the device from the backside (3 ns time, 1.5 μm space resolution).

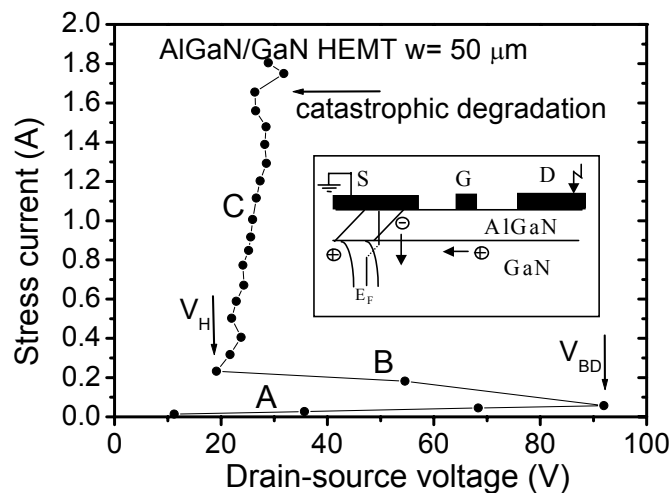


Fig. 1: Typical drain-source high current pulsed I - V curve of AlGaN/GaN HEMT. The inset illustrates the band diagram and assumed process of the hole accumulation and electron injection into the GaN buffer; after [1].

The measured drain-source high-current pulsed I - V characteristics exhibit S-shape with three regions [1] (see Fig. 1): A low-current/ high-impedance region A, a NDC region B, and a high-current/ low-voltage region C. The triggering voltage V_{BD} of the source-drain breakdown is 62 – 98 V for all measured devices and the holding voltage $V_H \sim 20$ V. When a critical current stress level of 1.65 A is reached, the device catastrophically

degrades (see arrow in Fig. 1). The device's DC transfer characteristics taken prior and after current stresses (below the catastrophic degradation level) are presented in Fig. 2. The pulsed operation of the HEMT in regions B and C causes a shift of the threshold voltage upwards, from the nominal value of $V_T = -0.9$ V to the value of $V_T \sim -0.4$ V (Fig. 2). Simultaneously the value of the Schottky contact built-in voltage was found to be unchanged. These together with the fact that the V_T shift has been observed to be reversible let us assume that the electron trapping at the buffer side of the buffer-channel interface occurs after the HEMT is triggered.

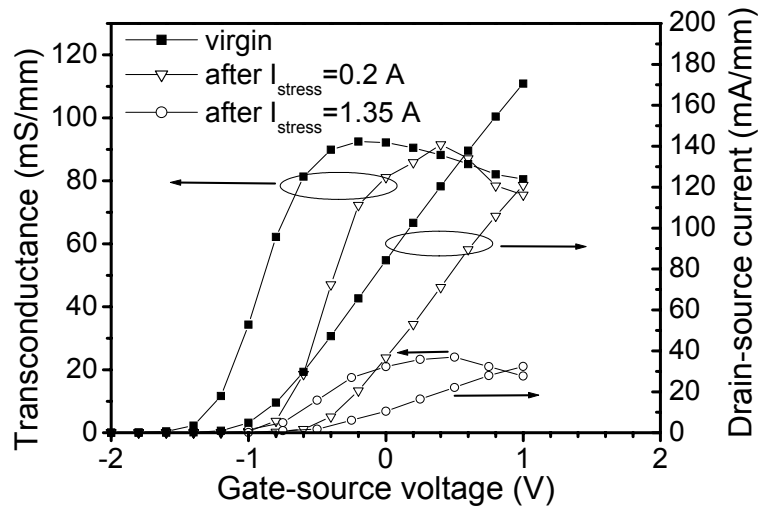


Fig. 2: Transconductance and drain current transfer characteristics of AlGaIn/GaN HEMT (at drain voltage 8 V) before and after selected stress pulses; after [1].

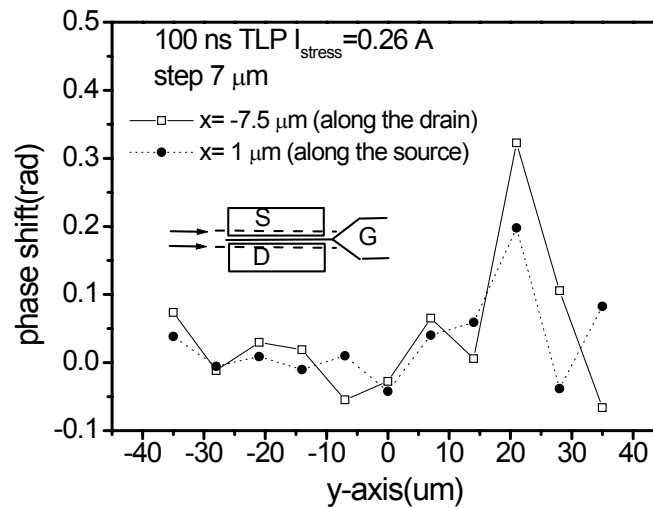


Fig. 3: Measured distribution of phase shift at $t = 100$ ns in AlGaIn/GaN HEMT along the source and drain at $I_{stress} = 0.26$ A. The HEMT active region spans from $y = -25$ to $y = 25$ μm ; after [1].

Figure 3 shows the phase shift (i.e. drain current) distribution as a function of position along the device width. The device was scanned along the drain and source contacts with steps of 7 μm at $I_{stress} = 0.26$ A (region C). A phase peak is found at the right edge

of the HEMT channel, indicating the current filamentation. This shows that the transition into the low-voltage/high-current region is followed by the current filament formation. Such a behavior is typical for current-controlled systems with NDC.

If we accept theoretical model of GaAs FETs [2] our observation of NDC and filamentation in the AlGaN/GaN HEMT may be linked to the avalanche-injection processes in the buffer layer (see inset of Fig. 1). The measured V_T shift, explained by the electron trapping in the buffer, supports this model. The decisive role of the buffer layer in the breakdown mechanism was also predicted by the theoretical model [2] showing that no NDC can be expected if the buffer layer is omitted. However, III-nitrides represent an unconventional material system, and other physical mechanisms cannot be ruled out completely.

References

- [1] J. Kuzmík, D. Pogany, E. Gornik, P. Javorka, P. Kordoš, *Applied Physics Letters*, **83**, 4655 (2003).
- [2] V. A. Vashchenko, N. A. Kozlov, Y. B. Martynov, V. F. Sinkevitch, and A. S. Tager, *IEEE Transaction on Electron Devices* **43**, 513 (1996).

Development of a Silicon Deep Reactive Ion Etching Process for the Fabrication of Large Area Silicon Phase Gratings

M. Trinker

Atominstitut der Österreichischen Universitäten, Technische Universität
Wien, Stadionallee 2, 1020 Vienna, Austria

We report on the development of a reactive ion etching (RIE) process using the new inductively coupled plasma reactive ion etcher Plasmalab 100, which was installed at the cleanroom area of the Microstructure Center recently. Periodic structures with aspect ratios up to 15 and periods from 12 μm to 28 μm were produced. The patterned areas in these samples were 22 x 22 mm^2 .

Using the black silicon method (BSM) described in [1] we developed a process with etch rates of approximately 1 $\mu\text{m}/\text{min}$ and good profile control for aspect ratios up to 15. Photoresist Shipley 5214 was chosen as mask material with a layer thickness of 1 – 1.5 μm . To go beyond aspect ratios of 15, SiO_2 would have to be used, since thicker layers of photoresist tend to crack under cryogenic conditions (-110°C in this process). On the other hand, layers thinner than 1 μm showed premature erosion in this process [2].

The design of our samples made it necessary to use carrier wafers. It turned out that GaAs wafers influenced the etching process, so Si wafers were used instead. Sufficient thermal contact between sample and carrier was ensured by bonding with photoresist.

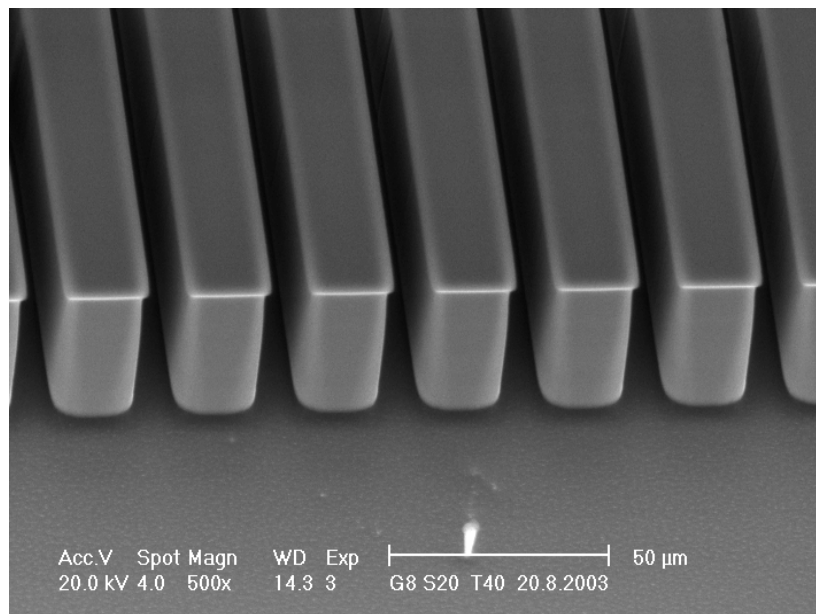


Fig. 1: trench 8 μm , ridge 20 μm , depth 40 μm

Figure 1 shows one of the regular structures with a trench width of 8 μm and a period of 28 μm . Note the excellent trench profile. Figure 2 shows one of the high aspect ratio samples. The smallest feature in this sample is 4 μm , giving an aspect ratio of 10.

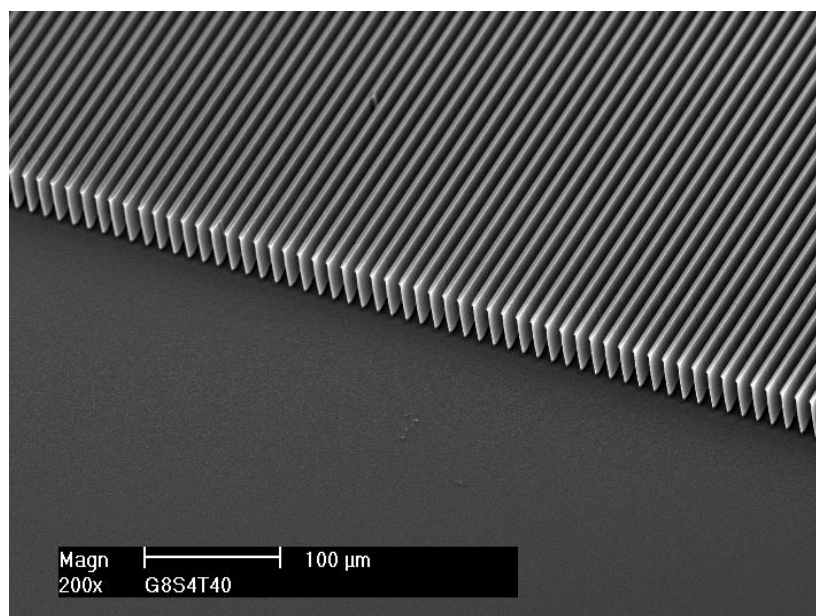


Fig. 2: trench 8 μm , ridge 4 μm , depth 40 μm

These samples will provide unique test procedures in neutron scattering. For details, see [3].

References

- [1] H. Jansen, M. de Boer, H. Wensink, B. Kloeck, M. Elwenspoek, *Microelectronics Journal* 32 (2001) 769
- [2] M.J. Walker, Oxford Instruments Plasma Technology, "Comparison of Bosch and cryogenic processes for patterning high aspect ratio features in silicon", 2001
- [3] E. Jericha, M. Baron, M. Hainbuchner, R. Loidl, M. Villa, H. Rauch, *J. Appl. Cryst.* 36 (2003) 778

Microelectronics Technology — Cleanroom Linz

Micro- and Nanostructure Research: Cleanroom Linz

G. Bauer, H. Heinrich and G. Brunthaler
Institut für Halbleiter- und Festkörperphysik
Johannes Kepler Universität Linz, A-4040 Linz, Austria

The micro- and nanostructure research in the cleanrooms of the "Institut für Halbleiter- und Festkörperphysik" is supported by the Society for Microelectronics (GMe). In 2003, emphasis was put on the research and development of optoelectronics, nanostructures and devices for spintronics. For optoelectronics, Si/SiGe cascade injectors for voltage tunable two-band detection, lead salt structures with continuous-wave photoluminescence and Erbium doped SOI waveguides for the mid-infrared were developed. Further a CD lab was founded which is dedicated to the simulation and fabrication of photonic crystals for various optical applications. Nanostructures were produced by the top-down approach with electron beam lithography in Si and AlGaAs structures and by the bottom-up approach of self organized growth inside PbSe superlattices. The morphology of the structures was investigated by numerous techniques like transmission electron microscopy, x-ray diffraction of atomic force microscopy. The basic spin relaxation properties of Si-based materials were investigated as a prerequisite for spintronic applications.

The funding of the activities in the cleanrooms at the University of Linz which are jointly used by several groups is of vital importance for our micro- and nanostructure research activities. This basic funding allows for investigations which are made possible through additional funding coming from the FWF, the FFF, the Christian-Doppler society, the European Commission, as well as through cooperation with industrial groups as listed in the report.

The activities of the year 2003 in the cleanrooms in Linz are described in a short overview here. The basic equipment which is available in these clean rooms allows for MBE growth of SiGe, II-VI and IV-VI heterostructures, for the deposition of ferromagnetic layers like Fe on II-VI compounds, as well as GaN deposition by MOCVD with *in-situ* control. For deposition of dielectric layers like SiO₂ and TiO₂ for the visible and MgF and Si for the infrared spectral range a new deposition system from Leybold Optics was installed. Apart from *in-situ* and *ex-situ* structural characterization, lateral patterning is made possible through equipment like optical, holographic and electron beam lithography. In 2003 also a new "LEO Supra 35" electron beam lithography system was installed, which allows the preparation of lateral structures down to about 20 nm. Processing includes also facilities for the deposition on insulating as well as contact layers, in particular a plasma deposition system for silicon nitrides. A transmission electron microscope is intensively used for the characterization of thin SiGeC layers. Research and development of a new Christian-Doppler Laboratory on photonic crystals is also conducted in the same cleanrooms.

The emphasis of the research work in and around the cleanrooms was put mainly on optoelectronics, nanostructures and devices for spintronics as described in the following.

Optoelectronics

Optoelectronic devices are used today for communication, as light sources and for detectors. In the Si/SiGe cascade injectors a resonator enhanced, voltage tunable two-band detector was realized. This device not only allows the detection of mid-infrared radiation, but also the distinction between different wavelengths from (from 5.2 μm to 3.2 μm), in order to identify e.g. different air pollution gasses. The tunability of the photoresponse is a consequence of an electric field induced transfer of holes from the deepest to the shallowest quantum well of the injector sequence. Depending on the bias voltage, dark current limited peak detectivities in excess of $D^* = 1 \times 10^9 \text{ cmHz}^{0.5}\text{W}^{-1}$ were obtained at a temperature of 77 K.

Lead salt structures for continuous-wave photoluminescence are also suited for emission in the mid-infrared. The PbSe/PbEuSe and PbTe/PbEuTe multiquantum well structures as well as the PbSe and PbTe bulklike structures were excited by a semiconductor laser diode. All the samples were grown by molecular-beam epitaxy on BaF₂(111) substrates under the same growth conditions. Both for the Te-based systems and for the Se-based systems, it turns out that bulk-like structures show photoluminescence up to higher temperatures than multi-quantumwell structures. In particular, emission spectra from PbTe/PbEuTe multiquantum wells were obtained up to temperatures of 200 K and from PbSe/PbEuSe multiquantum well structures up to 60 °C whereas for bulklike PbSe photoluminescence at temperatures as high as 190 °C is demonstrated.

Among the various attempts to obtain light emission from Si, optical doping with rare earth elements like Er has been particularly fruitful at first glance as this approach is compatible with standard Si technology. Light emitting diodes emitting at a wavelength of 1.54 μm at room temperature have been fabricated. The low efficiency, however, and the slow response of such diodes limit their use to a few special applications. The main hope, namely application in optical communication systems, appears unrealistic unless laser action can be achieved. In order to come closer to that goal, the recently found increased solubility of Erbium in silicon in the presence of hydrogen was investigated by producing Erbium-doped waveguides in Silicon-on-insulator layers by photolithography. Applying the variable stripe length method a net gain of 32 cm^{-1} at 10 K was estimated.

In 2003 the Christian Doppler Laboratory for Surface Science Methods was established at the University Linz in cooperation with Photeon Technologies located in Bregenz, Austria. The main goal is to bridge the gap between basic research and applied research on the topic of photonic devices. Although it is planned that also prototypes of such devices are fabricated in the cleanroom, in the first year the main emphasis was laid on novel design schemes and on establishing process steps as e-beam or UV lithography, etching, RIE etching, mask preparation and characterization methods like AFM etc.

Nanostructures and Characterization

Nanostructures are the natural consequence of the ongoing miniaturization in microelectronics. As the devices become increasingly smaller, new effects like quantum effects appear. The investigation and understanding of such quantization effects is important in order to continue the functionality of devices but also to use them for completely new types.

Lateral quantum dots have been fabricated on strained Si/SiGe substrates with a mobility of about 200,000 cm^2/Vs using a split gates geometry, where the gates consist of Pd. The gate structures were realized by e-beam lithography. By applying negative voltages to the gates the underlying 2DEG can be depleted. Similar samples showed

fractional quantum Hall effect up to filling factors of $1/3$. The e-beam lithography was performed with a JEOL 6400. In the 4th quarter of 2003, a LEO Supra 35 FESEM (field emission scanning electron microscope) with a Schottky field emitter (SFE) has been purchased and the fabrication of quantum dots will be continued with the new equipment.

Lateral quantum dots were also fabricated from two-dimensional GaAs/AlGaAs heterostructures by electron beam lithography. In a new design, the split gate geometry, which defines the dot electrostatically by metal gates, has been modified. The devices were electrically characterized in a ^3He cryostat at 300 mK. Due to improvements in device design and measurement conditions, the number of electrons in the dot can now be controlled over a wider range. Additionally, reproducible conductance fluctuations overlaid on the Coulomb oscillations were observed and will be investigated in more detail.

Anomalous x-ray diffraction is used to investigate self-organized three dimensional PbSe quantum dot lattices formed by multilayer heteroepitaxial growth. Using a short-range dot ordering model in combination with a finite domain size, the ordering parameters are determined from the x-ray spectra. It is shown that the variance of the nearest-neighbor distances is significantly smaller and the laterally ordered domain size larger for the case of three dimensional trigonal PbSe dot lattices with *fcc*-stacking as compared to those with three dimensional hexagonal dot arrangement.

Transmission electron microscopy (TEM) is a powerful tool for detailed analysis of both crystalline and amorphous structures ranging from the micro to the nanometer scale. TEM is capable to display not only the real but also the reciprocal space of a sample; i.e. the diffraction pattern. The analytical capabilities of the JEOL FastEM 2011 with CCD-camera and EDS X-ray detector were used to investigate e.g. the element specific composition of a hetero-bipolar-transistor, to determine the dislocation density at a Si-Ge interface, for the investigation of facets on a prestructured and annealed Si surface, the analysis of size and shape of SiC precipitations, and the alignment of self-arranged Ge dots.

The combination of lithography and self-assembly techniques results in long-range two-dimensionally ordered Ge islands. Island lattices with perpendicular but also with obliquely oriented unit vectors were realized. Quantitative analysis of the island topographies demonstrates that the size dispersion of these islands is much smaller than that found on flat substrates. Furthermore, island formation on the patterned substrates is observed already for a smaller amount of Ge deposition than on unpatterned ones.

Strain relaxation of heteroepitaxial PbTe layers on PbSe (001) by misfit dislocation formation is shown to take place near equilibrium without kinetic barriers. The comparison of the experimental data with different strain relaxation models shows that mutual dislocation interactions are of crucial importance for the strain relaxation process. This results in a faster relaxation than predicted by the Frank and van der Merwe model for non-interacting dislocation arrays.

X-ray diffraction is used for the *in situ* characterization of the growth of cubic GaN by metalorganic chemical vapor deposition. The installed setup permits the simultaneous measurement of a wide angular range and requires neither goniometer nor exact sample positioning. Time-resolved measurements during growth give access to film thickness and growth rate as well as information on the chemical composition of ternary compounds. Additionally, the relaxation of the crystal lattice during heteroepitaxial growth of GaN on AlGaN can be measured directly.

Spintronics

The SiGe material system is a promising candidate for solid-state spintronics application due to its very long relaxation lifetimes and compatibility to standard Si device processing technology. In contrast to predictions of the classical model of D'yakonov-Perel, a strong anisotropy of spin relaxation and a decrease of the spin relaxation rate with increasing electron mobility were found. For high electron mobility, the cyclotron motion causes an additional modulation of spin-orbit coupling leading to an effective suppression of the spin relaxation rate.

The possibilities of g-factor tuning of conduction electrons in SiGe heterostructures as proposed for spin transistors were investigated. The g-factor dependence on the Ge content in SiGe quantum wells was investigated, showing promising results. Devices for demonstrating a high enough shift of the electron g-factor to bring electrons in and out of resonance with an external microwave field — thus allowing spin manipulation — are being developed.

In order to understand the electron-electron interaction in Si-based structures, also the metal-insulator phase transition was investigated. In silicon-on-insulator metal oxide semiconductor structures with a peak mobility of 25,000 cm²/Vs a strong drop of the resistivity towards low temperature has been observed. This metallic effect can be explained by a linear-in-T term, which can be interpreted with both, the ballistic interaction corrections and the temperature dependent screening of impurity scattering.

Project Information for 2003

Project Manager

Gerhard Brunthaler

Institut für Halbleiter-und Festkörperphysik, Johannes Kepler Universität Linz, A-4040 Linz, Austria

Project Group

Last Name	First Name	Status	Remarks
Bauer	Günther	University professor	
Heinrich	Helmuth	University professor	
Jantsch	Wolfgang	University professor	
Schäffler	Friedrich	University professor	
Thim	Hartwig	University professor	
Brunthaler	Gerhard	Associate professor	
Diskus	Christian	Associate professor	
Heiss	Wolfgang	Assistant professor	
Palmethofer	Leopold	Associate professor	
Springholz	Gunther	Associate professor	
Sitter	Helmut	Associate professor	
Bonanni	Alberta	Assistant professor	
Fromherz	Thomas	Assistant professor	
Kolmhofer	Erich	Assistant professor	
Lübke	Kurt	Assistant professor	retired Nov. 2003
Stangl	Julian	Assistant professor	
Andreev	Andrej	Assistant professor	
Kocher	Gudrun	Assistant professor	Partly FWF
Binder	Fritz	Technician	
Bräuer	Stephan	Technician	
Fuchs	Othmar	Technician	
Jägermüller	Josef	Technician	
Katzenmayer	Hans	Technician	
Nusko	Ekkehard	Electronics Engineer	
Vorhauer	Ernst	Electronics engineer	
Andreeva	Svetlana	Lab Technician	FWF-START
Halilovic	Alma	Lab Technician	½ paid by GME
Haslgrübler	Klaus	Lab Technician	½ paid by GME
Kainz	Ursula	Lab Technician	½ position
Firmberger	Johanna	Apprentice	

Last Name	First Name	Status	Remarks
Hingerl	Kurt	Guest researcher	Austrian Academy of Sciences + Company Profactor, until June 30
Stifter	David	Guest researcher	Company Profactor
Meduna	Mojmir	Guest Researcher	EC (SigeNET)
Andreev	Andrej	Post Doc	FWF
Zhong	Zhenyang	Post Doc	Finished 2003
Chen	Gang	Post Doc	FWF
Prinz	Adrian	Post Doc	OeNB/FWF
Roch	Thomas	Post Doc	
Abtin	Laurel	Ph.D. student	FWF
Achleitner	Joachim	Ph.D. student	
Berer	Thomas	Ph.D. student	FWF, Uni Linz
Böberl	Michaela	Ph.D. student	FWF-START
Gruber	Daniel	Ph.D. student	FWF, Uni Start
Hesse	Anke	Ph.D. student	EC, Brussels
Kaufmann	Erich	Ph.D. student	FWF-START
Lechner	Rainer	Ph.D. student	FWF
Lichtenberger	Herbert	Ph.D. student	FWF
Lugovyy	Dmytro	Ph.D. student	FWF
Malissa	Hans	Ph.D. student	FWF, WIMAUS
Montaigne-R.	Alberto	Ph.D. student	Eu-Project ISCE-MOCVD
Mühlberger	Michael	Ph.D. student	Finished Aug 2003
Novak	Jri	Ph.D. student	FWF, finished
Pillwein	Georg	Ph.D. student	FWF
Raab	Anneliese	Ph.D. student	FWF, finished 2003
Rehman-Khan	Aaliya	Ph.D. student	ÖAD
Roither	Jörgen	Ph.D. student	FWF
Schüllli	Tobias	Ph.D. student	EC, Brussels, finished 03
Schmidegg	Klaus	Ph.D. student	EU-Projekt ISCE-MOCVD
Schwarzl	Thomas	Ph.D. student	FWF
Söllinger	Walter	Ph.D. student	FWF
Wiesauer	Karin	Ph.D. student	FWF, finished 2003
Griesser	Stefan	Diploma student	finished 2003
Grydlik	Martyna	Diploma student	stipendat
Janecek	Stefan	Diploma student	
Hörmann	Thomas	Diploma student	
Kirchschlager	Raimund	Diploma student	
Lindner	Benjamin	Diploma student	
Pachinger	Dietmar	Diploma student	finished 2003
Rauter	Patrick	Diploma student	finished 2003
Roither	Jürgen	Diploma student	finished 2003
Söllinger	Walter	Diploma student	finished 2003

Last Name	First Name	Status	Remarks
Schwinger	Wolfgang	Diploma student	finished 2003
Simma	Matthias	Diploma student	
Wintersberger	Eugen	Diploma student	

Publications in Reviewed Journals

published 2003

1. M. Böberl, W. Heiss, T. Schwarzl, K. Wiesauer, G. Springholz, "Mid-infrared continuous-wave photoluminescence of lead salt structures up to temperatures of 190°C", Appl. Phys. Lett. **82**, 4065-4067 (2003).
2. G. Brunthaler, A. Prinz, and G. Bauer, "The role of quantum interference for the metallic state in high-mobility Silicon inversion layers" in "Physics of Semiconductors 2002", Proceedings of the 26th Int. Conf. on the Physics of Semiconductors, Eds. A.R. Long and J.H. Davies, Institut of physics, conference series No. 171, p. 161, Bristol (2003).
3. L. Diehl, S. Mentese, E. Müller, D. Grützmacher, H. Sigg, T. Fromherz, J. Faist, U. Gennser, Y. Campidelli, O. Kermarrec and D. Bensahel, "Strain compensated Si/SiGe quantum well and quantum cascade on Si_{0.5}Ge_{0.5} pseudosubstrates", Physica E **16**, 315-320 (2003).
4. T. Fromherz, G. Bauer, "Light from silicon: SiGe quantum cascade structures", GMe annual report 2002, ISBN 3-901578-11-0 (2003).
5. G. Grabecki, J. Wrobel, T. Dietl, E. Papis, E. Kaminska, A. Piotrowska, A. Ratuszna, G. Springholz, G. Bauer, "Ballistic transport in PbTe-based nanostructures", Physica E **20**, 236 - 245 (2004).
6. A. Hesse, J. Stangl, V. Holy, G. Bauer, U. Denker, O.G. Schmidt, "Strained silicon above and below Ge islands", GMe annual report 2002, ISBN 3-901578-11-0 (2003).
7. A. Hesse, J. Stangl, V. Holy, G. Bauer, O. Kirfel, E. Müller, D. Grützmacher, "Influence of capping on strain, composition and shape of SiGe islands", Mat. Sci. Eng. B **101**, 71-76 (2003).
8. S. Janecek, P. Granitzer, H. Krenn, "Influence of dipolar coupling on the magnetic phase diagram of few (111)-monolayer EuTe", Journal of Superconductivity Including Novel Magnetism **16/1**, 87 (2003).
9. H. Kepa, G. Springholz, T.M. Giebultowicz, K.I. Goldman, C.F. Majkrzak, P. Kacman, J. Blinowski, S. Holl, H. Krenn, G. Bauer, "Magnetic interactions in EuTe epitaxial layers and EuTe/PbTe superlattices", Phys. Rev. B **68**, 024419-1/16 (2003).
10. R.T. Lechner, T. Schüllli, V. Holy, G. Springholz, J. Stangl, A. Raab, T.H. Metzger, G. Bauer, "Ordering parameters of self-organized 3D quantum dot lattices determined by anomalous x-ray diffraction", Appl. Phys. Lett. **84**, 885-888 (2004).
11. R.T. Lechner, T. Schüllli, V. Holy, J. Stangl, A. Raab, G. Springholz, G. Bauer, "3D hexagonal versus trigonal ordering in self-organized PbSe quantum dot superlattices", Physica E **21**, 611-614 (2004).

12. H. Lichtenberger, M. Mühlberger, C. Schelling, F. Schäffler, "Transient-enhanced surface diffusion on natural-oxide-covered Si(001) templates during vacuum annealing", GMe annual report 2002, ISBN 3-901578-11-0 (2003).
13. H. Lichtenberger, M. Mühlberger, F. Schäffler, "Transient-enhanced surface diffusion on native-oxide-covered Si(001) nano-structures during vacuum annealing", Appl. Phys. Lett. **82**, 3650-3652 (2003).
14. G.J. Matt, N. S. Sariciftci, T. Fromherz, "Anomalous charge transport behavior of Fullerene based diodes", Appl. Phys. Lett. **84**, 1570-1572 (2004).
15. M. Mühlberger, H. Malissa, N. Sandersfeld, W. Jantsch, F. Schäffler, A. Tyryshkin, S. Lyon, "High-mobility strained Si for spintronics applications", GMe annual report 2002, ISBN 3-901578-11-0 (2003).
16. M. Mühlberger, C. Schelling, G. Springholz, F. Schäffler, "Step-bunching in SiGe layers and superlattices on Si(001)", Surface Science **532-535**, 721-726 (2003).
17. M. Mühlberger, C. Schelling, G. Springholz, F. Schäffler, J. Myslivecek, B. Voigtländer, P. Šmilauer, J. Krug, "Growth instabilities in Si/SiGe homo- and heteroepitaxy", GMe annual report 2002, ISBN 3-901578-11-0 (2003).
18. J. Myslivecek, C. Schelling, F. Schäffler, G. Springholz, P. Šmilauer, J. Krug, B. Voigtländer, "Step bunching during Si(001) homoepitaxy caused by the surface diffusion anisotropy", Mat. Res. Soc. Symp. Proc. Vol. **749**, W1.8.1-W.1.8.6 (2003).
19. G. Pillwein, G. Brunthaler, G. Strasser, "Characterization of lateral quantum dots fabricated by e-beam lithography", GMe annual report 2002, ISBN 3-901578-11-0 (2003).
20. G. Pillwein, A. Prinz, G. Brunthaler, P. E. Lindelof, J. Ahopelto, "Screening behavior of the two-dimensional metallic state in silicon-on-insulator structures", in "Physics of Semiconductors 2002", Proceedings of the 26th Int. Conf. on the Physics of Semiconductors, Eds. A.R. Long and J.H. Davies, Institut of physics, conference series No. 171, CD No. D121, Bristol (2003).
21. V.M. Pudalov, M.E. Gershenson, H. Kojima, G. Brunthaler, A. Prinz, G. Bauer, "Interaction effects in conductivity of Si inversion layers at intermediate temperatures", Phys. Rev. Lett. **91**, 126403/1-4 (2003).
22. A. Raab, G. Springholz, "Intermixing and shape transitions of PbSe quantum dots during overgrowth", GMe annual report 2002, ISBN 3-901578-11-0 (2003).
23. A. Raab, G. Springholz, R.T. Lechner, "Growth temperature and coverage dependence of vertical and lateral ordering in self-assembled PbSe quantum-dot superlattices", Phys. Rev. B **67**, 165321-1/7 (2003).
24. P. Rauter, T. Fromherz, G. Bauer, L. Diehl, G. Dehlinger, H. Sigg, D. Grützmacher, H. Schneider, "Voltage-tunable, two-band mid-infrared detection based on Si/SiGe quantum-cascade injector structures", Appl. Phys. Lett. **83**, 3879 - 3881 (2003)
25. T.U. Schüllli, J. Stangl, Z. Zhong, R.T. Lechner, M. Sztucki, T.H. Metzger, G. Bauer, "Direct determination of strain and composition profiles in SiGe islands by anomalous x-ray diffraction at high momentum transfer", Phys. Rev. Lett. **90**, 066105-1/4 (2003)
26. G. Springholz, A. Raab, R.T. Lechner, V. Holy, "Dot size dependence of vertical and lateral ordering in self-organized PbSe/Pb_{1-x}Eu_xTe quantum dot superlattices", Appl. Phys. Lett. **82**, 799-801 (2003).
27. K. Wiesauer, G. Springholz, "Near-equilibrium strain relaxation and misfit dislocation interactions in PbTe on PbSe(001) heteroepitaxy", Appl. Phys. Lett. **83**, 5160-5162 (2003).

28. Z. Zhong, G. Chen, J. Stangl, Th. Fromherz, F. Schäffler, G. Bauer, "Two-dimensional lateral ordering of self-assembled Ge islands on patterned substrates", *Physica E* **21**, 588-591 (2004).
29. Z. Zhong, A. Halilovic, T. Fromherz, F. Schäffler, G. Bauer, "Two-dimensional periodic positioning of self-assembled Ge islands on prepatterned Si(001) substrates", *Appl. Phys. Lett.* **82**, 4779-4781 (2003).
30. Z. Zhong, A. Halilovic, M. Mühlberger, H. Lichtenberger, F. Schäffler, G. Bauer, "Laterally ordered Ge islands on pre-patterned Si(001) substrates", GMe annual report 2002, ISBN 3-901578-11-0 (2003).
31. Z. Zhong, A. Halilovic, M. Mühlberger, F. Schäffler, G. Bauer, "Ge island formation on stripe-patterned Si (001) substrates", *Appl. Phys. Lett.* **82**, 445-447 (2003).
32. Z. Zhong, A. Halilovic, M. Mühlberger, F. Schäffler, G. Bauer, "Positioning of self-assembled Ge islands on stripe-patterned Si (001) substrates", *J. Appl. Phys.* **93**, 6258-6264 (2003).
33. Z. Zhong, J. Stangl, F. Schäffler, G. Bauer, "Evolution of shape, height, and in-plane lattice constant of Ge-rich islands during capping with Si", *Appl. Phys. Lett.* **83**, 3695-3697 (2003).
34. A. Bonanni, D. Stifter, A. Montaigne-Ramil, K. Schmidegg, K. Hingerl, H. Sitter, "In situ spectroscopic ellipsometry of MOCVD-grown GaN compounds for on-line composition determination and growth control", *J. Cryst. Growth* **249**, 211-215 (2003).
35. A. Bonanni, K. Schmidegg, A. Montaigne-Ramil, H. Sitter, K. Hingerl, D. Stifter, "Virtual interface approximation model applied to spectroscopic ellipsometry for on-line composition determination of metal-organic chemical vapor deposition grown ternary nitrides", *J. Vac. Sci. Technol.* B21(4), 1825 (2003).
36. A. Kozanecki, V. Glukhanyuk, W. Jantsch, "High resolution spectroscopy of Er³⁺ ions in 6H SiC", *Mat. Sci. Eng. B105*, 169-174 (2003)
37. A. Kozanecki, V. Glukhanyuk, W. Jantsch, and B.J. Sealy, (invited), "Implantation Erbium Doping In 6H SiC For Optimum Optical Efficiency at 1.54 μm", *Proc. CAARI 2002 Denton*.
38. D. Kuritsyn, A. Kozanecki, H. Przybylinska, W. Jantsch, "Defect mediated and resonant optical excitation of Er³⁺ ions in silicon-rich silicon oxide", *MRS Symp. Proc.* **770**, 107 (2003).
39. D. Kuritsyn, A. Kozanecki, H. Przybylinska, W. Jantsch, "Defect mediated and resonant optical excitation of Er³⁺ ions in silicon-rich silicon oxide", *Appl. Phys. Lett.* **83**, 4160 (2003)
40. G. Kocher-Oberlehner, W. Jantsch, A. Ulyashin, L. Palmetshofer, "Hydrogen enhanced luminescence of Erbium doped Silicon", *Inst. of Phys. Conference Series Number 171*, A. R. Long and J H Davies (eds.), Publ.: Inst. of Phys. Publ.(Bristol UK and Philadelphia USA), ISBN-7503-0924-5 (2003).
41. G. Kocher-Oberlehner, W. Jantsch, L. Palmetshofer, A. Ulyashin, "On the Influence of Hydrogen on the Erbium-Related Luminescence in Silicon", *Appl. Phys. Lett.* **83**, 623-625 (2003).
42. G. Kocher-Oberlehner, W. Jantsch, L. Palmetshofer, A. Ulyashin, "Luminescence Enhancement by Hydrogenation of Si:Er,O", *Physica E* **16**, 347-350 (2003).
43. H. Sitter, A. Andreev, G. Matt, N.S. Sariciftci, "Hot wall epitaxial growth of highly ordered organic epilayers", *Synthetic Metals*, **138** (2003), 9-13.

44. K. Hingerl, L. Mao, V. Rinnerbauer, J. Schermer, V. Holý, "*Reflection and Transmission of Finite 2D Photonic Crystals*", European Conference on Optical Communication, Ravenna, 2003.
45. K. Schmidegg, A. Bonanni, A. Montaigne Ramil, H. Sitter, "*In situ growth monitoring and on-line composition determination of MOCVD GaN by spectroscopic ellipsometry*", GMe annual report 2002, ISBN 3-901578-11-0 (2003).
46. L. D. Sun M. Hohage P. Zeppenfeld, R. E. Balderas-Navarro and K. Hingerl, "*Enhanced Optical Sensitivity to Adsorption due to Depolarization of Anisotropic Surface States*", Phys. Rev. Lett. 90, (2003), 106104
47. L. D. Sun, M. Hohage, P. Zeppenfeld, R. Balderas- Navarro and K. Hingerl, "*Surface induced d-band anisotropy on Cu (110)*", Surf. Sci. Lett. 527, L184, (2003)
48. M. Böberl, W. Heiss, T. Schwarzl, K. Wiesauer, G. Springholz, "*Midinfrared continuous-wave photoluminescence of lead-salt structures up to temperatures of 190 °C*", Appl. Phys. Lett.82, 4065 (2003).
49. W. Heiss, M. Böberl, T. Schwarzl, G. Springholz, J. Fürst, H. Pascher, "*Applications of lead-salt microcavities for mid-infrared devices*", IEE-Proc.- Optoelectronics 150, 332 (2003).
50. Z. Wilamowski, W. Jantsch, N. Sandersfeld, M. Mühlberger, F. Schäffler, S. Lyon, "*Spin relaxation and g-factor of two-dimensional electrons in Si/SiGe quantum wells*", Physica E 16, 111-120 (2003).

Submitted 2003 / in print

1. G. Brunthaler, B. Lindner, G. Pillwein, S. Griesser, M. Prunnila, J. Ahopelto, "*Two-Dimensional Metallic State in Silicon-on-Insulator Structures*", Physica E, in print (2004).
2. W. Heiss, M. Böberl, T. Schwarzl, G. Springholz, J. Fürst, H. Pascher, "*Applications of lead-salt microcavities for mid-infrared devices*", in Proc. IEEE- Optoelectronics, in print.
3. W. Heiss, R. Kirchschrager, G. Springholz, Z. Chen, M. Debnath, Y. Oka, "*Magnetic polaron induced near-bandgap luminescence in epitaxial EuTe*", Phys. Rev. B, submitted.
4. R. Kirchschrager, W. Heiss, R.T. Lechner, G. Springholz, "*Energy band gap hysteresis loops in metamagnetic EuSe epilayers with effective g-factors up to 18000*", Appl. Phys. Lett., submitted.
5. R.T. Lechner, T.U. Schüllli, A. Wildes, R. Cubitt, D. Lott, A. Schreyer, G. Springholz, G. Bauer, "*Magnetic properties of metamagnetic EuSe grown by molecular beam epitaxy*", ILL Annual Report, in print.
6. M. Meduna, J. Novak, G. Bauer, V. Holy, C.V. Falub, E. Müller, D. Grützmacher, Y. Campidelli, O. Kermarrec, D. Bensahel, "*Annealing studies of high Ge composition Si/SiGe multilayers*", Z. Kristallogr. **219**, in print.
7. T.U. Schüllli, M. Sztucki, T.H. Metzger, R.T. Lechner, J. Stangl, G. Springholz, G. Bauer, "*Strain determination by complementary anomalous x-ray diffraction*", Phys. Rev. B, in print.
8. T.U. Schüllli, R.T. Lechner, J. Stangl, G. Springholz, G. Bauer, S. Dhesi, P. Bencok, "*Soft x-ray magnetic scattering from ordered EuSe nanoislands*", Appl. Phys. Lett., in print.

9. J. Stangl, V. Holý, G. Bauer, "Structural properties of self-organized semiconductor nanostructures", Rev. Mod. Phys., in print.
10. A.M. Tyryshkin, S.A. Lyon, W. Jantsch, F. Schäffler, "Spin Manipulation of Free 2-Dimensional Electrons in Si/SiGe Quantum Wells", Phys. Rev. Lett., submitted.
11. K. Wiesauer, G. Springholz, "Critical thickness and strain relaxation in high misfit heteroepitaxial systems: results for $PbTe_{1-x}Se_x$ on PbSe (001)", Phys. Rev. B, in print.
12. Z. Zhong, A. Halilovic, H. Lichtenberger, F. Schäffler, G. Bauer, "Growth of Ge islands on prepatterned Si(001) substrates", Physica E (Proceedings ESPS-NIS Conference, Stuttgart 2003), submitted.
13. A.M. Tyryshkin, S.A. Lyon, W. Jantsch, F. Schäffler, "Spin Manipulation of free 2-dimensional electrons in Si/SiGe quantum wells", cond-mat/0304284, submitted.
14. F. Quochi, F. Cordella, R. Orru, J. E. Communal, P. Verzeroli, A. Mura, G. Bongiovanni, A. Andreev, H. Sitter, N. S. Sariciftci, "Laser action in self-organized para-sexiphenyl single nanocrystals grown by Hot Wall Epitaxy", Appl. Phys. Lett., submitted.
15. H. Malissa, W. Jantsch, M. Mühlberger, F. Schäffler, Z. Wilamowski, M. Draxler, P. Bauer, "Anisotropy of g-factor and ESR linewidth in modulation doped SiGe quantum wells", Appl. Phys. Lett., submitted.
16. J. Fürst, H. Pascher, T. Schwarzl, M. Böberl, G. Springholz, G. Bauer, W. Heiss, "Continuous wave emission from a mid-infrared IV-VI vertical-cavity surface-emitting laser", Appl. Phys. Lett., in print.
17. J. Fürst, T. Schwarzl, M. Böberl, H. Pascher, G. Springholz, W. Heiss, "Continuous wave and pulsed emission from a vertical-cavity surface-emitting laser in the 8 mm mid-infrared spectral range", IEEE J. of Quantum Electronics, submitted.

Presentations

Invited Talks:

1. G. Bauer, "Nanotomography of Semiconductor Quantum Dots", European Vacuum Congress, Berlin, Germany, 23. - 26. June 2003.
2. J. Stangl, A. Hesse, T. Roch, V. Holy, G. Bauer, T. Schuelli, T.H. Metzger, "Structural investigation of semiconductor nanostructures by x-ray techniques", European Materials Research Society, Strasbourg, France, June 2003.
3. F. Schäffler, "Heteroepitaxial Growth Instabilities on Si(001) and their Modelling by Kinetic Growth Instabilities", 5th Workshop on MBE and VPE, e-MRS Fall Meeting, Warsaw 17. Sept. 2003.
4. G. Springholz, "Ordering and shape transitions in self-organized PbSe quantum dot superlattices", invited talk at the Fall Meeting of the Materials Research Society, Boston, USA, 28. Nov. - 2. Dec. 2003.
5. G. Springholz, "Size effects in self-organized ordering of PbSe/PbEuSe quantum dot superlattices", invited talk at the 5th International Conference on Epitaxial Semiconductors on Patterned Substrates and Novel Indexed Surfaces (ESPS-NIS), Stuttgart, Germany, 13.-16. Sept. 2003.
6. G. Springholz, "Self-Organized Vertical and Lateral Ordering in Quantum Dot Superlattices", invited talk at the Gordon Research Conference on Thin Film and Crystal Growth Mechanisms, Mount Holyoke, USA, 22.-27. June 2003.

7. J. Stangl, “*High resolution x-ray scattering from self-organized nanostructures*”, EMRS Fall Meeting, Warsaw, Poland, 15. Sept. 2003.
8. J. Stangl, “*Structural investigation of semiconductor Nanostructures by X-ray diffraction*”, ÖPG Jahrestagung, Salzburg, Austria, 01. Oct. 2003.
9. W. Heiss, M. Böberl, T. Schwarzl, J. Fürst, H. Pascher, K. Wiesauer, G. Springholz, “*IV-VI compound semiconductor VCSELs*”, The 11th International Conference on Narrow Gap Semiconductors, Buffalo, USA (June 16-20, 2003).

Seminar Talks:

1. F. Schäffler, “Transport and Spin Properties of 2DEGs in Strained Si”, Walter-Schottky-Institut der TU München, 01. July 2003
2. F. Schäffler, “*Kinetic and Strain-Induced Growth Instabilities*”, University of Milano-Bicocca, Milano, 17. July 2003
3. F. Schäffler, “*Transport and Spin Properties of 2DEGs in Strained Si*”, Politecnico di Milano-Como, Como, 18. July 2003
4. F. Schäffler, “*Quanten-Dot Bauelemente*”, Mikroelektronik-Tagung, Wien, 01. Oct. 2003
5. F. Schäffler, “*Silizium-basierende Heterostrukturen: von elementaren Materialeigenschaften zu Hochleistungsbauelementen*”, Universität Erlangen, 18. Nov. 2003
6. W. Heiss, M. Böberl, T. Schwarzl, G. Springholz, J. Fürst, H. Pascher, “*Funktionelle optische Mikroresonatoren*”, Physikerkolloquium an der Gesamthochschule in Paderborn, Germany (February 6th 2003).

Conference presentations (talks and posters):

1. M. Böberl, T. Schwarzl, W. Heiss, G. Springholz, Z. Wang, K. Reimann, M. Woerner, “*Two-color mid-infrared pump-probe studies of IV-VI microcavity lasers*”, poster at the 11th International Conference on Modulated Semiconductor Structures, Nara, Japan, 14. -18. Jul. 2003.
2. G. Brunthaler, B. Lindner, G. Pillwein, S. Griesser, M. Prunnila, J. Ahopelto, “*Two-Dimensional Metallic State in Silicon-on-Insulator Structures*”, poster at the 15th Int. Conf. on Electronic Properties of Two-Dimensional Systems, Nara, Japan, 14. - 18. July 2003.
3. T. Fromherz, G. Bauer, “*Light from Silicon: SiGe Quantum Cascade Structures*”, GME Forum 2003, Vienna, Austria, 10. – 11. April 2003.
4. T. Fromherz, P. Rauter, L. Diehl, G. Dehlinger, H. Sigg, D. Grützmacher, G. Bauer, “*Voltage-tuneable QWIPs Based on Si/SiGe Cascade Injector Structures for Two Colour Detection*”, 7th International Conference on Intersubbandtransitions in Quantum wells (ITQW7), Evolène, Switzerland, 1. – 5. Sept. 2003.
5. T. Fromherz, P. Rauter, L. Diehl, G. Dehlinger, H. Sigg, D. Grützmacher, G. Bauer, “*SiGe cascade injector structures for voltage-tuneable, two-colour detection in the 3-6 μ m spectral range*”, 11th International Conference on Modulated Semiconductor Structures (MSS11), Nara, Japan, 14. – 18. July 2003.
6. G. Grabecki, J. Wróbel, T. Dietl, E. Papis, E. Kamiska, A. Piotrowska, G. Springholz, G. Bauer, “*Transport in PbTe based nanostructures*”, invited talk at the

- 11th International Conference on Narrow Gap Semiconductors and Related Small Energy Phenomena, Physics and Applications, Buffalo, USA, 16. - 20. June 2003.
7. W. Heiss, T. Schwarzl, M. Böberl, M. Kaufmann, G. Springholz, M. Aigle, J. Fürst, H. Pascher, “*IV-VI Mid-Infrared Vertical Cavity Surface Emitting Lasers*”, invited talk at the 11th International Conference on Narrow Gap Semiconductors and Related Small Energy Phenomena, Physics and Applications, Buffalo, USA, 16. - 20. June 2003.
 8. S. Janecek, P. Granitzer, H. Krenn, “*Spin Patterns and Phase Diagrams of few (111)-monolayer EuTe including shape anisotropy*”, poster at the ICM 2003, Rome, Aug. 2003.
 9. R. Kirchschrager, W. Heiss, J. Achleitner, G. Springholz, Z. Chen, M. Debnath, and Y. Oka “*Large Stokes shift in magnetic EuTe epitaxial layers*”, poster at the 2th European Workshop on Molecular Beam Epitaxy, Bad Hofgastein, Austria, 16. - 19. Feb. 2003.
 10. R. Kirchschrager, W. Heiss, R.T. Lechner, G. Springholz, “*Peculiar photoluminescence transitions in Eu based magnetic superlattices*”, poster at the 11th International Conference on Modulated Semiconductor Structures, Nara, Japan, 14. -18. Jul. 2003.
 11. R. T. Lechner, A. Hallbauer, T. Schwarzl, and G. Springholz, “*Molecular beam epitaxy of PbSe_{1-x}Te_x for strain engineering in IV-VI semiconductor heterostructures*”, poster at the GME Forum 2003, TU-Wien, Austria, 10. - 11. Apr. 2003.
 12. R.T. Lechner, T. Schüllli, S. Dhési, J. Stangl, G. Springholz, G. Bauer, “*Soft x-ray magnetic scattering from a single EuSe quantum dot layer*”, International Conference on Narrow Gap Semiconductors, Buffalo, USA, 16. -19. June 2003.
 13. R.T. Lechner, T. Schüllli, V. Holy, J. Stangl, A. Raab, G. Springholz, G. Bauer, “*3D hexagonal versus trigonal ordering in self-organized PbSe quantum dot superlattices*”, Int. Conf. Modulated Semiconductor Structures 11, Nara, Japan, 14. - 18. July 2003.
 14. R.T. Lechner, T. Schüllli, V. Holy, J. Stangl, G. Springholz, G. Bauer, “*3D hexagonal versus trigonal ordering in self-organized PbSe quantum dot superlattices*”, poster at the 11th International Conference on Modulated Semiconductor Structures, Nara, Japan, 14. -18. Jul. 2003.
 15. R.T. Lechner, T.U. Schüllli, J. Stangl, G. Springholz, S. Dhési, P. Bencok and G. Bauer, “*Magnetic properties of self org,anized EuSe quantum dots*”, poster at the 11th International Conference on Modulated Semiconductor Structures, Nara, Japan, 14. -18. Jul. 2003.
 16. R. T. Lechner, G. Springholz, T. Schüllli, H. Krenn, G. Bauer, D. Lott, A. Schreyer, “*Molecular beam epitaxy, structural and magnetic properties of EuSe/PbSeTe and EuSe/EuTe superlattices*”, 12th European Workshop on Molecular Beam Epitaxy, Bad Hofgastein, Austria, 16. - 19. Feb. 2003.
 17. H. Lichtenberger, M. Mühlberger, C. Schelling, S. Senz, F. Schäffler “*Transient-enhanced Surface diffusion on Natural-Oxide-Covered Si(001) Templates during Vacuum Annealing*”, talk at the ICS13 2003, Santa Fe (NM), Mar. 2003.
 18. H. Lichtenberger, M. Mühlberger, C. Schelling, S. Senz, F. Schäffler “*Transient-enhanced Surface diffusion on Natural-Oxide-Covered Si(001) Templates during Vacuum Annealing*”, poster at the Euro-MBE 2003, Bad Hofgastein, Feb. 2003.

19. H. Lichtenberger, M. Mühlberger, C. Schelling, S. Senz, F. Schäffler “*Transient-enhanced Surface diffusion on Natural-Oxide-Covered Si(001) Templates during Vacuum Annealing*”, talk at the ESPS-NIS 2003, Stuttgart, Oct. 2003.
20. H. Lichtenberger, M. Mühlberger, C. Schelling, S. Senz, F. Schäffler “*Transient-enhanced Surface diffusion on Natural-Oxide-Covered Si(001) Templates during Vacuum Annealing*”, poster at the Gme-Forum 2003, Vienna, Apr. 2003.
21. M. Mühlberger, H. Malissa, N. Sandersfeld, W. Jantsch, F. Schäffler, A. Tyryshkin, S. Lyon “*High-Mobility Strained Si for Spintronics Applications*”, poster at the Gme-Forum 2003, Vienna, Apr. 2003.
22. M. Mühlberger, H. Malissa, N. Sandersfeld, W. Jantsch, F. Schäffler, A. Tyryshkin, S. Lyon “*Modulation-doped Si/SiGe quantum well for spintronics*”, talk at the Euro-MBE 2003, Bad Hofgastein, Feb. 2003.
23. M. Mühlberger, H. Malissa, N. Sandersfeld, W. Jantsch, F. Schäffler, A. Tyryshkin, S. Lyon “*Modulation-doped Si/SiGe quantum well for spintronics*”, talk at the ICSI3 2003, Santa Fe (NM), Mar. 2003.
24. M. Mühlberger, C. Schelling, G. Springholz, F. Schäffler, J. Myslivecek, B. Voigtländer, P. Smilauer, J. Krug “*Growth instabilities in Si/SiGe Homo- and Heteroepitaxy*”, poster at the Gme-Forum 2003, Vienna, Apr. 2003.
25. Z. Zhong, A. Halilovic, M. Mühlberger, H. Lichtenberger, F. Schäffler, G. Bauer “*Mask-free two-dimensional periodic positioning of self-assembled Ge islands on pre-patterned Si(001) substrates*”, talk at the ICSI3 2003, Santa Fe (NM), Mar. 2003.
26. A. Raab, G. Springholz “*Intermixing and shape transitions of PbSe quantum dot during overgrowth*”, poster at the 12th European Workshop on Molecular Beam Epitaxy, Bad Hofgastein, Austria, 16. - 19. Feb. 2003.
27. A. Raab, G. Springholz, “*Intermixing and shape transitions of PbSe quantum dot during overgrowth*”, poster at the GME Forum 2003, TU-Wien, Austria, 10. - 11. Apr. 2003.
28. T. Schwarzl, M. Böberl, J. Fürst, W. Heiss, H. Pascher, G. Springholz, “*Comparison of MBE grown IV-VI microcavity lasers for the mid-infrared with active regions of different dimensionality*”, poster at the 12th European Workshop on Molecular Beam Epitaxy, Bad Hofgastein, Austria, 16. - 19. Feb. 2003.
29. T. Schwarzl, M. Böberl, J. Fürst, W. Heiss, H. Pascher, G. Springholz “*Comparison of MBE grown IV-VI microcavity lasers for the mid-infrared with active regions of different dimensionality*”, poster at the GME Forum 2003, TU-Wien, Austria, 10. - 11. Apr. 2003.
30. A. Hallbauer, T. Schwarzl, R. T. Lechner and G. Springholz, “*Molecular beam epitaxy of PbSe_{1-x}Te_x for strain engineering in IV-VI semiconductor heterostructures*”, poster at the 12th European Workshop on Molecular Beam Epitaxy, Bad Hofgastein, Austria, 16. - 19. Feb. 2003.
31. K. Wiesauer and G. Springholz, “*Determination of the critical cluster size and diffusion length in PbTe (111) MBE*” talk at the 12th European Workshop on Molecular Beam Epitaxy, Bad Hofgastein, Austria, 16. - 19. Feb. 2003.
32. Z. Zhong, G. Chen, H. Lichtenberger, F. Schäffler, G. Bauer, “*Growth of Ge islands on prepatterned Si (001) substrates*”, 5th International Conference on Epitaxial Semiconductors on Patterned Substrates and Novel Indexed Surfaces (ESPS-NIS), Stuttgart, Germany, 13. - 16. Sept. 2003.

33. Z. Zhong, G. Chen, J. Stangl, Th. Fromherz, F. Schäffler, G. Bauer, “*Three-dimensional ordering of self-assembled Ge islands*”, Fall Meeting, Materials Research Society Boston, USA, 1. - 5. Dec. 2003.
34. Z. Zhong, G. Chen, J. Stangl, T. Fromherz, F. Schäffler, G. Bauer, “*Two dimensional lateral ordering of self-assembled Ge islands on patterned substrates*”, 11th International Conference on Modulated Semiconductor Structures (MSS11), Nara, Japan, 14. – 18. July 2003.
35. A. Andreev, H. Hoppe, H. Sitter, N.S. Sariciftci, R. Resel, D.-M. Smilgies “*Crystalline nano-wires of para-sexiphenyl grown by Hot Wall Epitaxy*”, poster at the Nanoscience & Technology Conference, Groningen, Netherlands (May 18-21 2003).
36. A. Andreev, H. Sitter, N. S. Sariciftci, A. Kadashchuk, C. Winder, R. Resel, D.-M. Smilgies “*Anisotropic Optoelectronic Properties of Self-Assembled Nano-Wires of Para-sexiphenyl Grown by Hot Wall Epitaxy*”, poster at the GME Forum 2003, Vienna, Austria (April 10-11 2003).
37. A. Andreev, H. Sitter, S. Sariciftci, R. Resel, D.-M. Smilgies “*Growth mechanism of well ordered organic nano-wires*”, talk at the 12th Euro-MBE Workshop, Bad Hofgastein, Austria (February 16-19, 2003).
38. A. Yu. Andreev, H. Sitter, C. Winder, H. Hoppe, S. Sariciftci, R. Resel, D.-M. Smilgies “*Highly ordered thin film structures based on para-sexiphenyl*”, poster at the E-MRS 2003 Spring Meeting, Strasbourg, France (June 10-17 2003).
39. A. Andreev, C. Teichert, G. Hlawacek, H. Hoppe, R. Resel, D.-M. Smilgies, H. Sitter, N. S. Sariciftci “*Anisotropic properties of self-assembled nano-wires of para-sexiphenyl grown by Hot Wall Epitaxy*”, poster at the Informationstagung Mikroelektronik 2003, Vienna, Austria (Oktober 1-2 2003).
40. M. Böberl, T. Schwarzl, W. Heiss, G. Springholz, Z. Wang, K. Reimann, M. Wörner, “*Femtosecond dynamics of lead-salt vertical-cavity surface-emitting mid-infrared lasers*”, Conference on Lasers and Electro-Optics/Europe (CLEO Europe 2003), Munich, Germany (June 22-27, 2003).
41. M. Böberl, T. Schwarzl, W. Heiss, G. Springholz, Z. Wang, K. Reimann, M. Wörner, “*Two-color mid-infrared pump-probe studies of IV-VI microcavity lasers*”, The 11th International Conference on Modulated Semiconductor Structures (MSS 11), Nara, Japan (July 14-18, 2003).
42. A. Hallbauer, T. Schwarzl, R. T. Lechner and G. Springholz, “*Molecular beam epitaxy of $PbSe_{1-x}Tex$ for strain engineering in IV-VI semiconductor heterostructures*”, 12th EURO-MBE Workshop, Bad Hofgastein, Austria (February 16-19, 2003).
43. T. Schwarzl, M. Böberl, J. Fürst, W. Heiss, H. Pascher, G. Springholz, “*Comparison of IV-VI microcavity lasers for the mid-infrared with active regions of different dimensionality*”, Conference on Lasers and Electro-Optics/Europe (CLEO Europe 2003), Munich, Germany (June 22-27, 2003).
44. T. Schwarzl, M. Böberl, J. Fürst, W. Heiss, H. Pascher, G. Springholz, “*Comparison of MBE grown IV-VI microcavity lasers for the mid-infrared with active regions of different dimensionality*”, 12th Euro-MBE Workshop, Bad Hofgastein, Austria (February 16-19, 2003).

Patent

1. J. Zarbakhsh, K. Hingerl, "Anordnung von dielektrischen Strukturen innerhalb eines Mediums", Pat. No. 17243.0-P832-54, filed by PHOTEON Technologies GmbH (2003).

Doctor's Theses

Finished in 2003:

1. Dipl. Phys. Tobias Schüllli
"Anomalous x-ray diffraction from semiconductor nanostructures"
2. Dipl. Ing. Karin Wiesauer
"Dislocation structures in epitaxial IV-VI semiconductor heterostructures"
3. Dipl. Ing. Anna Elisabeth Raab
"Investigation of PbSe quantum dot growth on single layers and in quantum dot superlattices"
4. Dipl. Ing. Michael Mühlberger
"Silicon-based heterostructures: growth, modulation-doping and spin properties"

Current works:

1. M.Sc. Laurel Abtin
"STM investigation on self-assembled IV-VI semiconductor nanostructures"
2. Dipl. Ing. Thomas Berer
"Electronic and spin properties of Si/SiGe heterostructures"
3. Dipl. Ing. Daniel Gruber
"Si/SiGe Heterostructure Devices for Spintronic Applications"
4. Dipl. Phys. Anke Hesse
"Strukturelle Untersuchungen an Halbleiternanostrukturen"
5. Mag. Rainer T. Lechner
"Herstellung und Charakterisierung von EuSe-Nanostrukturen"
6. Dipl. Ing. Herbert Lichtenberger
"Kinetic and strain-induced self-organization of SiGe heterostructures"
7. M.Sc. Dmytro Lugovyy
"Investigation of vertical and lateral ordering in self-organized PbSe quantum dot superlattices"
8. Mag. Jiri Novak
"Untersuchung der strukturellen Eigenschaften von Quantenpunkten"
9. Dipl. Ing. Georg Pillwein
"Elektrische Untersuchungen von Quanteneffekten an Nanostrukturen"
10. M.Sc. Aaliya Rehman Khan
"Growth and structural characterisation of Si/SiGe hetero- and nanostructures"

Diploma Theses

Finished in 2003:

1. Stefan Griesser
"Magnetowiderstandsmessungen des zweidimensionalen metallischen Zustandes in Silizium-Feldeffekttransistoren bei tiefen Temperaturen"
2. Wolfgang Schwinger
"Transmissionselektronenmikroskopie an Halbleiter-Nanostrukturen" (Lehramt Physik)
3. Wolfgang Schwinger
"Epitaxial Overgrowth of Fullerenes on Si (100)"
4. Dietmar Pachinger
"High Mobility Si/SiGe Heterostructures for Spintronic Applications"
5. Patrick Rauter
"Intraband Absorption and Photospectroscopy of SiGe Quantum Cascades"

Current works:

1. Martyna Grydlik
"Si/SiGe resonant cavity enhanced, tunable mid-infrared quantum well detectors."
2. Stefan Janecek
"Simulation of the magnetic order of few-monolayer-(111)-EuTe in oblique magnetic fields"
3. Mathias Simma
"Photoleitungsuntersuchungen an Quantenpunkten"
4. Benjamin Lindner
"Metall-Isolator-Übergang in zweidimensionalen Siliziumstrukturen"
5. Eugen Wintersberger
"Röntgenbeugung und -reflexion an Si/SiGe/GaAs Hetero- und Nanostrukturen"
6. Thomas Hörmann
"Modellrechnungen und Auswertungen zum Metall-Isolator-Übergang in zweidimensionalen Halbleiterstrukturen"

Cooperations

1. Academy of Sciences, Bratislava, Slovakia
2. Aixtron, Aachen, Deutschland
3. Akademie der Wissenschaften, Warschau, Polen
4. AMS Unterpremstätten, Österreich
5. Balzers (Unaxis), Trübach, Schweiz
6. Bosch (Stefan Holl), Linz
7. CENG Grenoble, France
8. CNRS-CRMC2-Marseille, France
9. Daimler Benz Reserach Laboratories, Dr. Presting, Dr. König, Ulm

10. DESY, Hasylab, Hamburg, Deutschland
11. E+E Electronic GmbH, Engerwitzdorf, Österreich
12. ELETTRA, Trieste, Italy
13. ESRF Grenoble, France
14. ETH, Zürich, Swiss
15. FOM Institute Rijnhuizen, Niederlande
16. FORTH, Crete, Greece
17. Politecnico Milano
18. Fraunhofer-Institut (IAF) Freiburg (Chiptechnologie), Deutschland
19. Fraunhofer-Institut für Physikalische Meßtechnik (Freiburg, Deutschland)
20. Heriot Watt University, Edinburgh, Scotland
21. High Magnetic Field Lab., Grenoble, France
22. INFINEON Villach, Österreich
23. INSA, Lyon, France
24. Inst. f. Experimentalphysik I, Universität Bayreuth, Deutschland
25. Institut für Festkörperelektronik, TU Wien
26. Institute for Physics of Microstructures RAS, 603600 Nizhny Novgorod, Russland
27. Institute of Physics, Polish Academy of Sciences, Warschau, POLEN
28. Ioffe Physico-Technical Institute RAS, 194021 St.Petersburg, Russland
29. KEBA, Ing.G.Krippner, Linz, Österreich
30. Lebedev Institut, Russian Academy of Sciences, Moskau, Russland
31. Masaryk University, Brno, Czech Republic
32. Charles University, Prague, Czech Republic
33. Max-Born Institut für Nichtlineare Optik, Berlin, Germany
34. Max-Planck Institut für Festkörperforschung, Stuttgart
35. MIT, Cambridge, MA, USA
36. Nanoelectronics Research Center, University of Glasgow, Scotland
37. NIST, Gaithersburg, MD, USA
38. North Carolina State University, NC, USA
39. Ørsted Institut, Kopenhagen, Dänemark
40. Paul Scherrer Institut, Villigen, Schweiz
41. Philips Analytics, Almelo, Niederlande
42. Physics Department, Cornell University
43. Profactor, Steyr, Upper Austria
44. Purdue University, Lafayette, IN, USA
45. Sektion Physik, Ludwig-Maximilians Universität München
46. Sentech, Berlin

47. Siemens München, Zentrale Technik, Bereich Halbleiter
48. ST Microelectronics, Crolles, Grenoble
49. TASC Triest, Italy
50. Thomson, Paris, France
51. Tohoku University, Sendai, Japan
52. TU Berlin, Institut für Festkörperphysik, Deutschland
53. TU-München (Mikrowellentechnik), Deutschland
54. Unipress, High Pressure Research Center, Polish Academy of Sciences, Warschau
55. Universita Padova, Italia
56. Universität Bayreuth, Experimentalphysik I, Bayreuth, Germany
57. Universität Bremen, Deutschland
58. Universität Graz, Institut für Experimentalphysik
59. Universität Paderborn, Deutschland
60. Universität Potsdam, Deutschland
61. Universität Würzburg, Deutschland
62. Université de Montpellier, France
63. Universiteit Instelling, Antwerpen, Niederlande
64. University of Erlangen-Nürnberg, D-91058 Erlangen, Deutschland
65. University of Lund, Solid State Physics, Lund, Sweden
66. University of Maryland, MD, USA
67. University of Southampton, England
68. University of Warwick, Coventry, England
69. Van der Waals-Zeeman Institute, University of Amsterdam, NL
70. VOEST ALPINE, Dr.Angerer, Linz
71. Walter Schottky Institut, TU München, Deutschland

Si/SiGe Cascade Injector QWIPs for Resonator Enhanced, Voltage Tuneable Two-Band Detection

T. Fromherz, P. Rauter, M. Grydlik and G. Bauer
Institut for Semiconductor and Solid State Physics, University of Linz
Altenbergerstraße 69, A-4040 Linz, Austria

Photocurrent spectroscopy has been performed on doped Si/SiGe valence band cascade injector structures in the mid-infrared spectral region. A large tunability of the photoresponse peak wavelength (from 5.2 μm to 3.2 μm) by an externally applied electric field is observed. The tunability of the photoresponse is a consequence of an electric field induced transfer of holes from the deepest to the shallowest quantum well of the injector sequence. Depending on the bias voltage, dark current limited peak detectivities in excess of $D^* = 1 \times 10^9 \text{ cm Hz}^{0.5} \text{ W}^{-1}$ were obtained at a temperature of 77 K.

Introduction

Infrared detection employing optical transitions in quantum wells has attracted a lot of research interest in the past several years. Due to the design freedom a variety of detector figures like for example the spectral region of sensitivity, the response time, the detector noise etc. can be adjusted over a large parameter range [1], [2] and optimized detector performance can be achieved for several areas of applications. In this work, we demonstrate that for quantum well infrared photo-detectors (QWIPs) in addition a large wavelength tunability can be achieved by employing the injector concept originally developed for quantum cascade electroluminescence and laser structures. In these structures, the large tunability results from the charge transfer from a deep to shallower wells. The charge transfer becomes possible by the alignment of the ground-states of adjacent quantum wells in an externally applied electric field.

Experimental

Photocurrent spectroscopy in the mid-infrared (MIR) spectral region has been performed on p-type Si/SiGe quantum cascade injector structures. The samples were grown by molecular beam epitaxy (MBE) at a low nominal growth temperature (350 °C) pseudomorphically on a Si substrate. The active region of the samples contains 5 SiGe valence band quantum wells (widths: 39, 26, 24, 23, and 35 Å; Ge content x : 0.42, 0.42, 0.40, 0.37, and 0.28, respectively) separated by Si barriers (thickness: 30, 25, 25, and 25 Å). These wells will be denoted w_1 , w_2 , w_3 , w_4 and w_5 in the following. The set of quantum wells $w_1 - w_5$ and barriers is p-type doped ($2.5 \times 10^{17} \text{ cm}^{-3}$) and repeated 10 times with an undoped 500 Å Si barrier between the subsequent quantum well sets. The 10 periods were sandwiched between 300 nm (100 nm) p-type ($2 \times 10^{18} \text{ cm}^{-3}$) bottom (top) contact layers.

For an externally applied bias of 1 V, the valence band edges and the wavefunctions as contour plots centred at the corresponding eigenenergies of a period of a typical sample are shown in Fig. 1 (a) for 1 V externally applied bias. The details of the calculations are given in Ref. [3]. For the photocurrent measurements, the samples were processed into $300 \times 300 \mu\text{m}^2$ mesas and contacted by Al:Si metallization.

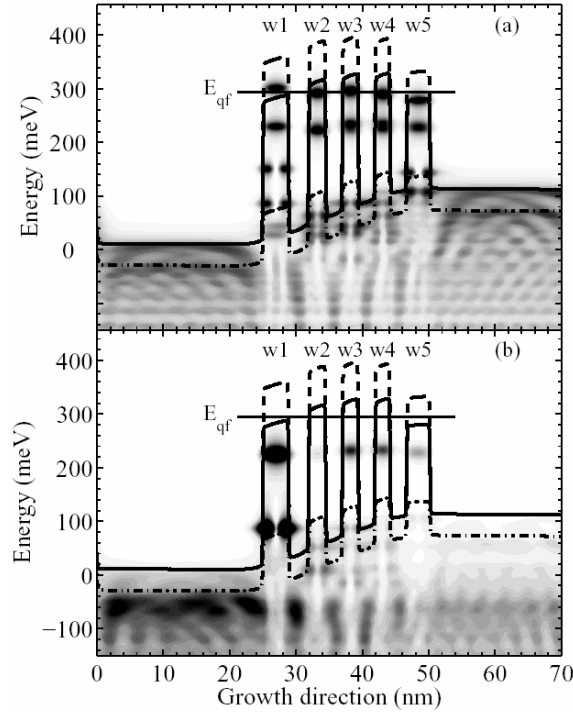


Fig. 1: (a) Contour plot of the wavefunctions and band edge profiles for the HH (dashed), LH (full) and SO (dashed dotted) valence bands for an externally applied bias of $-1V$. (b) For the same situation as in (a), contour plot of excited state wavefunctions integrated over the in-plane dispersion and weighted by their contribution to the absorption of normal incident radiation.

Figure 2 shows photocurrent spectra measured at $T = 77$ K for various bias voltages. The spectra were measured for MIR radiation propagating perpendicular to the sample surface. Since the quantum wells are formed in the *valence band* of the SiGe quantum wells, intersubband transitions are allowed for this polarization. The bias voltages indicated in the plot were applied to the top contact with respect to the bottom contact. A huge tuneability of the responsivity is observed for our samples: Depending on the bias voltage, the photoresponse of the cascade samples can be shifted between two MIR detection bands with maxima at 240 meV ($5.2 \mu\text{m}$) and 370 meV ($3.4 \mu\text{m}$). Both detection bands are slightly asymmetric showing a high-energy tail, the full widths at half maximum (FWHM) are 140 meV and 110 meV for the low- and high-energy band, respectively. For detection in the low-energy band, the ground states of the five coupled quantum wells are tuned into resonance by the applied negative bias voltage and a hole transfer from w1 to w5 occurs. For this bias, the photocurrent spectra are determined by bound to continuum transitions of the shallowest quantum well. For positive bias, most of the holes populate the ground state of w1 and consequently, photocurrent spectra due to bound to continuum transitions of the deepest quantum well with peaks around 370 meV are observed. At -1 V bias, a reversal of the sign of the photocurrent is observed for energies above and below 340 meV. From the simulations shown in Fig. 1 (b) it becomes clear that the sign reversal is due to resonances of the wavefunctions above the barriers: The final states of the transitions at higher energies are localized above the thick barriers separating the quantum well sequences. Due to the doping profile and the charge redistribution in the ground states, the thick barriers are virtually field free at this bias, and therefore, the direction of the photocurrent is determined by the center of gravity of the final state wavefunction, since on average, a transition from the ground state to this state implies a shift of the hole in the direction opposite to the applied electric field.

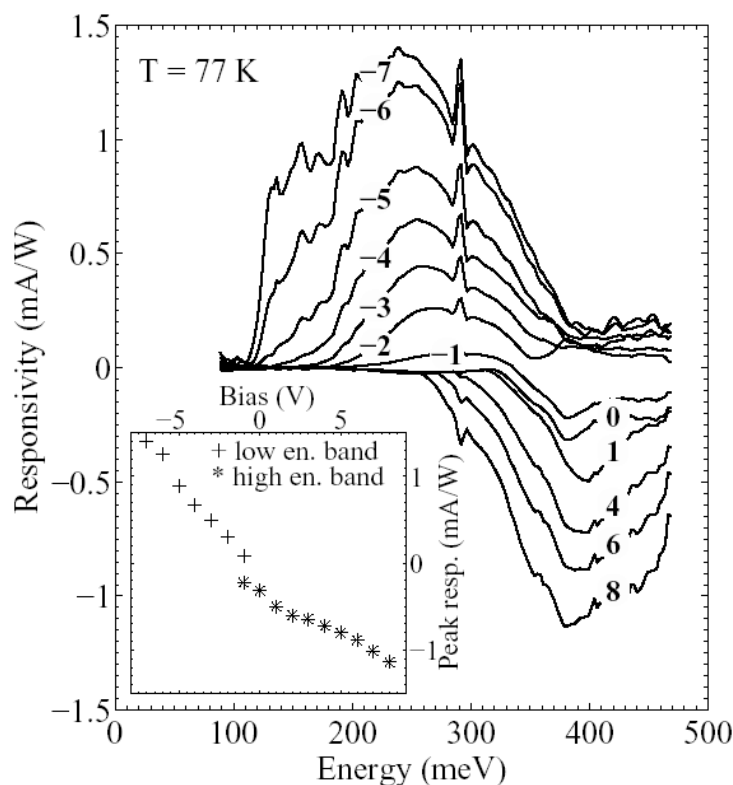


Fig. 2: Photocurrent spectra of Si/SiGe quantum cascade injector structures measured at the bias voltages indicated in the plot. At -1V , a different sign of the photocurrent is observed for MIR radiation with energy below and above 340 meV .

The final states of the transitions at around 270 meV are localized in the region above w_2 in which a strong electrical field is present that determines the direction of the photocurrent.

Depending on the applied bias, in both detection bands, the detectivity D^* of the QWIPs is approx. $1.5 \times 10^9\text{ cmHz}^{0.5}/\text{W}$. In order to enhance the detectivity and eliminate the spectral overlap of the high and low energy detection bands, the QWIP structures will be integrated in a vertical cavity. QWIP samples grown on SOI substrates show similar spectral response as shown in Fig. 2. With these samples, an integration of the QWIP structure in a resonator appears to be feasible by etching from the wafer backside to the buried oxide layer and by subsequent mirror deposition. Since the photoreponse of the QWIPs can be tuned for example from an energy to twice that energy (for example, 200 meV to 400 meV as shown in Fig. 2), both detection bands can be tuned into resonance with the cavity

Conclusions

In conclusion, we have demonstrated a QWIP based on a doped cascade injector structure that can be tuned over a large spectral region. The tunability of the device allows detection in two broad bands in the MIR that can be selected by the applied bias voltage. Up to now detectivities approximately 1 order of magnitude smaller than those of standard normal incidence QWIPs [4] compatible with standard Si technology could be demonstrated. However, the additional feature of the large tunability broadens the window of possible application significantly and makes these structures interesting for applications where high detectivity is not an absolute demand.

Acknowledgements

Work was supported under European Community project SHINE (Proj. Nr. IST-2001-38035)

References

- [1] B. F. Levine, "Quantum-well infrared photodetectors", *J. Appl. Phys.* 74, R1-R81 (1993).
- [2] H. Schneider, P. Koidl, M. Walther, J. Fleissner, R. Rehm, E. Diwo, K. Schwarz, G. Weimann, "Ten years of QWIP development at Fraunhofer IAF", *Infrared Phys. Technol.* 42, 283-289 (2001).
- [3] P. Rauter, T. Fromherz, G. Bauer, L. Diehl, G. Dehlinger, H. Sigg, D. Grützmacher, H. Schneider, "Voltage tuneable, two-band MIR detection based on Si/SiGe quantum cascade injector structures", *Appl. Phys. Lett.* 83, 3879-3881 (2003).
- [4] P. Kruck, M. Helm, T. Fromherz, G. Bauer, J.F. Nützel, G. Abstreiter, "Medium-wavelength, normal-incidence, p-type Si/SiGe quantum well infrared photodetector with background limited performance up to 85 K", *Appl. Phys. Lett.* 69, 3372-3374 (1996).

Midinfrared Continuous-Wave Photoluminescence of Lead Salt Structures up to Temperatures of 190 °C

M. Böberl, W. Heiss, T. Schwarzl, K. Wiesauer and G. Springholz
Institut für Halbleiter- und Festkörperphysik, Johannes Kepler Universität,
A-4040 Linz, Austria

Continuous-wave photoluminescence in the midinfrared for PbSe/PbEuSe and PbTe/PbEuTe multiquantum well structures as well as for PbSe and PbTe bulklike structures, excited by a semiconductor laser diode, is investigated. All samples are grown by molecular-beam epitaxy on BaF₂(111) substrates under the same growth conditions. Both for the Te-based systems and for the Se-based systems, it turns out that bulklike structures show photoluminescence up to higher temperatures than multiquantum well structures. In particular, emission spectra from PbTe/PbEuTe multiquantum wells are obtained up to temperatures of 200 K and from PbSe/PbEuSe multiquantum well structures up to 60 °C whereas for bulklike PbSe photoluminescence at temperatures as high as 190 °C is demonstrated.

Introduction

Lead salt materials are of high interest for midinfrared optical coherent emitters and detectors applied for molecular spectroscopy. The IV–VI narrow gap semiconductors have a multi-valley band structure with band extrema at the L point of the Brillouin zone. Due to the favorable mirrorlike band structure, the nonradiative Auger recombination rate is reduced by one or two orders of magnitude below that of narrow gap III–V and II–VI materials [1], [2]. Therefore, the highest continuous-wave (cw) operation temperatures (223 K) [3] of midinfrared diode lasers are achieved by lead salt devices. In spite of the fact that the use of quantum wells (QWs) as laser active media usually allows one to reduce threshold currents [4], it is remarkable that the highest cw operation temperature for lead-salt diode lasers was achieved so far by separate confinement buried heterostructure devices with bulklike active regions [3]. Recently, a comparative study of optically pumped vertical-cavity surface-emitting PbTe lasers (VCSELs) containing active regions of different dimensionality also showed no advantageous operation of QW devices over that containing a bulklike active region [5]. To rule out that the superior emission of bulklike lead-salt materials is caused by the high excitation required for laser emission, we study in this work the spontaneous emission of lead-salt structures under moderate optical excitation using a cw InGaAs pump laser diode. The results of these photoluminescence (PL) experiments performed for PbTe/Pb_{1-x}Eu_xTe and PbSe/Pb_{1-x}Eu_xSe multiple QWs (MQWs) as well as for thick bulklike PbSe and PbTe epilayers confirm the higher operation temperature achieved for bulklike samples, in contrast to observations in other semiconductor material systems [6]. In particular, for PbSe, strong luminescence is demonstrated even far above room temperature, namely, up to 190 °C.

Experimental

The PbSe and PbTe epilayers, as well as the PbSe/PbEuSe and PbTe/PbEuTe MQW structures, were grown by molecular-beam epitaxy (MBE) on (111)-oriented BaF₂ sub-

strates. The 50 period PbTe/PbEuTe MQW structures have QW thicknesses between 54 Å and 120 Å and Pb_{0.90}Eu_{0.1}Te barrier layer thicknesses between 240 Å and 300 Å, and were grown on a 1.5–2 µm thick buffer layer of Pb_{0.90}Eu_{0.1}Te. For the three investigated samples, S1, S2, and S3, the QW thickness is 53, 80, and 120 Å, respectively. The 30 period PbSe/PbEuSe MQW sample has a well layer thickness of 100 Å and a Pb_{0.93}Eu_{0.07}Se barrier thickness of 400 Å and was grown on a 3 µm thick buffer layer of Pb_{0.93}Eu_{0.07}Se. The bulklike PbSe and PbTe samples have a layer thickness of 3 µm and were fabricated with and without excess group-VI flux during MBE growth. For the PL investigations, the samples were mounted in a He flow cryostat for measurements below room temperature or on a heating element for above room-temperature measurements. In both cases, the temperature was measured close to the sample with either a Si diode or a thermocouple within an accuracy of 5 K. PL experiments were performed using a 970 nm InGaAs pump laser diode with an output power of about 150 mW. The laser was focused on the sample to a spot size of about 1 mm² under an angle of about 45°. The luminescence from the sample was analyzed using a grating monochromator and recorded by an InSb detector.

Results

In detail, the highest cw emission temperature from the PbTe/PbEuTe MQW structures is about 200 K. In contrast, for bulk-like PbTe epilayers, cw PL emission is obtained even above room temperature, as is seen in Fig. 1 (a).

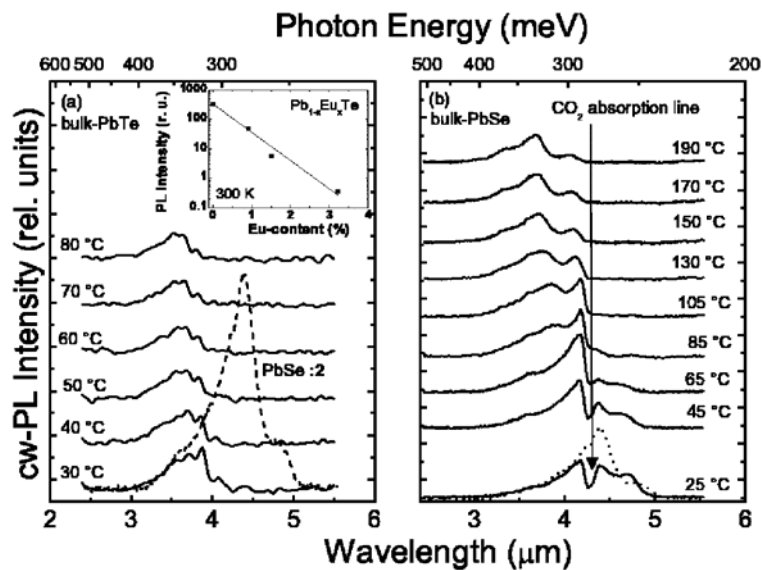


Fig. 1: (a) Temperature dependent cw PL spectra of a bulklike PbTe epilayer on BaF₂(111). The inset shows the integrated room temperature PL intensity emitted from Pb_{1-x}Eu_xTe epilayers as a function of the Eu-content x . (b) PL spectra of various temperatures of the PbSe epilayer. The dashed line at 25 °C shows the PL spectrum measured in an evacuated sample chamber.

Even at 80 °C, strong PL emission between 300 meV and 400 meV is observed, indicating a higher PL efficiency for bulk-like PbTe as compared to the QWs. This surprising observation is attributed to the increased nonradiative carrier recombination in the QWs due to intermixing of Eu at the heterointerfaces, as evidenced by x-ray and secondary ion mass spectroscopy experiments [7]. This interpretation is further supported by the observation of a very rapid drop in the PL efficiency of bulk-like Pb_{1-x}Eu_xTe epi-

layers with increasing Eu content demonstrated in the inset of Fig. 1 (a), with an intensity decrease by a factor of 100 already for Eu concentrations as low as 1.5 %. We attribute this to the intermixing between the localized Eu 4f states and the valence band, leading to reduced interband matrix elements. The 4f levels are located close to the valence-band maximum and for Eu contents above 7 % the Eu 4f level energies are even above the PbTe-like valence-band maximum [8].

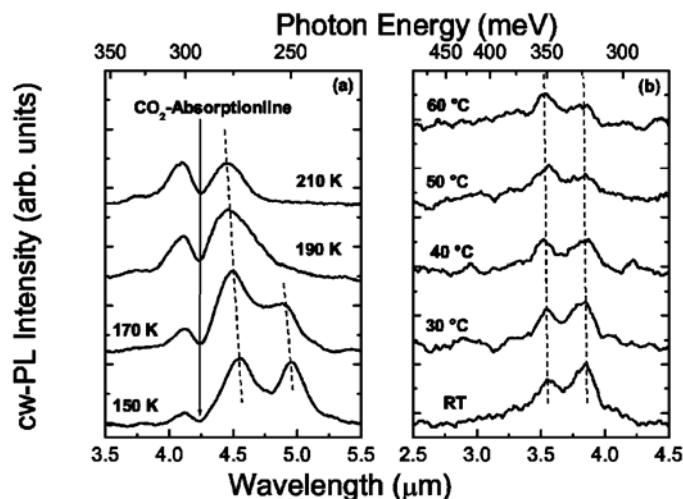


Fig. 2: Temperature dependent PL spectra of a PbSe/Pb_{0.93}Eu_{0.07}Se MQW structure with a well width of 100 Å.

For comparison, we have also investigated the cw PL emission behavior of the PbSe/PbEuSe material system. Figure 2 shows the observed cw-emission spectra of a 30 period PbSe/PbEuSe MQW structure with 10 nm well width below and above room temperature (Figs. 2 (a) and 2 (b), respectively). The dip in the low-temperature spectra of Fig. 2 (a) at $\lambda = 4.23 \mu\text{m}$ is due to the strong absorption of atmospheric CO₂ in the open path of the PL setup. With respect to the bulk PbSe band gap, the QW emission is blueshifted by about 50 meV due to the quantum size effect. In contrast to the PbTe MQWs, cw emission from the PbSe MQW sample is obtained even up to 60 °C (see Fig. 2 (b)), which is comparable with the reported value of PbSe/PbSrSe MQWs [9]. For pure PbSe bulk-like reference layers, the corresponding above room-temperature cw-emission spectra are shown in Fig. 1 (b). Clearly, a strong band-gap cw emission is found even at temperatures up to 190 °C. This is again higher than that obtained for the PbSe/PbEuSe MQWs, which we also attribute to increased nonradiative interface recombination. Even more interesting, however, is the fact that the PbSe cw emission is also much stronger than that observed for the PbTe epilayers (Fig. 1 (a)) persisting also to much higher temperatures. Since the PbSe emission spectra are strongly distorted by the strong absorption band of CO₂ in the optical path of the measurement setup, we have also measured the PL emission in an evacuated sample chamber. As is indicated by the dashed line in Fig. 1 (b), the PL emission obtained such is even stronger (increased by about a factor of 2) and shows a much more Gaussian-type line shape. It is centered at about 282 meV (4.3 μm), corresponding to the PbSe band gap at 30 °C as determined from FTIR transmission measurements on this sample.

For a direct comparison of the PbTe and PbSe emission, the measured room-temperature PbSe PL spectrum is plotted as a dotted line on top of the PbTe data in Fig. 1 (a) on the same intensity scale. Clearly, the PbSe emission is by about a factor of 20 stronger than the PbTe emission. We can exclude that this marked difference is due to differences in sample quality. This leads to the important conclusion that the

higher PL efficiency of PbSe is really an intrinsic effect. It can be explained by the higher band edge density of states of PbSe as compared to PbTe, but also by the significantly lower nonradiative Auger recombination rate of PbSe as previously reported by Klann *et al.* [2]. The latter is closely related to the factor of 5 smaller effective mass anisotropy of the conduction and valence bands of PbSe as compared to PbTe.

Conclusion

To conclude, our systematic PL investigations have clearly demonstrated above room-temperature cw emission in the midinfrared spectral region from various lead salt structures. The comparison of MQW and bulk-like samples revealed a significantly higher cw-emission efficiency of the bulk-like samples. In particular, for PbSe epilayers, strong PL emission was demonstrated up to a temperature as high as 190 °C, whereas the highest emission temperature of MQWs was only about 60 °C. This explains the fact that until now no superior performance of lead-salt QW lasers could be achieved as compared to their bulk-like counterpart (see, e.g., Ref. 5). On the other hand, the high spontaneous cw-emission temperatures observed, in particular, for the PbSe system clearly demonstrates that there are still great potentials for significant improvements of lead salt midinfrared lasers.

Acknowledgements

This work was supported by FWF, and ÖAW (APART), Vienna, Austria.

References

- [1] P. C. Findlay, *et al.*: “Auger recombination dynamics of lead salts under picosecond free-electron-laser excitation”, *Phys. Rev. B*, Vol. 58, 1998, p. 12908.
- [2] R. Klann, *et al.*: “Fast recombination processes in lead chalcogenide semiconductors studied via transient ...”, *J. Appl. Phys.*, Vol. 77, 1995, p. 277.
- [3] Z. Feit, M. McDonald, R. J. Woods, V. Archambault, and P. Mak: “Low threshold PbEuSeTe/PbTe separate confinement buried heterostructure diode laser”, *Appl. Phys. Lett.*, Vol. 68, 1996, p. 738.
- [4] Z. Alferov, in *Nano-Optoelectronics: Concepts, Physics, and Devices*, edited by M. Grundmann (Springer, Berlin, 2002), p. 4.
- [5] J. Fürst, *et al.*: “Midinfrared IV-VI vertical-cavity surface-emitting lasers with zero-, two- and three-dimensional systems ...”, *Appl. Phys. Lett.*, Vol. 81, 2002, p. 208.
- [6] G. Biwa, H. Yaguchi, K. Onabe, and Y. Shiraki: “PL and PLE spectroscopy of GaPAsN/GaP lattice-matched MQW structures”, *J. Cryst. Growth*, Vol. 195, 1998, p. 574.
- [7] G. Springholz, A. Holzinger, H. Krenn, H. Clemens, G. Bauer, H. Böttner, P. Norton, and M. Maier: “Interdiffusion in PbEuSe/PbSe multi-quantum-well structures”, *J. Cryst. Growth*, Vol. 113, 1991, p. 593.
- [8] M. Iida, T. Shimizu, H. Enomoto, and H. Ozaki: “Experimental Studies in the Electronic Structure of PbEuTe,” *Jpn. J. Appl. Phys.*, Part 1, Vol. 32, 1993, p. 4449.
- [9] P. J. McCann, K. Namjou, and X. M. Fang: “Above-room-temperature continuous-wave mid-infrared photoluminescence from PbSe/PbSrSe quantum wells”, *Appl. Phys. Lett.* Vol. 75, 1999, p. 3608.

Erbium Doped Waveguides in SOI Layers

G. Kocher-Oberlehner, W. Jantsch and K. Hingerl
Institut für Halbleiterphysik, Johannes Kepler Universität, A-4040 Linz

Waveguides were made in Silicon-on-insulator layers by photolithography. In order to test quality and gain we made use of the recently found increased solubility of Erbium in silicon in the presence of hydrogen. Applying the variable stripe length method we estimate a net gain of 32 cm^{-1} at 10 K.

Introduction

Among the various attempts to obtain light emission from Si, optical doping with rare earth elements like Er has been particularly fruitful at first glance as this approach is compatible with standard Si technology. Light emitting diodes emitting at a wavelength of $1.54 \mu\text{m}$ at room temperature have been successfully made. The low efficiency, however, and the slow response of such diodes limit their use to a few special applications. The main hope, namely application in optical communication systems, appears unrealistic unless laser action can be achieved.

The main problem with a possible Si:Er laser is the low gain which is a consequence of the rather low concentration of optically active Er and the small excitation cross section. Therefore any such concept requires low loss cavities. We tried to build waveguide structures involving a SiGe layer as active medium where the cladding of the active layer by Si (lower refractive index) was used to form a waveguide. It turned out however, that in SiGe structures the quenching of the Er luminescence sets in already at still lower temperatures and therefore the acceptable Ge content was lowered which reduces, however, the index contrast and thus the quality of the resonator.

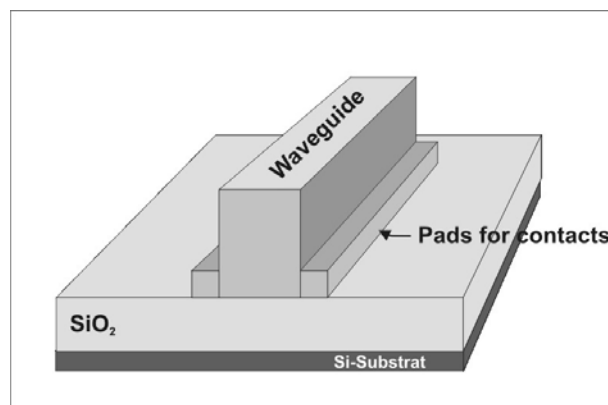


Fig. 1: Waveguide structure formed from SOI material; the dimensions are not to scale. The structure can be used for PL and EL measurements. For EL, electric contacts are put on top of the waveguide and on the pads on either side.

Therefore we recently turned to Si-on-insulator as waveguide material; thin Si-wafers bonded to an oxidized layer as available from SOITEC. In order to test waveguide structures made from this material, we first optimized photo-luminescence in that material and built waveguide structures containing Er in a p-n avalanche diode. Normally,

diodes designed for room temperature operation make use of $\text{SiO}_{2-\delta}:\text{Er}$ precipitates since only these allow to avoid excessive thermal quenching. We prepared different samples, however, in which Er is incorporated as isolated cubic center at high concentrations for testing purposes. The isolated cubic center exhibits very high quantum efficiency (up to 12% were reported in the literature) at temperatures up to 80 K. The reasoning behind using such centers was that they should permit to study waveguides and laser cavities, to optimize those and transfer the information gained to devices making use of the $\text{SiO}_{2-\delta}:\text{Er}$ precipitates in the future.

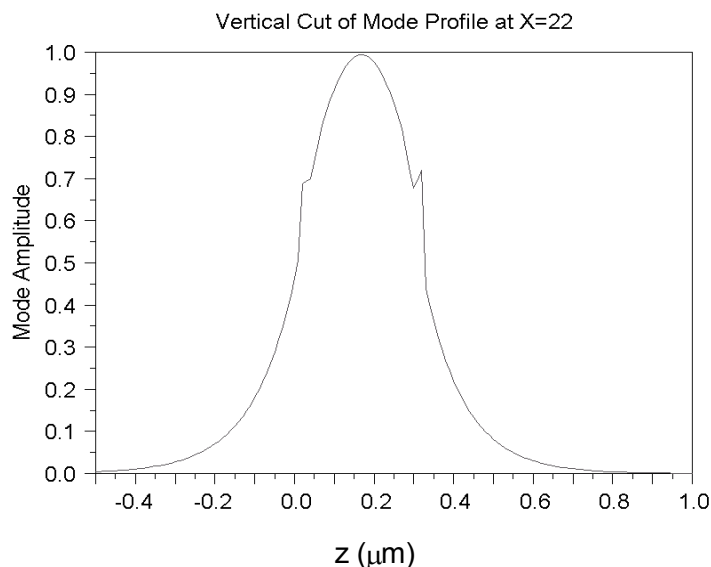


Fig. 2: Simulation of mode propagation in TE polarization in the waveguide structure shown in Fig. 1. Here “z” designates the vertical direction of the waveguide (x-axis: propagation direction).

In order to increase the concentration of optically active isolated Er we made use of a feature discovered in the course of this work. In order to lower the relatively high temperature necessary for the formation of $\text{SiO}_{2-\delta}:\text{Er}$ precipitates, we added hydrogen to our samples. Hydrogenation in Si is known to increase the diffusion of oxygen. We thus anticipated formation of precipitates already at lower temperatures. We found the opposite result: After annealing samples containing Er, O and H, erbium was found to produce the sharp spectra of the isolated interstitial Er-center at the Td site. Apparently, H mobilizes the O to an extent that it is driven out of the sample at temperatures well below 900 °C already. At this temperature, the Er is still immobile and thus neither oxide- nor Er-precipitates are formed. Consequently, the concentration of the optically active cubic Er centers can be increased by an order of magnitude. This type of center is the most promising candidate for gain: its concentration is high, it has high quantum efficiency and the linewidth of its 5 luminescence lines is less than 1 nm in contrast to that of the precipitates which is at least 20 times higher.

Experimental

Waveguides were made according to the scheme of Fig. 1, including a horizontal p-n junction and a top contact and two side contacts. The Er implantation profile was designed to include the full Si-layer thickness of 340 nm. In order to achieve recrystallization it was necessary to mask the side parts of the sample during implantation. Later

on, these side parts are used for contacts for electroluminescent devices. After recrystallization, these waveguides produce photoluminescence at temperatures up to 150 K. The simulated mode distribution is shown in Fig. 2.

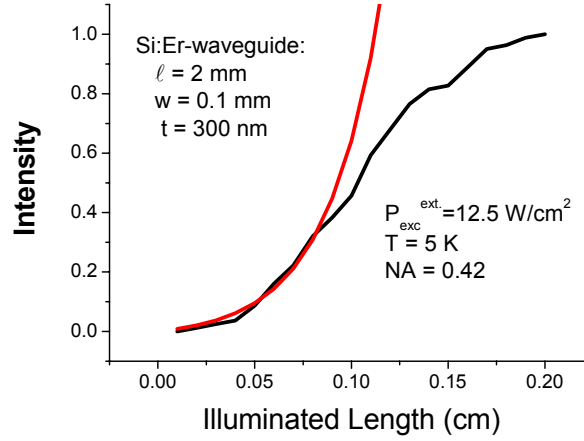


Fig. 3: Determination of the net gain of an optically pumped ($\lambda = 514$ nm) Si:Er waveguide. In this sample, Er is incorporated as cubic interstitials making use of the hydrogen co-doping method. Black curve: experimental, red curve: model. As a result a net gain of 35 cm^{-1} is estimated.

In order to measure the gain a defined part of the sample is optically pumped ("Variable strip length"- VSL method). In VSL, the laser light used for excitation is focused into a rectangular shape, usually by a cylindrical lens. The elongated spot of the beam starts at the facet of the sample. The illumination of the sample is regulated by a moveable shield, which can provide controlled coverage of the specimen. The detection optics collects light emitted from the facet of the sample perpendicular to the incident laser beam. If population inversion is achieved, the illuminated (excited) stripe of the waveguide acts as a single-pass amplifier for PL photons travelling inside the stripe. The net gain is defined as a relative change of detected intensity dI along the stripe. When the stripe length x is increased by a length dx , the detected intensity dI changes as well. The increment of this change in intensity dI_{tot} is a sum of a gain amplification of the incoming light and of the spontaneous emission $I_{sp}(\lambda)$ from a part dx of the waveguide. Solving this differential equation for the total length of the waveguide l , we get the "classical" VSL equation:

$$I_{tot}(l, \lambda) = \frac{I_{sp}(\lambda)}{G(\lambda)} \{ \exp[G(\lambda) \cdot l] - 1 \} \quad (1)$$

where the net optical gain $G(\lambda)$ is given by

$$G(\lambda) = g(\lambda) - \alpha \quad (2)$$

with α representing the losses and $g(\lambda)$ as a gain coefficient or negative absorption coefficient. The results are supposed to clarify the origin of losses occurring in the waveguide and achievable gain under optimum conditions before an attempt is made using the precipitate centers. Results are given in Fig. 3.

The simple model yields a net gain of about 32 cm^{-1} , a value that appears very promising. A more detailed modeling is developed at present which should allow understanding also the deviations from the standard model seen at illumination lengths exceeding 0.8 mm. Such structures will allow us to test and to optimize waveguide and laser structures at low temperatures.

Conclusion

Waveguides were made in Silicon-on-insulator layers by photolithography. In order to test the quality and gain we made use of the recently found increased solubility of interstitial ("cubic") Erbium in silicon in the presence of hydrogen. The concentration of the optically active cubic Er centers can be increased by an order of magnitude. This type of center is the most promising candidate for gain: its concentration is high, it has high quantum efficiency and the linewidth of its 5 luminescence lines is less than 1 nm in contrast to that of the precipitates which is at least 20 times higher. VSLM was applied on these structures, leading to an estimated net gain of 32 cm^{-1} at 10 K.

Acknowledgements

Work supported also by the *FWF*, and *ÖAD*, both Vienna.

References

- [1] G. Kocher-Oberlehner, W. Jantsch, A. Ulyashin, L. Palmetshofer: "On the Influence of hydrogen on the erbium related luminescence in Si", *Appl. Phys. Lett.* **83**, 623 (2003)

Simulation and Fabrication of Photonic Crystals

**J. Zarbakhsh, E. Heissl, C. Hasenfuss, G. Kocher-Oberlehner and
K. Hingerl**

**Christian Doppler Labor für Oberflächenoptische Methoden
Institut für Halbleiter und Festkörperphysik, Universität Linz,
Altenbergerstr. 69, A-4040 Linz, Austria**

Beginning 2003 the Christian Doppler Laboratory for Surface Science Methods was established at University Linz. The main goal is to bridge the gap between basic research and applied research on the topic of photonic devices. Although it is ultimately planned that also prototypes of these devices are fabricated in the cleanroom, in the first year the main emphasis was laid on novel designs. In this report these novel designs are described which will be fabricated in this year and in the future years experimentally with e-beam lithography resp. nanoimprint lithography.

Introduction

On 1st of January 2003 the Christian Doppler Laboratory for Surface Science Methods (CDLOOM) has been established at the Institute for Semiconductor and Solid State Physics at University Linz. The cooperating industry partner of CDLOOM is Photeon Technologies GmbH, Bregenz, Austria. The main work packages of the CDLOOM are twofold, namely two industrial topics: (1) Simulation of devices based on photonic crystals (PhC), (2) Prototype fabrication and parameter measurements.

CDLOOM has been established as interdepartmental group reporting to the department of semiconductor physics (Prof. Bauer) as well as to the department of solid state physics (Prof. Heinrich), because CDLOOM is using mainly the spatial and organizational infrastructure of the solid state physics department and the technical infrastructure of the semiconductor physics department, especially the clean room. Although it is ultimately planned that also prototypes of these devices are fabricated in the cleanroom, in the first year the main emphasis was laid on novel designs. Furthermore, due to the fact that almost all coworkers have not been at the physics department, within the first year the e-beam or UV lithography, etching, RIE etching, mask preparation, etc. characterization by AFM etc. had to be learned.

Theory

In 2003 the group worked in cooperation with Photeon on the following devices:

Efficient Fiber-High Index Waveguide Coupling by 1D Photonic Crystals

We investigated different technologies to couple light from a silica fiber into a high index waveguide. Finally we came up with a design, which is displayed in Fig. 1, where an omnidirectional Bragg reflector is used to squeeze the light together (Fig. 2 reduction of mode diameter), so that it can be coupled well into an high index waveguide, e.g. a Si waveguide on SOI material.

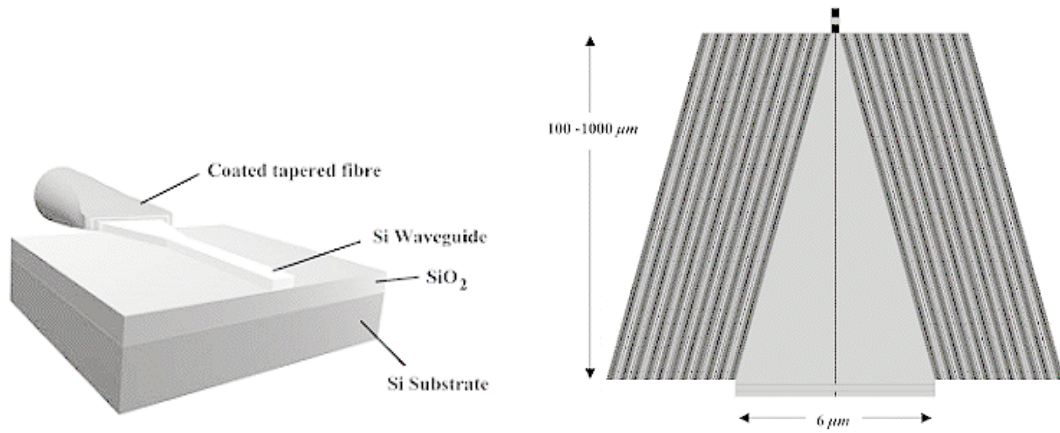


Fig. 1: Schematic drawing of the coupler

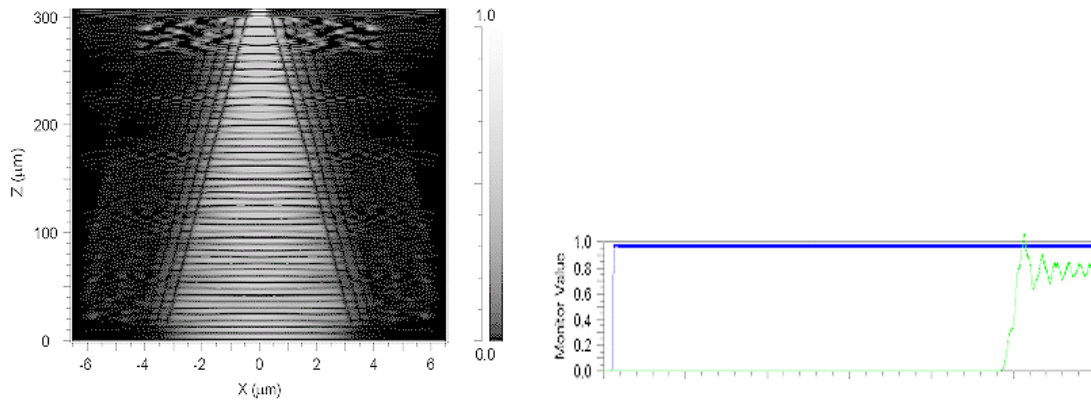


Fig. 2: Calculated efficiency of the coupler for TE modes.

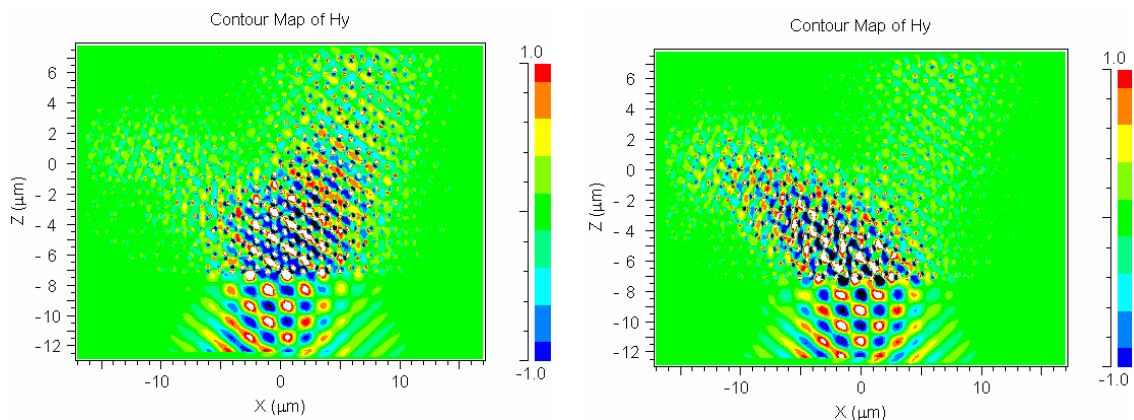


Fig. 3: Superprism effect for $(a/\lambda) = 0.58$ and $(a/\lambda) = 0.585$;

Wavelength Demultiplexers Employing the Superprism Effect

Photonic crystals show a very strong dispersion, which can modify the group velocity as well as the propagation direction strongly. The propagation direction can be calcu-

lated by calculating $\partial/\partial\vec{k} \omega(k)$ and due to the strong dispersion also small wavelength changes can modify the propagation direction enormously. In Fig. 3 2D simulations are shown for holes in Si with a period of 0.58 and neighboring of the free space wavelength, where this phenomenon is displayed. Although the simulation shows that angular deviations up to 90° can be achieved by varying the wavelength less than 1%, the high intensity of backscattered light as well as the scattering losses in forward direction exclude device applications.

Nonperiodic and Curvilinear photonic crystals

What we call photonic nonperiodic and curvilinear photonic crystals in this report does not need to possess crystal symmetries nor the rotational and translational properties of quasicrystals. We apply transformations as e.g. stretching (along one or both dimensions) or shearing (changing the angle between the basis vectors) on the well known quadratic and hexagonal structures. This operations allow to construct rod / hole assemblies, which show on a short range scale a periodic order, however on a scale of the order of 10 lattice constants the (Bravais) lattice type is changed (Fig. 4). Although such a non-periodic system would in principle have no complete band gap (for all directions), for given stretching and shearing parameters not exceeding certain values, each lattice will form, infinitely repeated, a photonic band gap. In the example below (Fig. 4 (a)) we display the case of 2D silicon rods (refractive index $n = 3.4$), surrounded by air and positioned on circles with radii of 1 – 6 periods (a) with a radial and tangential distance of a . In the 3rd circle the rods are carved out, leaving a waveguide. Nevertheless, such a structure guides light extremely well, as can be seen in Fig. 4 (b) where for a wavelength of $a/\lambda = 0.4$, the power transmission is plotted as a function of time. Recently there have been many efforts to design waveguide bends with high transmission for a broader bandwidth by adding additional holes and moving existing ones in 90° and 60° bends.

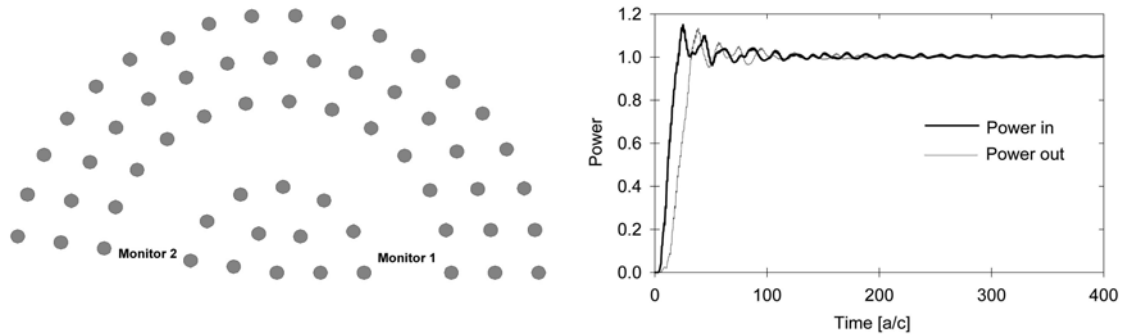


Fig. 4: (a) Nonperiodic (curvilinear) PhC; (b) Loss less propagation in the displayed curvilinear defect.

In our ring structure, which obviously allows coupling light out in any angle, such a procedure is not necessary. The question arises, why a non-periodic structure can localize light so well. The main underlying physics is the localization criterion applied for periodic systems. If the light frequency ω_0 is within a forbidden bandgap with band edge ω_c , the penetration depth $\lambda_{\text{envelope}}$ of the field into the photonic crystal can be calculated in a good parabolic approximation as $\lambda_{\text{envelope}} = \sqrt{\alpha/(\omega_c - \omega_0)}$ with the inverse effective photonic mass $\alpha = \partial^2\omega/\partial k^2$ where k_c is the wavevector at the Brillouin zone boundary. For our almost hexagonal / almost quadratic rod structures even for the worst case (quadratic Γ - M direction) the field penetration depth is less than $0.75a$. This finding

opens up the possibility to design new devices as e.g. circular resonators, whispering gallery mode devices and point defect structures in PhQCs.

Conclusion

The above examples, as well as conventional waveguides, are currently fabricated in the cleanroom on Silicon on Insulator (SOI) materials, which have a slab thickness of 300 nm. The following processing steps are used: resist spinning, e-beam lithography (Jeol and since recently Zeiss LEO), RIE etching, atomic force microscopy, partially metallization and dielectric coating. Furthermore, in October last year an industrial PhD thesis from an employee of EVG Schärding started, where nanoimprint technologies for the fabrication of 3D photonic crystals are evaluated.

Acknowledgements

Christian Doppler Gesellschaft

References

- [1] B. Lehner, K. Hingerl, "The Finite Difference Time Domain Method as a Numerical Tool for Studying the Polarization Optical Response of Rough Surfaces" *Thin Solid Films*, in press.
- [2] Javad Zarbakhsh, Frank Hagemann, Sergei F. Mingaleev, Kurt Busch, Kurt Hingerl, "Arbitrary angle waveguiding applications of 2D curvilinear-lattice photonic crystals", submitted to *Appl. Phys. Lett.*
- [3] (together with Photeon) K. Hingerl, L. Mao, V. Rinnerbauer, J. Schermer, V. Holý, "Reflection and Transmission of Finite 2D Photonic Crystals" *European Conference on Optical Communication*, Ravenna, 2003.
- [4] (Patent) J. Zarbakhsh, K. Hingerl, "Anordnung von dielektrischen Strukturen innerhalb eines Mediums", Pat. No. 17243.0-P832-54, filed by PHOTEON Technologies GmbH (2003).

Electron Beam Lithography of Silicon-Based SET Structures

T. Berer¹, F. Schäffler¹, M. Mühlberger¹, K. Lai² and D.C. Tsui²

¹Institute for Semiconductor Physics, Univ. Linz, Austria

²Department of Electrical Engineering, Univ. Princeton, USA

Lateral quantum dots have been fabricated on strained Si/SiGe substrates with a mobility of about 200,000 cm²/Vs using a split gates geometry, where the gates consist of Pd. The gate structures were realized by e-beam lithography. By applying negative voltages to the gates the underlying 2DEG can be depleted. Similar samples showed fractional quantum Hall effect up to filling factors of 1/3. Furthermore the $\nu=1/3$, 4/7 and 4/9 are observed for the first time in the Si/SiGe system. e-beam lithography was performed with an JEOL 6400. In the 4th quarter of 2003 a LEO Supra 35 FESEM (field emission scanning electron microscope) with a Schottky field emitter (SFE) has been purchased.

Introduction

Lateral quantum dot structures have been of strong interest in the recent years. However, most of this work was done on III-V-compounds (mostly in AlGaAs). Only few papers of silicon based SET (single electron transistor) structures were released so far. Therefore our goal is to realize a SET on a SiGe heterostructure. The main differences between SiGe and AlGaAs are the twofold valley degeneracy and the low Fermi level relative to the ground state, which can lead to pinch-off of devices already at small potential fluctuations.

Experimental

The quantum dot structures are prepared on ion etched Hall bars with alloyed AuSb contacts on Sb modulation-doped SiGe heterostructures with a mobility of about 200,000 cm²/Vs. Similar samples show fractional QHE down to filling factors of 1/3 at high magnetic fields and 30 mK [1]. Around $\nu = 1/2$ the two flux composite fermion (CF) series of the fractional quantum Hall effect (FQHE) at $\nu = 2/3, 3/5, 4/7$, and at $4/9, 2/5, 1/3$ are observed (Fig. 1). The $\nu = 1/3, 4/7$ and $4/9$ states are seen for the first time in the Si/SiGe system. This result demonstrates the CF model also applies in the Si/SiGe system. As a remarkable detail of the CF series, the $3/5$ state is weaker than the nearby $4/7$ state and the $3/7$ state is missing. This resembles the observation in the integer quantum Hall regime where $\nu = 3$ is weaker than the $\nu = 4$ state.

The SET gates itself consist of Pd which has, besides Pt, the highest Schottky barrier on n-type silicon. By applying negative voltages to the gates the underlying 2DEG can be depleted and a zero-dimensional constriction is formed – the quantum dot. At low temperatures electrical measurements will show quantization effects caused by localization of electrons.

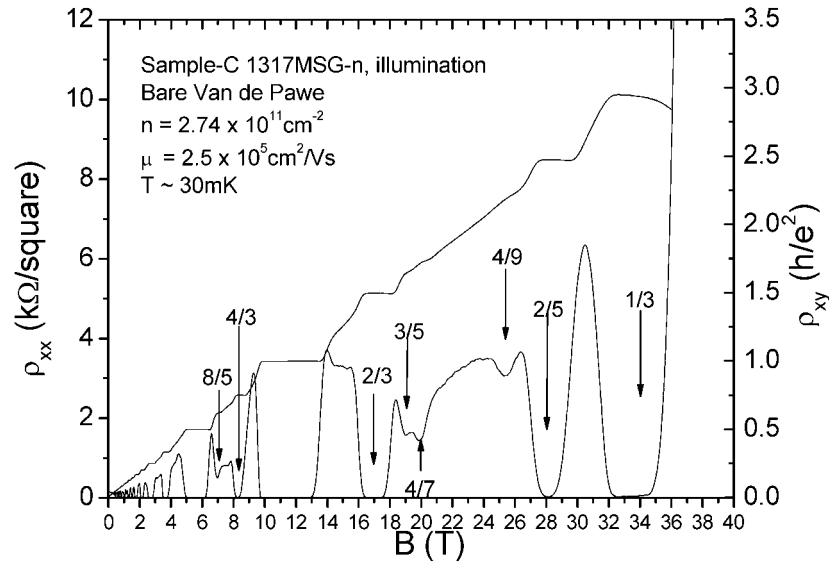


Fig. 1: Diagonal resistivity ρ_{xx} and Hall resistivity ρ_{xy} of the 2DEG measured in Van de Pauw geometry at $T = 30$ mK [1]. The 2DEG has a carrier density of $n = 2.7 \times 10^{11} \text{ cm}^{-2}$ and a mobility $\mu = 250,000 \text{ cm}^2/\text{Vs}$. Major fractional quantum Hall states are marked by arrows.

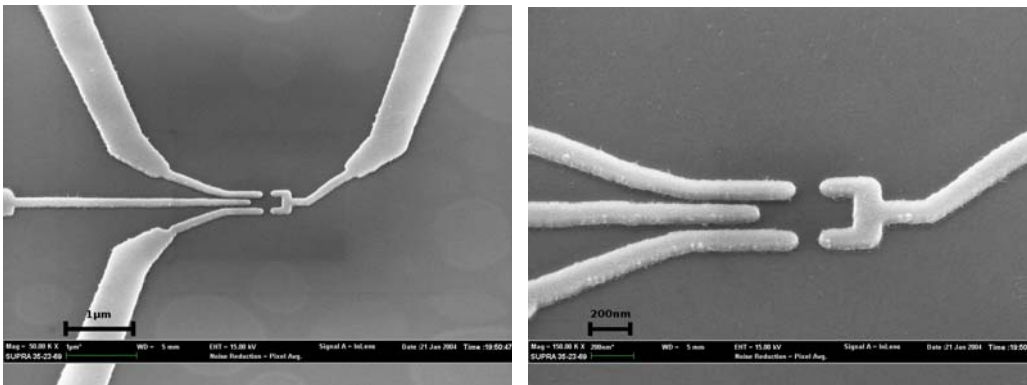


Fig. 2: (a) Electron microscope image of Pd-Schottky gates. (b) The inner part of the gates has a pitch of 175 nm. By depleting the underlying electron gas a lateral quantum dot can be formed

Measurements at 300 mK showed that the electron gas can be depleted by applying negative gate voltages and the conductivity decreases below e^2/h . Further improvements are, however, required to observe quantization and Coulomb blockade effects.

E-beam lithography was performed with a Raith Elphy Plus e-beam lithography system attached to a JEOL 6400 SEM with a thermionic LaB_6 cathode. In the 4th quarter of 2003 a LEO Supra 35 FESEM (field emission scanning electron microscope) with a Schottky field emitter (SFE) has been purchased. In comparison to thermionic emission the SFE has much higher beam brightness and much lower energy spread.

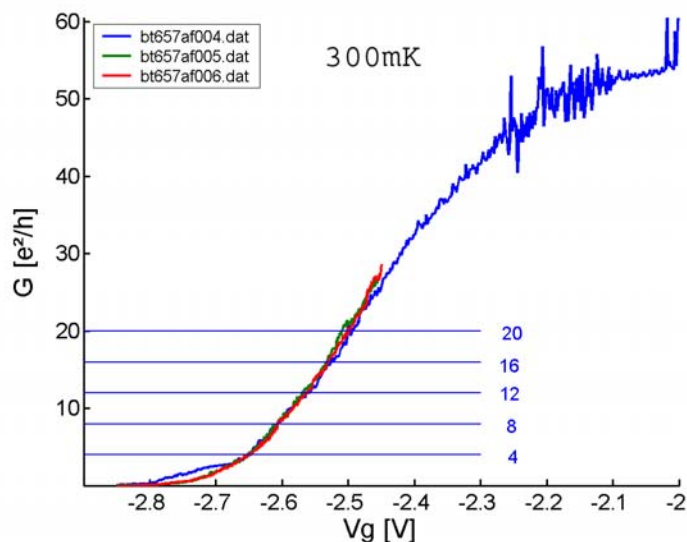


Fig. 3: Measurement of a SET structure at 300mK. The 2DEG gets depleted by an applied negative gate voltage and conductivity decreases below e^2/h . However no quantization steps are observed.

Two unique features of the column design enhance the resolution limit of the microscope: the beam booster and the cross-over-free column. The beam booster always maintains a high energy throughout the column, regardless of the electron energy selected by the operator. After passing the scanning system the beam is decelerated to the chosen energy. Because of the high beam energy throughout the column the beam is well protected against stray magnetic fields, even when operated at low voltages. Also the column has been designed to eliminate cross-overs in the beam path. Cross-overs lead to Coulomb interactions between beam electrons and hence reduce brightness and resolution.

The combination of cross-over-free beam path and high beam energy leads to high resolution, even at low operating voltages. This is extremely important, as with low beam energy the charging of non-conducting materials (e.g. PMMA e-beam photo resist – see Fig. 4) can be minimized.

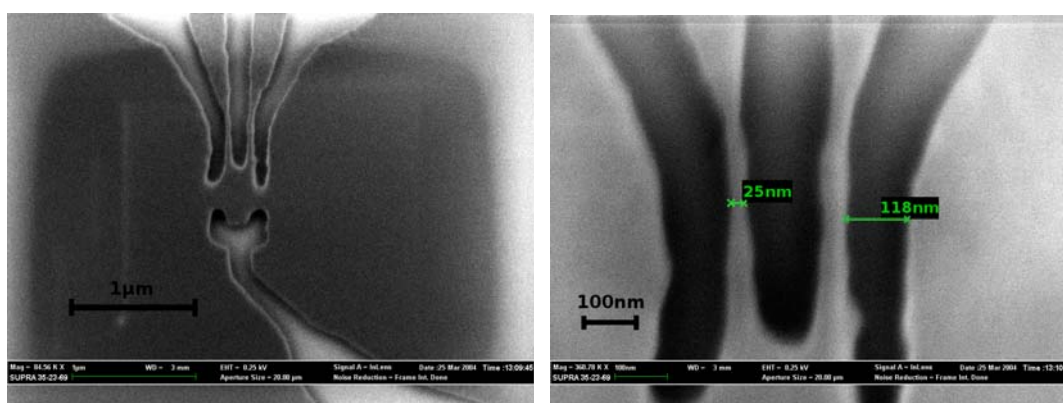


Fig. 4: (a) Electron microscope image of an exposed and developed photo resist (100nm thick PMMA) at 0.25kV acceleration voltage, preventing charging effects. (b) Detail of the SET structure. The areas of removed resist have a width of about 120nm, the PMMA stripe between two fingers is about 25nm thick.

Another interesting feature of the microscope is the in-lens detector. Besides the usual backscatter detector (for backscattered electrons (BE)) and the Everhart-Thornley detector (for mostly secondary electrons (SE)), an in-lens detector is located above the objective lens. Low-energy secondary electrons are intercepted by the weak electrical field at the sample surface and accelerated to a high energy by the field of the electrostatic lens. The electrons are then focused on the in-lens detector. With the in-lens detector one gets only information of the SE and not a mixture of SE and BE (due to generation of secondary electron at the chamber walls by impact of backscattered electrons) as with the Everhart-Thornley detector.

Conclusion

Lateral quantum dots were fabricated on strained Si/SiGe substrates with a mobility of about $200,000 \text{ cm}^2/\text{Vs}$ using a split gates geometry. The gate structures were realized by e-beam lithography. First measurements at 300 mK showed that the electron gas can be depleted by applying negative gate voltages and the conductivity decreases below e^2/h . However further improvements are required to observe quantization and Coulomb blockade effects.

Similar samples showed fractional quantum Hall effect up to filling factors of $1/3$. The $\nu = 1/3$, $4/7$ and $4/9$ are observed for the first time in the Si/SiGe system. This result demonstrates the CF model also applies in the Si/SiGe system.

The e-beam lithography was performed with a JEOL 6400 up to now. A new LEO Supra 35 FESEM has been purchased and brought to operation conditions.

Acknowledgements

This work was financially supported by FWF (P16223-N08)

References

- [1] K. Lai, W. Pan, D.C. Tsui, S. Lyon, M. Mühlberger and F. Schäffler: "*The Two-flux Composite Fermion Series of Fractional Quantum Hall States in Strained Si*", submitted to PRL

Step-Bunching in Si with Faceted $\text{Si}_{0.55}\text{Ge}_{0.45}$ Top-Layers on High-Miscut Substrates

H. Lichtenberger, M. Mühlberger, C. Schelling and F. Schäffler
Institute for Semiconductor and Solid State Physics, JKU Linz

We report on the influence of layer miscut on the step-bunching properties of the Si(001) surface. It is shown that for growth on substrates with a miscut of 4° along [110] the purely kinetic step-bunching instability is shifted to lower temperatures around 425°C . Our epitaxial layers exhibit ripples with periods of $\sim 90\text{ nm}$ and a height-modulation of more than 4 nm . Highly strained $\text{Si}_{0.55}\text{Ge}_{0.45}$ epilayers deposited on top of such rippled buffers decompose into faceted islands and additionally show preferential nucleation on the flanks of the step bunches in a narrow temperature range. Our experiments bridge the regimes of purely kinetic step-bunching and of strain-driven Stranski-Krastanov growth.

Introduction

The slightly miscut Si(001) surface is intrinsically unstable against kinetic-step-bunching. By using Si substrates with 4° miscut (along [110]) the period of the evolving ripple structure can be decreased to typically 90 nm . p-modulation-doped layers on such substrates are expected to show pronounced interface roughness scattering in addition to alloy scattering. A variation of the interface roughness parameters should allow for a discrimination between these two mechanisms.

Experiments

We have reported, that the step-bunching instability is mainly influenced by the growth temperature [1], [2]. Concomitant with the decreasing period also the substrate temperature, where pronounced ripples are found, shifts to lower values. At Si growth rates of 0.2 \AA/s a ripple pattern with few defects develops within a small temperature window around 425°C . At slightly lower temperatures many defects are incorporated and the ripples decompose into islands, which are aligned in chains (Fig. 1, 400°C).

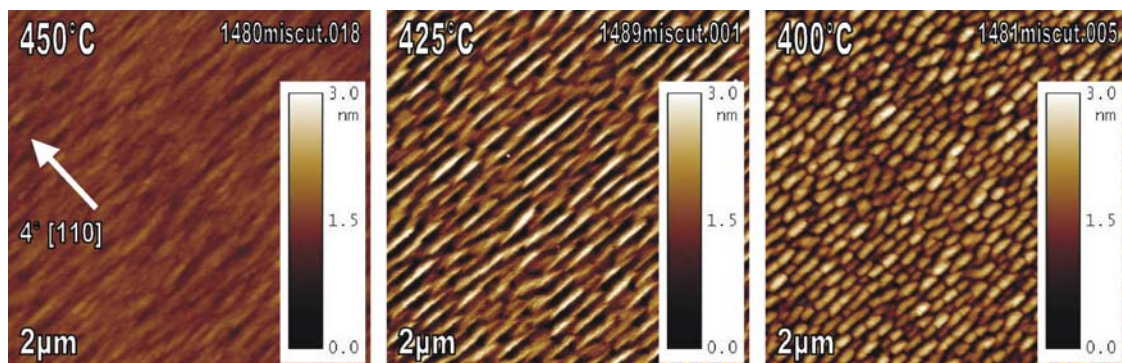


Fig. 1: AFM-images showing the substrate temperature dependence of step-bunching. The series of 500 \AA thick Si-buffers grown on 4° [110] miscut samples (at 0.2 \AA/s Si) proves that only within a small temperature range around 425°C a pronounced ripple-structure is found.

For marginally higher temperatures the ripple structure fades away (Fig. 1, 450 °C).

Not only the influence of temperature was investigated, also a series of different Si-buffer layers was grown (Fig. 2). In the early stage of step-bunching (Fig. 2, 250 Å) there are many uncorrelated localized step-bunches. With increasing layer-thickness (500 Å) the individual bunch-segments merge and form well pronounced elongated ripples (500 Å), which finally span several micrometer (1000 Å). The low growth temperature of 425 °C influences growth as the number of accumulated defects is also increased with layer thickness. This shows up as holes and constricted bunches (Fig. 2, 3000 Å).

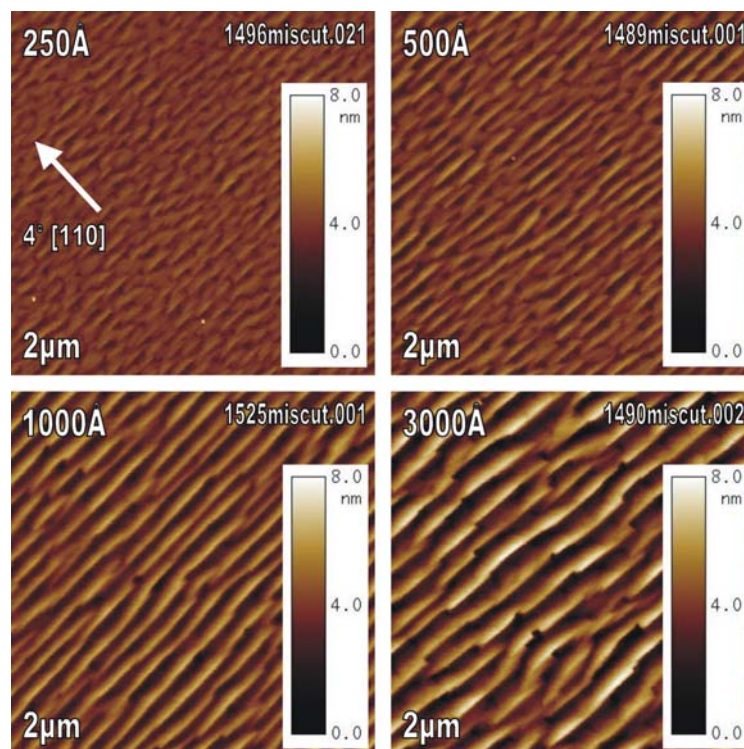


Fig. 2: AFM-images showing the layer thickness-dependence of step-bunching. The series of 250Å, 500Å, 1000Å and 3000Å thick Si-buffers grown on 4° [110] miscut samples (@ 0.2 Å/s Si) indicate that the ripple structure gets even more pronounced with increasing layer thickness. An increase in the period and the structure height of the step-bunches is clearly visible.

Further experiments were conducted with 1000 Å thick Si-buffers (@ 425°C, 0.2 Å/s Si), which show typical dimensions of 100 nm for the ripple period and 4 nm for the ripple height (miscut 4° [110]). Figure 3 shows the comparison and evaluation of AFM-data for a pure, 1000Å thick Si-buffer, and a Si-buffer covered with 50Å Si_{0.55}Ge_{0.45} at 425 °C and 550 °C, respectively. In the case where the substrate-temperature was increased to 550 °C for the Si_{0.55}Ge_{0.45} top-layer, the highly strained epilayer relieves stress forming {105}-faceted islands, which are known from the hut-clusters of relaxed SiGe-films. On our miscut-samples the islands are bound by two {105}- and the (001)-facet on top, while the underlying ripple pattern is widely conserved. Even at the low temperature of 425 °C the Si_{0.55}Ge_{0.45} film does not replicate the underlying ripples of the Si-buffer in a conform manner. The stress in the top-layer leads to the formation of ridges at the ripple-flanks, perpendicular to the main structure. This marks the transition from conformal Si/SiGe epilayer growth [3] to strain-driven 3D-growth and is illustrated with 3D-AFM data in Fig. 3 (c). FFT evaluations reveal a period of approximately

100 nm for the step-bunches on the Si-buffer. The $\text{Si}_{0.55}\text{Ge}_{0.45}$ islands decorate the kinetic step-bunches, but have a somewhat smaller spacing of ~ 70 Å along the ripples (Fig. 3 (b)).

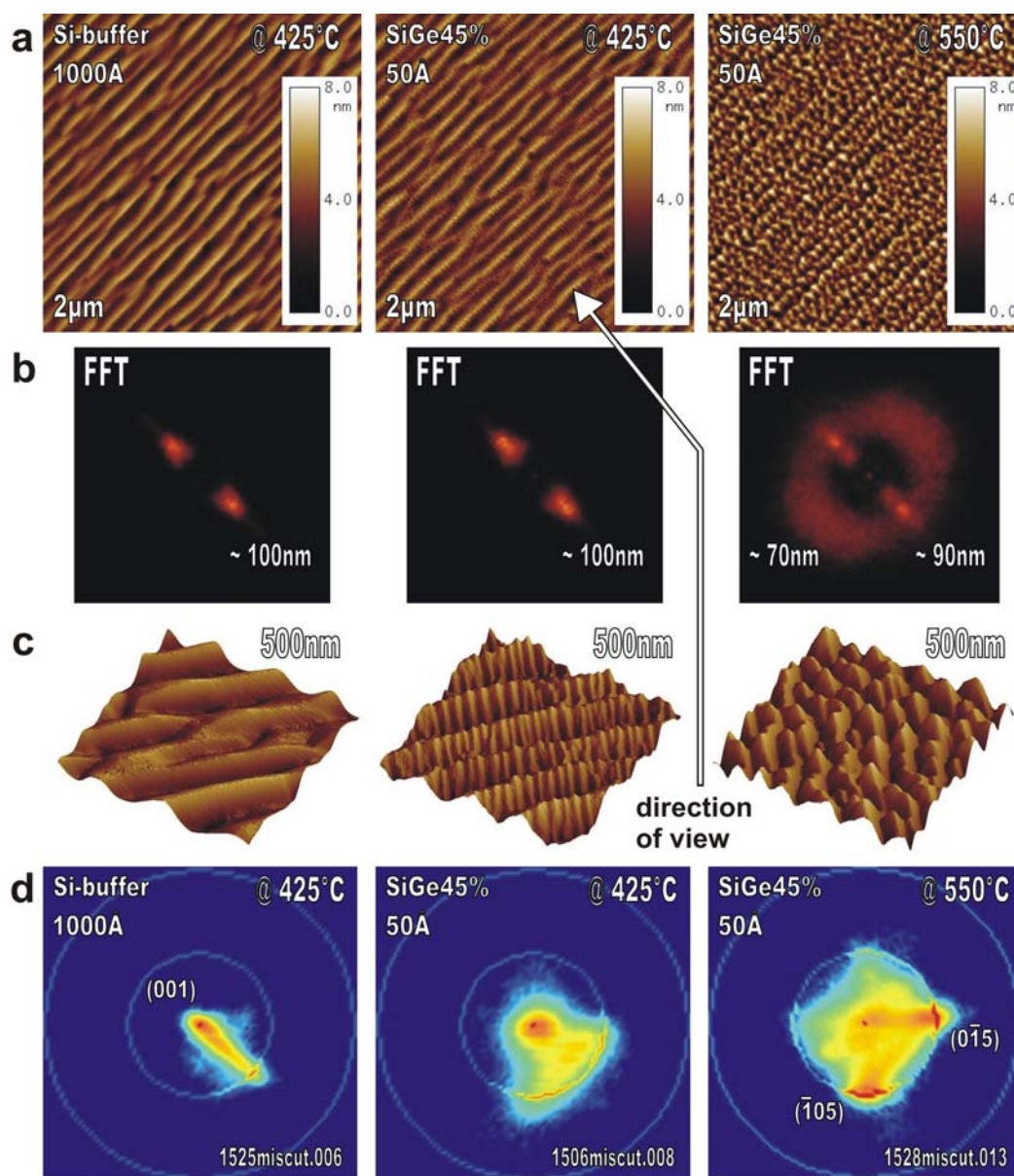


Fig. 3: AFM-data for the pure 1000 Å Si-buffer, the Si-buffer covered with 50 Å $\text{Si}_{0.55}\text{Ge}_{0.45}$ (all 4° [110] miscut) at 425 °C and 550 °C, respectively. Conventional 2D-AFM images (a) are completed with corresponding FFTs (b), 3D-AFM representations (c) and surface-orientation histograms (d) to illustrate the transition from pure step-bunching to {105}-faceted islands.

The individual facets of the islands are determined from a surface-orientation-histogram, which is derived from tilt-corrected AFM-data (Fig. 3 (d)).

In Fig. 4 a schematic drawing illustrates the faceted layer morphology next to distorted 3D-AFM data of the 50 Å $\text{Si}_{0.75}\text{Ge}_{0.25}$ 425 °C sample used for the surface normal vector analysis. The formerly straight steps with the flat terraces oriented in (001) direction and the flanks with angles of typical $\sim 8^\circ$ for Si-homoepitaxy are now confined by zigzag edges. As the slope of the ripples matches the angle of the intersection edge of two

adjacent $\{105\}$ -facets, these flanks form perfect nucleation sites for the highly strained SiGe-layers to relief strain. Therefore at medium temperatures ridges organize perpendicular to the step-bunching pattern (Fig. 4). For growth at 550 °C relaxed islands and asymmetric hut-clusters align in chains along the bunches and result in an ordered decoration of the step-bunching pattern.

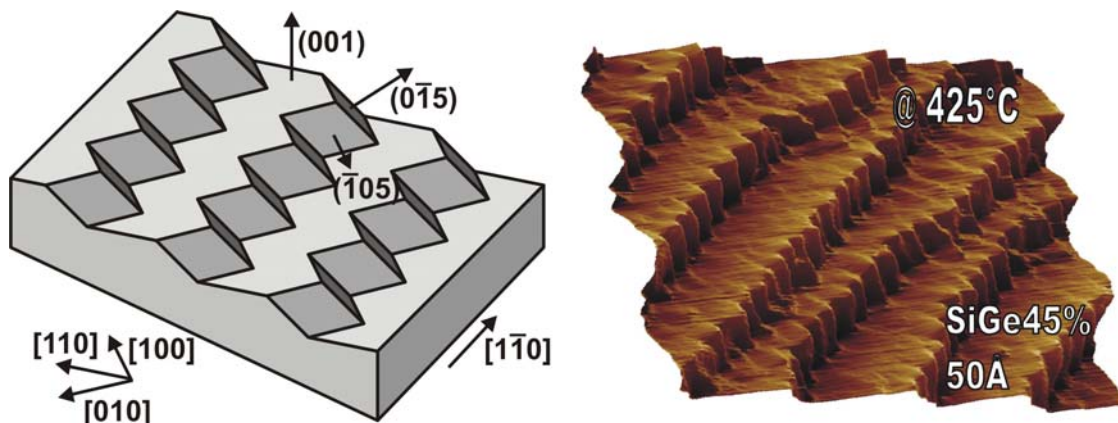


Fig. 4: Schematic drawing and 3D-AFM data for a 1000 Å Si-buffer covered with 50 Å $\text{Si}_{0.75}\text{Ge}_{0.25}$ at 425 °C. The distorted AFM-data representation (scan-size 500 nm) shows that the ripples with the (001)-oriented terraces exhibit a zigzag at the edges. The smooth flanks with typically $\sim 8^\circ$ with respect to [001] for homoepitaxy are energetically favourable nucleation sites for the strained SiGe-epilayer leading to a $\{105\}$ -faceted ridge structure, which is perpendicular to the step-bunches.

By optimizing the growth parameters improvements in size-uniformity and ordering are expected [4].

Conclusion

Step-bunching is a purely kinetic growth instability which occurs during homoepitaxy on Si(001). For a miscut of 4° [110] the period of the ripple-pattern can be reduced to 90nm still exhibiting a height modulation of ~ 4 nm. Highly strained $\text{Si}_{0.55}\text{Ge}_{0.45}$ epilayers grown on top of such rippled Si-buffers reveal additional features by decomposing into faceted islands and decorating the underlying ripple-pattern in an organized manner.

Acknowledgements

This work was financially supported by FWF (P16229N08).

References

- [1] J. Myslivecek, C. Schelling, F. Schäffler *et al.*, *Surf. Sci.* **520** (2002), 193
- [2] C. Schelling, G. Springholz, F. Schäffler, *Phys. Rev. Lett.* **83** (1999), 995
- [3] M. Mühlberger, C. Schelling, G. Springholz, F. Schäffler, *Physica E* **13** (2002), 990
- [4] C. Teichert, *Phys. Rep.* **365** (2002), 335

Fabrication and Characterization of Lateral Quantum Dots in GaAs Heterostructures

G. Pillwein¹, G. Brunthaler¹ and G. Strasser²

¹ Institute for Semiconductor Physics, Univ. Linz, Austria

² Institute of Solid State Electronics, TU Vienna, Austria

We have improved the design of our lateral quantum dots, which are fabricated from a two-dimensional GaAs/AlGaAs heterostructure by electron beam lithography. Our split gate geometry, which defines the dot electrostatically by metal gates, has been modified. The devices were characterized electrically in a ³He cryostat at 300 mK. Due to improvements in device design and measurement conditions we can now control the number of electrons in the dot over a wider range. Additionally we have observed reproducible conductance fluctuations overlaid on the Coulomb oscillations.

Introduction

In several recent proposals [1], [2] lateral quantum dots were discussed as a promising option to realize the quantum entanglement necessary for doing quantum computation. We have fabricated quantum point contacts and single lateral quantum dots in the two dimensional electron gas (2DEG) of a GaAs/AlGaAs heterostructure, which are basic elements for more sophisticated devices. Already one year ago we have presented first working devices of this type, but the fabrication process was not very reliable then and measurement results were not reproducible from one device to the next. In the meantime we have improved both the fabrication process and the electrical measurements. In our present devices we have thus greater control over the number of electrons in the quantum dot. Now we can think of combining two or more lateral dots, which will allow us to investigate effects, in coupled dot systems.

Experimental

Our samples are based on a MBE grown GaAs/Al_{0.3}Ga_{0.7}As heterostructure with a 2DEG situated approximately 100 nm below the sample surface. They have a carrier concentration of about $2 \times 10^{11} \text{ cm}^{-2}$ and a mobility of up to $1.4 \times 10^6 \text{ cm}^2/\text{Vs}$. Ohmic contacts were made from an Au/Ni/Ge alloy and Hall bar mesas were wet-etched with H₂SO₄:H₂O₂:H₂O (1:6:150). The quantum dot structure was defined by e-beam lithography and subsequent deposition of Cr/Au metal electrodes (i.e. the split gates) on top of the hall bar mesa. Figure 1 shows all important parts of the sample in different magnifications. By applying a negative voltage to the split gates the underlying 2DEG can be completely depleted. Our new dot design consists of four gate fingers, which define a quantum dot. The two outer gates in connection with the bottom gate define the tunnel barriers, which separate the quantum dot area from the surrounding 2DEG. The top center gate (the plunger gate) can be used to change the electrostatic potential of the dot. In comparison to our previous design the tunnel junctions are further away from the plunger gate, and are thus not so easily influenced by the plunger gate voltage, which has been one of the major problems with the former design. A SEM image of the new split gate geometry is shown in Fig. 1 (b), the old geometry is shown for comparison in the inset. The quantum dot area defined by the metal gates is approximately circle shaped with a diameter of roughly 400 nm in the investigated sample.

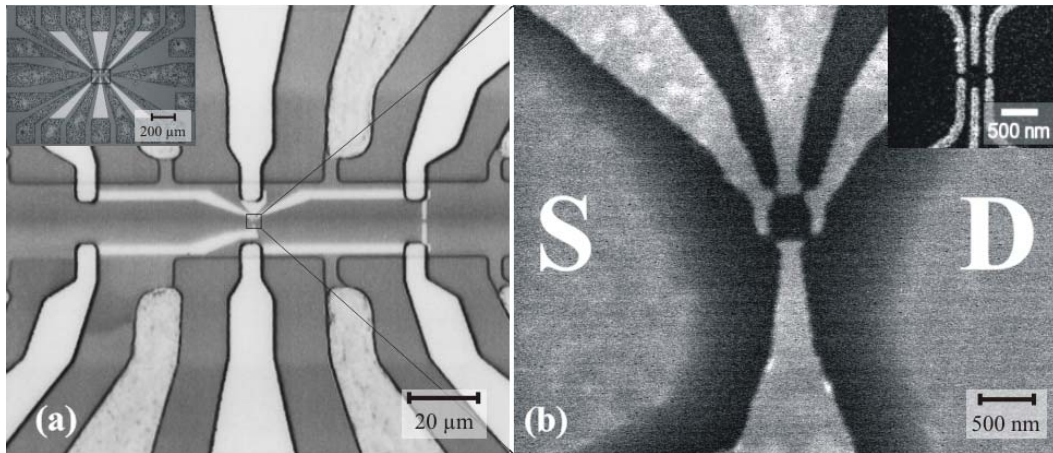


Fig. 1: (a) shows an SEM image of a part of the hall bar containing the split-gate structure. The inset shows the entire structure including the ohmic contacts. (b) SEM image showing enlarged view of the center region marked in Fig. 1 (a). The inset shows the old gate geometry for comparison.

Electrical measurements were carried out in a ^3He cryostat at a temperature of 300 mK using a low frequency lock-in technique ($f = 10$ Hz). To avoid heating of the electrons it is important to keep the excitation voltage lower than the thermal energy, which corresponds to $25 \mu\text{V}$ at 300 mK, thus excitation voltages of $10 \mu\text{V}$ or below have been used. In order to define the quantum dot in the 2DEG, negative voltages have to be applied to the split-gates. By sweeping the plunger gate voltage the number of electrons in the dot is changed. Such a measurement is shown in Fig. 2 (a), where the conductance through the dot is plotted versus the plunger gate voltage. From the period of the conductance peaks a gate capacitance of $C_G = 8.9 \times 10^{-18}$ F can be calculated. Because the plunger gate voltage also has an influence on the tunnel barriers, the peak conductance decreases towards more negative voltages, until it is finally totally pinched off at about $V_G = -0.2$ V.

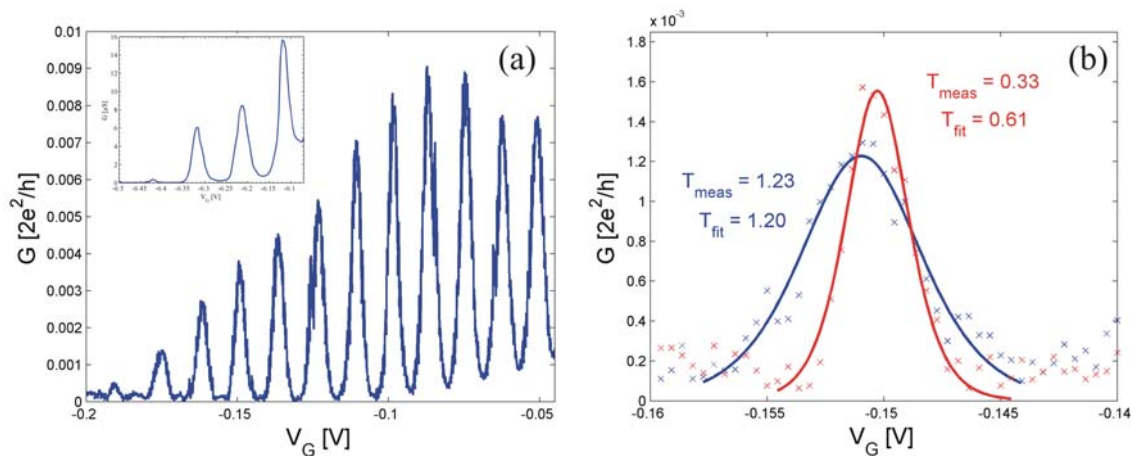


Fig. 2: (a) Coulomb oscillations observed in the conductance G versus plunger gate voltage V_g . The spacing of the peaks gives an estimate of the gate capacitance $C_g = 8.9$ aF. (b) Fit of Coulomb peak lineshape at two different temperatures.

When compared to measurements in our first samples, where only very few for two temperatures are shown in Fig. 2 (b), while at the higher temperature (1.2 K) the fitted temperature is in good agreement with the measured temperature value, at a measured temperature of 0.3 K the fit indicates that the electron gas is heated up to 0.6 K. Therefore we have to further improve our measurement equipment by installation of additional filters, which eliminate any disturbing signals.

Closely looking at the data shown in Fig. 2 (a), one can see that there is a fluctuation superimposed upon the Coulomb oscillations (Fig. 3 (a)). So far we observed these fluctuations in two samples, where the fluctuations have been bigger for the larger dot with a diameter of 900 nm. Figure 3 (b) shows a measurement in the larger dot where the gate voltage was swept up and down (curves are offset for clarity), from which it is obvious that the fluctuation is not some random noise but a reproducible effect. The origin of these fluctuations is not yet clear to us. Oscillations could be seen, the improvement is clearly visible. One of our goals is now to design the gate geometry in a way that transport is possible until only one electron remains in the dot.

The Coulomb peaks have a thermally broadened lineshape and can thus be used to determine the temperature of the electron gas, which may be heated up with respect to the crystal lattice by stray pick-up of RF signals. A fit of the lineshape

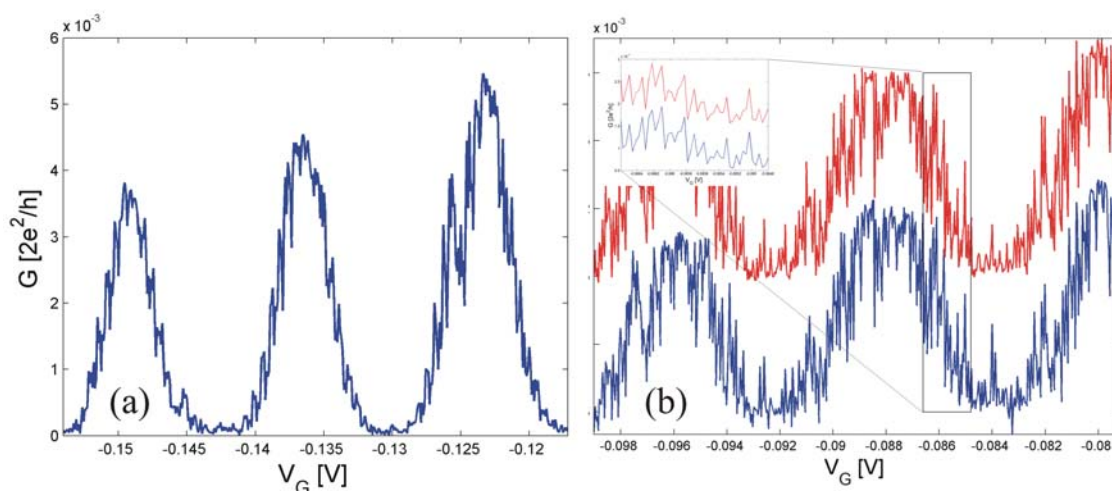


Fig. 3: Conductance fluctuations superimposed on Coulomb oscillations for two dots: (a) 400 nm dot; (b) 900 nm dot: the fluctuations are reproducible on a very small voltage scale.

In addition to changing the plunger gate voltage, we may apply a large DC source drain bias, superimposed by a small AC signal, which is detected by lock-in amplifiers. By doing so we measure the differential conductance dependent on both V_G and V_{SD} . With such a measurement the basic properties of the quantum dot are obtained, including total and source capacitance as well as an estimate of the actual size of the quantum dot. Figure 4 shows a grayscale plot of such a measurement. The horizontal axis corresponds to the plunger gate voltage V_G , the vertical axis to the source-drain voltage V_{SD} . The dark (bright) areas correspond to low (high) G . In the dark parallelogram-shaped regions marked by lines the number of electrons is fixed and no transport is possible due to Coulomb blockade.

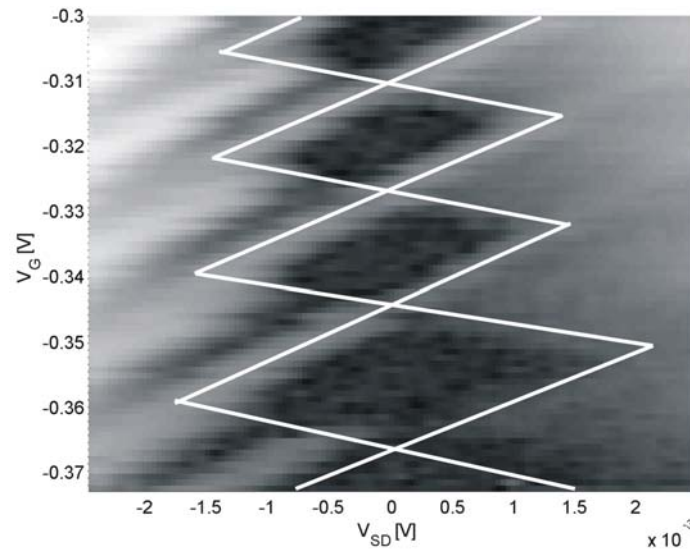


Fig. 4: Differential conductance G versus source-drain voltage V_{SD} and plunger gate voltage V_G . The dark (bright) areas correspond to low (high) G . Coulomb blocked regions are enclosed by the lines.

From the conductance peak spacing ΔV_G at zero source drain voltage the capacitance C_G of the plunger gate can be calculated to be 8.9 aF. From the slopes of the peak lines we obtained the total and the source capacitance to be $C = 103.8$ aF and $C_S = 27.2$ aF. Via the known relation for the charging energy $E_C = e^2/C$ we related the gate voltage scale to an energy scale. From the capacitance of a 2D disk $C = 4\epsilon_0\epsilon_r d$ (for GaAs $\epsilon_r = 12.9$) we estimated the diameter of the electron island to be about 225 nm. Considering that the depletion region will extend around the contours of the split-gates (by a length comparable to the depth of the 2DEG, which is ~ 100 nm), this is in good agreement with the structural diameter of 400 nm.

Conclusion

We have refined the processing our split-gate quantum dot devices and our results confirm that their electrical properties have improved. Further measurements will be performed on these structures to investigate the origin of the observed conductance fluctuations. Because the optimized fabrication process now gives very reproducible results and a good yield, as a next step we will integrate two or more dots into a quantum dot circuit, which may be combined with quantum point contacts for charge readout [3]. A dilution refrigerator, which is currently being installed in our lab, will allow us to reach lower temperature and increase the resolution in upcoming measurements.

References

- [1] D. Loss and D. P. Vincenzo: "Quantum computation with quantum dots", Phys. Rev. A Vol. 57, 1998, pp. 120 – 126.
- [2] L.M.K. Vandersypen et al.: "Quantum computation with electron spins in quantum dots", quant-ph/0207059, 2002.
- [3] J.M: Elzerman et al.: "Few-electron quantum dot circuit with integrated charge read out", Phys. Rev. B Vol. 67, 2003, p. 161308(R).

Ordering in PbSe Quantum Dot Superlattices Investigated by Anomalous X-Ray Diffraction

R.T. Lechner, G. Springholz, T. U. Schüllli, V. Holy, J. Stangl,
A. Raab and G. Bauer

Institut für Halbleiterphysik, Universität Linz, A-4040 Linz, Austria

Anomalous x-ray diffraction is used to investigate self-organized three dimensional PbSe quantum dot lattices formed by multilayer heteroepitaxial growth. Using a short-range dot ordering model in combination with a finite domain size, the ordering parameters are determined from the x-ray spectra. It is shown that the variance of the nearest-neighbor distances is significantly smaller and the laterally ordered domain size larger for the case of three dimensional trigonal PbSe dot lattices with *fcc*-stacking as compared to those with three dimensional hexagonal dot arrangement.

Introduction

High-resolution x-ray diffraction is a powerful tool for investigation of vertical and lateral correlations in three dimensional self-assembled quantum dots structures [1] – [3] obtained by multilayer heteroepitaxial growth. These correlations are caused by the elastic dot interactions [4], [5]. This not only results in a significant narrowing of the size distribution [6], but also provides an effective means for tuning the size and spacing of the dots by changes in the superlattice period [1], [7]. For different material systems, different ordered dot arrangements have been observed [1] – [5], which is due to the strong dependence of the dot interactions on the growth orientation as well as on the anisotropy of the elastic material properties [7]. The PbSe/ $\text{Pb}_{1-x}\text{Eu}_x\text{Te}$ system is unique in this respect because different interlayer correlations can be achieved in the superlattices by changes in the spacer thickness [8], dot size, or growth temperature [9].

In the present work, we employ anomalous x-ray diffraction with synchrotron radiation to drastically enhance the chemical contrast in multilayers by tuning the wavelength close to an inner shell absorption resonance [3]. This technique is applied to determine the ordering parameters of differently stacked self-assembled PbSe quantum dot lattices fabricated by molecular beam epitaxy based on the combination of a short-range order model with a finite domain size. As a result, it is shown that the lateral ordering is significantly better for *fcc*-stacked PbSe dot superlattices with 3D trigonal dot structure as compared to those with 3D hexagonal dot arrangement. This is due to the more efficient ordering mechanism based on the elastic interlayer dot interactions.

Experimental and Results

The samples were grown by molecular beam epitaxy onto on (111) BaF_2 substrates. Each superlattice stack (SL) consists of 50 to 60 periods of 5 monolayers (ML) PbSe alternating with $\text{Pb}_{1-x}\text{Eu}_x\text{Te}$ spacer layers with $x_{\text{Eu}} = 8\%$. Due to the corresponding -5.4% lattice mismatch, strain-induced coherent islands are formed in each PbSe layer when its thickness exceeds 1.5 ML. For the investigation of the ordering process as a function of the PbEuTe spacer layer thickness, a series of samples was prepared with spacer thicknesses d_s varying from 80 to 500 Å. After growth, the final PbSe dot layer

was characterized by atomic force microscopy (AFM). To analyze the lateral and vertical dot correlations anomalous coplanar high-resolution x-ray diffraction is used at a very low energy of 2400eV, where the x-ray wavelength is tuned to the Pb M-shell to suppress the scattering of the (111) reflection of the matrix material. These measurements were performed with an in-vacuum diffractometer at the ID 1 beamline of the European synchrotron radiation facility in Grenoble and high resolution reciprocal space maps (RSMs) were recorded for all samples around the (111) Bragg reflection.

Here, we focus on four different superlattice samples with a spacer thickness of 104, 164, 214, and 454 Å for sample A to D, respectively. The (111) anomalous reciprocal space maps are shown in Fig. 1 (a) – (d) with the primary beam along the $[101]$ azimuthal direction. Clearly, for all samples a large number of satellite peaks is observed both in the q_z direction along the surface normal, as well as in the direction q_x parallel to the surface. This clearly reflects the excellent order of the dots both vertically and laterally. However, whereas for samples A to C with thin spacer layers the lateral satellites are all aligned parallel to the q_x direction, the satellites for sample D are aligned in a direction inclined by 38° to the surface (dashed lines in Fig. 1). This indicates that in the latter case, the dots form a 3D trigonal dot lattice with *fcc*-like *ABCABC* stacking [1], whereas the dots for the other samples are aligned on top of each other in the vertical growth direction, corresponding to an overall 3D hexagonal dot arrangement [8].

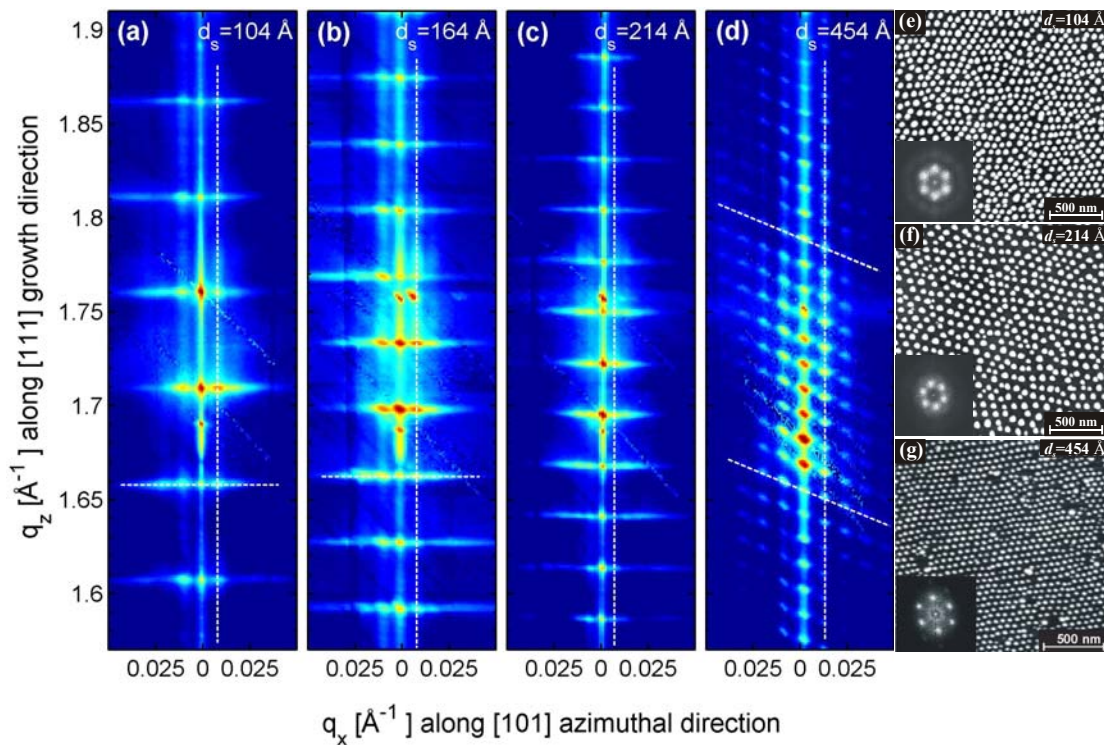


Fig. 1: (111) Reciprocal space maps (a) – (d) and atomic force microscopy images (e)-(g) of PbSe dot superlattice samples A - D with different PbEuTe spacer layers $d_s = 104, 164, 214, 454$ Å, respectively. The satellite arrangement indicates a 3D hexagonal dot lattice for (a) – (c) and 3D trigonal dot lattice for (d). The dashed lines mark the positions of the line scans along the q_x and the q_z direction used for the analysis of the order parameters.

To determine the quality of the dot ordering, diffraction line scans representing cross-sections of the reciprocal space maps in various q directions parallel (q_x) or perpen-

dicular (q_z) to the surface were recorded as indicated by the dashed lines in Fig. 1. Figure 2 shows the q_x -line scans along the lateral superlattice satellite peaks for the samples B and D. For comparison, in Fig. 2 (a) a line scan of sample B is included recorded at a 1.5 Å wavelength at the ROBL beamline. The improved contrast of the lateral dot satellite peaks for the longer wavelength is clearly visible in Fig. 2 (a) and (b).

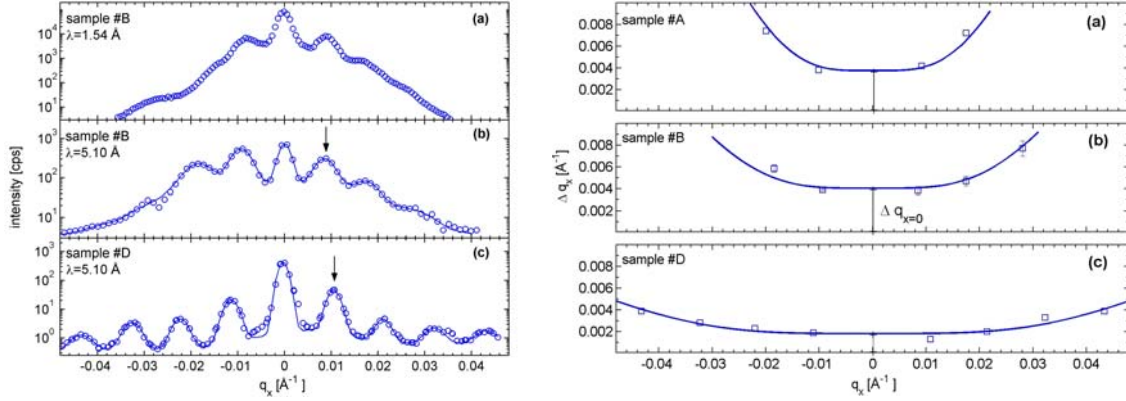


Fig. 2: *Left hand side*: Cross-sectional line scans of the XRD maps along the q_x direction for the vertically aligned dot sample B recorded with an x-ray wavelength of 1.5 Å (a) and 5.1 Å (b). The same is plotted in (c) for the ABCABC stacked sample D. The measured data (circles) are fitted with Gaussians with adjustable width (solid line). *Right hand side*: measured (symbols) and calculated (solid lines) FWHM Δq_x values of the peaks plotted over q_x . From the fits (solid lines), a variance σ_L and a domain size M of $\sigma_L = \pm 15\%$ and $M \approx 2$ is obtained for sample A, $\sigma_L = \pm 10\%$ and $M \approx 2$ for B, and $\sigma_L = \pm 5\%$ and $M \approx 5$ for sample C.

From the spacing of these lateral satellite peaks, the lateral in-plane dot distances L within the layers can be determined. For the vertically aligned samples A to C, respective L values of 780, 850 and 950 Å are obtained, as compared to $L = 670 \text{ \AA}$ for the *fcc*-stacked superlattice of sample D, in good agreement to the results obtained by AFM.

For the quantitative analysis of the order parameters, the full width at half maximum (FWHM) of the satellite peaks in q_x and q_z direction were determined as a function of the scattering vector q . This was achieved by fitting the cross-sectional line scans with Gaussians with adjustable width (solid lines in Fig. 2). To account for the broadening due the finite instrumental resolution, these values were corrected with the measured FWHMs of the PbSe-buffer peaks. The corrected FWHM, plotted on the right hand side of Fig. 2 as a function of q_x then represents the peak broadening caused by deviations of the ordered dot arrangement from an ideal perfect 3D lattice. Clearly for all samples the Δq_x half widths increase with increasing q_x scattering vector.

To analyze this behavior, we have adopted a model of short range ordering in the dot samples caused by the interlayer dot interactions during growth [2]. As the nature of the ordering is different perpendicular and parallel to the growth direction, we distinguish between the lateral correlations of the in-plane lateral dot positions (LL-correlation), the vertical correlations of the lateral dot positions (VL-correlation) and the vertical correlations of the vertical dot positions (VV-correlation). Assuming a short range order (SRO) model [2] for each correlation type, we can derive the lateral (Δq_x) and vertical (Δq_z) FWHM of the intensity satellite maxima as a function of the q_x position parallel to sample surface and the q_z position normal to the surface relative to the central 0th order peak within the reciprocal scattering plane as:

$$\Delta q_x \approx \sqrt{\left(\frac{1}{L}(q_x^2 \sigma_L^2)\right)^2 + M^2}; \quad \Delta q_z \approx \frac{1}{D}(q_x^2 \sigma_{DL}^2 + q_z^2 \sigma_D^2) \quad \text{with} \quad M \approx \frac{2\pi}{\Delta q_{x=0}} \cdot \frac{1}{L} \quad (1)$$

where D and L are the average vertical, respectively, lateral separation of the dots. In this expression, σ_D characterizes the degree of VV-correlations, σ_{DL} the degree of VL-correlations and σ_L the degree of LL-correlations in the samples in terms of the dispersion of the nearest neighbor dot-dot separations and M characterizes the finite domain size. For Δq_z we do not find a dependence of the values on q_z . Therefore, the VV-correlation along the superlattice growth axis is nearly perfect and is limited only by the stability of the epitaxial growth process. From the mean Δq_z values we derive a VL-correlation of the dot positions of about 25 times D_{SL} for the three vertically aligned samples, whereas for the sample with *fcc*-stacking we obtain a VL-correlation of only 7 times the SL period. This proves that the *vertical* ordering of the dots is more efficient in the 3D hexagonal samples, which is due to the fact that the strength of the elastic interactions in these samples is much stronger due to the smaller spacer thickness.

As is indicated by the solid lines in on the right hand side of Fig. 2, the q_x dependence of the Δq_x FWHM shows approximately a parabolic behavior. From the fits of the data using Eq. (1) we obtain σ_L values of 117, 86 and 36 Å for the samples A, B and D, respectively. Thus, the relative variance of the nearest neighbor lateral dot distance for the 3D hexagonal samples A and B is $\pm 15\%$ and $\pm 10\%$, respectively. In contrast, for the 3D trigonal sample D with $L = 670$ Å we obtain a variance of only $\pm 5\%$, indicating the lateral ordering is substantially better than for the 3D hexagonal dot samples. This agrees with the observation that the width of the lateral satellites of the trigonal dot sample is much smaller as compared to that of the 3D hexagonal dot samples (see Fig. 2). The same general trend applies also for the domain size values M , for which a value of $M \approx 2$ is obtained for the vertically aligned samples A and B, whereas a much larger value of $M \approx 5$ is obtained for sample D with *fcc*-stacking.

Conclusions

In conclusion, anomalous high resolution x-ray diffraction is a powerful technique for investigation of the ordering parameters of 3D quantum dot multilayers and superlattices. Exploiting the advantages of anomalous diffraction we were able to enhance the scattering contrast between the PbSe dots and the matrix material to record a large number of satellite peaks for detailed analysis. We have obtained information not only on the different kinds of 3D ordering mechanisms; we can also determine the quality of the lateral and vertical correlation of the dot positions. This work was supported by the FWF, GME and the Academy of Science (APART) of Austria.

References

- [1] G. Springholz, V. Holy, M. Pinczolits, and G. Bauer, *Science* **282**, 734-737 (1998).
- [2] V. Holý, J. Stangl, G. Springholz, M. Pinczolits, G. Bauer, I. Kegel, and T.H. Metzger, *Physica B* **283**, 65-68 (2000).
- [3] T.U. Schüllli, J. Stangl, Z. Zhong, R.T. Lechner, M. Sztucki, T.H. Metzger, and G. Bauer, *Phys. Rev. Lett.* **90**, 066105 (2003).
- [4] Q. Xie, A. Madhukar, P. Chen, N. Kobayashi, *Phys. Rev. Lett.* **75**, 2542 (1995).
- [5] J. Tersoff, C. Teichert, and M. G. Lagally, *Phys. Rev. Lett.* **76**, 1675 (1996).
- [6] M. Pinczolits, G. Springholz, and G. Bauer, *Phys. Rev. B* **60**, 11524 (1999).
- [7] V. Holy, G. Springholz, M. Pinczolits, G. Bauer, *Phys. Rev. Lett.* **83**, 356 (1999).

- [8] G. Springholz, M. Pinczolit, P. Mayer, V. Holy, G. Bauer, H. H. Kang, and L. Salamanca-Riba, Phys. Rev. Lett. **84**, 4669 (2000).
- [9] G. Springholz, A. Raab, R. T. Lechner, V. Holy, Appl. Phys. Lett. **82**, 799 (2003).
- [10] A. Raab, R. T. Lechner, and G. Springholz, Phys. Rev. B **67**, 165321 (2003).

Transmission Electron Microscopy of Nanostructures

W. Schwinger, G. Hesser, H. Lichtenberger and F. Schäffler
Institute of Semiconductor Physics, University Linz,
Altenbergerstr. 69, 4020 Linz

Transmission electron microscopy (TEM) is a powerful tool for detailed analysis of both crystalline and amorphous structures ranging from the micro to the nanometer scale. TEM is capable to display not only the real but also the reciprocal space of a sample; i.e. the diffraction pattern. In this report we will show – using selected examples – the analytical capabilities of the JEOL FasTEM 2011 with CCD-camera and EDS X-ray detector like the element specific composition of a hetero-bipolar-transistor, the determination of the dislocation density at a Si-Ge interface, the investigation of facets on a prestructured and annealed Si surface, the analysis of size and shape of SiC precipitations and the alignment of self-arranged Ge dots.

Introduction

Transmission electron microscopy is a powerful tool for detailed analysis of both crystalline and amorphous structures ranging from the micro to the nanometer scale. The JEOL 2011 FasTEM can be used for the investigation of interfaces, grain boundaries, nanocrystals, and hetero- and monocrystalline structures as well as for polymeric and organic samples.

TEM is capable to display not only the real but also the reciprocal space of a sample; i.e. the diffraction pattern. The recently installed CCD-camera and the EDS microprobe for qualitative and quantitative element-specific X-ray analysis are an excellent upgrade. The combination of all three devices TEM, CCD, and EDS results in a faster and more comprehensive analysis of samples.

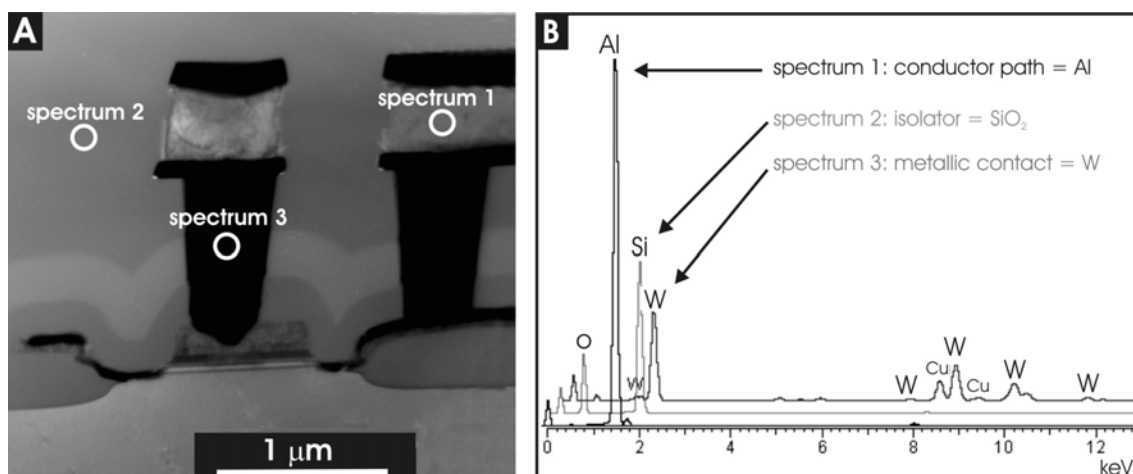


Fig. 1: (a) Cross section image of a transistor produced at austriamicrosystems at medium magnification (sample: 110X). (b) X-ray-spectra reveal the element-specific composition of the sample.

Experimental

Figure 1 (a) shows, at medium magnification, a cross section of a hetero-bipolar-transistor fabricated at austriamicrosystems. Using the EDS microprobe one can evaluate the local composition of the sample (Fig. 1 (b)). The conductor path is made of aluminum; the contacts consist mainly of tungsten and are isolated by SiO_2 . The brightness contrast in the TEM-image is due to the different atomic numbers of the elements resulting in different scattering cross section.

When growing heterostructures or other layer sequences the quality of the interface between two layers is of particular interest. With TEM it is possible to investigate interfaces in detail and to determine whether the overgrowth is mono-crystalline, poly-crystalline, amorphous, or disordered. The formation of dislocations is also of particular interest. Tilting the sample increases the contrast of these dislocations. The tilt direction is related to the burgers-vector characterizing the dislocations. One can thus not only determine the density of dislocations at an interface but also the type of dislocations.

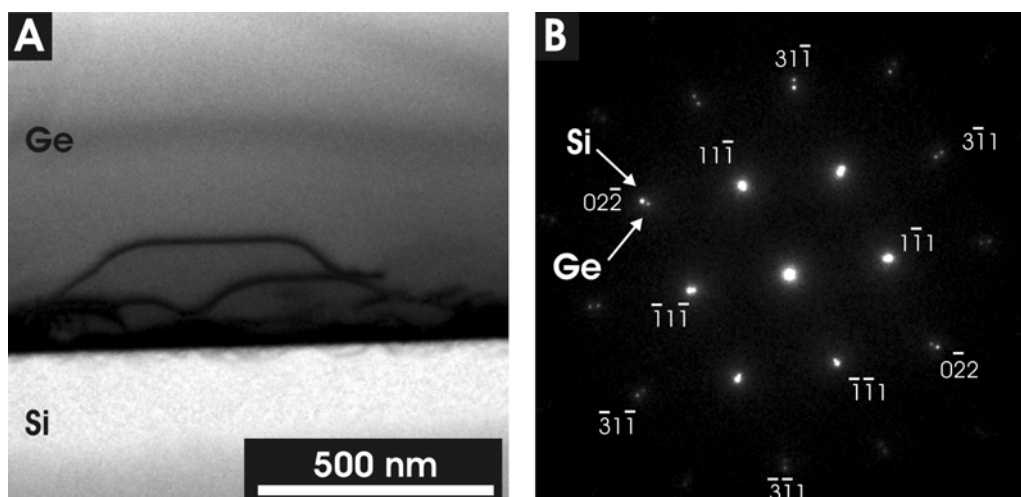


Fig. 2: (a) Dislocation at a Si-Ge interface (sample: 158X). Tilting the sample increases the dislocation contrast. (b) Diffraction image reveals that both the Si- and Ge-layer are mono-crystalline with the same crystal orientation. A split of the diffraction spots is due to the lattice mismatch of about 4% between Si and Ge having the larger lattice constant.

To get atomic resolution the sample has to be aligned along a main crystal axis. When tilting a sample atomic resolution is lost. Figure 2 (a) shows dislocations at an interface between pure Ge deposited on pure Si. Building a multi-image-collage one can thereby determine the defect density and defect depth at the Si-Ge-interface.

The diffraction images of that interface (Fig. 2 (b)) shows that both the Si- and the Ge-layer are mono-crystalline with the same crystal orientation. Since the lattice constant of Ge is about 4% larger than the one of Si, diffraction spots split, with the Ge-spot lying closer to the central (000)-spot (reciprocal space!). This can be especially seen at the higher order spots like the $\{022\}$ and the $\{311\}$. The nonindexed spots result from rescattered spots and thus do not correspond to certain lattice planes and are therefore called forbidden spots.

Two main preparation techniques for solid TEM-sample are common: cross-sectional and plan-view showing either a view along the surface or perpendicular to the surface.

A cross-sectional view not only reveals the surface structures but also the layer sequence, which is not detectable with e.g. AFM.

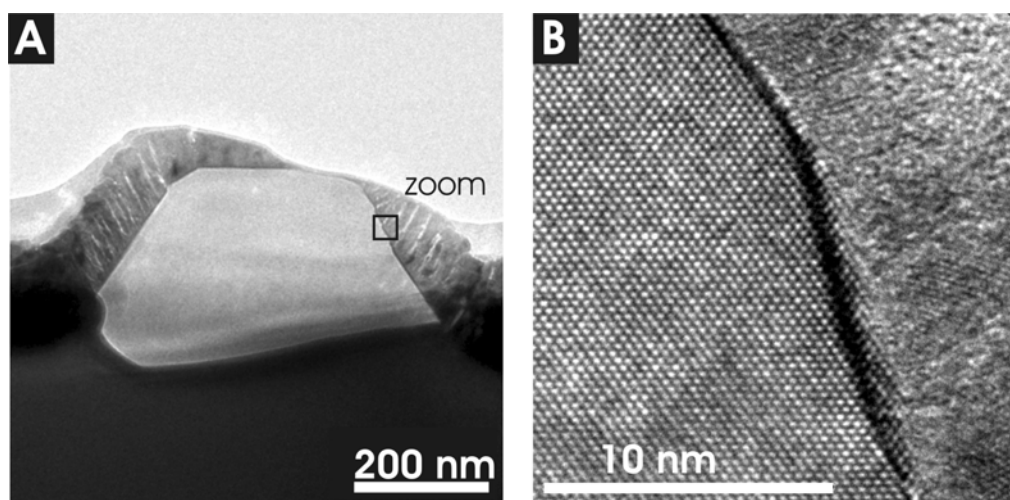


Fig. 3: (a) Cross-section of an originally rectangular Si-wire after annealing and covering with titanium (sample: 082X). Transient-enhanced Si diffusion leads to the formation of stable facets, which can be seen in high-resolution images like (b) with atomic resolution; [1] for more details.

Figure 3 (a) shows a cross-section through a capped wire structure. Originally rectangular Si-wires changed their shape during vacuum annealing and formed facets before covered with titanium. The high-resolution image Fig. 3 (b) shows not only these small facets in detail but also the structure of the deposited titanium. See [1] for more details.

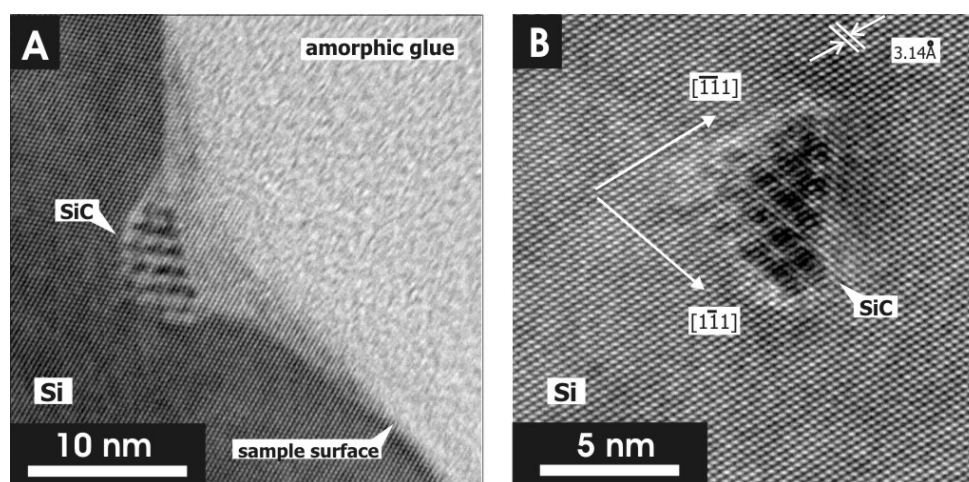


Fig.4: A: High-resolution image showing a cross-section of a SiC-precipitate, which disrupted further overgrowth (sample: 47X). B: High-resolution image showing a buried SiC precipitate (sample: 47X).

Annealing a submonolayer of Fullerene-molecules deposited on Si(100) and buried with Si leads to the formation of SiC precipitates. High resolution TEM-images reveal Moiré-fringes resulting from the overlap of crystalline Si and SiC as shown in Figs. 4 (a) and 4 (b). Knowing the lattice constant of Si and measuring the period of the Moiré-pattern one can calculate the lattice constant of SiC and thus can determine whether

the precipitates are relaxed or strained. One can also see that large precipitates disrupt further overgrowth leading to a funnel-shaped surface (Fig. 5 (a)) whereas small precipitates are covered by crystalline Si (Fig. 4 (b)).

Figure 5 shows the arrangement of Ge-dot in 3-layer-sequence. TEM images show the perfect self-arrangement of the dots. In Fig. 5 (a) in addition to the layers structure also the tension contrast can be seen. Figure 5 (b) displays mainly mass contrast between Si and Ge due to their different atomic mass.

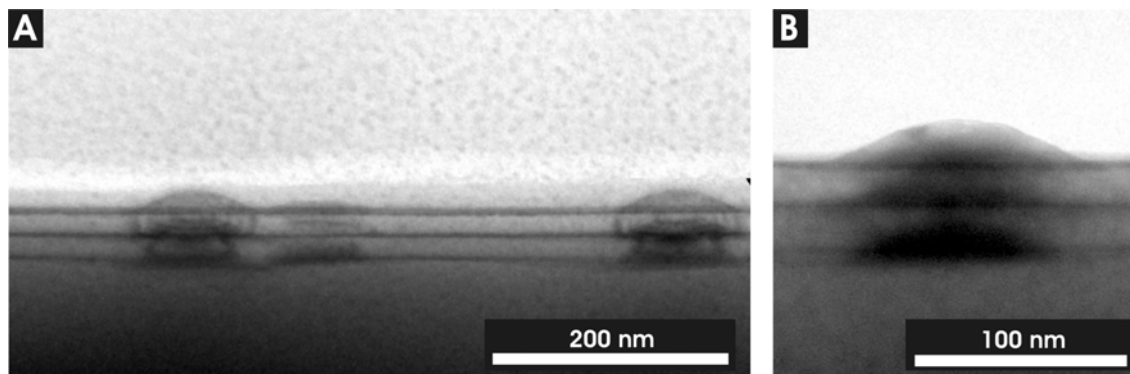


Fig. 5: (a) 3-layer-sequence of self-arranged Ge-dots on Si. Bows between the layers indicate tension; (b) Detail of (a) focused on mass-contrast; [2] for details (131X).

Conclusion

These examples show that TEM is a powerful tool for the detailed analysis with atomic resolution of crystalline mono- and hetero-structures revealing details of the sample composition since in addition to an image of the sample in real space also the reciprocal space of the sample, i.e. the diffraction pattern – which gives information of the crystal growth in more detail – can be displayed. The additional EDS X-ray detection system is a perfect upgrade allowing a qualitative and quantitative element specific analysis of the sample composition. The modern CCD-camera allows electronic image processing giving instant results.

References

- [1] H. Lichtenberger, M. Mühlberger, “Transient-enhanced Si diffusion on native-oxide-covered Si(001) nanostructures during vacuum annealing”, *Appl. Phys. Lett.* **82**, 3650 (2003)
- [2] Zhenyang Zhong, A. Halilovic, “Positioning of self-assembled Ge islands on stripe-patterned Si(001) substrates”, *J. Appl. Phys.* **93**, 6258 (2003)

Acknowledgements

A. Bonanni, H. Sitter, Institut für Festkörperphysik, JKU Linz

fke - Institut für Festkörperelektronik, TU Wien

AMS - austriamicrosystems AG, A-8141 Schloss Premstätten

E+E - Elektronik Ges.m.b.H., A-4209 Engerwitzdorf

Site-Controlled and Size-Homogeneous Ge Islands on Prepatterned Si

Z. Zhong, A. Halilovic, F. Schäffler and G. Bauer

Institut für Halbleiter-und Festkörperphysik, Universität Linz, A-4040 Linz

We report on a combination of lithography and self-assembly techniques which results in long-range two-dimensionally ordered Ge islands. Island lattices with perpendicular but also with obliquely oriented unit vectors were realized. Quantitative analysis of the island topographies demonstrates that the size dispersion of these islands is much smaller than that found on flat substrates. Furthermore, island formation on the patterned substrates is observed already for a smaller amount of Ge deposition than on unpatterned ones.

Introduction

Semiconductor islands have attracted a lot of interest because of their physical properties and their potential for devices. A simple route to obtain such islands is to exploit the so-called Stranski-Krastanow (SK) growth mode. Beyond a critical thickness of a wetting layer, three-dimensional (3D) islands form spontaneously to reduce the misfit strain. In general, these defect-free islands nucleate at random positions and exhibit rather large size dispersions. In the Ge/Si system for growth temperatures around 600°C, typically a bimodal distribution is found, consisting of pyramid- and dome-shaped islands. However, islands with a narrow size distribution and a site-control are demanded both for fundamental investigations and for applications. Recently, major progress was reported by combining lithography and self-assembly techniques for the positioning of islands. So far two-dimensionally long-range ordered islands were reported for a square lattice, either by using oxide masks or by growing directly on prepatterned substrates, which was demonstrated by our group [1], [2]. However, this is not entirely sufficient to demonstrate the intentional site-control of the islands. Furthermore, no quantitative analysis of the size homogeneity of the islands on patterned substrates has been done so far. In this letter, Ge islands grown on prepatterned Si (001) substrates in a parallelogram lattice, as well as in a square lattice, are shown. A detailed analysis of their surface morphology demonstrates that a breakthrough was achieved as far as the intentional site-control and the size homogeneity of the islands are concerned [3].

Experimental

Sample Preparation

The Si (001) templates were fabricated by holographic lithography via double exposure and reactive ion etching (RIE), which result in 2D periodic pits on the surface. In these 2D lattices of the pits, the length and the orientations of the unit vectors can be intentionally changed. After an ex-situ chemical cleaning and an in-situ thermal desorption of the patterned and flat substrates, a 130 nm Si buffer layer was grown at a rate of 0.5 Å/s ramping the temperature from 500 °C to 650 °C. Subsequently 4 – 10 monolayers (MLs) Ge were deposited at a rate of 0.05 Å/s at 700 °C with 7 s growth interruption after each monolayer. For comparison, islands on patterned and flat substrates were

strates were grown simultaneously. In the following, the samples with n MLs Ge deposition on prepatterned and flat substrates are named as P n and F n , respectively. Their surface morphologies were investigated in air with a Park Scientific atomic-force microscope (AFM) using the contact mode with an ultra-sharp tip. The AFM images with 512 x 512 points are analyzed in detail.

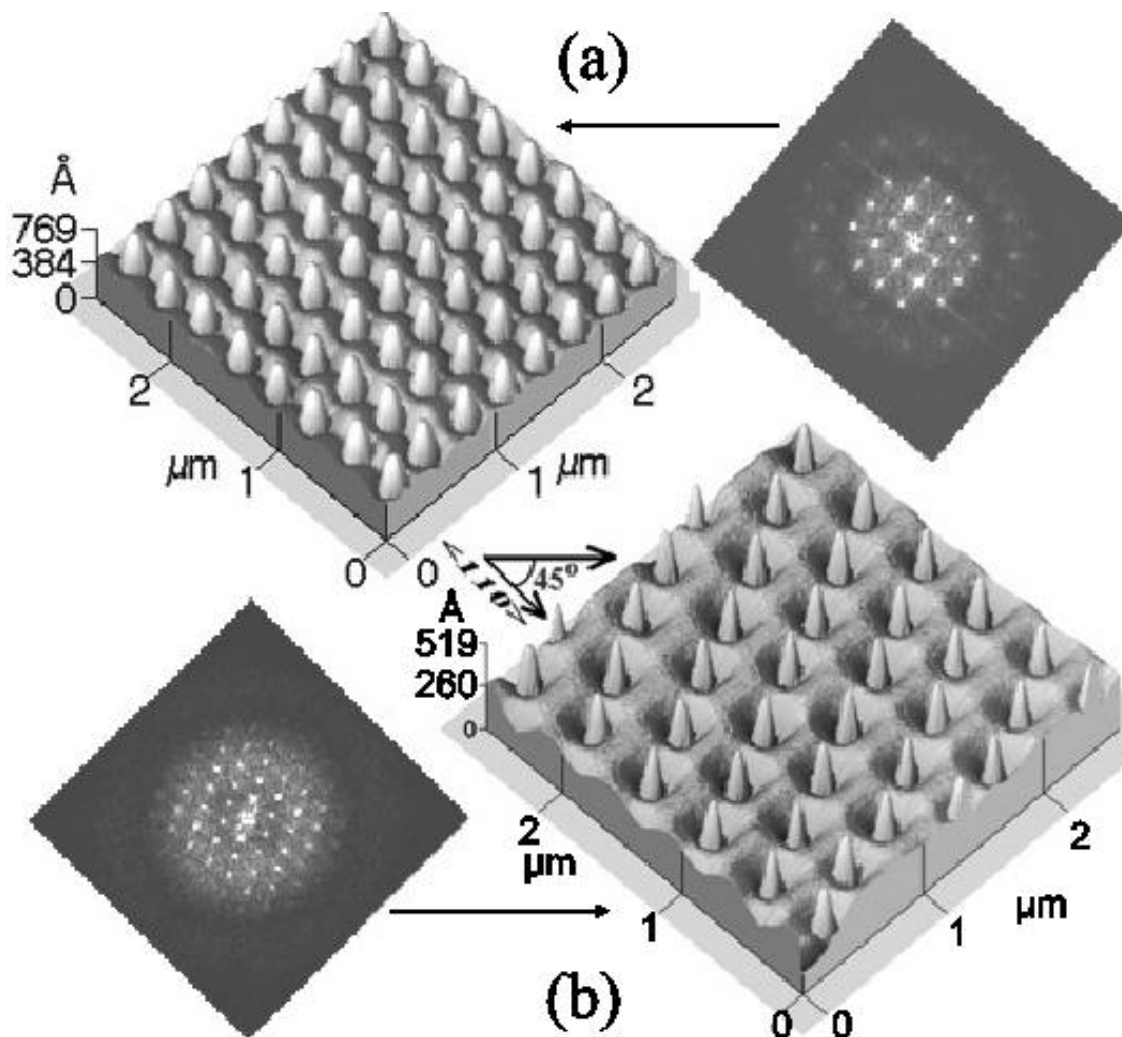


Fig. 1: 3D topography of the islands in (a) sample P10 (period: 370 x 370 nm, along $\langle 110 \rangle$ directions), (b) sample P6 (period: 400 x 400 nm, along $[110]$ and $[100]$ directions). The Fourier transforms (FT) of the topographies are also shown at the left in (a) and right in (b), their sizes are 0.034 nm^{-1} , after Ref. [3].

Measurements

The 3D topographies and their 2D Fourier transforms (FT) of samples P10 and P6 are shown in Figs.1 (a) and (b), respectively. Evidently, the islands on these patterned substrates are perfectly two-dimensionally arranged. In the FT images, a number of narrow satellite peaks in 2D plane are clearly visible. Higher-order satellite peaks are damped, primarily due to the envelope function that is determined mainly by the size and the shape of the islands. These FT images explicitly demonstrate the 2D long-range ordering (LRO) of the islands, in a square lattice along two $\langle 110 \rangle$ directions in Fig. 1 (a), and in a parallelogram lattice along $[110]$ and $[100]$ directions in Fig. 1 (b). It also implies that the regular arrangement of the islands can be intentionally determined

on the prepatterned substrates. For comparison, the 3D topographies of the islands grown on flat substrates (samples F10 and F6) were investigated as well, for which the islands are randomly distributed. Another important result of the islands grown on patterned substrates is that they are mono-modal. From the aspect ratios and the morphologies of the island, it can be seen that only dome-shaped islands grow in these samples. Our surface orientation analyses of the islands in samples P6 and P10 show that the dominant facets of these islands are $\{15\ 3\ 23\}$ and $\{1\ 1\ 3\}$, like for the growth on unpatterned substrates. On the other hand, in sample F10, some superdome-shaped islands (4.5% out of $16/\mu\text{m}^2$) appear.

The 2D periodic pits after Si buffer layer growth look like inverted truncated-pyramids, in general with sidewall slopes in the range of about $4.5^\circ \sim 15^\circ$ and depths smaller than 20 nm. The sidewalls of the pits are composed of steps. In analogy to the growth of Ge on stripe-patterned substrates, Ge (or Ge-Si) ad-dimers on the terraces between the pits readily migrate to the edges and tend to diffuse to the sidewalls. Those at the sidewalls prefer to migrate downwards. As a result, Ge atoms tend to accumulate at the bottom, i.e. at the intersections of the sidewalls, facilitating there the nucleation of Ge-rich islands. Given the small pit bottom area, only one island per pit can be grown. This qualitative model for the growth process is confirmed by the island ($\langle H \rangle = 95 \text{ \AA}$) formation in sample P4 with only 4 MLs Ge depositions, as shown in Fig. 1 (b). In sample F4 grown on a flat substrate, however, no islands are observed. The islands in sample P4 are all lens-shaped without particular facets. During growth, the Si-Ge intermixing impact on the size and/or shape of the islands, but it essentially does not affect the positioning of the islands. The photoluminescence data of capped islands on patterned and on flat substrates¹⁶ indicate that the amount of SiGe intermixing is similar. From preliminary x-ray data we obtained for the growth temperature of 700°C an average Ge content of about 45% for the dome-shaped islands on both patterned and flat substrates.

The excellent size homogeneity of the islands in samples P_n ($n > 6$) is mainly attributed to the periodic structure on patterned substrates. The surface on patterned substrates is composed of 'unit cells'. Based on the above discussion, it is reasonable to assume that only Ge atoms deposited within these unit cells can take part in the islanding in the corresponding pits. Consequently, the number of Ge atoms that can contribute to each island is about the same. In addition, the island average size in samples P_{10} , P_6 and $P_6(A1)$ is larger than that in the corresponding samples F_{10} and F_6 , respectively. Therefore, with same amount of Ge deposition, larger islands are formed in samples P_n than in samples F_n ($n > 6$). To some extent we can adjust the size of the coherent islands to the desired value with excellent homogeneity, only via changing the amount of the deposited Ge.

Conclusion

In summary, we realized both two-dimensional long-range ordering and size homogeneity of Ge-rich islands via depositing Ge on the prepatterned Si (001) substrates. The main features of the island growth on the patterned substrates are explained qualitatively. Our results demonstrate that the regular island arrangement and their homogeneous size can be adjusted within certain limits to the desired ones by combining the lithographic and the self-assembly techniques. These achievements on the site-control and the homogeneity of the islands will stimulate both fundamental investigations and device applications.

Acknowledgements

This work was supported by the FWF, Vienna (project No 14684), the EC project ECOPRO.

References

- [1] Z. Zhong, A. Halilovic, M. Mühlberger, F. Schäffler, and G. Bauer, *J. Appl. Phys.* 93, 6258 (2003).
- [2] Z. Zhong, A. Halilovic, M. Mühlberger, F. Schäffler, and G. Bauer, *Appl. Phys. Lett.* 82, 4779 (2003).
- [3] Z. Zhong, G. Bauer, *Appl. Phys. Lett.* 84, 1922 (2004).

Strain Relaxation and Misfit Dislocation Interactions in PbTe on PbSe (001) Heteroepitaxy

K. Wiesauer and G. Springholz
Institut für Halbleiterphysik, Universität Linz, A-4040 Linz, Austria

Strain relaxation of heteroepitaxial PbTe layers on PbSe (001) by misfit dislocation formation is shown to take place near equilibrium without kinetic barriers. The comparison of the experimental data with different strain relaxation models shows that mutual dislocation interactions are of crucial importance for the strain relaxation process. This results in a faster relaxation than predicted by the Frank and van der Merwe model for non-interacting dislocation arrays.

Introduction

Strain relaxation is a key issue in lattice-mismatched heteroepitaxy [1], [2]. It occurs via formation of coherent three-dimensional (3D) islands in the Stranski-Krastanow growth mode or by the formation of interfacial misfit dislocations. The latter is usually described by the Matthews-Blakeslee [3] or Frank-van der Merwe [4] strain relaxation models, which yield the critical layer thickness as well as average dislocation densities in thermodynamic equilibrium. For the case of semiconductors, however, many experimental works have demonstrated that the actual course of strain relaxation is strongly affected by the dislocation kinetics [1], [2], which are determined by various processes such as nucleation, multiplication, thermally activated glide as well as blocking of dislocations. These processes impose kinetic barriers for misfit dislocation formation and therefore strongly retard the relaxation process. In the present work, we actually demonstrate the opposite behavior for PbTe on PbSe (001) heteroepitaxy with a lattice-mismatch of 5.2%. We not only find that a near-equilibrium strain state is formed in the layers but even more that the actual course of strain relaxation is significantly faster than predicted by the Mathews-Blakeslee (MB) or Frank-van der Merwe (FdM) models. This remarkable fact is shown to be due to the strong influence of mutual dislocation interactions on the energetics of the dislocation network. Comparing our results with recent models that have incorporated these dislocation interactions [5], we still find a significant deviation of our experimental data from the model calculations. Our result can be explained quite well under the assumption that the dislocation self-energy is essentially independent of the layer thickness.

Experimental and Results

The PbTe/PbSe samples were grown by molecular beam epitaxy. First, several μm thick PbSe buffer layers were deposited onto (001) oriented PbSe substrates at a temperature of 380°C. Then, PbTe layers were grown on top with thicknesses ranging from 1 to 50 monolayers (ML), where 1 ML corresponds to a layer thickness of 3.23 Å. *In situ* reflection high-energy electron diffraction (RHEED) was employed to monitor the growth process and determine the strain-state of the layers as a function of layer thickness. Complementary investigations were carried out using ultra-high vacuum STM as described in Ref. [6]. Here we focus on the question of how strain relaxation is influenced by the growth conditions, which were varied over a wide range of substrate tem-

peratures of 70 to 360°C and growth rates of 0.12 to 1.13 ML/sec. Complementary post-growth annealing studies were carried out for layers for which the growth was interrupted at layer thicknesses between 1 and 10 ML.

Figure 1 (a) shows the RHEED patterns recorded at a PbTe layer thickness of 14 ML. The elongated shape of the diffraction streaks indicates that a 2D surface is retained during PbTe growth in spite of the rather large lattice-mismatch. This is in agreement with our previous scanning tunneling microscopy studies [6]. Due to the small scattering angles, the lateral spacing of the diffraction streaks directly corresponds to the reciprocal space lattice vector, which is inversely proportional to the in-plane surface lattice constant. To determine the course of strain relaxation, intensity line profiles were recorded across the diffractions streaks as indicated by the white line in Fig. 1 (a) and shown in Fig. 1 (b). The evolution of these profiles as a function of layer thickness is displayed in the grey scale image of Fig. 1 (c). At a PbTe layer thickness of 1 ML, clearly the streaks start to shift inwardly, signifying the onset of strain relaxation. Using the initial PbSe surface with its bulk lattice parameter of $a_{0,\text{sub}} = 6.124 \text{ \AA}$ as a reference, the relative change of the streak spacing directly yields the relaxed strain ϵ_{rel} of the layer as a function of layer thickness h .

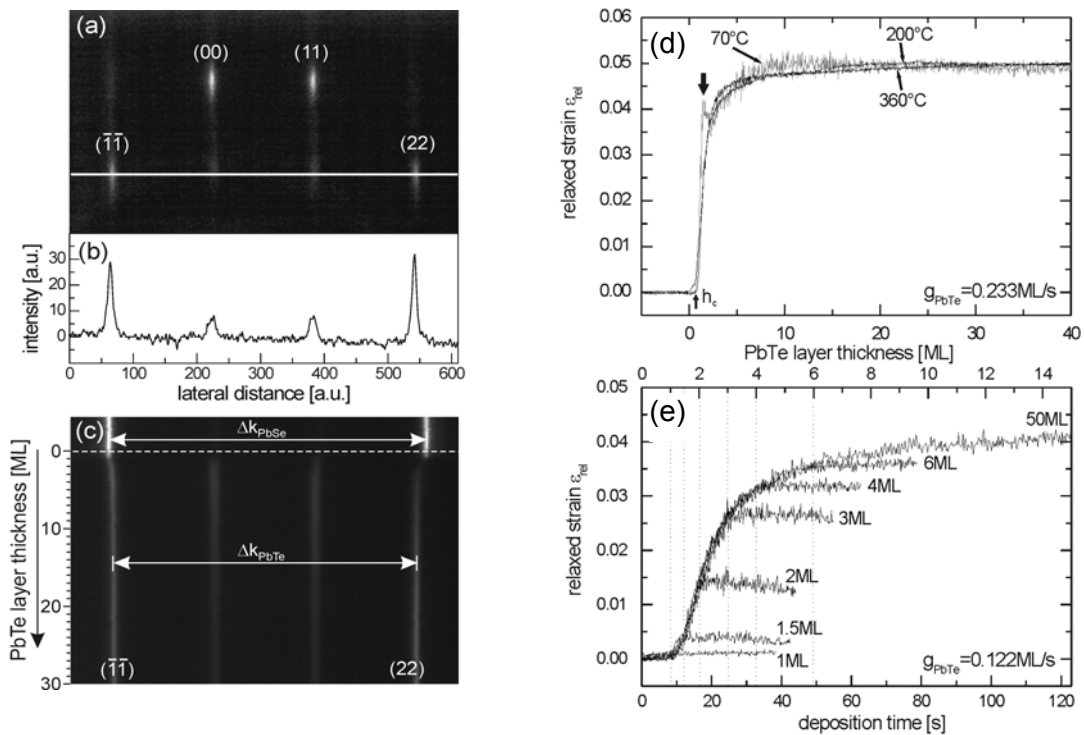


Fig. 1: Left hand side: (a) RHEED pattern of 14 ML PbTe on PbSe (001) recorded along the [100] azimuth. (b) Intensity profile across the (-1-1) and (22) streaks as indicated by the white line in (a). (c) Grey-scale image of the intensity profiles as function of the PbTe layer thickness. Right hand side: Strain relaxation curves of PbTe/PbSe (001) as a function of the epilayer thickness measured at different deposition temperatures (d) and during post-growth annealing (e) at 360°C after interruption of the growth at 1, 1.5, 2, 3, 4 and 6 ML.

The resulting relaxation curves for PbTe epilayers deposited at different growth temperatures of 70, 200 and 360 °C are shown in Fig. 1 (d). In all cases, the onset of strain relaxation occurs at a critical thickness of 1 ML, and no retardation of strain relaxation occurs as the temperature decreases. Furthermore, when interrupting the growth at

PbTe thicknesses of 1, 1.5, 2, 3, 4 and 6 ML (see Fig. 1 (e)), no further post-growth relaxation was observed during subsequent sample annealing. Identical results were obtained when the growth rate was varied between 0.12 to 1.13 ML/sec. This clearly demonstrates that strain relaxation in the PbTe/PbSe (001) heteroepitaxial system is not influenced by dislocation kinetics but takes place at near-equilibrium conditions.

To gain more insight on the strain relaxation process, the course of strain relaxation was modeled using the FdM approach in which the total energy of the layer/substrate system is minimized with respect to the dislocation density [4]. This facilitates the introduction of dislocation interactions [5]. Even more, the nearly perfect square network of pure edge misfit dislocations formed in the PbTe layers [6] represents a nearly ideal realization of the dislocation configuration envisioned by the original FdM model. This is illustrated by the STM image of a 9 ML PbTe layer displayed as insert in Fig. 2, in which the dark lines represent the grid of subsurface edge dislocations with a Burgers vector of $b = \frac{1}{2}[110]a_0$. Neglecting surface and interface energies, the total energy density e_{tot} of a 2D epilayer on a non-compliant substrate is given by the sum of the coherency energy e_{coh} due to the biaxial strain in the layer and the self-energy e_{MD} of the misfit dislocation network. For relaxed layers, the initial misfit strain ε_0 is reduced by $-(\rho_{\text{MD}} b_{\parallel, \text{edge}})$ by misfit dislocations, where $b_{\parallel, \text{edge}}$ is the edge component of the Burgers vector within the interface plane (here equal to b) and ρ_{MD} is the 1D dislocation line density.

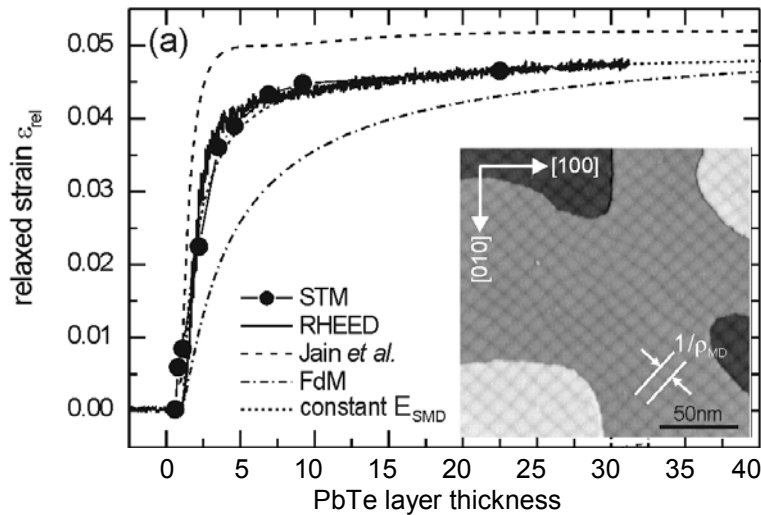


Fig. 2: Comparison of PbTe/PbSe (001) relaxation curves measured by RHEED (solid) and STM (dots) with the FdM model for non-interacting dislocations (dash-dotted), the model of Jain *et al.* for interacting dislocation arrays (dashed), and the model of constant dislocation energy for $\delta = 0.05$ (dotted). Insert: STM image of a 9 ML PbTe layer on PbSe (001), where the dark lines indicate the quasi-periodic subsurface network of edge dislocations.

Thus, the coherency energy can be written as $e_{\text{coh}} = B h (e_0 - \rho_{\text{MD}} b_{\parallel, \text{edge}})^2$ where the elastic energy factor $B = 2\mu(1 + \nu)/(1 - \nu)$ contains the shear modulus μ and Poisson ratio ν of the epilayer. The self-energy of the dislocation network e_{MD} is calculated by summation of the self-energies E_{SMD} of each misfit dislocation as $e_{\text{MD}} = 2 \rho_{\text{MD}} E_{\text{SMD}}$, where the factor of two accounts for the fact that two orthogonal misfit dislocation arrays are required to relax the biaxial lattice-mismatch.

In the original FdM model, the self-energy of each isolated single misfit dislocation is given by the logarithmic expression $E_{\text{SMD}} = Kb^2 (4\pi)^{-1} \ln(h\alpha/b)$ where $K = \mu/(1-\nu)$ is the dislocation energy coefficient, here for pure edge dislocations, and the parameter α accounts for the energy at the dislocation core, which is usually chosen as 4 for semiconductors. Minimizing the total energy e_{tot} with respect to the dislocation density ρ_{MD} yields the critical thickness h_c as well as the equilibrium relaxed strain ε_{rel} as a function of layer thickness as:

$$h_c = \frac{Kb^2}{4\pi B \varepsilon_0 b_{\parallel, \text{edge}}} \cdot \ln(h_c \alpha / b) \quad \varepsilon_{\text{rel}}^{\text{FdM}}(h) = -\varepsilon_0 \left[1 - \frac{h_c}{h} \frac{\ln(h\alpha/b)}{\ln(h_c \alpha / b)} \right] \quad (1)$$

Figure 2 shows the comparison of the calculated strain relaxation ε_{rel} with the data obtained by RHEED and STM. For the latter, ρ_{MD} was directly determined from the average dislocation spacing [6] observed in the STM images as indicated in the insert of Fig. 2. Whereas both experimental results fall onto the same line, the calculated $\varepsilon_{\text{rel}}(h)$ is considerably lower, *i.e.*, the experimentally observed strain relaxation is much *faster* than predicted by the FdM model. This is in spite of the fact that the calculated critical thickness of $h_c = 1\text{ML}$ is in excellent agreement with the experimental value.

To resolve the disagreement, the expression for the dislocation self-energy has to be modified in order to include the mutual dislocation interactions that become important when the dislocation spacing is comparable to the layer thickness. Here we follow the calculation of Jain *et al.* [5], who have derived the self-energy of a periodic array of interacting dislocations. The minimization of the total energy as a function of dislocation density can then be done only numerically. To obtain the same critical thickness as in the FdM model and the experiments, a slightly larger core parameter α has to be used. The result of this model is plotted as dashed line in Fig. 2. In this case, a very fast initial strain relaxation is predicted, similar as observed in the experiments. However, the model yields an almost complete strain relaxation already at 5 ML layer thickness, where the experimental values are still considerably lower. This indicates that the Jain model overestimates the effect of dislocation interactions.

To resolve this problem, we propose a new model that assumes a constant dislocation self-energy of $E_{\text{SMD}} = Kb^2 / 4\pi$ independent of the layer thickness. In this case, straightforward explicit expressions for h_c and ε_{rel} are obtained, with

$$h_c = K b^2 (4\pi B b_{\parallel, \text{edge}} \varepsilon_0)^{-1} \quad \text{and} \quad \varepsilon_{\text{rel}} = \varepsilon_0 [(1 - \delta) - h_c / h] \quad (2)$$

where δ is a small correction parameter to account for a possible residual strain at large layer thicknesses. As is demonstrated by the dotted line in Fig. 2 with this new functional dependence the experimental data can be exactly reproduced.

Conclusions

In conclusion, dislocation interactions are of great importance for the strain relaxation process in heteroepitaxial layers. For PbTe on PbSe (001) system we therefore find a significantly faster strain relaxation as compared to the FdM model for non-interacting dislocations. This can be explained only by the effect of the dislocation interactions on the formation energies of the dislocations. Using a model in which the dislocation self-energies are assumed to be constant as a function of layer thickness, an excellent agreement with the experimental data is obtained. This work was supported by the FWF and the Academy of Sciences of Austria.

References

- [1] S. Jain, M. Willander and R. Van Overstraeten, *Compound Semiconductors Strained Layers and Devices* (Kluwer Academic, Boston, 2000).
- [2] R. Hull and J. Bean, *Crit. Rev. Solid State Mater. Sci.* **17**, 507 (1994); and J. H. van der Merwe, *Crit. Rev. Solid State Mater. Sci.* **17**, 187 (1991).
- [3] J. W. Matthews and A. E. Blakeslee, *J. Cryst. Growth* **72**, 118 (1974).
- [4] F. C. Frank and J. H. van der Merwe, *Proc. Roy. Soc. A* **198**, 205 (1949).
- [5] S.C. Jain, A.H. Harker and R.A. Cowley, *Phil. Mag. A* **75**, 1461 (1997); and J.R. Willis, S.C. Jain and R. Bullough, *Phil. Mag. A* **62**, 115 (1990).
- [6] G. Springholz and K. Wiesauer, *Phys. Rev. Lett.* **88**, 015507 (2002).

***In situ* Characterization of MOCVD Growth by High Resolution X-Ray Diffraction**

K. Schmidegg, A. Bonanni and H. Sitter

**Institut für Halbleiter- und Festkörperphysik, Johannes Kepler Universität,
Altenbergerstr. 69, A-4040 Linz**

X-ray diffraction is used for the *in situ* characterization of the growth of cubic GaN by metalorganic chemical vapor deposition. Our setup permits the simultaneous measurement of a wide angular range and requires neither goniometer nor exact sample positioning. Time-resolved measurements during growth give access to film thickness and growth rate as well as information on the chemical composition of ternary compounds. Additionally, the relaxation of the crystal lattice during heteroepitaxial growth of GaN on AlGaN can be measured directly.

Introduction

In situ monitoring and process control is an increasingly important point for the epitaxial growth of semiconductor layers. In high vacuum environments, reflection high energy electron diffraction (RHEED) is well established and provides real time information about growth rate and surface reconstruction. Metalorganic chemical vapor deposition (MOCVD), the favorite growth technique for industrial production of compound semiconductors, operates near atmospheric pressure and has to rely on techniques which are not sensitive to the presence of a gas atmosphere in the reactor. Optical methods such as spectroscopic ellipsometry (SE) [1], [2], reflectance difference spectroscopy (RDS) [3], [4] or laser reflectometry have been developed for that purpose. Most of the information needed for growth control can however only be accessed through models and careful calibration of the device and none of these methods gives direct access to structural parameters of the sample.

Our intent was to show that X-ray diffraction (XRD), a powerful tool for *ex situ* characterization, can also be used for real time measurements during MOCVD growth. It provides detailed information on the crystallographic structure of the growing layers. Up to now, synchrotron radiation was necessary to perform measurements with both time and angular resolution [5] – [8]. Our setup has the advantage that neither a goniometer nor exact sample positioning are required and it is compact enough to be attached to an industrial size MOCVD reactor. We have applied this method to monitor the growth of cubic GaN yielding information on growth rate, ternary compound composition, strain relaxation and thermal expansion.

Experimental

Our MOCVD system is an AIXTRON AIX 200 RF-S horizontal flow reactor designed for nitride compound semiconductor growth. Trimethylgallium (TMGa) and Ammonia (NH₃) are used as Ga and N precursors, respectively, and N₂ and H₂ as carrier gases. The sample is mounted on a graphite susceptor which is inductively heated by a radio-frequency (RF) generator. Beryllium windows were mounted to the top and lateral reactor viewports to allow the passage of the incident and diffracted X-ray beam, respectively. The X-ray system consists of a standard Cu X-ray ($\lambda_{\text{CuK}\alpha} = 1.5418 \text{ \AA}$) source and a position sensitive detector which permits the simultaneous acquisition of an angular

range of about 2° . The main difference to conventional systems lies in the fact that neither a goniometer nor exact sample positioning are required. The diffraction angle will be called $\Delta\varepsilon$ to reflect the fact that relative measurements were performed. The angular resolution of this system is mainly dependent on the distance between sample and detector and can be adjusted to the desired accuracy and angular range.

All overgrowth experiments were performed on cubic GaN (001) templates which were grown on GaAs (001) substrates by molecular beam epitaxy (MBE) [9]. The size of these samples was about 1 cm^2 and the thickness of the MBE GaN layer around 400 nm. Prior to introduction into the MOCVD reactor, all samples were cleaned in a sequence of Acetone, Ethanol and Methanol to remove organic surface contaminations. Sample heating and cooling was done in N_2 atmosphere to ensure inert conditions. An additional surface cleaning step had to be performed in the reactor before growth initiation to remove native oxide layers. Pre-running H_2 gas for 30 s at growth temperature etched the topmost layer of the template and created a bare GaN surface. The growth process was performed under H_2 ambient with a constant NH_3 flux of $5.56 \times 10^{-3}\text{ mol/min}$ at temperatures ranging between $700\text{ }^\circ\text{C}$ and $800\text{ }^\circ\text{C}$. The TMGa flux was varied between $8.837 \times 10^{-6}\text{ mol/min}$ and $7.953 \times 10^{-5}\text{ mol/min}$ to test the dependence of the growth rate and to determine a stable growth regime. Similar parameters were used for the growth of a GaN layer on an AlGaIn/GaN template containing 14% Al.

Results and Discussion

Time-resolved measurements yielded diffraction spectra in an angular range of about 2° with a temporal resolution of 2 s. Figure 1 (a) shows typical spectra of the GaN (224) diffraction peak as acquired during the growth of c-GaN on an MBE template. The spectrum at $t = 0\text{ s}$ represents the XRD signal of the MBE template at growth temperature. Due to the lattice mismatch of about 20% between GaAs and GaN, the substrate peak is out of range of our setup. This data was used to determine the thickness of the growing layer as the intensity of the diffraction peak is linearly dependent on its thickness for thin epitaxial films. The solid lines in the figure are fits using a pseudo-Voigt function which gave the peak intensity, position and full width at half maximum (FWHM) of the curve. The intensity from the MBE layer alone was taken as a reference for thickness calculations. Deviations from the linear behavior were found for thicknesses above $1.5\text{ }\mu\text{m}$, when the intensity began to saturate due to the fact that the path length of the X-rays in the sample approached the extinction length. Layer thicknesses were cross-calibrated with optical methods to verify the values found by XRD.

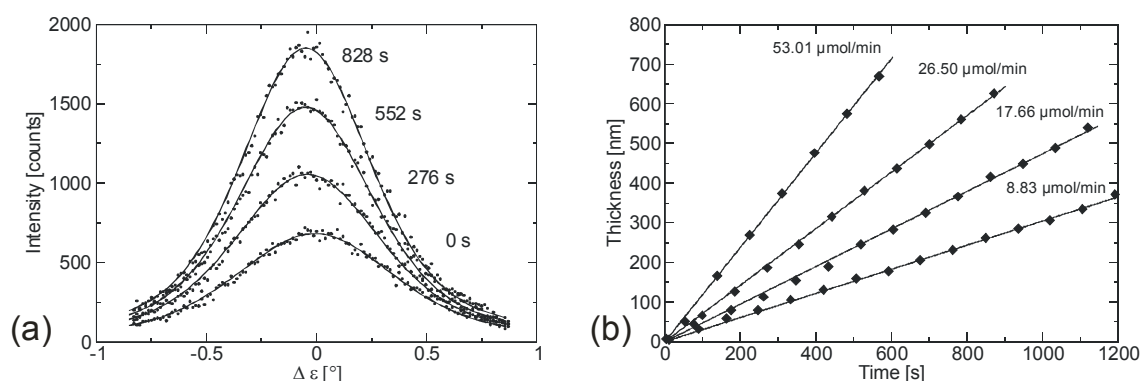


Fig. 1: (a) *In situ* XRD spectra from the GaN (224) reflection acquired during the MOCVD growth of c-GaN on c-GaN. Numbers on the right side give the time after growth initiation. The integration time was 30 s each. (b) Thickness of the MOCVD layer as a function of time for different TMGa fluxes.

The thickness data was used to calculate the growth rate of the MOCVD film, as shown in Fig. 1 (b), where the layer thickness is plotted against the growth time for different fluxes of TMGa. The slope of the curves is equivalent to the growth rate.

During heating and cooling of the sample in the reactor, a shift of the GaN peak was measured due to thermal expansion. A calculation of the thermal expansion coefficient yielded a value of $5.0 \times 10^{-6} \text{ K}^{-1}$, which is consistent with previously reported results [10], [11].

A frequent application of *ex situ* X-ray diffraction is the determination of ternary compound compositions and strain in epitaxial layers [12]. *In situ* measurement of these parameters is highly desirable to ensure proper device operation. To demonstrate this feature, we used an MBE-grown AlGaIn/GaN template with initial thicknesses of 250 nm GaN and 440 nm AlGaIn and deposited a c-GaN layer on the AlGaIn film. *In situ* XRD spectra are shown in Fig. 2 (a), and two peaks could clearly be distinguished. During growth, the intensity of the AlGaIn peak remained constant, while the GaN peak continued to increase. The spectrum could again be fitted with the sum of two pseudo-Voigt functions to determine the exact size and position of both peaks. From their angular separation, the AlN content was determined to be 14% using Vegard's law.

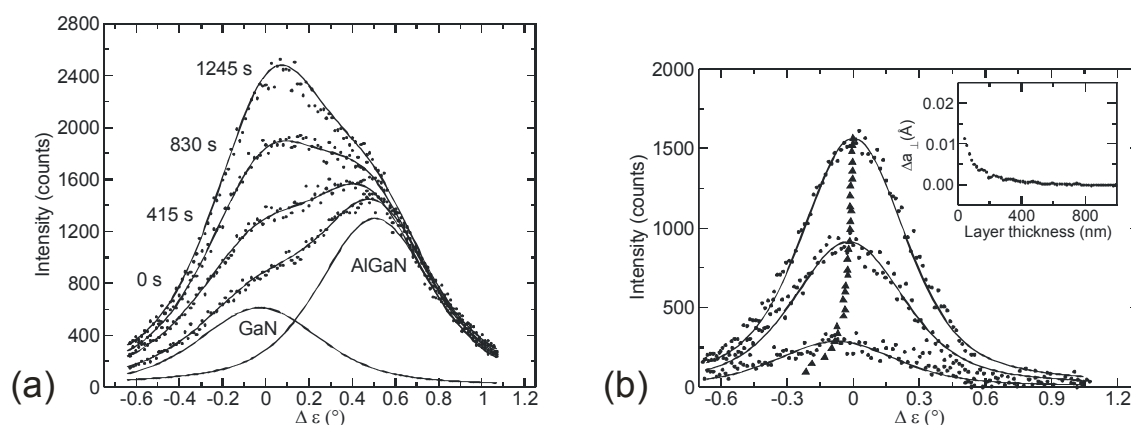


Fig. 2: (a) *In situ* XRD spectra acquired during the growth of GaN on an AlGaIn/GaN template. The solid lines represent fits using pseudo-Voigt functions. (b) Difference spectra obtained by subtracting the template signal from the current spectrum. The inset shows the change in the vertical lattice parameter as calculated from the shift of the GaN peak.

To evaluate the strain in the GaN layer, difference spectra relative to the template signal were calculated as shown in Fig. 2 (b). In this case, only the peak of the MOCVD layer is found. The angular shift of the peak position can be interpreted as a change in the vertical lattice parameter of the growing layer. The equilibrium lattice constant of $\text{Al}_{0.14}\text{Ga}_{0.86}\text{N}$ (4.50 Å) is slightly smaller than that of GaN (4.52 Å) yielding an initially compressively strained epitaxial layer. This leads to an expansion in the vertical direction, which is monitored by our setup. The inset of Fig. 2 (b) shows the change in the vertical lattice constant (Δa_{\perp}) as a function of layer thickness. The data shown in this figure can however only give qualitative information about the relaxation process, as the peak represents a convolution of the whole MOCVD layer.

Conclusion

We have successfully demonstrated the application of high resolution X-ray diffraction for the *in situ* monitoring of MOCVD growth. Measurements on cubic GaN yielded in-

formation about the layer thickness and growth rate as well as on ternary compound compositions and strain relaxation. We think that this method can provide the crystal grower with valuable complementary information on the state of the crystal lattice, which is not available with current optical methods. An application to other material systems like hexagonal GaN, III-V compounds or SiGe could provide new insights on growth processes and is currently under investigation.

Acknowledgements

The authors would like to acknowledge the cooperation of A. Kharchenko and K. Lischka (University of Paderborn, Germany) and J. Bethke (PANalytical B.V., The Netherlands).

References

- [1] A. Bonanni, K. Schmidegg, A. Montaigne-Ramil, H. Sitter, D. Stifter, and K. Hingerl, *J. Vac. Sci. Technol. B* 21(4), 1825 (2003).
- [2] S. Peters, T. Schmidting, T. Trepk, U. W. Pohl, J.-T. Zettler, and W. Richter, *J. Appl. Phys.* 88, 4085 (2000).
- [3] D. E. Aspnes, *Mat. Sci. Eng. B* 30, 109 (1995).
- [4] W. Richter and J.-T. Zettler, *Appl. Surf. Sci.* 100/101, 465 (1996).
- [5] G. B. Stephenson, E. A. Eastman, C. Thompson, O. Auciello, L. J. Thompson, A. Munkholm, P. Fini, S. P. DenBaars, and J. S. Speck, *Appl. Phys. Lett.* 74, 3326 (1999).
- [6] R. L. Headrick, S. Kycia, A. R. Woll, J. D. Brock, and M. V. Ramana Murty, *Phys. Rev. B* 58, 4818 (1998).
- [7] R. L. Headrick, S. Kycia, Y. K. Park, A. R. Woll, and J. D. Brock, *Phys. Rev. B* 54, 14686 (1996).
- [8] P. H. Fuoss, D. W. Kisker, F. J. Lamelas, G. B. Stephenson, P. Imperatori, and S. Brennan, *Phys. Rev. Lett.* 69, 2791 (1992).
- [9] D. J. As, D. Schikora, and K. Lischka, *phys. stat. sol. (c)* 0(6), 1607 (2003).
- [10] D. N. Talwar, *Appl. Phys. Lett.* 80, 1553 (2002).
- [11] R. R. Reeber and K. Wang, *J. Mater. Res.* 15, 40 (2000).
- [12] G. Bauer and W. Richter, *Optical characterization of epitaxial semiconductor layers* (Springer, Berlin, 1996).

Spin Relaxation in Si Quantum Wells Suppressed by an Applied Magnetic Field

W. Jantsch, H. Malissa, M. Mühlberger and F. Schäffler
Institut für Halbleiterphysik, Joh. Kepler Universität, A-4040 Linz, Austria

Z. Wilamowski
Institute of Physics, Polish Academy of Sciences, Al Lotników 32/46,
PL 0668 Warsaw, Poland

We investigate spin properties of the two-dimensional electron gas in Si quantum wells defined by SiGe barriers. We find, in contrast to predictions of the classical model of D'yakonov-Perel, a strong anisotropy of spin relaxation and a decrease of the spin relaxation rate with increasing electron mobility. We show that for high electron mobility the cyclotron motion causes an additional modulation of spin-orbit coupling which leads to an effective suppression of spin relaxation rate.

In spintronics, the aim is to make use of the spin degrees of freedom in addition to the electronic ones. Therefore, spintronic devices based on spins of carriers in semiconductors appear particularly promising. In such elements carriers can be easily moved by applying external voltages, the well known tool of classical electronics. The utilization of spin properties, however, usually is limited by the fast spin relaxation of conduction electrons. Therefore analysis of the spin relaxation mechanisms and the search for a suitable material and optimum conditions are of primary interest in this field. In III-V compounds the spin relaxation time is below one nanosecond [1]. Silicon based devices, due to much weaker spin-orbit coupling, appear much more promising.

2D Si layers in Si/SiGe structures exhibit a spin relaxation time of the order of a few microseconds by measurements of electron spin resonance (ESR) [2] – [5]. We also proved that the Bychkov-Rashba (BR) spin-orbit coupling [6] is the main origin of spin relaxation in one sided modulation doped quantum wells with high mobility [5]. We also found an anisotropy of the line width which implies an anisotropy of the transverse spin relaxation time of more than an order of magnitude whereas the usual theory can explain only a factor of two. In this work we show that motional narrowing due to the cyclotron motion is an important ingredient in the understanding of the transverse spin relaxation time in high mobility systems and the same holds for the longitudinal one.

The effect of BR coupling on spin, σ , of a conduction electron can be described by an effective magnetic field, \mathbf{B}_{BR} . This field is oriented in-plane and perpendicular to electron momentum, $\hbar\mathbf{k}$. The resulting zero field splitting is given by: $\Omega_{BR} = g\mu_B\mathbf{B}_{BR}\cdot\sigma$.

The direction of the BR field depends on the direction of electron k-vector, and therefore the spread of k-vectors results in a spread of the BR field. Consequently, the ESR resonance is shifted and broadened. Momentum scattering, described by a rate $1/\tau_k$, causes a modulation of the BR field in time which leads to the so called D'yakonov-Perel (DP) spin relaxation [7]. Modulation of the BR field leads to motional narrowing of the spread of BR field. The narrowed linewidth, i.e., the spin decoherence rate, $1/T_2$, is thus expected to be proportional to τ_k . Also the longitudinal spin relaxation rate, $1/T_1$, (the inverse spin lifetime, T_1) is predicted to be proportional to τ_k . The DP model explains the ESR frequency shift and the linewidth well for an external magnetic field directed in sample plane [5]. For an electron concentration of the order of a few times 10^{11} cm^{-2} the (un narrowed) BR field is of the order of 100 G.

The total line width caused by BR field, predicted by the classical DP mechanism, is expected to be isotropic [8]. In spite of that, the observed linewidth is strongly anisotropic. Sample data for the anisotropy of the ESR linewidth are given in Fig. 1. For perpendicular orientation of the magnetic field, $\theta = 0^\circ$, the linewidth, $\Delta\omega(0^\circ)$, is by an order of magnitude smaller as compared to in-plane orientation, $\Delta\omega(90^\circ)$. The anisotropy ratio, $\Delta\omega(90^\circ)/\Delta\omega(0^\circ)$, increases with increasing electron mobility and reaches a value of about 1.5 for $\tau_k^{-1} = 10^{12} \text{ s}^{-1}$ and increases up to 10 for $\tau_k^{-1} = 5 \cdot 10^{10} \text{ s}^{-1}$.

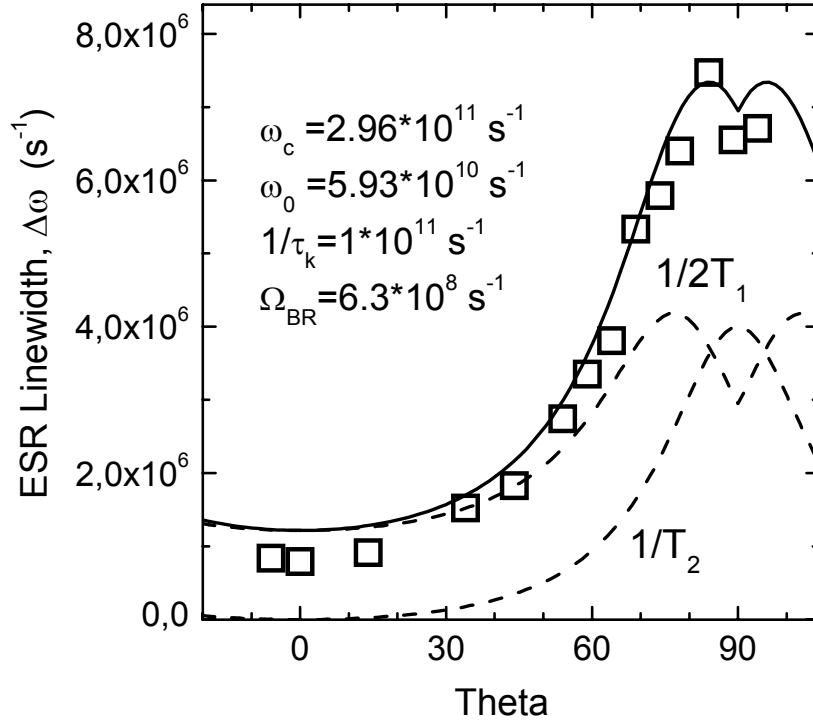


Fig. 1: Dependence of the ESR linewidth of conduction electrons in a 2D Si/SiGe structure on the direction of applied magnetic field. $\theta = 0$ stands for perpendicular direction to the layer. The solid line describing the linewidth corresponds to Eq. (4), while the transverse and longitudinal components are marked by dashed lines and described by Eqs (3, 4)

To explain the observed peculiarities we consider the influence of the cyclotron motion on the spin relaxation. In an external magnetic field, \mathbf{B} , the curvature of the cyclotron trajectory is equivalent to a change of the BR field. As a consequence, the BR field is additionally modulated leading to a suppression of the spin relaxation. The cyclotron frequency of 2D electrons, ω_c , scales with the perpendicular component of the applied field, $B \cdot \cos\theta$. Therefore, the effective modulation frequency, and the resulting spin relaxation rate also depend on θ .

According to general rules, both components of spin relaxation are ruled by Fourier components of the correlation function of the perturbing field [9]. Momentum scattering and cyclotron motion lead to the following correlation function of the BR perturbation:

$$C(\tau) = \langle \mathbf{\Omega}_{BR}(\tau), \mathbf{\Omega}_{BR}(0) \rangle = \Omega_{BR}^2 \exp\left(i\omega_c\tau - \frac{\tau}{\tau_k}\right) \quad (1)$$

The resulting expressions for the longitudinal and the transverse spin relaxation rates take the form:

$$\frac{1}{T_1} = \Omega_{BR}^2 (1 + \cos^2 \theta) \frac{\tau_k}{1 + (\omega_0 - \omega_c)^2 \tau_k^2} \quad (2)$$

$$\frac{1}{T_2} = \Omega_{BR}^2 \frac{\sin^2 \theta}{2} \frac{\tau_k}{1 + \omega_c^2 \tau_k^2} \quad (3)$$

Here ω_0 is the Larmor frequency and $\Omega_{BR}^2 (1 + \cos^2 \theta)$ is the variance of the perpendicular component of the BR field and $\Omega_{BR}^2 \sin^2 \theta$ its longitudinal component.

The total linewidth is:

$$\Delta\omega = \frac{1}{2T_1} + \frac{1}{T_2} \quad (4)$$

The lines in Fig. 1 correspond to Eqs. (2) – (4). The observed angular dependence is well described. The characteristic maximum of the linewidth, which occurs at $\theta \cong 80^\circ$, corresponds to a resonance-like condition at $\omega_0 \cong \omega_c$, where the energy of the cyclotron motion can be transferred to the spin system. Ω_{BR} is the only fitting parameter, but the anisotropy ratio does not depend on Ω_{BR} . In that sense, the theoretical prediction of the suppression of the spin relaxation, equivalent to the anisotropy ratio, is described without any fitting parameter.

The present model implies also a strong dependence of the suppression of spin relaxation on the electron mobility. For low mobility, $\omega_c \tau_k \ll 1$, Eqs.(2) and (3) take the classical form. The DP relaxation rate is expected to be proportional to the momentum relaxation time. The spin relaxation rate thus should increase with increasing mobility. For $\omega_c \tau_k > 1$, however, the opposite dependence is expected for the spin relaxation rates according to Eqs. (3) and (4): here the higher mobility leads to slower spin relaxation.

Acknowledgements

Work supported also by the FWF, and ÖAD, both Vienna and in Poland within the KBN grants PBZ -044/P03/2001 and 2 P03B 054 23.

References

- [1] J.M. Kikkawa and D.D. Awschalom, Phys. Rev. Lett. **80**, 4313 (1998)
- [2] W. Jantsch, Z. Wilamowski, N. Sandersfeld and F. Schäffler, Phys. stat. sol. (b) **210**, 643 (1998)
- [3] C.F.O. Graeff, M.S. Brandt, M. Stutzmann, M. Holzmann, G. Abstreiter, F. Schäffler, Phys. Rev. **B59**, 13242 (1999)
- [4] Z. Wilamowski, N.Sandersfeld, W. Jantsch, D. Töben, F. Schäffler, Phys. Rev. Lett. **87**, 026401 (2001).
- [5] Z. Wilamowski, W. Jantsch, H. Malisa, and U. Rössler, Phys. Rev. B, **66**, 195315 (2002)
- [6] Yu. L. Bychkov, E.I. Rashba, J. Phys. C **17**, 6039 (1984)
- [7] M.I. D'yakonov and V.I. Perel', Sov. Phys. JRTP **38**, 177 (1973)

- [8] N.S. Avierkiev, L.E. Golub, and M. Willandr, *J. Phys. Condens. Mat.* **14**, R271 (2002)
- [9] A. Abragam, "*Principles of Nuclear Magnetism*" ed. Oxford at the Clarendon Press, 1961.

Device Processing for Spintronics Applications

D. Gruber, H. Malissa, D. Pachinger, M. Mühlberger, F. Schäffler and
W. Jantsch

Institute for Semiconductor and Solid State Physics
University of Linz, Altenbergerstr 69, 4030 Linz, Austria

The SiGe material system is a promising candidate for solid-state spintronics application due to its very long relaxation lifetimes and compatibility to standard Si device processing technology. We investigate the possibilities of g-factor tuning of conduction electrons in SiGe heterostructures as proposed for spin transistors. The g-factor dependence on the Ge content in SiGe quantum wells was investigated, showing promising results. Devices for demonstrating a high enough shift of the electron g-factor to bring electrons in and out of resonance with an external microwave field - thus allowing spin manipulation - are being developed.

Introduction

Recently, the new area of spintronics has attracted great attention in connection with quantum computing. Vrijen et al. [4] proposed the use of Si/SiGe heterostructures as spin transistors for a quantum computer, in which the spins of electrons in a quantum well act as qubits. Our experimental results revealed long spin coherence times of several μs [1], [2] in this material system. One of the key requirements for qubit operation is the ability of tuning the electron g-factor, hence bringing electrons into and out of resonance with an applied microwave frequency magnetic field.

Experimental

g-factor Dependence on the Ge Content in SiGe Quantum Wells

An important issue for the realization of spintronics in the SiGe material system is a sufficiently strong dependence of the electronic g-factor on the Ge content in the SiGe quantum wells. To investigate this, we have grown SiGe quantum wells with 3 different Ge contents (0%, 4%, and 9.5%) on relaxed SiGe buffers with SiGe barriers (Ge content between 19 and 25%). The samples were modulation-doped with Sb after growth of a spacer layer on top of the quantum well. Low-energy Rutherford backscattering experiments [3] were performed to measure the exact Ge contents of the barriers and wells as well the thicknesses thereof.

Electron spin resonance (ESR) [3] experiments reveal sharp resonances and g-factor shifts that clearly separate the ESR resonances. The g-factor dependence (see Fig. 1) is found to be linear in the investigated Ge content range.

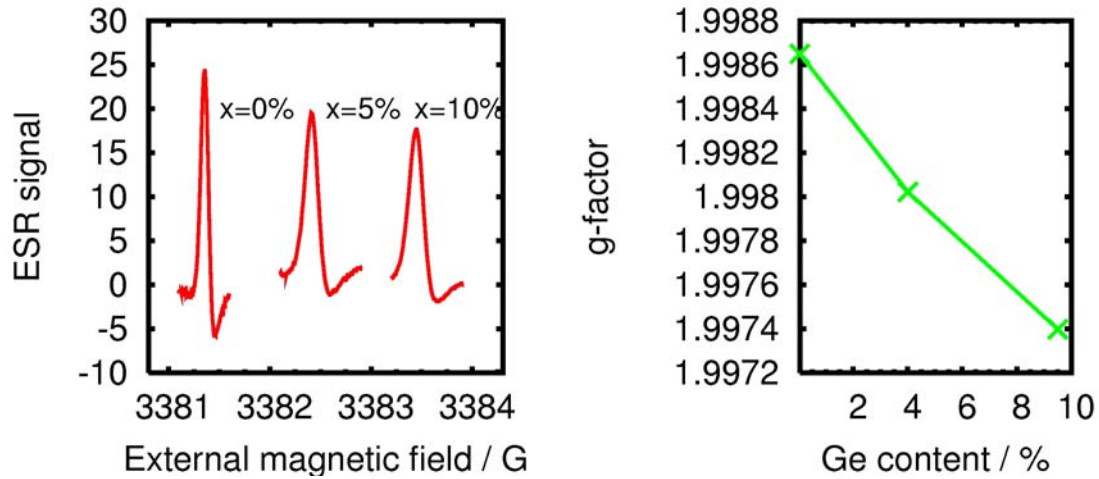


Fig. 1: Electron spin resonance lines for the three samples investigated for in-plane magnetic field (left). The corresponding g-factors are shown on the right.

Self Consistent Simulations

Using data from [3], our simulations [5] show that it should be possible to reach a large enough electron g-factor shift in a suitable Si/SiGe quantum well structure. This is achieved by applying electrical fields on both top and bottom gates of the structure, shifting the wave function to areas with different Ge content while keeping the carrier density constant. Figure 2 shows the simulated electron wave function in the ground state for two different gate voltage sets in the proposed structure. The estimated change of the electron g-factor is sufficiently large to clearly separate the resonance frequencies in an ESR experiment, thus allowing spin manipulation in a pulsed ESR experiment.

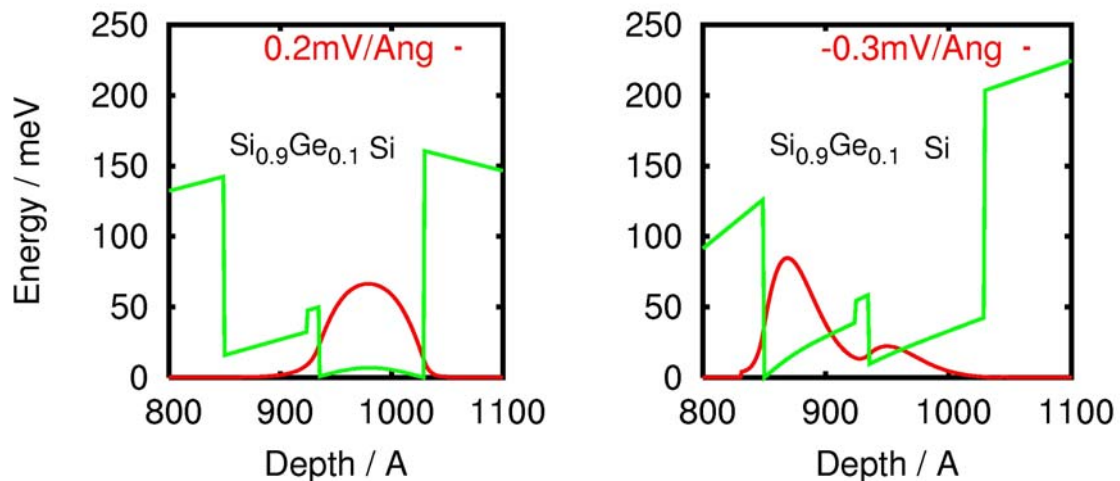


Fig. 2: Simulated electron wave function of the ground state in the region of the proposed SiGe double quantum well structure for different top and bottom gate voltages. The wave function can be shifted from the Si part to the SiGe part, hence changing the g-factor of the electrons. The carrier density is constant and only the ground levels of the quantum wells are populated.

Device Processing

For the experimental demonstration, Si quantum wells and the simulated SiGe double quantum well structure with SiGe barriers with Ge contents between 25 and 30% were grown on graded SiGe buffers. The layers are low temperature modulation-doped with Sb and have a thick, highly p-doped layer beneath the graded buffer, which acts as a bottom gate. For the samples a special mask with a small Hall-bar structure for transport measurements and larger areas for ESR measurements together with the contacts for both top and bottom gate was designed. The ohmic contacts are implanted with As and annealed. For the top gate a Pd Schottky gate and for the bottom contact annealed Al contacts are used. So far, the samples have been characterized and the process has been established. I-V curves of top and bottom gates on the processed samples work as expected (see Fig. 3 (a)). Figure 3 (b) shows the variation of the carrier density as a function of the top gate voltage.

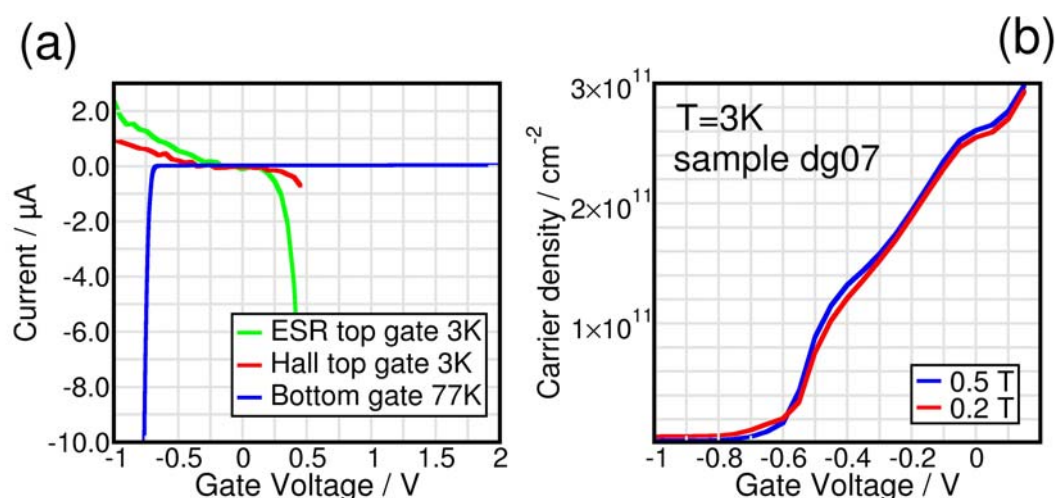


Fig. 3: I-V curves for the processed gates (left). Influence of top gate voltage on the carrier concentration in a Si quantum well structure without bottom gate measured *in-situ* (right). The channel can be fully depleted.

Additionally, a Bruker X-band ESR machine was adapted to allow in-situ electrical measurements. For this a special sample holder (see Fig. 4) and a computer-controlled goniometer were designed and built.

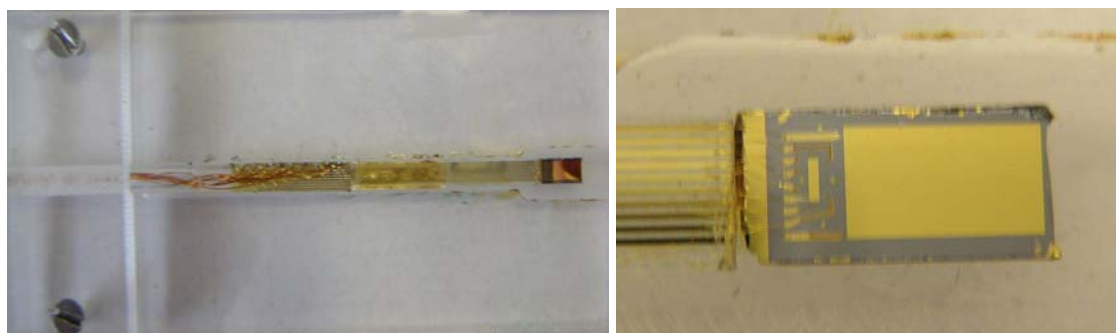


Fig. 4: ESR sample holder with mounted sample (left). The part reaching into the cavity is made of quartz with Au leads out of the cavity. On the sample (right) the large top gate for the ESR structure can be seen.

Conclusion

We investigated the dependence of the electron g-factor of conduction electrons on the Ge content in SiGe quantum wells. The resonances found are very sharp and well separated with respect to the Ge content. The promising results are used to develop devices that will give us the possibility to change the g-factor of the electrons in the quantum wells, thus allowing selective spin manipulation by pulsed Electron Spin Resonance techniques.

Acknowledgements

This work is funded by FWF grants no. P16223 and P13497.

References

- [1] Z. Wilamowski, N. Sandersfeld, W. Jantsch, D. Többen, F. Schäffler: "Screening Breakdown on the Route toward the Metal-Insulator Transition in Modulation Doped Si/SiGe Quantum Wells", PRL 87, 26401 (2001)
- [2] A. Tyrishkin, S. Lyon, W. Jantsch, F. Schäffler: "Spin Manipulation of Free 2-Dimensional Electrons in Si/SiGe Quantum Wells", cond-mat/0304284 (2003)
- [3] H. Malissa, W. Jantsch, M. Mühlberger, F. Schäffler: "Anisotropy of g-factor and ESR linewidth in modulation doped SiGe quantum wells", submitted to APL
- [4] R. Vrijen, E. Yablonovich, K. Wang, H. Jiang, A. Balandin, V. Roychowdhury, T. Mor, D. DiVincenzo: "Electron-spin-resonance transistors for quantum computers in silicon-germanium heterostructures", PRA 62, 12306 (2000)
- [5] D. Pachinger: "High mobility Si/SiGe heterostructures for spintronic applications", Masters Thesis, University of Linz (2003)

Two-Dimensional Metallic State in Silicon-on-Insulator Structures

G. Brunthaler¹, B. Lindner¹, G. Pillwein¹, M. Prunnila² and J. Ahopelto²

¹Institute for Semiconductor Physics, University Linz, Austria

²VTT Centre for Microelectronics, Tietotie, Espoo, Finland

In silicon-on-insulator metal oxide semiconductor structures with a peak mobility of 25,000 cm²/Vs a strong drop of the resistivity towards low temperature has been observed. This metallic effect can be fitted by a linear-in-T term, which can be interpreted with both, the ballistic interaction corrections and the temperature dependent screening of impurity scattering. At low temperature and density in addition a strong increase of the resistivity towards lower T was observed, which is attributed to the contact regions of the sample.

Introduction

The metallic state (MS) in Si-metal oxide semiconductor (MOS) structures and other two-dimensional (2D) electron structures was completely unexpected as the influence of electron-electron interaction effects was probably strongly underestimated in the past. In order to investigate the effects in a similar structure as Si-MOS, we performed experimental work on the metallic state in high-mobility silicon-on-insulator (SOI) MOS structures. By comparing the differences in the behavior of the two systems, one can get information on the underlying physical mechanisms.

Experiment and Analysis

Recently, new SOI-MOS structures became available, which reach a maximum electron mobility of 25,000 cm²/Vs at 0.3 K – a value comparable to many investigated high-mobility Si-MOS structures in the literature.

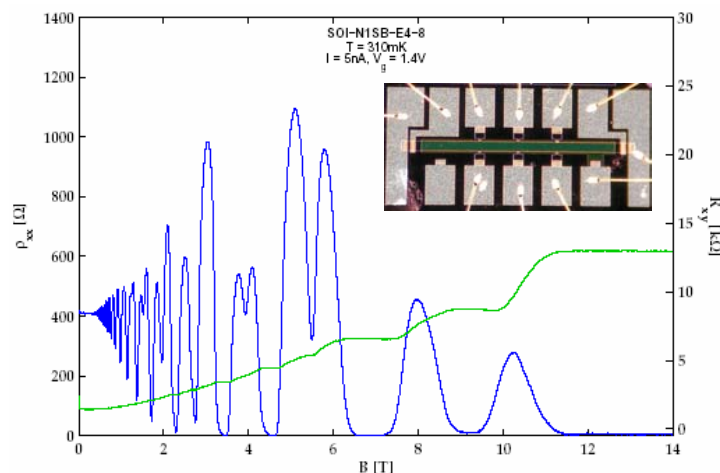


Fig. 1: Shubnikov-de Haas and Quantum Hall effect of high-mobility SOI-MOS structure at a temperature of 300 mK (inset shows etched Hall bar).

Our SOI-MOS samples were fabricated on commercially available bonded SOI. After the processing steps, the final SOI film thickness was just 40 nm with a gate oxide of also 40 nm. The resistivity and Hall measurements on such samples were performed in a ^3He -cryostat down to 0.3 K.

As can be seen in Fig. 2 (a), at high electron densities the typical resistivity drop in $\rho(T)$ towards low T is observed. However, at low densities $\rho(T)$ shows a strong non-monotonic behavior with a strong increase below 2 K towards lower T. The latter effect can probably be described by contact resistivity effects, whereas the decreasing parts towards lower T represent the interesting metallic behavior.

We further observed a non-monotonic behavior of $\rho(n)$ in the ‘insulating’ part at low T, which is shown in Fig. 2 (b). The observed fluctuations can be reproduced at 0.26 K by sweeping the gate voltage V_g up and down. Only at an elevated T of e.g. 1.26 K, the fluctuations become weak and finally disappear. Such fluctuations in $\rho(n)$ might be due to universal potential fluctuations (UFC), despite it is surprising that such fluctuations exist over large distances of 800 μm between the potential probes.

For the analysis of the metallic state, we concentrate on the $\rho(T)$ dependence of that part where the fluctuations are not important. This is for high electron densities or for higher temperatures. In our analysis, the experimental data are compared with i) coherent interaction corrections in the ballistic regime and ii) temperature dependent screening of impurity scattering.

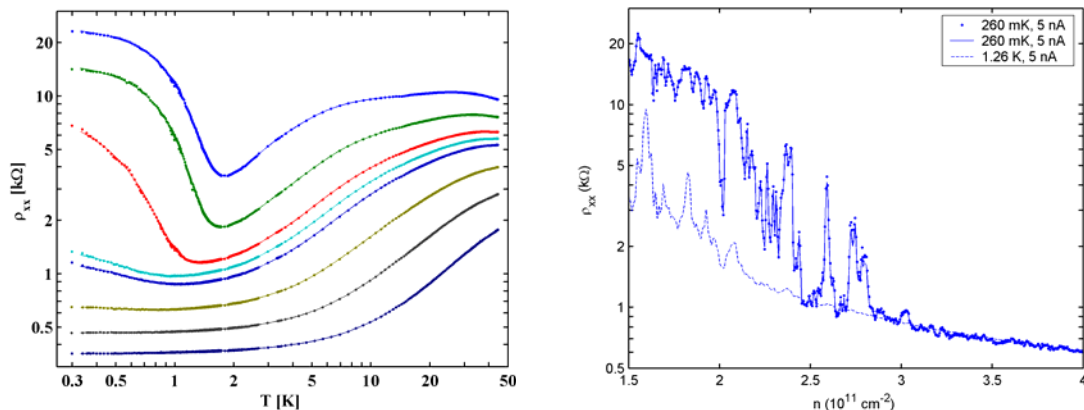


Fig. 2: (a) Longitudinal resistivity $\rho(T)$ for SOI sample N1SB-E4-8. The electron density is in the range from 1.45 to $7.61 \times 10^{11} \text{ cm}^{-2}$ from top to bottom traces. (b) Resistivity $\rho(n)$ at 260 mK from 1.5 to $4 \times 10^{11} \text{ cm}^{-2}$ (small dot symbols) and backward (full line) at 260 mK and at 1.26 K (dashed line).

The theory i) on ballistic interaction correction was recently introduced by Zala *et al.* [1] and describes the electron-electron interaction corrections at intermediate temperature where $k_B T > \hbar/T$. The corrections to the conductivity σ are due to the charge channel and due to the triplet channels with F_0^σ the characterizing Fermi liquid parameter. The correction is in first order linear in T . The 2-fold valley degeneracy for 2D n-type Si enters also into the analytic description.

According to recent works, there is some discrepancy whether F_0^σ in Si-MOS structures is rather towards -0.6 or closer towards -0.25 . This discrepancy seems to depend largely on the detailed method of analysis. In the original work on the ballistic electron-electron interaction [1], the correction is given in terms of $\Delta\sigma$, whereas it was also argued that rather $\Delta\rho$ should be fitted. In the analysis of experimental data, both approaches were used.

In a linear approximation, the two corrections are related to each other as $\Delta\rho = -\rho_0^2\Delta\sigma$, with $\rho_0 = 1/\sigma_0$. As long as $\Delta\sigma/\sigma_0 \ll 1$ the two approaches are equivalent, but as soon as the deviation becomes large, there is a difference in fitting the data either with a linear-in-T term in $\Delta\sigma$ or in $\Delta\rho$.

We have performed true multi-parameter least-square fits for both $\Delta\sigma$ and $\Delta\rho$ in order to determine F_0^σ and the conductivity σ_0 . The lower temperature boundary for the fit was chosen so that only data with a monotonic increase in $\rho(T)$ were taken into account, i.e. leaving out the region with the fluctuation as described above. As the upper limit, $k_B T = E_F/4$ was taken. The Fermi energy E_F was calculated with $m_0^* = 0.19 m_e$ and was thus not renormalized, whereas a renormalized mass of $m^* = (1 + 0.0585r_s + 0.00522 r_s^2) \times m_0^*$ was used in order to calculate the momentum relaxation time τ ($r_s = 1/(a_B(p n)^{1/2})$ is the Wigner-Seitz or interaction parameter and a_B the effective Bohr radius.) With these values, the conductivity corrections due to the charge channel and the triplet channels could be calculated according to Zala et al. [1].

Figure 3 compares the fit for $\Delta\sigma$ and $\Delta\rho$, taking fully into account the two terms according to Zala et al. [1]. We find that the fit in $\Delta\sigma$ gives a clearly better agreement with the experimental data than the $\Delta\rho$ fit. As the corrections in $\Delta\sigma$ ($\Delta\rho$) are not so small anymore, the prefactor of the corrections has to be different in order to fulfill the least-square condition of the fitting procedure. Accordingly, the deduced F_0^σ values are different for the two different fits as shown in Fig. 4.

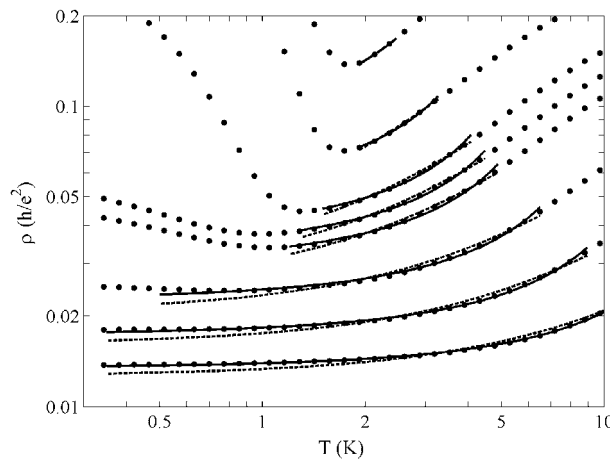


Fig. 3: Fit of $\rho(T)$ by $\Delta\sigma$ - (full line) and $\Delta\rho$ - (dashed line) approximations as described in the text.

For a comparison, we have also plotted the relation $F_0^\sigma \sim -r_s/[2(r_s+\sqrt{2})]$ (full line) according to the description of Eq. 2.16c in Ref. [1]. As one can see, the theoretically expected value of F_0^σ is closer to the $\Delta\rho$ -fit than to the $\Delta\sigma$ -fit. But neither the observation that the $\Delta\sigma$ -fit gives a better description of $\rho(T)$ data nor the better consistency of F_0^σ for the $\Delta\rho$ -fit can give a clear criterion what type of fit should be performed. It would be very helpful to have more rigorous theoretical arguments or to perform the theoretical calculations to higher order in T.

It can be concluded that the ballistic interaction corrections are able to describe the temperature dependence in r for SOI-MOS samples in the intermediate T-range. But due to the uncertainty whether $\Delta\rho$ or $\Delta\sigma$ should be fitted, there is also a relative large uncertainty for a precise determination of the Fermi liquid parameter F_0^σ .

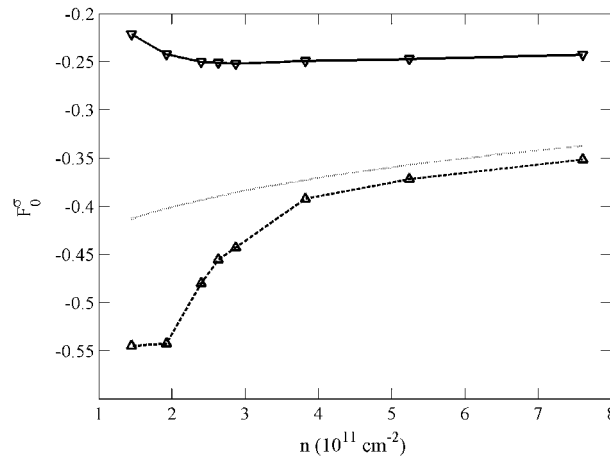


Fig. 4: The Fermi liquid parameter F_0^σ as obtained from the $\Delta\sigma$ - (full line) and $\Delta\rho$ - (dashed line) fit. The theoretical estimate of F_0^σ (dotted line) is shown for comparison.

There is still the mechanism ii) of temperature dependent screening of impurity scattering under discussion. As this effect also leads to a linear-in-T term [2], the data can be fitted similarly well as with the ballistic interaction corrections. The prefactor of the linear T term is not in direct agreement with the earlier calculation, but a local field correction $G(2k_F)$ which takes into account both, exchange and correlation effects seems to be able to describe also the size of the slope [3].

Conclusion

Our experiments on silicon-on-insulator metal oxide semiconductor structures with a peak mobility of $25,000 \text{ cm}^2/\text{Vs}$ show a clear metallic effect, i.e. a strong drop of the resistivity towards low temperature. This behavior can be described in principle with both, ballistic interaction correction and temperature dependent screening of impurity scattering as both theories give a leading linear-in-T term. A qualitative comparison of the slope has still some uncertainties for both theories. Further measurements and calculations should be performed in order to clarify the situation.

Acknowledgements

We like to acknowledge the help of T. Hörmann in the data fitting procedure. The work was supported by FWF (Austrian science fund) project.

References

- [1] G. Zala, B. N. Narozhny, and I. L. Aleiner, *Phys. Rev. B* **64**, 214204 (2001).
- [2] A. Gold and V. T. Dolgoplov, *Phys. Rev. B* **33**, 1076 (1986).
- [3] G. Brunthaler, G. Pillwein, P.E. Lindelof, and J. Ahopelto cond-mat/0207170.

Sensor Systems

Sensor Systems

M.J. Vellekoop

Institute of Sensor and Actuator Systems, TU Wien, Austria¹

In the following, a short overview over those activities of the Sensor Systems group which received support from the GMe will be given. The Sensor System group uses the facilities of the Center for Micro- and Nanostructures of the Vienna University of Technology (formerly "Microstructure Center " – MISZ) but also operates its own technology laboratories due to inherent incompatibilities of some processes and materials. The support received from the GMe allowed the purchase of a piece of equipment (a spray coater), which has been installed on the premises of the Center for Micro- and Nanostructures and consequently is also available to the other groups working there.

Introduction

In 2003, a spray coater has been installed in the MISZ (EVG 101 Advanced Spray Coater System, total costs € 50.000 of which € 20.000 was contributed by the GMe). Together with wafer-to-wafer bonding equipment, a back side aligner, and micro-machining equipment, it forms a processing line for integrated sensors and actuators. Several different substrate materials can be applied in the coater, e.g. silicon, pyrex glass or calcium fluoride wafers. The spray coater allows us to perform lithographic processing of wafers which already contain mechanical structures such as channels, cantilevers, or suspended membranes. These structures are the basis of integrated sensors and actuators. Spin coating cannot be used in this case because the resist would not form a uniform film over the irregular wafer surface.

After the installation, mid 2003, the equipment was tested together with EVG. Since the summer of that year, several new devices have been designed and fabricated using spray coating photolithography.

General

Spray processes are more complicated than spin-on processes. Many parameters like wafer rotation, resist volume, spray arm speed distribution and nitrogen pressure have to be evaluated to achieve homogeneously distributed layers. The consumption of resist is much lower than for spin coating (300 µl vs. 2 ml for 4 inch wafers).

Different spray coating processes were developed using the EVG 101 spray coater:

Deposition of positive resist "AZ 1512 HS"

For the fabrication of the particle shape sensor and the particle sorter device positive resist has to be deposited on a topographic surface in order to pattern a metal layer on top of a thick (60 µm) SU-8 layer which is exposed and softbaked. Due to the swelling of the exposed areas the surface of the SU-8 shows height differences of 5 µm. Homogenous layers with a thickness of 1.5 µm could be deposited.

¹ in 2003, "Institute of Industrial Electronics and Material Science", TU Wien

Deposition of image reversal resist "TI Spray"

In general, the viscosity of resists to be sprayed has to be lower than 20 cSt. The standard image reversal resist TI 35 ES is not suitable for spray processes because of its high viscosity. Dilution of this resist is not possible due to chemical problems.

"TI Spray" is an image reversal resist which can be deposited by spray coating. Additionally, it is possible to dilute the resist if necessary. A spray process for the deposition of 4 μm thick layers was developed. This allows the patterning of metal layers up to a thickness of 5 μm by evaporation and lift-off.

The new processes have been applied in several projects:

- Micromixers containing stacked channels (in cooperation with the Institute of Chemical Technologies and Analytics);
- Particle shape sensors containing optical detectors integrated in the channel (in cooperation with the Dutch Technology Foundation and the Delft University of Technology, NL);
- Particle sorters based on dielectrophoresis (in cooperation with the Delft University of Technology, NL);
- Particle separators based on dielectrophoresis; and
- Electrowetting devices (EU project MicroPROTEIN).

Project Information

Project Manager

M.J. Vellekoop

Institute of Sensor and Actuator Systems, Vienna University of Technology
Gusshausstrasse 27–29, 1040 Vienna, Austria

Project Group

Last Name	First Name	Status	Remarks
Agoston	Attila	PhD student	
Art	Georg	Student	
Chabicoovsky	Rupert	Univ. Prof.	
Hairer	Gabriel	PhD student	
Jachimowicz	Artur	Postdoc	
Jakoby	Bernhard	Assoc. Prof.	
Keplinger	Franz	Ass. Prof.	
Klinger	Franz	Student	
Kohl	Franz	Postdoc	
Kostner	Stefan	Student	
Kuntner	Jochen	PhD student	
Kvasnica	Samuel	PhD student	
Nieuwenhuis	Jeroen Hans	Ass. Prof.	
Oliveira	Sara	Student	ERASMUS
Pirker	Ewald	Technician	
Rakohl	Manfred	Technician	
Rocha Wiese Meneses	Daniel Paolo	Ass. Prof.	
Rogler	Gerhard	Technician	
Schalko	Johannes	Postdoc	
Stangl	Günther	Technician	
Strobach	Michael	Student	
Svasek	Edeltraud	Technician	
Svasek	Peter	Technician	
Valentin	Bernhard	Student	
Vellekoop	Michiel J.	Univ. Prof.	
Wölfl	Christoph	Technician	
Zoppel	Sandra	PhD student	

Books and Contributions to Books

1. M. Ando, H. Steffes, R. Chabicovsky, M. Haruta, G. Stangl:
"*Optical and Electrical Gas Sensing Properties of $In_xO_yN_z$ Films*";
in: "[*sensor & packaging*]", ÖVE, Wien, Austria, 2003, ISBN: 3-85133-032-3, 139 - 144.
2. D. Bajalan, I. Groiss, G. Stangl, H. Hauser, P. Fulmek, P. Haumer:
"*Co/Pt Multi-Layer Production for Magnetic Nanostructures*";
in: "[*sensor & packaging*]", ÖVE, Wien, Austria, 2003, ISBN: 3-85133-032-3, 193 - 199.
3. R. Fasching, F. Keplinger, G. Hanreich, G. Jobst, G. Urban, F. Kohl, R. Chabicovsky:
"*A Novel Miniaturized Sensor for Carbon Dioxide Dissolved in Liquids*";
in: "[*sensor & packaging*]", ÖVE, Wien, Austria, 2003, ISBN: 3-85133-032-3, 151 - 158.
4. A. Glaninger, A. Jachimowicz, F. Kohl, R. Chabicovsky, G. Urban:
"*Wide Range Semiconductor Flow Sensors*";
in: "[*sensor & packaging*]", ÖVE, Wien, Austria, 2003, ISBN: 3-85133-032-3, 163 - 168.
5. G. Hanreich, M. Mündlein, H. Hauser, J. Nicolics, G. Stangl, R. Grössinger, J. Espina-Hernandez:
"*Ultra Thin Pick-up Coil for Surface Flux Detection*";
in: "[*sensor & packaging*]", ÖVE, Wien, Austria, 2003, ISBN: 3-85133-032-3, 171 - 176.
6. G. Hanreich, J. Nicolics, M. Mündlein, H. Hauser, R. Chabicovsky:
"*Development of a New Bonding Technique for Human Skin Humidity Sensors*";
in: "[*sensor & packaging*]", ÖVE, Wien, Austria, 2003, ISBN: 3-85133-032-3, 145 - 150.
7. G. Hanreich, J. Nicolics, G. Stangl:
"*Investigation of the Thermal Performance of Micro-Whisker Structured Silicon Heat Spreaders for Power Devices*";
in: "[*sensor & packaging*]", ÖVE, Wien, Austria, 2003, ISBN: 3-85133-032-3, 267 - 274.
8. H. Hauser, G. Stangl, J. Hochreiter, R. Chabicovsky, P. Aigner, R. Kloibhofer, W. Krenn, M. Janiba, K. Riedling:
"*Magneto-Resistive Sensors*";
in: "[*sensor & packaging*]", ÖVE, Wien, Austria, 2003, ISBN: 3-85133-032-3, 49 - 56.
9. H. Hauser, R. Steindl, C. Hausleitner, J. Nicolics, A. Pohl:
"*Miniaturized Magnetic Field Sensors Utilizing GMI Effect and SAW Technology*";
in: "[*sensor & packaging*]", ÖVE, Wien, Austria, 2003, ISBN: 3-85133-032-3, 127 - 136.
10. P. Hudek, I. Rangelow, I. Kostic, G. Stangl, P. Grabiec, E. Rangelow, M. Belov, F. Shi:
"*Chemically Amplified Deep UV Resists for Micromachining Using Electron Beam Lithography and Dry Etching*";
in: "[*sensor & packaging*]", ÖVE, Wien, Austria, 2003, ISBN: 3-85133-032-3, 249 - 254.
11. B. Jakoby, F. Herrmann:
"*Chemical Sensors for Liquid Media*";

- in: "*Sensors for Automotive Applications*", WILEY-VCH GmbH & Co. KGaA, 2003, (invited), 516 - 527.
12. F. Keplinger, S. Kvasnica, H. Hauser, R. Grössinger:
"*Magnetic Cantilever Sensors*";
in: "[*sensor & packaging*]", ÖVE, Wien, Austria, 2003, ISBN: 3-85133-032-3, 75 - 80.
 13. M. Mündlein, J. Nicolics, A. Aghzout, G. Hanreich, R. Chabicovsky, J. Morris:
"*Investigation of Conductive Adhesives*";
in: "[*sensor & packaging*]", ÖVE, Wien, Austria, 2003, ISBN: 3-85133-032-3, 199 - 220.
 14. M. Mündlein, J. Nicolics, R. Chabicovsky, N. Sekiguchi, T. Komeda, H. Funakubo, G. Stangl:
"*Innovative Packaging Concept of a Miniaturized Skin Moisture Sensor and First Measuring Results*";
in: "[*sensor & packaging*]", ÖVE, Wien, Austria, 2003, ISBN: 3-85133-032-3, 159 - 162.
 15. G. Stangl, G. Ehrenfels, F. Rüdener, J. Romstedt:
"*Stardust Collection Surfaces*";
in: "[*sensor & packaging*]", ÖVE, Wien, Austria, 2003, ISBN: 3-85133-032-3, 177 - 180.
 16. G. Stangl, P. Hudek, I. Kostic, F. Rüdener, I. Rangelow, K. Riedling, W. Fallmann:
"*Micro-Technology of Densely Spaced Non-Conventional Patterns for Space Applications*";
in: "[*sensor & packaging*]", ÖVE, Wien, Austria, 2003, ISBN: 3-85133-032-3, 187 - 190.
 17. M. Vellekoop (ed.):
"*IEEE Sensors 2003 - Tutorial Lecture Notes*";
IEEE Sensors, 2003, ISBN: 0-7803-8133-5.

Publications in Reviewed Journals

1. R. Fasching, F. Kohl, G. Urban:
"*A miniaturized amperometric CO₂ sensor based on dissociation of copper complexes*";
Sensors and Actuators B, **93** (2003), 197 - 204.
2. B. Jakoby, M. Scherer, M. Buskies, H. Eisenschmid:
"*An Automotive Engine Oil Viscosity Sensor*";
IEEE Sensors Journal, **3** (2003), 5; 562 - 568.
3. F. Keplinger, S. Kvasnica, H. Hauser, R. Grössinger:
"*Optical Readouts of Cantilever Bending Designed for High Magnetic Field Application*";
IEEE Transactions on Magnetics, **39** (2003), 5; 3304 - 3306.
4. F. Kohl, R. Fasching, F. Keplinger, R. Chabicovsky, A. Jachimowicz, G. Urban:
"*Development of miniaturized semiconductor flow sensors*";
Measurement, **33** (2003), 109 - 119.
5. F. Laugere, R. Guijt, J. Bastemeijer, G. Van der Steen, A. Berthold, E. Baltussen, P. Sarro, G.W.K. Van Dedem, M. Vellekoop, A. Bossche:
"*On-Chip Contactless Four-Electrode Conductivity Detection for Capillary*

- Electrophoresis Devices*;
Anal. Chem., **75** (2003), 2; 306 - 312.
6. J. Nieuwenhuis, J. Bastemeijer, A. Bossche, M. Vellekoop:
"Near-Field Optical Sensors for Particle shape Measurements";
IEEE Sensors Journal, **3** (2003), 5; 646 - 651.
 7. J. Nieuwenhuis, J. Bastemeijer, P. Sarro, M. Vellekoop:
"Integrated flow-cells for novel adjustable sheath flows";
Lab on a Chip, **3** (2003), 56 - 61.
 8. A. Pauschitz, J. Schalko, Th. Koch, C. Eisenmenger-Sittner, S. Kvasnica, M. Roy:
"Nanoindentation and AFM studies of PECVD DLC and reactively sputtered Ti containing carbon films";
Bull. Mater. Sci., **26** (2003), 6; 585 - 591.
 9. F. Seifert, G. Riha:
"Evolution der akustischen Oberflächenwellen-Bauelemente";
Elektrotechnik und Informationstechnik (e&i), **3** (2003), 79 - 90.
 10. M. Vellekoop, B. Jakoby, R. Chabicovsky:
"Development trends in the field of sensors";
Elektrotechnik und Informationstechnik (e&i), **11** (2003), 120; 388 - 394.

Conference Presentations with Proceedings

1. A. Agoston, C. Ötsch, A. Ecker, F. Novotny-Farkas, H. Eisenschmid, S. Chvatal, M. Scherer, W.J. Bartz, B. Jakoby:
"Online-Monitoring of Lubrication Oil For Gas Engines";
Presentation: Zuverlässige Tribosysteme - Symposium 2003, Schwechat, Austria; 11-20-2003; in: *"Zuverlässige Tribosysteme - Werkstoffwahl - Berechnung - Sensorik"*, F. Franek, A. Pauschitz (ed.); (2003), ISBN: 3-901657-13-4; 109 - 116.
2. J. Espina-Hernandez, R. Grössinger, S. Kato, F. Keplinger, H. Hauser, E. Estévez-Rams:
"New Sensors for Measuring M and H in High Magnetic Fields";
Poster: 7th International Symposium on Research in High Magnetic Fields, Toulouse, France; 07-20-2003 - 07-23-2003; in: *"Proceedings"*, (2003), 129.
3. R. Grössinger, F. Keplinger, H. Hauser, E. Wagner:
"The Design and Construction of a Thin Foil High Field Magnet";
Poster: 7th International Symposium on Research in High Magnetic Fields, Toulouse, France; 07-20-2003 - 07-23-2003; in: *"Proceedings"*, (2003), 130.
4. V. Jordanov, J. Bastemeijer, A. Bossche, P. Sarro, M. Malátek, I. T. Young, G.W.K. Van Dedem, M. Vellekoop:
"PCR Array on Chip - Thermal Characterization";
Presentation: IEEE International Conference on Sensors 2003, Toronto, Canada; 10-21-2003; in: *"Proceedings of IEEE International Conference on Sensors"*, (2003), ISBN: 0-7803-8133-5; 1045 - 1048.
5. B. Jakoby:
"Sensors and Interface Electronics for Oil Condition Monitoring";
Presentation: GMe Forum 2003, Wien, Ö (invited); 04-10-2003 - 04-11-2003; in: *"Proceedings of the Seminar GMe Forum 2003"*, K. Riedling (ed.); (2003), ISBN: 3-901578-10-2; 45 - 48.
6. B. Jakoby, G. Art, J. Bastemeijer:
"Novel Readout Electronics for TSM Viscosity Sensors";

- Presentation: IEEE International Conference on Sensors 2003, Toronto, Canada; 10-21-2003; in: "*Proceedings of the IEEE International Conference on Sensors 2003*", (2003), ISBN: 0-7803-8133-5; 839 - 842.
7. B. Jakoby, R. Beigelbeck:
"*Hydrodynamical Analysis of Compressional Wave Excitation by Microacoustic TSM Liquid Sensors*";
Presentation: 6. Dresdner Sensor-Symposium - Sensoren für zukünftige Hochtechnologien und Neuentwicklungen für die Verfahrenstechnik, Dresden, D; 12-08-2003 - 12-10-2003; in: "*Tagungsband des 6. Dresdner Sensor-Symposium*", J.P. Baselt, G. Gerlach (ed.); w.e.b. Universitätsverlag, (2003), ISBN: 3-935712-92-8; 47 - 50.
 8. B. Jakoby, A. Ecker, M. Vellekoop:
"*Physical Sensors for Macro- and Microemulsions*";
Presentation: 17th European Conference on Solid-State Transducers (Eurosensors XVII), Guimaraes, Portugal; 09-21-2003 - 09-24-2003; in: "*Proceedings of EUROSENSORS XVII*", (2003), ISBN: 972-98603-1-9; 805 - 808.
 9. B. Jakoby, M. Vellekoop:
"*The Influence of Water Contamination on the Performance of Oil Condition Sensors*";
Presentation: 11th International Conference Sensors 2003, Nuremberg, Germany; 05-13-2003 - 05-15-2003; in: "*Proceedings Sensor 2003*", (2003), 123 - 128.
 10. F. Keplinger, S. Kvasnica, H. Hauser:
"*Measuring High Magnetic Fields With A U-Shaped Micro Machined Cantilever Using an Optical Readout*";
Presentation: INTERMAG 2003 (International Magnetism Conference Boston, March 30 - April 3), Boston, Massachusetts; 03-28-2003 - 04-03-2003; in: "*INTERMAG 2003 Diges CD-ROM*", (2003), 2 pages.
 11. F. Keplinger, S. Kvasnica, F. Kohl, H. Hauser:
"*Simulated and Measured Characteristic of a Micromachined Cantilever Sensor*";
Poster: GMe Forum 2003, Wien, Ö (invited); 04-10-2003 - 04-11-2003; in: "*Proceedings of the Seminar GMe Forum 2003*", K. Riedling (ed.); (2003), ISBN: 3-901578-10-2; 173 - 176.
 12. J. Kuntner, B. Jakoby:
"*Finite Element Analysis of Spurious Compressional Wave Excitation by Transverse-Shear-Mode Liquid Sensors*";
Poster: 17th European Conference on Solid-State Transducers (Eurosensors XVII), Guimaraes, Portugal; 09-21-2003 - 09-24-2003; in: "*Proceedings of EUROSENSORS XVII*", (2003), ISBN: 972-98603-1-9; 552 - 555.
 13. J. Kuntner, B. Jakoby:
"*Recent Advances in the Design and Analysis of Microacoustic Sensors*";
Presentation: 1st Congress of Alps-Adria Acoustics Association, Portoroz, Slovenia; 09-01-2003 - 09-02-2003; in: "*Proceedings of Alps-Adria Acoustics Association*", M. Cudina (ed.); (2003), ISBN: 961-6238-73-6; 543 - 548.
 14. J. Kuntner, G. Stangl, B. Jakoby:
"*Analyzing the Non-Newtonian Behavior of Oil-Based Liquids Using Microacoustic Sensors*";
Presentation: IEEE International Conference on Sensors 2003, Toronto, Canada; 10-21-2003; in: "*Proceedings of IEEE International Conference on Sensors 2003*", (2003), ISBN: 0-7803-8133-5; 956 - 960.
 15. J. Kuntner, G. Stangl, B. Jakoby:
"*Sensing Physical Parameters for the Characterization of Oil Based Liquids*";

- Poster: Mikroelektronik 2003 (ME 2003), Wien, Ö; 10-01-2003 - 10-02-2003; in: "*Beiträge der Informationstagung ME03*", G. Fiedler, D. Donhoffer (ed.); 33 (2003), ISBN: 3-85133-030-7; 431 - 435.
16. S. Kvasnica, P. Adamek, P. Spatenka:
"*Investigation of unbalanced planar magnetron discharge - experimentally acquired and simulated plasma parameters*";
Poster: 16th International Symposium on Plasma Chemistry, Taormina, Italy; 06-22-2003 - 06-27-2003; in: "*Book of Abstract: 16th Intern. Symposium on Plasma Chemistry*", (2003).
17. S. Kvasnica, P. Adamek, P. Spatenka:
"*Mapping of the internal plasma parameters of an unbalanced magnetron DC discharge*";
Poster: 16th International Symposium on Plasma Chemistry, Taormina, Italy; 06-22-2003 - 06-27-2003; in: "*Book of Abstract: 16th International Symposium on Plasma Chemistry*", ID 523 (2003), 6 pages.
18. M. Mündlein, R. Chabicovsky, J. Nicolics, B. Valentin, P. Svasek, E. Svasek, T. Komeda, H. Funakubo, T. Nagashima, T. Itoh:
"*Mikrosensor zur Bestimmung des Transepidermalen Wasserverlustes der Menschlichen Haut*";
Poster: Mikroelektronik 2003 (ME 2003), Wien, Ö; 10-01-2003 - 10-02-2003; in: "*Tagungsband Mikroelektronik 2003*", (2003), ISBN: 3-85133-030-7; 349 - 354.
19. M. Mündlein, H. Hauser, J. Nicolics, R. Chabicovsky:
"*Partial Discharge Current Measurement in High Permittivity Dielectrics and their Meaning for Quality Control*";
Poster: 26th International Spring Seminar on Electronics Technology, Stará Lesná, Slovak Republic; 05-08-2003 - 05-11-2003; in: "*Proceedings ISSE 2003*", (2003), ISBN: 0-7803-8002-9; 438 - 443.
20. M. Mündlein, J. Nicolics, R. Chabicovsky, P. Svasek, E. Svasek, T. Komeda, H. Funakubo, T. Nagashima, M. Ito:
"*Packaging of a thin film sensor for transepidermal water loss measurements*";
Presentation: 26th International Spring Seminar on Electronics Technology, Stará Lesná, Slovak Republic; 05-08-2003 - 05-11-2003; in: "*Proceedings ISSE 2003*", (2003), ISBN: 0-7803-8002-9; 328 - 333.
21. J. Nieuwenhuis:
"*Particle Behaviour in a Non-Coaxial Sheath Flow for Application in an Integrated Coulter-Counter*";
Presentation: 11th International Conference Sensors 2003, Nuremberg, Germany; 05-13-2003 - 05-15-2003; in: "*Proceedings of the 11th Intern. Conf. SENSOR 2003*", (2003), 81 - 83.
22. J. Nieuwenhuis, J. Bastemeijer, P. Sarro, M. Vellekoop:
"*First Measurement Results with an Integrated Projection Cytometer*";
Poster: Seventh International Conference on Micro Total Analysis Systems (μ TAS2003), Squaw Valley, California, USA; 10-03-2003 - 10-09-2003; in: "*Proceedings of μ TAS 2003*", M. Northrup, K.F. Jensen, D.J. Harrison (ed.); (2003), ISBN: 0-9743611-0-0; 1219 - 1222.
23. J. Nieuwenhuis, J. Bastemeijer, P. Sarro, M. Vellekoop:
"*Novel Flow-Cell to Create a Sheath Flow with Adaptable Sample Flow Dimensions*";
Poster: GMe Forum 2003, Wien, Ö (invited); 04-10-2003 - 04-11-2003; in: "*Proceedings of the Seminar GMe Forum 2003*", K. Riedling (ed.); (2003), ISBN: 3-901578-10-2; 177 - 181.

24. J. Nieuwenhuis, J. Bastemeijer, P. Sarro, M. Vellekoop:
"Novel Flow-Cell to Create a Sheath Flow with Adaptable Sample Flow Dimensions";
Poster: Mikroelektronik 2003 (ME 2003), Wien, Ö; 10-01-2003 - 10-02-2003; in:
"Beiträge der Informationstagung ME03", 33 (2003), ISBN: 3-85133-030-7; 1 - 5.
25. J. Nieuwenhuis, F. Kohl, J. Bastemeijer, M. Vellekoop:
"First Particle Measurements with an Integrated Coulter Counter based on 2-Dimensional Aperture Control";
Presentation: 12th International Conference on Solid-State Sensors, Actuators and Microsystems (TRANSDUCERS 03), Boston, Massachusetts, USA; 06-08-2003 - 06-12-2003; in: "Digest of Technical Papers - Transducers 03", 1 (2003), ISBN: 0-7803-7731-1; 296 - 299.
26. J. Nieuwenhuis, M. Vellekoop:
"Improved Dielectrophoretic Particle Actuators for Microfluidics";
Presentation: IEEE International Conference on Sensors 2003, Toronto, Canada; 10-21-2003; in: "Proceedings of IEEE International Conference on Sensors ", (2003), ISBN: 0-7803-8133-5; 573 - 577.
27. J. Nieuwenhuis, M. Vellekoop:
"Performance Comparison of Dielectrophoretic Particle Sorters based on a Novel Analysis Method";
Poster: 17th European Conference on Solid-State Transducers (Eurosensors XVII), Guimaraes, Portugal; 09-21-2003 - 09-24-2003; in: "Proceedings of EUROSENSORS XVII", (2003), ISBN: 972-98603-1-9; 276 - 279.
28. G. Stangl, A. Gabriel, A. Eder, E. Wintner, W. Fallmann:
"Study on excimer laser applications in dentistry with special consideration of the ArF line ($\lambda = 193$ nm wavelength) ";
Presentation: 2nd Congress of the European Society for Oral Laser Applications ESOLA, Florence, Italy; 05-15-2003 - 05-18-2003; in: "Digest", (2003), 41.
29. A. Steinschaden, G. Urban, R. Chabicovsky:
"Thin film conductometric urea sensor";
Poster: 17th European Conference on Solid-State Transducers (Eurosensors XVII), Guimaraes, Portugal; 09-21-2003 - 09-24-2003; in: "CD-ROM Proceedings EUROSENSOR XVII", (2003), ISBN: 972-98603-1-9; 240 - 243.
30. P. Svasek, E. Svasek, P. Hinsmann, B. Lendl, M. Harasek, M. Vellekoop:
"Micromachined Mixing Device for FTIR-Spectroscopy";
Poster: GMe Forum 2003, Wien, Ö (invited); 04-10-2003 - 04-11-2003; in:
"Proceedings of the Seminar GMe Forum 2003", K. Riedling (ed.); (2003), ISBN: 3-901578-10-2; 183 - 187.
31. P. Svasek, E. Svasek, B. Lendl, M. Vellekoop:
"SU-8-Based Fluidic Devices";
Poster: 17th European Conference on Solid-State Transducers (Eurosensors XVII), Guimaraes, Portugal; 09-21-2003 - 09-24-2003; in: "Eurosensors XVII - Book of Abstracts", (2003), ISBN: 972-98603-1-9; 283 - 286.

Other Presentations

1. M. Vellekoop:
"Integrated Sensor Systems";
Presentation: Österreichische Akademie der Wissenschaft, Vienna, Austria (invited); 06-26-2003.

2. M. Vellekoop:
"*Physical Chemosensors*";
Presentation: Smart Sensor Systems Course 2003, Delft, The Netherlands (invited); 05-13-2003.
3. M. Vellekoop:
"*Sensing in Microfluidic Systems*";
Presentation: 6. Dresdner Sensor-Symposium - Sensoren für zukünftige Hochtechnologien und Neuentwicklungen für die Verfahrenstechnik, Dresden, Germany (invited); 12-09-2003.
4. M. Vellekoop:
"*Sensors for Medical Applications*";
Presentation: Chirurgen Kongress 2003, Bregenz, Austria (invited); 06-21-2003.

Patents

1. J. Nieuwenhuis, M. Vellekoop:
"Teilchen- und Zellentektor basierend auf der Coulter-Methode unter Verwendung einer nicht-koaxialen partiellen Schichtströmung und einer zweidimensionalen Dynamischen Apertursteuerung";
Patent: Austria, No. A672-2002; submitted: 05-02-2002, granted: 02-24-2003.

Diploma Theses

1. G. Art:
"*Entwurf und Aufbau einer neuen Auswertelektronik für den Prototyp eines Viskositätssensors*";
Supervisor: B. Jakoby; Institut für Industrielle Elektronik und Materialwissenschaften, 2003.
2. W. Fürst:
"*Transducers for physical chemosensing*";
Supervisor: M. Vellekoop; Institut für Industrielle Elektronik und Materialwissenschaften, 2003.
3. D. Janneau:
"*Viscosity measurement techniques using Thickness-Shear Mode*";
Supervisor: B. Jakoby; Institut für Sensor- und Aktuatorssysteme, 2003.

Integrated Flow-Cells for Adjustable Sheath Flows

J.H. Nieuwenhuis¹, J. Bastemeijer², P.M. Sarro³ and M.J. Vellekoop¹

¹ Industrial Sensor Systems, Institute IEMW, Vienna University of Technology, Austria

² Electronic Instrumentation Lab. – DIMES, Delft University of Technology, The Netherlands

³ Laboratory of ECTM – DIMES, Delft University of Technology, The Netherlands

In this paper two integrated flow-cells are presented that can generate novel sheath flows. The flow-cells allow for dynamic orthogonal control of the sample flow dimensions. In addition to this, the sample flow can be freely positioned inside the channel. The flow-cells are attractive, because they are very simple to fabricate and are compatible with the integration of sensors. Experiments have been carried out demonstrating that the sample flow dimensions can be controlled over a wide range; also the results show good agreement with finite element simulation results.

Introduction

The flow-cells presented here allow dynamic orthogonal control of the sample flow dimensions. Also the sample flow can be freely positioned inside the flow-channel so that the sample flow touches or nearly touches one side of the channel; this assures a good contact with any integrated sensor interface. Finally, another attractive feature of the flow-cells presented here is that they are very simple to fabricate, consisting of a two layer structure and requiring only two etch-steps to fabricate.

The flow-cells presented in this paper distinguish themselves from the flow-cells known in the literature [1] – [9] by their versatility. Both layered sheath flows and coaxial sheath flows can be realized within the same device. What is even more important, due to a number of orthogonal control mechanisms both the dimensions and the position of the sample flow can accurately be controlled. As a consequence the flow-cells can create an optimal sample flow for each specific application. And because they can be fabricated by adding a few post-processing steps to a standard IC-process, many known sensors can be integrated into the device.

Some examples of applications are: an integrated Coulter counter [10], sensors for particle shape analysis [11] and sensors for cell analysis and (bio)chemical analysis.

Flow-Cell 1: Control of Sample Flow Dimensions

Flow-cell 1 has been developed to allow dynamic control of the dimensions of the sample flow (see Fig. 1). In this flow-cell a non-coaxial sheath flow is formed by vertically injecting a sample liquid into a channel through which sheath liquid is flowing. By hydrodynamic focusing a smooth flow of sample liquid is formed that still touches the bottom of the channel. A focusing section brings the channel width down from 625 μm to a width of 160 μm . The application of such a focusing section allows the use of fairly large inlets which are convenient in handling the liquid connections to the chip. The less critical alignment of the inlets and the lower pressure drop over the wider sections

are additional advantages. The non-coaxial type of sheath flow that is formed with this flow-cell is suitable for sensors that require contact with the sample liquid such as impedance sensors. The dimensions of the sample flow can dynamically be adapted by two orthogonal control mechanisms.

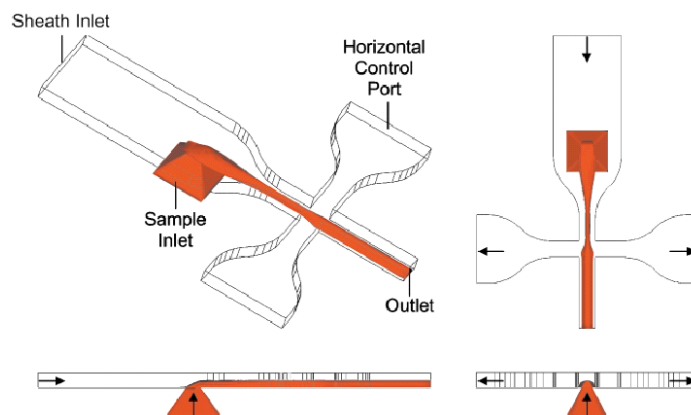


Fig. 1: Model of flow-cell 1, this flow-cell creates a non-coaxial sheath flow and allows control of the sample flow dimensions; here the control ports are used to widen the sample flow.

The vertical dimensions of the sample flow are controlled by the relative flow rate at which the sample liquid is injected in relation to the flow rate of the sheath flow. At higher relative flow rates of the sample liquid, it penetrates further into the sheath liquid thereby increasing the sample flow height. Lowering the relative flow rate of the sample liquid will result in a sample flow with less height.

The horizontal dimensions of the sample flow are controlled by two horizontal control ports that are located on the sides of the flow-channel, downstream of the sample inlet (see Fig. 1). By adding or removing sheath liquid through these control ports at an equal rate the already present sheath flow is horizontally compressed or expanded respectively which leads to a narrow or wider sample flow. Notice that the height of the sample flow is not affected by this control mechanism.

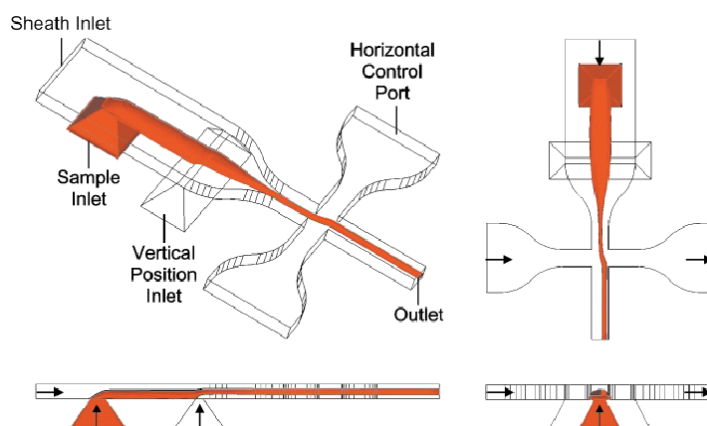


Fig. 2: Model of flow-cell 2, the additional vertical position inlet of this flow-cell also allows positioning of the sample flow in the channel; here the control ports are used to position the sample flow vertically in the centre of the channel with a horizontal shift.

Flow-Cell 2: Additional Control of Sample Flow Position

Flow-cell 2 looks quite similar to flow-cell 1, but there is one main difference. Flow-cell 2 has an additional inlet, located in between the focusing section and the sample inlet (see Fig. 2). This additional inlet gives flow-cell 2 the added functionality to freely position the sample flow anywhere inside the flow channel. Two control mechanisms are required to achieve this.

The vertical position of the sample flow is controlled by the additional vertical control inlet. When sheath liquid is added through this inlet the entire sheath flow in the channel is lifted up from the channel bottom. As a result a coaxial sheath flow is formed that no longer has any contact with the channel bottom. The more liquid is added through this inlet the higher the sample flow is positioned. This vertical position control inlet has a narrow shape ($625\ \mu\text{m} \times 350\ \mu\text{m}$) to create a flow profile through this inlet that is as uniform as possible. This means that the shape of the sample flow is hardly influenced by the vertical position control, except for some vertical compression.

The same horizontal control ports that are used to control the width of the sample flow can also be used to control its position. In this type of operation the direction of flow through both inlets is now opposite. By adding sheath liquid through one of the control ports and removing it from the other inlet at the same flow rate the sample flow is shifted in the horizontal plane. Apart from the additional inlet the configuration of the inlets of flow-cell 2 is similar to that of flow-cell 1, therefore the sample dimension control mechanisms described for that flow-cell work for flow-cell 2 as well. The coaxial flow that can be achieved with this flow-cell is very suitable for sensors that do not require any contact with the sample liquid and especially those sensors in which the interface might get polluted such as optical sensors.

Fabrication of the Flow-Cells

Both types of flow-cells can be fabricated using the same, relatively simple process. In a glass wafer by isotropic etching the channel is defined with a depth of $100\ \mu\text{m}$ and a minimum width of $160\ \mu\text{m}$. In a silicon wafer by isotropic etching through-holes are defined that form the liquid inlets of the device. The glass wafer and the silicon wafer are then anodically bonded together to form the complete devices. A photograph of a flow-cell chip is depicted in Fig. 3.

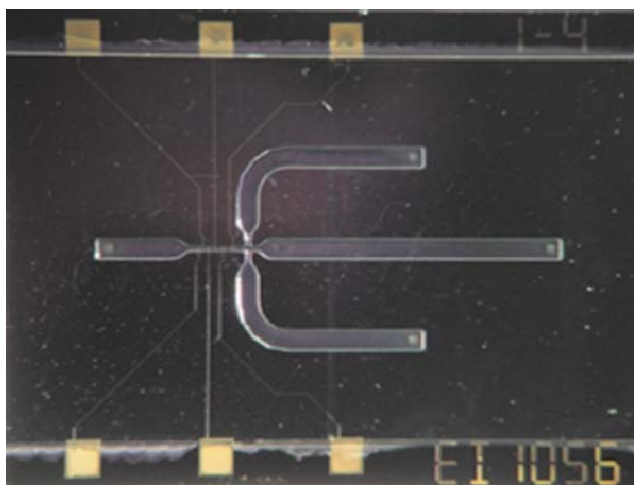


Fig. 3: The flow-cell chip with dimensions of 2 cm by 1.5 cm (the electrical contacts are not used in the experiments).

There are a number of reasons to make the devices like this. Firstly, the dimensions of the sample inlet need to be accurate and etching of silicon can be easier controlled than glass etching. Secondly, with the liquid inlets in the silicon part the glass side of the device is still available for optical inspection during operation. Finally, since the channel was etched in the glass wafer the surface of the silicon wafer is still smooth and suitable for future integration of sensors to form a complete integrated analysis system.

Experimental Verification

Sample Diffusion

First a reference experiment was carried out to determine the influence of diffusion and to see how well it can be modeled. In this experiment the ratios of the flow rate of the sample liquid, the flow rate through the control ports and the flow rate of the sheath-liquid were kept constant at 1:5:10. During the experiment the total flow rate was varied from 1 to 50 $\mu\text{l min}^{-1}$. The intensity of the dye was measured in the wider section following the narrow section (see Fig. 4), since in this location the visible area is not blocked so much by the rounded corners of the isotropic etching of the channel.

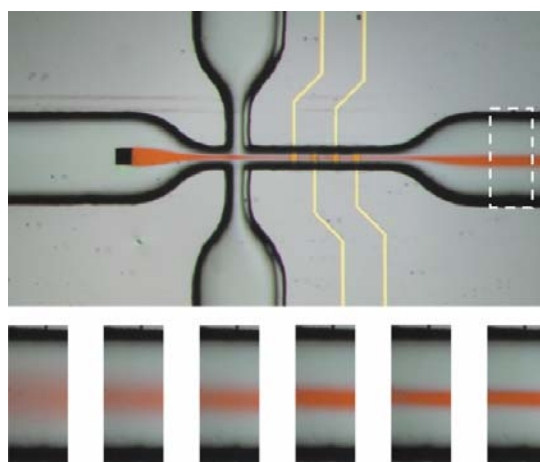


Fig. 4: Illustrative results from the diffusion experiment.

There is a very good agreement between experimental and simulation results. This means that the finite element model represents the real flow-cell very well and that this model can be used for the further experiments. The influence of diffusion is realistically taken into account in the experiments, and for a flow rate higher than 10 $\mu\text{l min}^{-1}$ the influence of diffusion is small, so measurements can be carried out at this flow rate.

Vertical Control of Sample Flow Dimensions

In the first control experiment the vertical dimensions of the sample flow were controlled. Since for this measurement the width control of the sample was not necessary, a device without horizontal control ports was used similar to flow-cell 1. During the experiment the flow rate of the sheath liquid was kept constant at 10 $\mu\text{l min}^{-1}$ and six different flow rates for the sample liquid were applied in a range from 0.05 to 2 $\mu\text{l min}^{-1}$, which correspond to relative sample flow rates of 0.5% to 20% of the sheath flow rate. Again the intensity of the dye was measured in the wide section of the channel, downstream of the narrow section. Some illustrative results are depicted in Fig. 5.

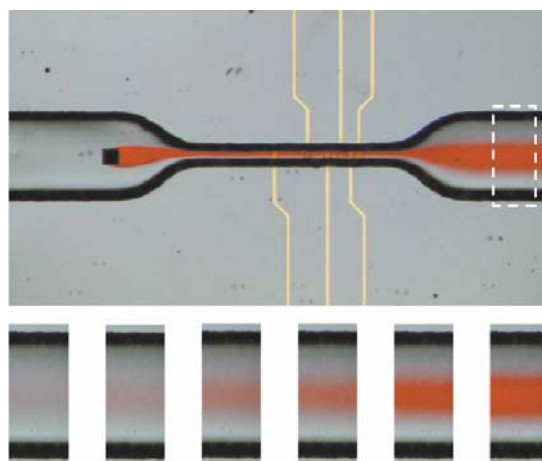


Fig. 5: Illustrative results from the sample height control experiment.

In Fig. 5 it can be seen that the width of the sample is constant for relative flow rates of the sample flow up to 10%; at the highest flow rate the sample flow becomes slightly wider. The results show that the height of the sample can be controlled over a wide range. For the relative flow rates used in the experiment the height of the sample flow can be controlled from 3 to 60 μm in a channel with a depth of 100 μm .

Horizontal Control of Sample Flow Dimensions

In the second control experiment the horizontal dimensions of the sample flow were controlled. During this experiment the sheath liquid and sample liquid flow rates were kept constant at 10 $\mu\text{l min}^{-1}$ and 1 $\mu\text{l min}^{-1}$ respectively. The flow rate through each control port was varied from -3 to $+25$ $\mu\text{l min}^{-1}$. The dye was measured at the same location as in the previous experiments; here it was even more important to have a visible area that is maximally wide. Some illustrative results are depicted in Fig. 6.

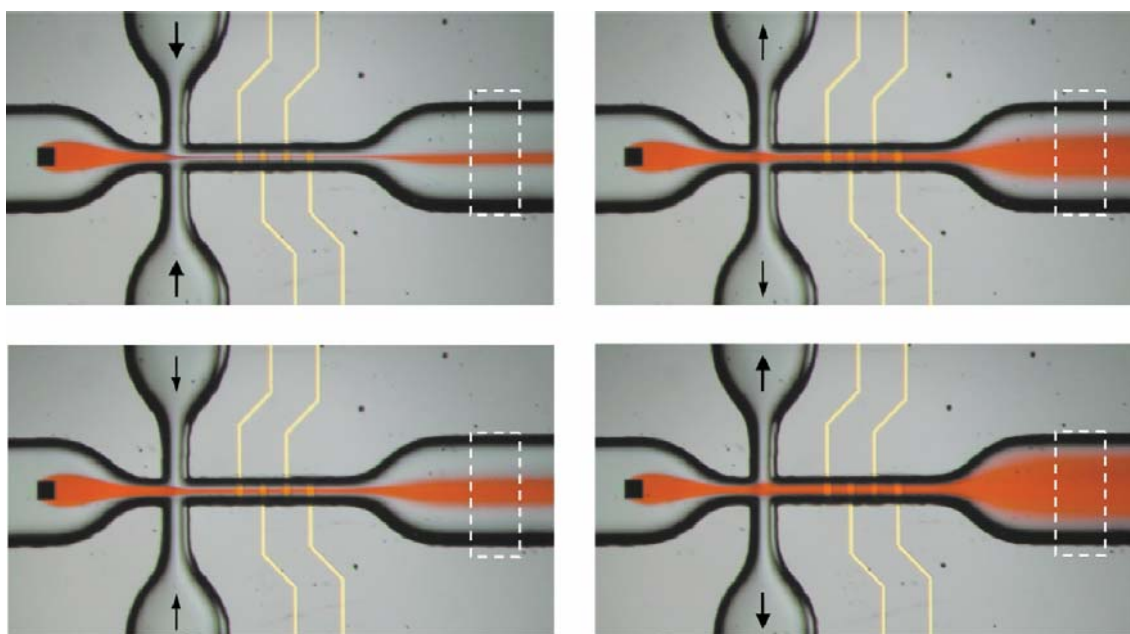


Fig. 6: Illustrative results from the sample width control experiment.

Sample flow splitting and switching

The flow-cell used in the experiment turned out to be a very flexible device. Besides the horizontal and vertical control of the sample also other useful functions can be realized. The first example is sample splitting. For this application only one control port is used. Through this inlet 50% of the total flow of liquid is removed. This results in an equal splitting of the sample (see Fig. 7). By removing more or less liquid through the control port an unequal splitting of the sample is also possible of course.

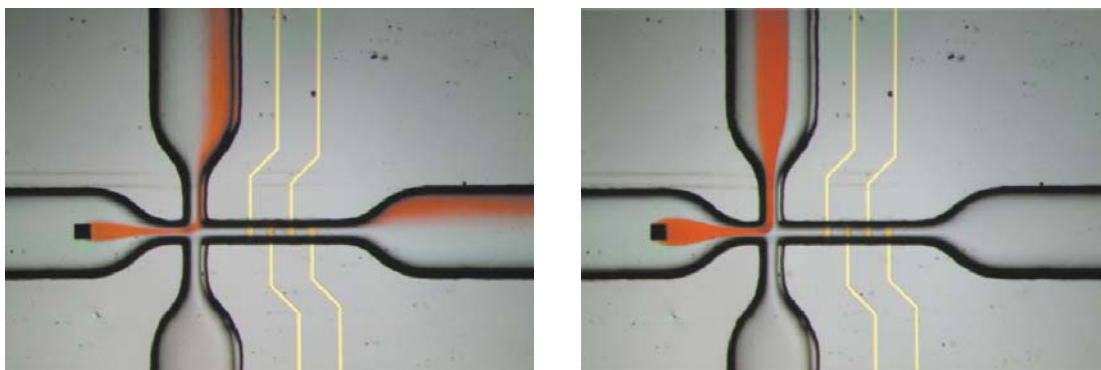


Fig. 7: The flow-cell applied for sample splitting (left) and flow-switching (right).

A second example of the flexibility of the flow-cell is sample switching. Here again only one control port needs to be active. This time the liquid is removed through the control port at a flow rate that equals the flow rate of the total flow of liquid. As a result the complete sheath flow including the sample liquid is switched (see Fig. 7). When a coaxial sheath flow is used such as can be generated with flow-cell 2 this is even possible without the sample liquid touching any wall of the channel.

Conclusions

Two new flow-cells have been developed that are very versatile. The flow-cells can generate both non-coaxial and coaxial sheath flows. Using an orthogonal control mechanism the flow-cells allow dynamic control of the sample flow dimensions. With one additional vertical position inlet the sample flow can also be freely positioned inside the channel. The processing of the flow-cells is very simple, and can be easily combined with the integration of sensors to form a complete integrated analysis system.

Experiments were carried out with one of the flow-cells and compared with finite element simulations performed with the Netflow-module of the finite element package Coventorware. Detailed models of up to 100 000 elements with a well designed grid were required to obtain a high-enough accuracy. Besides the geometry of the model and the flow rates also the diffusion constant of the dye was included in the simulations. A comparison of experimental results and simulation results shows that the complicated flow behavior of the device can be modeled very accurately. Also the influence of diffusion is realistically taken into account. The results on the horizontal and vertical control of the sample flow dimensions show that both mechanisms work well and that they can be predicted from simulation results. The control ports make the flow-cells very versatile so that they can also be used for other applications such as sample splitting and flow switching.

Acknowledgement

The authors would like to thank the DIMES Technology Centre of the Delft University of Technology for the fabrication of the device, especially Mr. C. R. de Boer and Mr. W. van der Vlist. The authors also would like to thank Dr. A. Bossche and Mr. P. Turmezei of the Electronic Instrumentation Laboratory, Delft University of Technology for fruitful cooperation and useful discussions. Finally, the authors thank the Hochschuljubiläumsstiftung der Stadt Wien for financial support.

References

- [1] M. Tidare, H. Roos and U. Lindberg, Hydrodynamic Addressing; A Flow Cell for Improved Signal Quality in Bioanalytical Systems, , in Proc. of Transducers '01, Munich, Germany, June 10–14, 2001, pp. 1154–1157.
- [2] O. Hofmann, P. Niedermann and A. Manz, Modular Approach to Fabrication of Three-Dimensional Microchannel Systems in PDMS – Application to Sheath Flow Microchips, *Lab Chip*, 2001, **1**(2), 108–114.
- [3] U. D. Larsen, G. Blankenstein and J. Branebjerg, Microchip Coulter particle counter, , in Proc. of Transducers '97, Chicago, June 16–19, 1997, pp. 1319–1322.
- [4] K. Roberts, M. Parameswaran, M. Moore and R. S. Muller, A Silicon Microfabricated Aperture for Counting Cells using the Aperture Impedance Technique, , Proc. of 1999 IEEE Canadian Conference on Electrical and Computer Engineering, Edmonton, Alberta, Canada, May 9–12, 1999, pp. 1668–1673.
- [5] G. Lee, B. Hwei and G. Huang, Microfluidic Chips with MxN Continuous Sample Introduction Function Using Hydrodynamic Flow Switching, , in Proc. of Transducers '01, Munich, Germany, June 10–14, 2001, pp. 1158–1161.
- [6] R. Miyake, H. Ohki, I. Yamazaki and R. Yabe, A Development of Micro Sheath Flow Chamber, in Proc. of MEMS '91, 1991, pp. 265–270.
- [7] K. Tashiro, T. Sekiguchi, S. Shoji, T. Funatsu, W. Masumoto and H. Sato, Design and Simulation of Particles and Biomolecules Handling Micro Flow Cells with Three Dimensional Sheath Flow, , in Proc. of μ TAS 2000, Enschede, The Netherlands, May 14–18, 2000, pp. 209–212.
- [8] A. Wolff, U. D. Larsen, P. Friis and P. Telleman, Chip-Integrated Microfluidic System for Cell Sorting and Cell Culturing, , in Proc. of Eurosensors XIV, Copenhagen, Denmark, August 27–30, 2000, pp. 235–238.
- [9] D. Huh, Y. Tung, H. Wei, J. B. Grothberg, S. J. Skerlos, K. Kurabayashi and S. Takayama, Use of Air-Liquid Two-Phase Flow in Hydrophobic Microfluidic Channels for Disposable Flow Cytometers, *Biomed. Microdev.*, 2002, **4**(2), 121–149.
- [10] J. H. Nieuwenhuis, J. Bastemeijer, P. M. Sarro and M. J. Vellekoop, Integrated Coulter counter with non-coaxial sheath-flow and dynamic aperture control, , in Proc. of Eurosensors XVI, Prague, Czech Republic, September 15–18, 2002, pp. 1194–1197.
- [11] J. H. Nieuwenhuis, J. Bastemeijer, A. Bossche and M. J. Vellekoop, Dynamic Particle-Shape Measurements Using a Near-Field Optical Sensor, in Proc. of 1st IEEE Sensors Conference, June 12–14, 2002, Orlando, Florida, USA.

Particle Behavior in a Non-Coaxial Sheath Flow

J.H. Nieuwenhuis and M.J. Vellekoop
Institute of Industrial Electronics and Material Science, TU Wien

Introduction

In this paper a study is presented on the behavior of particles in a sheath flow. In general a sheath flow in a micro-channel has many benefits [1], such as fewer problems with air-bubbles, a low detection limit and less critical fabrication tolerances. A series of experiments was designed to investigate whether it is feasible to have these benefits of a sheath flow also in micro-systems for the analysis of particles.

The studied sheath flow is to be applied in an integrated Coulter counter [2] with a liquid based aperture defined by a non-coaxial sheath flow [3]. The sheath flow consists of a non-conductive liquid that partially surrounds a flow of conductive liquid, which defines the Coulter aperture. The main advantage of this device is that the Coulter aperture can be optimized dynamically to the particle size.

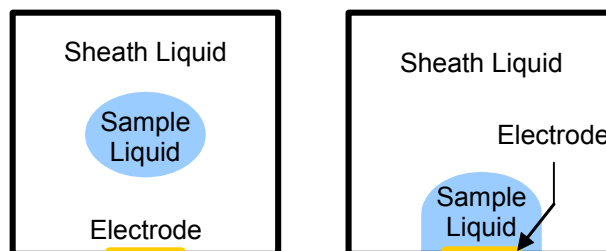


Fig. 1: In the traditional coaxial sheath flow, the sheath liquid completely surrounds the sample liquid (left); in the non-coaxial sheath-flow studied here the sample liquid still touches the channel wall.

Sheath Flow

A sheath flow can be defined as a combined flow profile in a channel that consists of two non-interacting liquids. One of these liquids is the sample liquid that is to be analyzed and the second liquid, the sheath liquid, has the function to control the position and to fix the dimensions of the flow of sample liquid. Micro-systems are very suitable to be used with a sheath flow because due to the small channel dimensions the Reynolds number is low and as a consequence the flow behavior is typically laminar.

The most common sheath flow is the coaxial sheath flow, where the sheath liquid completely surrounds the sample liquid in the channel cross-section (see Fig. 1 left). This particular flow-profile is most often combined with optical analysis systems. However, in our application an electrical contact with the sample liquid is required and therefore a non-coaxial flow profile will be used (see Fig. 1 right). In this flow profile the sample liquid still touches the channel wall which allows measuring the impedance of a certain section of the sample flow.

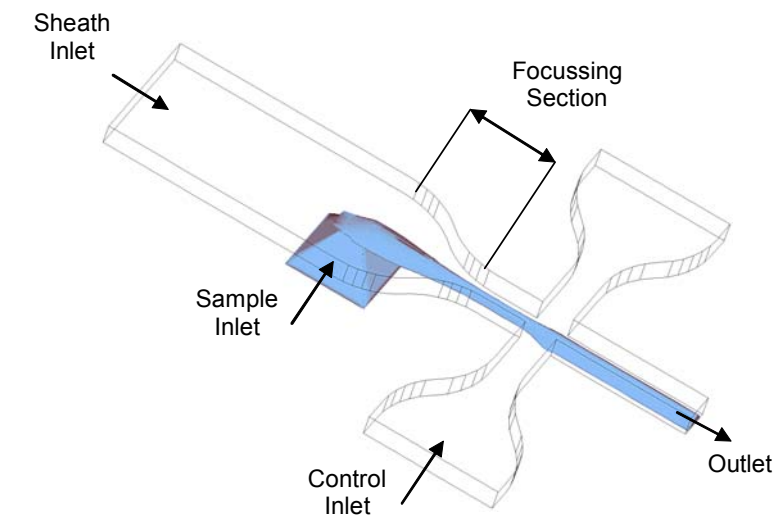


Fig. 2: The non-coaxial sheath flow is formed by injecting the sample liquid perpendicularly into a channel through which sheath-liquid is flowing.

The non-coaxial flow profile is obtained with a micro-machined flow-cell that is depicted in Fig. 2. The sheath-liquid flows through a micro-channel, and at a certain point, perpendicular to the direction of flow, the sample liquid is injected into the sheath liquid. Due to hydrodynamic focusing a narrow stream of sample liquid is formed that is partially surrounded by the sheath liquid. A focussing section down-stream of the sample inlet reduces the lateral dimensions of the sheath-flow to the right order of size. The two control inlets finally allow adapting the sample flow dimensions to the size of the particles to be analyzed [3].

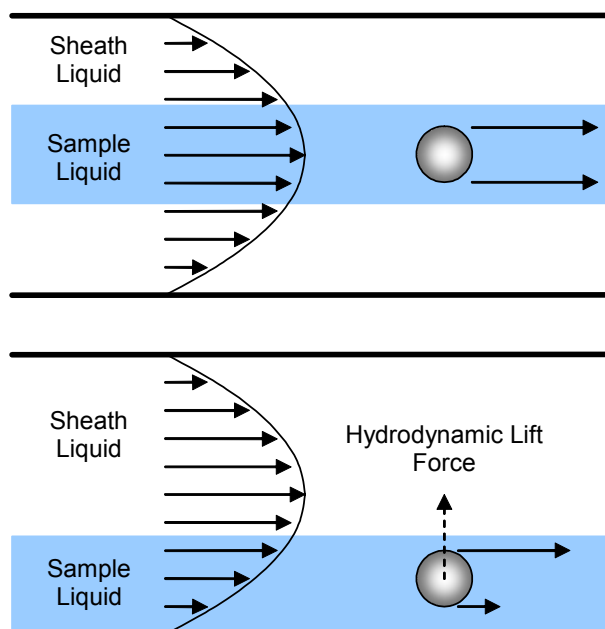


Fig. 3: In the coaxial sheath-flow the parabolic flow profile does not cause any net forces in the vertical plane (top); in the non-coaxial sheath flow the particle experiences a velocity gradient, which results in a hydrodynamic lift force (bottom).

Particle-Liquid Interaction in a Parabolic Flow Profile

The electrical particle size measurements with the Coulter counter are possible only when the particles remain in the core of conductive sample liquid, but this is not trivial. Since the integrated Coulter counter will use a pressure-driven flow to move the liquids through the device the velocity profile in the channel will be parabolic. In the case of the axis-symmetric flow-profile of the classical coaxial-sheath flow the particle will still undergo a symmetrical velocity gradient that does not give rise to any net force pushing the particles out of the centre of the flow.

However, for the non-coaxial sheath flow analyzed here the situation is quite different. The particles are located in the sample liquid at the bottom of the channel and will therefore experience a non-symmetrical velocity gradient (see Fig. 3) that will result in hydrodynamic lift forces that tend to push the particle in the direction of the highest flow velocity. The dominant effect is the Bernoulli effect: the pressure in a fluid decreases as the speed of the fluid increases. Since the speed over the particle is higher than the speed underneath the particle, the particle will experience an upward force.

Experiments

Due to the planar nature of the device (see Fig. 4) it is only possible to study the particle behavior from the top view, so only its behavior in the horizontal plane can be observed. To overcome this problem a series of controlled experiments was designed that not only allows to draw conclusions about particle behavior in the horizontal plane, but also permits conclusions about their behavior in the vertical plane from observations in the horizontal plane.

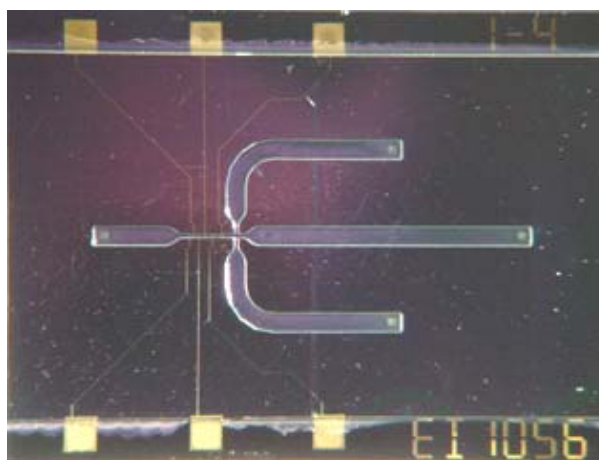


Fig. 4: Photograph of the sheath flow chip.

In the first experiment the flow-cell is used under normal operation conditions. The sample liquid is focused in the aforementioned non-coaxial sheath flow in the middle of the channel in the horizontal plane (see Fig. 5 (a)). It can be seen the particles do not leave the sample liquid, which was to be expected, since the particles do not experience a gradient in the velocity in the horizontal plane. From this experiment it can also be seen that a stable and smooth sheath flow is formed.

In the second experiment the control inlets that are normally used to control the width of the sample flow are now used to focus the sample liquid to one side of the device. The particles experience a steep velocity gradient in the horizontal plane and as a consequence they are exposed to a hydrodynamic force towards the middle of the chan-

nel. But from Fig. 5 (b) it becomes clear that in the horizontal plane the particles remain within the sample flow. From these results it can be concluded that under normal operation the particles (with a density equal to or higher than the density of the liquid) will not leave the sheath flow in the vertical plane, since the conditions are comparable in the vertical plane, and additionally the particles will also be pulled down by gravitation.

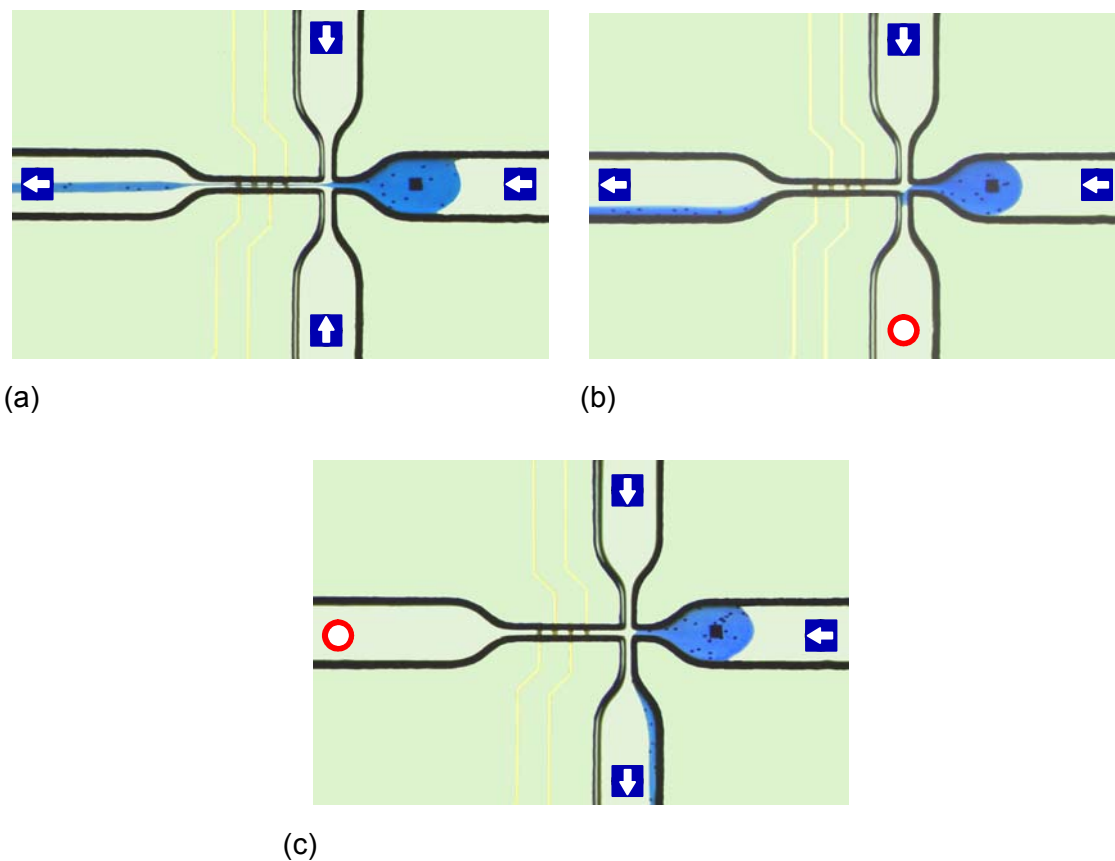


Fig. 5: Photographic results of the experiments; the sample liquid is successively focused in the center (a), to one side (b) and forced to make a steep turn (c).

From the previous two experiments it can be concluded that once the particles are located in the sample flow they will not leave it. To investigate whether the particles will stay in the sample flow just after the injection into the flow channel a third experiment was carried out. Now the sample flow with the particles is focused to one side and forced to make a steep turn. This experiment mimics the situation at the sample inlet, where the particles enter the flow channel from the bottom and are forced to make a steep 90 degree turn. If the particles would not be able to make such a steep turn at the sample inlet, they might end up in the sheath liquid as a consequence of centrifugal forces. This situation has been transformed into the horizontal plane with this experiment. In Fig. 5 (c) it can be seen that again the particles do not leave the sample liquid. This means that apparently the centrifugal forces are not dominant.

Conclusions

From the experiments it can be concluded that laminar flow conditions are present in the flow channel and that a stable sheath flow is formed. Once particles are in the sample liquid of the sheath flow they will remain there despite hydrodynamic lift forces that push the particle in the direction of the highest liquid velocity. Steep corners will

also not cause the particles to leave the sample liquid despite centrifugal forces. So, in summary, the particle behavior in the sheath flow studied here is such that the particles will always remain in the sample liquid which makes the sheath flow suitable for application in an integrated Coulter counter or other particle analysis instruments.

References

- [1] J.H. Nieuwenhuis, J. Bastemeijer, P.M. Sarro, M.J. Vellekoop, Virtual Flow Channel: A Novel Micro-Fluidics System with Orthogonal, Dynamic Control of Sample Flow Dimensions, Proc. of μ TAS 2002, November 3-7, Nara, Japan
- [2] W.H. Coulter, Means for counting particles suspended in a fluid, US patent no. 2,656,508, October 20, 1953
- [3] J.H. Nieuwenhuis, J. Bastemeijer, P.M. Sarro, M.J. Vellekoop, Integrated Coulter Counter with Non-Coaxial Sheath-Flow and Dynamic Aperture Control, Proc. of Eurosensors 2002, September 15-18, Prague, Czech Republic, p1194-1197

An Integrated Projection Cytometer

J.H. Nieuwenhuis¹, J. Bastemeijer², P.M. Sarro² and M.J. Vellekoop¹

¹ Industrial Sensor Systems, Institute of IEMW, Vienna University of Technology

² DIMES, Delft University of Technology, Delft, The Netherlands

Introduction

In this paper we present an integrated projection cytometer (see Fig. 1) and the first measurements results obtained. The device has a near-field optical sensor [1] capable of counting, sizing and measuring the shape of particles. Furthermore, it has a flow-cell that creates a non-coaxial sheath flow [2] that focuses the particles close over the sensor surface, thereby minimizing diffraction of the light.

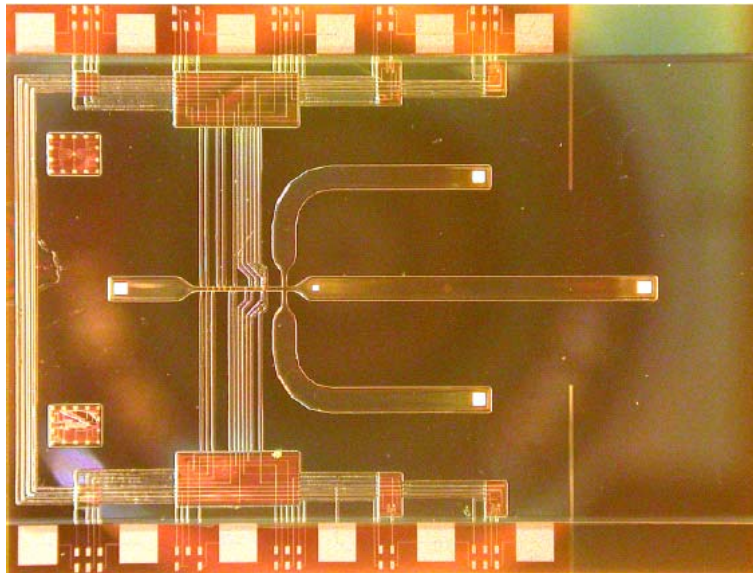


Fig. 1: The integrated projection cytometer chip (1.5 x 2 cm²)

Operation Principle

On the bottom of the flow-channel elongated photodiodes (see Fig. 2) are defined: length 50 μm , width 1 μm . The photodiodes are illuminated from the top by a parallel beam of light, and when a particle passes it partially blocks the light, resulting in a drop in photocurrent proportional to the width of the particle. From the obtained cast shadow particle size and shape properties can be extracted.

Device Fabrication

The device consists of a two-layer glass-silicon sandwich. The silicon wafer contains the photodiode sensors, which were made in a bipolar process. As a post-processing

step through-holes were etched to form the liquid inlets. In the glass wafer the channel was defined by wet-etching. Finally the wafers were bonded together using anodic bonding at 400 °C and 1 kV.

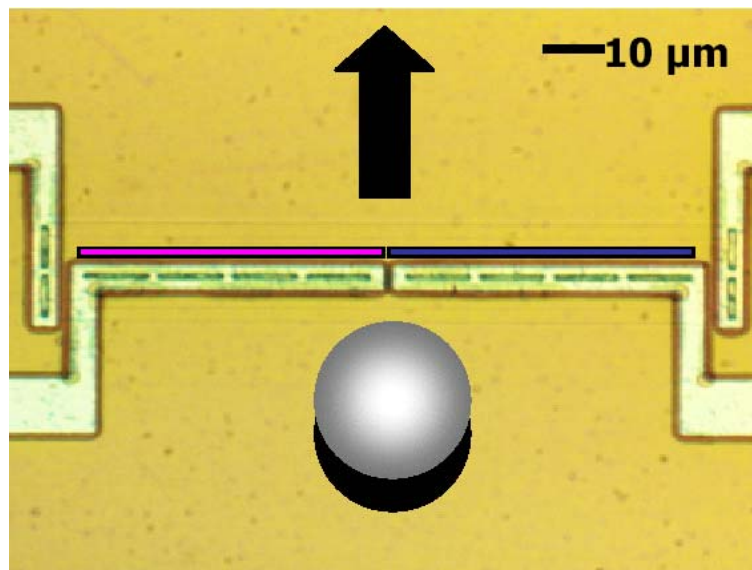


Fig. 2: The photodiodes (pink/blue squares) register the cast shadow of a passing particle

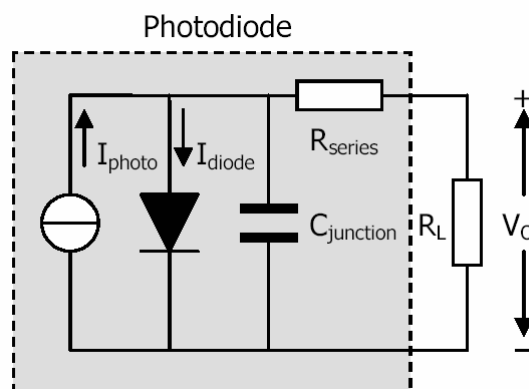


Fig. 3: A simplified equivalent circuit for the photodiode with photovoltaic readout

Measurements

The photodiodes were illuminated using a microscope light source; with an optical fiber the light was directed perpendicular to the device surface. The photodiodes were connected in photovoltaic mode (see Fig. 3) to minimize noise and dark currents using a 10 MΩ load resistor (R_L). In the first experiment the light intensity was increased in steps to verify reliable operation over a wide range of light intensities and to check the photodiode matching (see Fig. 4 (a)); the output voltage clips at 0.55V, here the PN-junction comes into forward bias. Next a suspension of spherical polystyrene particles (diameter 25 μm) was pumped through the device. The results (see Fig. 4 (b)) show

that the particles can be clearly detected when they pass the sensor and the shape of the signals seems quite consistent. The difference in drop of photocurrent for both photodiodes of the sensor indicates that particles do not pass over the middle of the sensor (off-set about 6 μm). This is probably due to some small geometrical asymmetry.

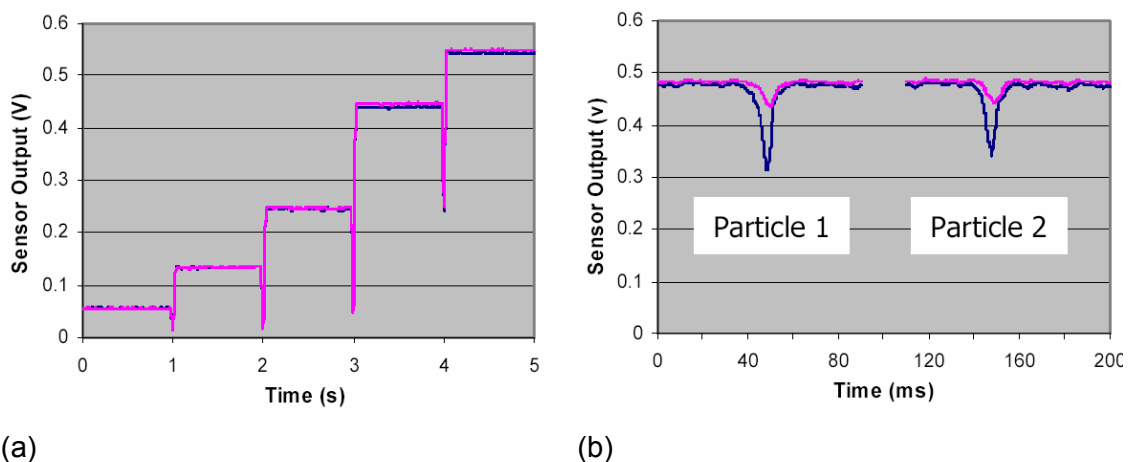


Fig. 4: (a) Sensor outputs (pink, blue) for different intensities of the light-source; (b) Measured sensor outputs (pink, blue) for two passing particles.

Discussion

The drop in photocurrent is slightly less than expected and also the height of the peaks between different particles shows some variation. This is most likely due to the non-ideal optical configuration. The rounded shape of the channel, caused by the wet etching, might cause refraction of the light rays (see Fig. 5). As a consequence, the incoming light-rays are no longer parallel and can create internal reflections which distort the projection. These effects can be reduced by carefully matching the refractive index of the liquid to that of the glass or by using a square channel, made with SU8.

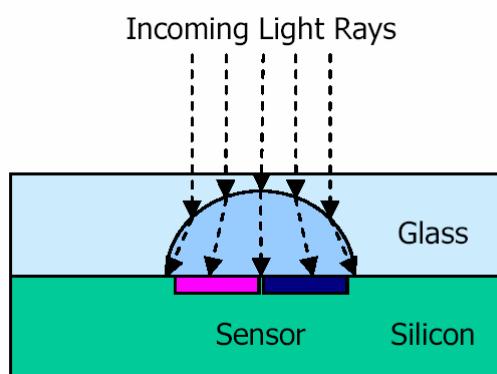


Fig. 5: A cross-sectional view of the optical setup showing possible refraction of the light

Conclusions

First measurement results were obtained with a fully integrated projection cytometer. Particles can clearly be detected, and the pulse shape is repeatable. A slight geometrical mismatch probably causes the particles not to move exactly over the middle of the sensor.

References

- [1] J.H. Nieuwenhuis, J. Bastemeijer, A. Bossche, M.J. Vellekoop, "Dynamic Particle-Shape Measurements Using a Near-Field Optical Sensor", Proc. of 1st IEEE Sensors Conference, June 12-14, Orlando, USA, 2002, pp. 130–133
- [2] J.H. Nieuwenhuis, J. Bastemeijer, P.M. Sarro, M.J. Vellekoop, "Integrated Flow-Cells for Novel Adjustable Sheath Flows", Lab On A Chip Journal, 2003, 3, 56–61

Micromachined Mixing Device for FTIR Spectroscopy

P. Svasek¹, E. Svasek¹, P. Hinsmann², B. Lendl², M. Harasek³
and M.J. Vellekoop⁴

¹ Ludwig Boltzmann Institute of Biomedical Microtechnology, Vienna

² Institute of Chemical Technologies and Analytics, Vienna University of Technology

³ Institute of Chemical Engineering, Vienna University of Technology

⁴ Institute of Industrial Electronics and Material Science, Vienna University of Technology

Time-resolved FTIR-spectroscopy is a powerful method for the investigation of chemical reactions, especially in the field of biochemistry. It allows obtaining structural information of molecular dynamics. This method requires fast mixing of at least two reactants as well as a very short optical pathlength because of the strong IR-absorption of water and organic solvents. To meet these requirements a micromachined mixing device was developed which combines fast diffusion based mixing and an optical pathlength of less than 20 μm . The devices are batch fabricated on 4" CaF_2 wafers.

Introduction

Time-resolved Fourier transform infrared spectroscopy is an efficient technique to study chemical reactions and obtain structural information of molecular dynamics [1], [2]. This method requires fast mixing of the reactants. Additionally, the event under study must be precisely repeatable to provide a good signal/noise ratio. Water and organic solvents show a very high absorption in the mid-IR range, therefore the optical pathlength of the device has to be very short, typically less than 20 μm . The principle of the mixing device is shown in Fig. 1.

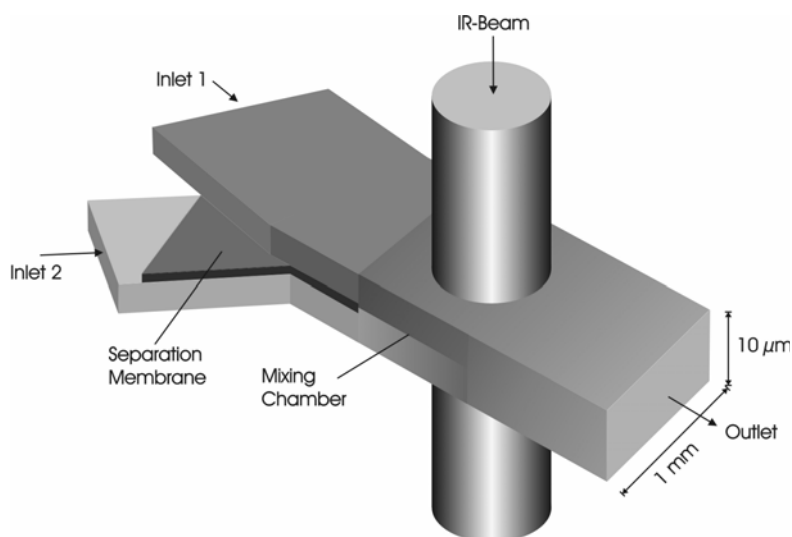


Fig. 1: Schematic drawing of the micromixer (drawing not to scale).

The mixer is operated in the “stopped flow” mode. Two liquids are injected by means of a double piston syringe pump into inlet 1 and inlet 2. These two streams are separated by a metal separation membrane until they enter the mixing chamber. Inside this chamber the liquids form two thin sheets which are superimposed. While the flow is on there is hardly any mixing due to laminar flow conditions in microfluidic devices. As soon as the flow is stopped, which is done by means of a dedicated fluidic setup [2], the liquids are mixed by diffusion. Diffusion is a rather slow process; therefore the distances have to be kept as short as possible. Fluid dynamic simulations performed with FLUENT V5.5 showed as a result a mixing time of 100 ms for water based solutions. The height of the mixing chamber was 20 μm [1]. The mixing chamber of the latest device is 10 μm high, therefore one can assume a mixing time of ~ 25 ms.

Preparation of the Mixing Device

The devices are fabricated using micromachining methods like photolithography and waferbonding. As a substrate material we use CaF_2 because of its superior optical properties. The fluid channels are formed by two layers of the negative-working epoxy based photoresist SU-8. During the last years this material has been widely used because of its very good mechanical and chemical properties.

The devices are built up as follows: A 4 μm thick layer of SU-8 is deposited by spin-coating, softbaked, exposed, post-exposure-baked, but not developed. On top of this layer a 2 μm thick layer of Ag is deposited by evaporation. This metal layer is then covered by positive photoresist AZ 1512 HS. The photoresist is patterned as usual and the Ag layer is etched to obtain the structure of the “separation membrane” (see Fig. 1). As an etchant a 45 % (WT) solution of $\text{Fe}(\text{NO}_3)_3$ in water is used. This solution does not attack the SU-8. Finally the SU-8 is developed with PGMEA. To dissolve unexposed SU-8 under the metal structure takes quite some time (approx. 2 hours for channels of 1 mm length). Wafer #1 (the “bottom” wafer) now carries the structures of Inlet 2 and the separation membrane.

On wafer #2 (the “top” wafer) the structure of inlet 1 is fabricated as usual from a 4 μm thick layer of SU-8. This wafer contains the holes for two inlets and one outlet per mixer. These holes are conventionally drilled by means of a high speed spindle attached to a computer-controlled mill. So far the SU-8 on both wafers is not hardbaked and therefore the polymer is not completely crosslinked. Both wafers are superimposed face to face, and aligned. Hardbaking is done in an EVG 501 wafer bonder. A force of 1700 N is applied and the wafers are heated to 200 $^\circ\text{C}$ for 1 hour. Because of this high temperature the polymer is completely crosslinked and a bond is established between SU-8 and the opposite Ag-structure (see Fig. 2).

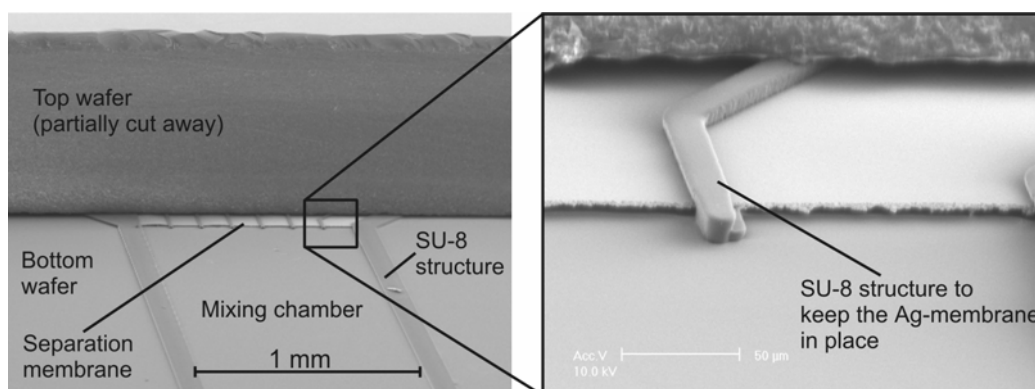


Fig. 2: SEM micrograph of the mixing device. The top wafer is partially cut away to show the SU-8-structures and the separation membrane.

The stream of liquid from inlet 1 flows between the top wafer and the separation membrane, the stream from inlet 2 flows between the separation membrane and the bottom wafer. At the edge of the membrane the streams meet and enter the mixing chamber (see Fig. 2).

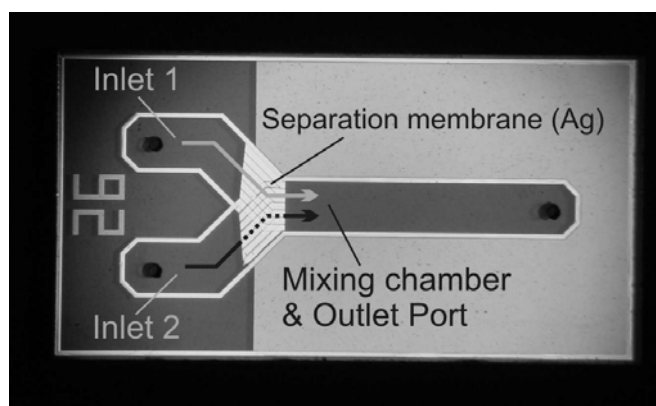


Fig. 3: Micrograph of the mixing device after dicing. The dimension of the device is $6 \times 12 \times 2 \text{ mm}^3$.

Results Obtained from Model Reactions

If reactants are used which react very fast, the reaction is limited by diffusion only. Consequently in this case the experiment is actually a test of the mixer performance (see Fig. 4). It can be observed clearly that the mixing time meets the result of the CFD simulation. Some premixing (i.e. formation of reaction product) can be observed while the flow is on. Premixing cannot be neglected in case of very fast reactions [1]. In case of a slow reaction no formation of the reaction product can be observed, as shown in Fig. 5. This reaction is completed after a few hundred milliseconds.

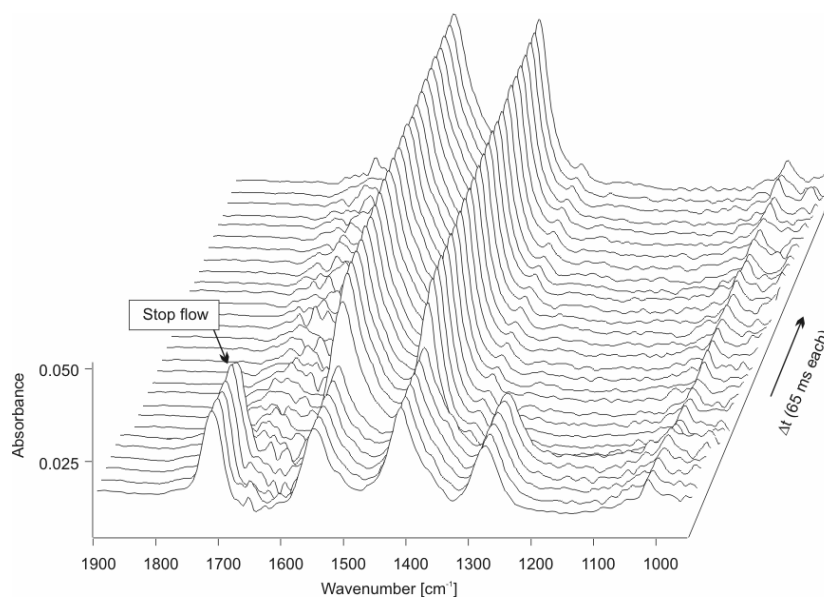


Fig. 4: Stack plot of FTIR spectra obtained from the reaction of CH_3COOH and NaOH . Time delay between subsequent spectra is 65 ms.

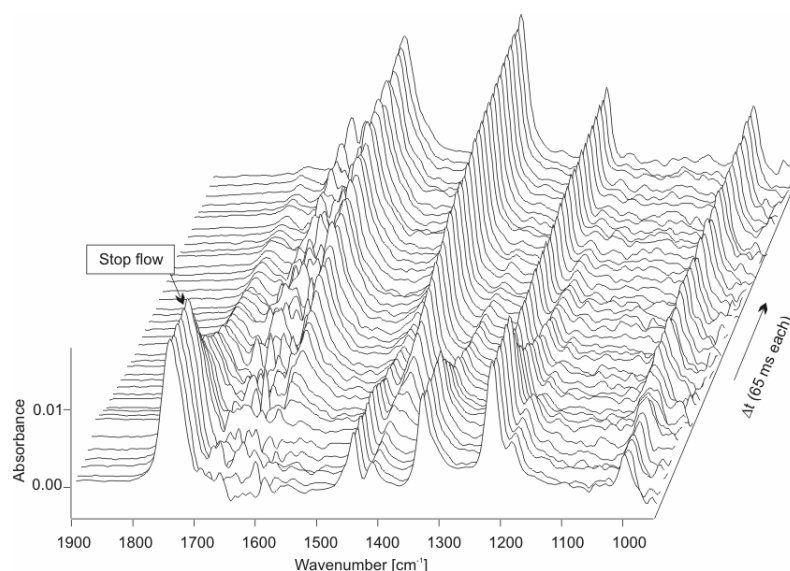


Fig. 5: Spectra obtained from the reaction of methyl monochloroacetate and sodium hydroxide. Time delay between subsequent spectra is 65 ms.

Conclusion

The micromachined mixing device presented in this paper offers the opportunity to investigate the dynamics of chemical reactions, especially in the field of biochemistry [3]. The results of the CFD simulations were confirmed by experiments. To realize this device a special technique was developed that combines two layers of SU-8 photoresist and one layer of metal. This technique is useful for the fabrication of other microfluidic devices as well. The devices are produced in a batch process using 4-inch wafers of Calcium Fluoride, a material that shows very good optical properties.

Acknowledgement

This work was supported by the *Ludwig Boltzmann Institute of Biomedical Microtechnology*, Vienna.

References

- [1] P. Hinsmann, J. Frank, P. Svasek, M. Harasek, B. Lendl; "Design, simulation and application of a new micromachining device for time resolved infrared spectroscopy of chemical reactions in solution", *Lab on a Chip*, 1(2001), 16-21
- [2] P. Hinsmann, M. Haberkorn, J. Frank, P. Svasek, M. Harasek, B. Lendl; "Time-resolved FT-IR spectroscopy of chemical reactions in solution by fast diffusion-based mixing in a micromachined flow cell", *Applied Spectroscopy*, 55 (2001), 3; 241 - 251.
- [3] B. Lendl, P. Hinsmann, P. Svasek, J. Frank; "Device for label-free bio-ligand interaction studies based on time resolved fourier transform infrared spectrometry", *Proceedings of the μ TAS 2002 Symposium (2002)*, ISBN: 1-420-1009-5; 221-223

ISBN: 3-901578-12-9

© 2004 Gesellschaft für Mikro- und Nanoelektronik (GMe)
c/o Technische Universität Wien
Institut für Sensor- und Aktuatorssysteme
Gusshausstraße 27-29/366, A-1040 Wien